UNIVERSIDADE DE SANTIAGO DE COMPOSTELA

Departamento de Física de Partículas
Instituto Galego de Física de Altas Enerxías

Study of the decays $B^0_{(s)} \to K^{*0}\overline{K}^{*0}$ and first observation of the $B^0_s \to \phi\overline{K}^{*0}$ decay at the LHCb experiment

Brais Sanmartín Sedes

Tese de doutoramento

Programa de Doutoramento
en Física Nuclear e de Partículas

USC
UNIVERSIDADE
DE SANTIAGO
DE COMPOSTELA

UNIVERSIDADE DE SANTIAGO DE COMPOSTELA

Departamento de Física de Partículas
Instituto Galego de Física de Altas Enerxías

Study of the decays $B^0_{(s)} \to K^{*0}\overline{K}^{*0}$ and first observation of the $B^0_s \to \phi\overline{K}^{*0}$ decay at the LHCb experiment

Brais Sanmartín Sedes

Tese de doutoramento

Programa de Doutoramento
en Física Nuclear e de Partículas

Author: Brais Sanmartín Sedes

Supervisor: Bernardo Adeva Andany
Supervisor: Cibrán Santamarina Ríos

Text printed in Santiago de Compostela
First edition, September 2017

D. BERNARDO ADEVA ANDANY, Catedrático de Física Atómica, Molecular e Nuclear da Universidade de Santiago de Compostela e D. CIBRÁN SANTAMARINA RÍOS, Profesor Contratado Doutor de Física Atómica, Molecular e Nuclear da Universidade de Santiago de Compostela, informan:

Que a memoria titulada "*Study of the decays* $B^0_{(s)} \to K^{*0}\overline{K}^{*0}$ *and first observation of the* $B^0_s \to \phi\overline{K}^{*0}$ *decay at the LHCb experiment*" foi realizada por Brais Sanmartín Sedes baixo a súa dirección e que constitúe a Tese que presenta para optar ao Grado de Doutor en Física.

Santiago de Compostela, a 27 de Setembro de 2017.

Asdo. Bernardo Adeva Andany

Asdo. Cibrán Santamarina Ríos

Asdo. Brais Sanmartín Sedes

USC
UNIVERSIDADE
DE SANTIAGO
DE COMPOSTELA

Acknowledgements

First of all, I would like to thank my supervisors, Bernardo and Cibrán, for inviting me to start this adventure, and for helping me to overcome all the problems that appeared along the way.

I would like to express my gratitude to the members of my thesis jury, Stéphane, Paula, Abraham, Sean, Arantza and Diego, for generously accepting the invitation. And to Carlos and Stefano, for reading this work as referees for the International Mention.

I would like to show my appreciation to the BnoC WG members, particularly its conveners, and to the referees of the analyses included in this thesis, who helped to improve the quality of the work presented here and from whom I learned a lot. I also take this opportunity to acknowledge all the members of the LHCb and LHC collaborations for making possible the operation of this beautiful experiment.

I am sincerely grateful to all the people working on the USC LHCb group, Máximo, Juan, Abraham, José Ángel, Pablo, Eliseo, Antonio P., Antonio F., Edgar, Marcos, Diego, Xabi, Jessica, Martino, Veronika, Miriam and Miguel, and to those with whom I had the pleasure to share an office, Álvaro, Carlos, Julián, María, Paula, Toño, Víctor, and especially to Pablo Rodríguez, the first person I met when I started here, and who made my arrival much easier with his smile and his kindness.

Y con el cambio de idioma pasamos a la parte más personal de estos agradecimientos. Antes de nada quería pediros perdón a los que salís aquí por mi falta de efusividad, pero supongo que siendo vosotros los que mejor me conocéis, no esperaríais otra cosa. Sabéis que aunque no lo diga muy a menudo, sois una parte fundamental de mí.

Primero me gustaría darle las gracias a mis amigos: Alberto C., Alberto V., Álvaro, César, Cris, David D., David H., Fer, Jorge, Gabriel, Luis, Miguel, Néstor y Sergi. Con mención especial para la casa de Cris, que tantos momentos y recuerdos nos ha dado durante todos estos años. Espero seguir teniendo el privilegio de formar parte de vuestras vidas durante muchos años más, especialmente ahora que llega una nueva generación.

En segundo lugar, agradecer a mi familia el afecto y el apoyo que recibo de ellos. A mis abuelos, que a pesar de no entender muy bien qué es lo que hago siempre tienen una palabra de cariño y de ánimo; a mis tíos, Sagrario y Pepe, y a mi prima Olalla, que sé que les va a hacer mucha ilusión aparecer aquí; a mis hermanos, Iago y David, por tantos años de peleas (David no te enfades, puse a Iago primero por sorteo). También a María, mi polo opuesto, mi antipartícula, mi bióloga favorita, espero seguir aprendiendo contigo día a día.

Y finalmente me gustaría dedicar esta tesis a mi madre y a mi padre, Yuri y Héctor, por haber hecho todo lo posible (y más) para ayudarme a llegar hasta aquí.

¡Gracias a todos!

Brais

USC
UNIVERSIDADE
DE SANTIAGO
DE COMPOSTELA

Abstract

This thesis describes the study of the decays $B^0 \to K^{*0}\overline{K}^{*0}$ and $B_s^0 \to K^{*0}\overline{K}^{*0}$ with $3\,\text{fb}^{-1}$ of data collected by the LHCb experiment, $1\,\text{fb}^{-1}$ in 2011 at an energy $\sqrt{s} = 7\,\text{TeV}$ and $2\,\text{fb}^{-1}$ in 2012 at $\sqrt{s} = 8\,\text{TeV}$; and the search for the $B_s^0 \to \phi\overline{K}^{*0}$ decay with the data taken in 2011.

Flavour-untagged and time-integrated amplitude analyses of the $B^0 \to K^{*0}\overline{K}^{*0}$ and $B_s^0 \to K^{*0}\overline{K}^{*0}$ decays are reported. For the former, it is the first study at LHCb, and the large longitudinal polarisation obtained, $f_L = 0.707 \pm 0.053$, confirms the previous measurement from the BaBar experiment. For the latter, an update of an earlier LHCb analysis is presented, corroborating the low longitudinal polarisation, $f_L = 0.233 \pm 0.030$. Moreover, the ratio of branching ratios between the two modes, $\mathcal{B}(B^0 \to K^{*0}\overline{K}^{*0})/\mathcal{B}(B_s^0 \to K^{*0}\overline{K}^{*0})$, is measured.

In addition, as a result of the work presented here, the $B_s^0 \to \phi\overline{K}^{*0}$ decay is observed for the first time, with a significance of 6.5σ. The branching ratio $\mathcal{B}(B_s^0 \to \phi\overline{K}^{*0})$ is measured and found to be compatible within 1σ with theoretical predictions. An angular analysis of the $B_s^0 \to \phi\overline{K}^{*0}$ decay is included. The small value obtained for the longitudinal polarisation fraction follows the trend of the $b \to s$ penguin decays. The result is smaller than the predictions.

USC
UNIVERSIDADE
DE SANTIAGO
DE COMPOSTELA

Limiar

Esta tese describe o estudo das desintegracións $B^0 \to K^{*0}\overline{K}^{*0}$ e $B_s^0 \to K^{*0}\overline{K}^{*0}$ con $3\,\text{fb}^{-1}$ de datos recollidos polo experimento LHCb, $1\,\text{fb}^{-1}$ en 2011 cunha enerxía de $\sqrt{s} = 7\,\text{TeV}$ e $2\,\text{fb}^{-1}$ en 2012 con $\sqrt{s} = 8\,\text{TeV}$; e a busca da desintegración $B_s^0 \to \phi\overline{K}^{*0}$ cos datos tomados en 2011.

Análises sen marcado de sabor e integradas no tempo das desintegracións $B^0 \to K^{*0}\overline{K}^{*0}$ e $B_s^0 \to K^{*0}\overline{K}^{*0}$ son descritas. Para a primeira canle é o primeiro estudo que se realiza en LHCb, e o alto valor da polarización lonxitudinal obtido, $f_L = 0{,}707 \pm 0{,}053$, confirma as medidas previas do experimento BaBar. Para a segunda canle, realízase unha actualización dunha análise previa de LHCb, corroborando a baixa polarización lonxitudinal, $f_L = 0{,}233 \pm 0{,}030$. Tamén se obtén o cociente de coeficientes de ramificación entre os dous modos, $\mathcal{B}(B^0 \to K^{*0}\overline{K}^{*0})/\mathcal{B}(B_s^0 \to K^{*0}\overline{K}^{*0})$.

Ademais, como resultado do traballo presentado aquí, a desintegración $B_s^0 \to \phi\overline{K}^{*0}$ é observada por primeira vez, cunha significancia estatística de $6{,}5\sigma$. O coeficiente de ramificación $\mathcal{B}(B_s^0 \to \phi\overline{K}^{*0})$ mídese e atópase que é compatible en 1σ coas predicións teóricas. Unha análise angular da desintegración $B_s^0 \to \phi\overline{K}^{*0}$ é incluída. O baixo valor da fracción de polarización lonxitudinal segue a tendencia das desintegracións de tipo pingüín $b \to s$. O resultado é menor que as predicións teóricas.

USC
UNIVERSIDADE
DE SANTIAGO
DE COMPOSTELA

Contents

1 Introduction **1**

2 Theory overview **3**
2.1 The Standard Model of Particle Physics . . . 5
2.1.1 Electroweak theory . . . 6
2.1.2 Spontaneous Symmetry Breaking . . . 8
2.1.3 Flavour dynamics . . . 10
2.2 *CP*-violation in the Standard Model . . . 11
2.2.1 Discrete symmetries . . . 12
2.2.2 CKM matrix . . . 13
2.2.3 Neutral meson system . . . 16
2.2.4 *B*-meson systems . . . 21
2.3 $B_s^0 \to K^{*0}\overline{K}^{*0}$ and $B^0 \to K^{*0}\overline{K}^{*0}$ decays . . . 23
2.4 Polarisation in *B* decays . . . 27

3 The LHCb experiment **31**
3.1 The Large Hadron Collider . . . 32
3.2 The LHCb detector . . . 34
3.2.1 Magnet . . . 36
3.2.2 VELO . . . 37
3.2.3 TT and tracking stations . . . 38
3.2.4 RICH detectors . . . 40
3.2.5 Calorimeter system . . . 41
3.2.6 Muon system . . . 42
3.3 LHCb operation in Run I . . . 43
3.3.1 Trigger . . . 45
3.3.1.1 L0 trigger . . . 46
3.3.1.2 High Level Trigger . . . 47
3.3.1.3 Trigger performance . . . 48
3.3.2 Online system . . . 49
3.3.3 Tracking and vertexing . . . 51
3.3.4 Particle identification . . . 53
3.3.5 Simulation . . . 56
3.3.5.1 Data/MC discrepancies . . . 58
3.4 Run I experimental conditions . . . 58

4 First observation of the $B_s^0 \to \phi\overline{K}^{*0}$ decay **61**
4.1 Introduction . . . 61
4.2 Selection . . . 62
4.2.1 Charmless backgrounds . . . 63
4.2.2 Charmed backgrounds . . . 64
4.3 Fit model for the four-body mass spectrum . . . 64

4.4 Initial MVA selection . . . 67
4.5 Final selection . . . 70
4.5.1 Removing the four-body high mass background . . . 70
4.5.2 Final fit model . . . 72
4.5.3 Significance . . . 73
4.6 K^{*0} and ϕ purity in the signal . . . 74
4.7 Measurement of the $B_s^0 \to \phi \overline{K}^{*0}$ branching ratio . . . 78
4.8 Angular analysis: measurement of the f_L polarisation fraction . . . 79
4.8.1 Angular acceptance . . . 80
4.8.1.1 Correction to the acceptance due to the pion p_T . . . 81
4.8.1.2 Acceptance dependence on the TIS and TOS triggers . . . 82
4.8.2 f_L determination . . . 82
4.8.3 Systematic errors of the angular analysis . . . 84
4.8.3.1 Systematic error due to the S-wave . . . 84
4.8.3.2 Systematic error due to the GL . . . 84
4.8.3.3 Systematic error due to the angular acceptance . . . 85
4.8.3.4 Systematic error due to the combinatorial background . . . 85
4.8.3.5 Total systematic error . . . 86
4.9 Systematic errors of the branching ratio . . . 86
4.9.1 Systematic error due to the four-body spectra fit model . . . 86
4.9.2 Systematic error due to the longitudinal polarisation . . . 86
4.9.3 Systematic error due to the purity . . . 87
4.9.4 Systematic error due to the efficiency . . . 87
4.9.5 Systematic error due to the PID . . . 88
4.9.6 Summary on systematic errors . . . 88
4.10 Significance tests . . . 89
4.11 Summary . . . 89

5 Study of the decays $B^0 \to K^{*0}\overline{K}^{*0}$ and $B_s^0 \to K^{*0}\overline{K}^{*0}$ 91
5.1 Introduction . . . 91
5.2 Dataset, Monte Carlo, trigger and stripping . . . 92
5.2.1 Stripping . . . 92
5.2.2 Trigger . . . 93
5.3 Background studies . . . 94
5.3.1 Peaking backgrounds with charm . . . 94
5.3.2 Reflections or cross-feed backgrounds . . . 96
5.3.3 Partially reconstructed and combinatorial backgrounds . . . 96
5.4 Four-body mass fit model . . . 97
5.4.1 Signal model . . . 97
5.4.2 Reflections . . . 98
5.4.3 Partially reconstructed background . . . 99
5.4.4 Combinatorial background . . . 99
5.5 Selection . . . 99
5.5.1 Fiducial region . . . 99
5.5.2 Preliminary cuts . . . 100
5.5.3 Multivariate analysis . . . 100
5.5.4 FoM optimisation . . . 103

5.5.5 PID cuts . . . 104
5.6 Efficiencies . . . 106
5.6.1 Generator efficiencies . . . 106
5.6.2 Reconstruction and stripping efficiencies . . . 106
5.6.3 Trigger efficiencies . . . 107
5.6.4 Selection efficiencies . . . 107
5.6.5 PID efficiencies . . . 107
5.7 Four-body invariant mass fit result . . . 110
5.7.1 Dealing with $B^0 \to \rho^0 K^{*0}$ decays . . . 111
5.7.2 Estimation of the $\Lambda_b^0 \to K^{*0} p\pi$ events . . . 112
5.7.3 $K^+\pi^-K^-\pi^+$ invariant mass fit result . . . 114
5.8 Amplitude analysis . . . 116
5.8.1 Angle-mass distribution at time t=0 . . . 118
5.8.2 Time dependent angle-mass distribution . . . 120
5.8.3 Invariant mass propagators . . . 122
5.8.3.1 P-wave . . . 122
5.8.3.2 S-wave . . . 123
5.8.3.3 Phase space factor and normalisation . . . 124
5.8.4 Acceptance . . . 124
5.8.5 Fit model . . . 126
5.8.6 Fit result . . . 126
5.8.7 Visualisation . . . 126
5.8.8 Fit of the Monte Carlo simulated data . . . 129
5.8.9 Fit biases . . . 129
5.9 Systematic uncertainties of the amplitude analysis . . . 131
5.9.1 Fit biases . . . 131
5.9.2 Acceptance model . . . 131
5.9.3 S-wave mass model . . . 131
5.9.4 Model parameters . . . 131
5.9.5 Monte Carlo statistics . . . 132
5.9.6 sWeighting procedure . . . 132
5.10 Comparative analysis of $B^0 \to K^{*0}\overline{K}^{*0}$ versus $B_s^0 \to K^{*0}\overline{K}^{*0}$ . . . 133
5.10.1 Amplitude analysis of the $B_s^0 \to K^+\pi^-K^-\pi^+$ decay . . . 133
5.10.2 Ratio of $B^0 \to K^{*0}\overline{K}^{*0}$ over $B_s^0 \to K^{*0}\overline{K}^{*0}$ . . . 137
5.11 Branching ratio . . . 138
5.11.1 Determination of $\kappa_{B^0 \to K^{*0}\overline{K}^{*0}}$ and $\kappa_{B_s^0 \to K^{*0}\overline{K}^{*0}}$ . . . 138
5.11.2 Systematic uncertainties . . . 140
5.11.2.1 Four-body invariant mass fit . . . 140
5.11.2.2 Efficiencies . . . 140
5.11.2.3 Amplitude analysis result . . . 140
5.11.3 $\mathcal{B}(B^0 \to K^{*0}\overline{K}^{*0})/\mathcal{B}(B_s^0 \to K^{*0}\overline{K}^{*0})$ result . . . 141
5.12 Summary . . . 141

6 Conclusions **143**

Summary **145**

USC UNIVERSIDADE DE SANTIAGO DE COMPOSTELA

Resumo **155**

Appendices **167**

Bibliography **183**

1 Introduction

The Standard Model of Particle Physics (SM) is the theory describing three of the four known fundamental forces in the universe (the electromagnetic, weak and strong interactions), as well as classiffying all known elementary particles. It has shown a great success in the past few decades, both in explaining the experimental data and in predicting new phenomena. The most known example being the description of the Higgs mechanism in the 60's and the observation of the associated particle, the Higgs boson, nearly fifty years later. Once the Higgs boson was observed, the last particle predicted by the SM to be discovered, the field of particle physics has entered a new era. It is known that the SM cannot be the complete theory describing particle physics, since there are fundamental physical phenomena which cannot be interpreted within its framework. During the past decades, many new theories have been postulated trying to explain the whole picture. Unfortunately all the measurements of processes calculable in the SM have been in agreement with the predictions. Therefore the search for contradictory results remains.

In particle physics there are two main ways to search for processes in disagreement with the SM. In direct searches, at the high-energy frontier one tries to produce and observe the new particles directly. To reach the energies needed to create these particles, very complex and large machines are needed. The most powerful experimental facility of this kind is the Large Hadron Collider (LHC), a pp collider built by the European Organization for Nuclear Research (CERN) where the beams collide at an energy of several TeV.[1] Four main experiments are located along the LHC ring, ATLAS, CMS, ALICE and LHCb. The work shown in this thesis has been obtained with the data taken by the LHCb spectrometer. This experiment, rather than trying to detect the new particles directly, is aimed to perform indirect searches, where at the high-precision frontier one analyzes the indirect virtual effects of these new particles within flavour or electroweak observables. The LHCb experiment is designed to study CP-violation processes and to search for rare B and D decays.

CP-symmetry, the combination of the charge conjugation and parity symmetries, states that the laws of physics should be the same if a particle is interchanged with its antiparticle while its spacial coordinates are inverted. The violation of the CP-symmetry is one of the needed conditions to explain the imbalance between matter and antimatter in the universe. The Big Bang should have produced equal amounts of matter and antimatter if CP-symmetry was preserved and there should have been total cancellation of both. Since this does not seem to have been the case, physical laws must have ac-

[1] In addition to proton beams, LHC was also designed to use beams of lead ions, allowing lead-lead and proton-lead collisions.

ted differently for matter and antimatter, *i.e.*, violating *CP*-symmetry. The SM contains a mean to explain *CP*-violation, through the Kobayashi-Maskawa mechanism (KM), but the amount of the asymmetry predicted by the theory is not enough to account for the observed imbalance. However, the KM mechanism has been successful to describe the current experimental data. New *CP*-violation processes not explained by the SM have therefore to exist.

Among the indirect searches, the measurement of *CP* asymmetries in Flavour Changing Neutral Current (FCNC) processes provides a crucial test of the Standard Model. Although forbidden at tree level, these processes may still occur through loop-mediated (penguin) diagrams. Heavy new particles can enter the loop, thus modifying the values predicted by the SM. Three FCNC processes are studied in this thesis: $B^0 \to K^{*0}\overline{K}^{*0}$, $B_s^0 \to K^{*0}\overline{K}^{*0}$ and $B_s^0 \to \phi\overline{K}^{*0}$. The decay of the ϕ and the K^{*0} mesons into long-lived charged particles and their known or expected production rate makes the aforementioned channels easily accessible at LHCb. These decays are of the type $B_{(s)}^0 \to VV'$, where V and V' are light vector mesons. Several combinations of the final-state polarisations are allowed by angular momentum conservation, and hence an amplitude analysis is needed to obtain the different fractions of each configuration.

Data taken by the LHCb experiment in 2011 is analyzed to search for the $B_s^0 \to \phi\overline{K}^{*0}$ decay, which had not been observed prior to the work here presented, and its branching ratio and polarisation fractions are measured. With the 2011 and 2012 data, an amplitude analysis of the $B^0 \to K^{*0}\overline{K}^{*0}$ decay is performed, being the first study of this mode at LHCb. Besides, an update of the $B_s^0 \to K^{*0}\overline{K}^{*0}$ amplitude analysis, previously performed with 2011 data, is reported. Finally, the ratio of branching ratios between the $B^0 \to K^{*0}\overline{K}^{*0}$ and $B_s^0 \to K^{*0}\overline{K}^{*0}$ decays is measured.

This thesis is organised as follows: in Chapter 2 an overview of the most important theoretical aspects related to the decays of interest is included, in Chapter 3 the description of the LHC and the LHCb spectrometer are reported, in Chapter 4 the search for the $B_s^0 \to \phi\overline{K}^{*0}$ decay with the 2011 data is presented, in Chapter 5 the amplitude analyses of the $B^0 \to K^{*0}\overline{K}^{*0}$ and $B_s^0 \to K^{*0}\overline{K}^{*0}$ decays are presented, along with the measurement of the ratio of branching ratios between the two modes, and finally in Chapter 6 conclusions are drawn.

2 Theory overview

The Standard Model of Particle Physics (SM) is the theory which better explains the behaviour of the elementary particles composing the universe and the interactions among them. It has provided accurate descriptions of the experimental measurements as well as demonstrating a huge predictive power (see for example the extensive review by the Particle Data Group [1]). The SM is a Quantum Field Theory (QFT) which describes the strong, the weak and the electromagnetic interactions, *i.e.*, all known interactions except the gravitation. The theory was developed along the second half of the twentieth century, with most of its main proponents awarded the Nobel Prize in Physics:[1][2] Feynman, Schwinger and Tomonaga received the Nobel Prize in 1965 for their seminal work in Quantum Electrodynamics (QED); Glashow, Salam and Weinberg obtained it in 1979 for their contributions to the theory that unifies the weak and electromagnetic interaction, including the prediction of the weak neutral current; in 1999, the Nobel Prize was given to Veltman and 't Hooft, for elucidating the quantum structure of the electroweak interactions; the development of Quantum Chromodynamics (QCD) has awarded Nobel Prizes to Gell-Mann in 1969 and to Gross, Politzer and Wilczek in 2004; in 2008 Kobayashi and Maskawa shared the prize for the discovery of the origin of *CP*-violation, which predicted the existence of the third quark family; and finally the most recent Nobel Prize awarded to a SM related study was the 2013 edition, given to Higgs and Englert for the theoretical description of the mechanism that explains the origin of the masses of the elementary particles.

Despite its great success, there are still phenomena which cannot be described within the SM. It does not provide an explanation for the amount of cold dark matter obtained from cosmological observations, it does not include gravitation since the SM is widely considered to be incompatible with General Relativity, it fails to explain the matter-antimatter imbalance or it has problems to include the masses of the neutrinos necessary to interpret the experimentally-proven neutrino oscillations (mass terms for the neutrinos can be added to the SM, but what the correct mechanism from which they acquire mass is and why their masses are so small remains unclear). Besides, there are some features of the SM that are difficult to understand in a fundamental theory that is thought to explain the behaviour of nature. Most physicists consider that it contains too many independent and arbitrary parameters, 19, and it does not provide an explanation for the values of these parameters, it does not explain the number of fermion generations nor their highly hierarchical structure in terms of mass, the fine-tuning cancellation necessary to account

[1] https://www.nobelprize.org

[2] Moreover, several Nobel prizes have been given to experimental observations related to the SM.

for a light Higgs boson between the quadratically-divergent corrections and the bare mass is deemed unnatural. Also, the SM does not seem to break *CP*-symmetry in the strong interactions, as there is no known reason for it to be conserved. Because of these problems, the SM is supposed to be an effective theory of a more general picture. Current efforts in particle physics, in both experimental and theoretical sides are focused on searching for the new theory able to explain the still unanswered questions. These new theories trying to supersede the SM are collectively known as Beyond Standard Model physics (BSM) or New Physics (NP) [2].

Among the phenomena that the SM cannot explain, one of the most interesting is matter-antimatter asymmetry. Experimental evidence, from the manned and unmaned exploration of the solar system to radioastronomy observation or cosmic ray detection shows that the universe is dominated by matter. If there were stars or galaxies made of antimatter, characteristic γ rays from matter–antimatter annihilation would be expected. There is no evidence for this. The prevailing theory nowadays is that the Universe started out baryon-symmetric, but nature has generated a baryon excess since then. Andrei Sakharov, in 1967, proposed three necessary conditions that have to be fulfilled in order to produce matter and antimatter at different rates [3]: at least one baryon number violating process, *C*- and *CP*-symmetry violation and the interactions must occur outside the thermal equilibrium. The first condition is obviously necessary to produce an excess of baryons over anti-baryons, the second one is needed such that the baryon number violation in a process will not be compensated by the equal amount of violation in the conjugated process, and the third condition is needed because at thermal equilibrium, the Boltzmann distribution dictates that there should be equal amounts of matter and antimatter. Even though the three conditions are compatible with the SM, the amount of matter in the Universe is much larger than predicted. The main problem being that *CP*-symmetry is only barely violated in the SM.

CP-violation was explained in the context of the SM by Makoto Kobayashi and Toshihide Maskawa in 1973 [4]. In this mechanism all the *CP*-violating observables depend on a unique phase. Since the Kobayashi-Maskawa (KM) mechanism requires three families of quarks, and only two of them were known when the mechanism was postulated, it allowed Kobayashi and Maskawa to predict the third quark generation, which was observed in 1976 with the discovery of the bottom quark. Apart from this astonishing success, the KM mechanism has been able to explain all the *CP*-violation measurements obtained in particle physics experiments to date. *CP*-violation was first observed in neutral K decays in 1964 by James Cronin and Val Fitch [5], who were awarded the Nobel Prize in Physics in 1980 for this discovery. In 2001, *CP*-violation was also detected in the B^0-meson system [6, 7] at the so called *B*-factories.[1] Many more *CP*-violating processes in B^0-meson decays have been measured afterwards. Recently, in 2013, the LHCb experiment announced the discovery of *CP*-violation in B_s^0 mesons [10]. The measured *CP*-violation is not enough to account for the total amount of matter-antimmater asymmetry seen in the Universe, thus new sources of *CP*-violation are expected to exist. The task is to measure *CP*-violation processes with reliable predictions by the SM and look for any disagreement. Moreover,

[1] A *B*-factory is a particle collider designed to produce and detect a large number of *B*-mesons. Two *B*-factories were built in the 1990s, the BaBar experiment at the PEP-II collider [8] and the Belle experiment at the KEKB collider [9]. Both are based on electron-positron colliders with the centre of mass energy tuned to the $\Upsilon(4S)$ resonance peak, which is just above the threshold for decay into two *B*-mesons.

essentially all the theoretical extensions of the SM introduce new sources of *CP*-violation. Finding a *CP*-violating process not accounted for in the SM would therefore be of great importance to constrain the models that correctly describe NP.

Violation of *CP* invariance has been observed in the interactions of neutral meson systems. Even though *CP*-violation was first observed in the K system, these particles are very difficult to model in the theory, due to the strong interaction. Instead, B-mesons are the ideal place to look for *CP*-violation since they are the lowest-mass processes where the three quark generations play a direct (tree-level) role. Moreover, theoretical calculations become easier with heavier quarks. *CP*-violation should also be observable in the D-meson (charm) sector, although this will be a small effect that will be very difficult to measure. With the observation that neutrinos have mass, it is expected that *CP*-violation will also be observed in the neutrino sector.

Loop-mediated penguin decays of B-mesons are sensitive probes for physics beyond the SM, since they may induce phenomena that have not yet been observed in experiment. These channels provide an excellent probe of new heavy particles entering the penguin quantum loops. Transitions between the quarks of the third and second generation ($b \to s$) or between the quarks of the third and first generation ($b \to d$) are complementary since SM *CP*-violation is tiny in $b \to s$ transitions and an observation of *CP*-violation would indicate physics beyond the SM. The $B_s^0 \to K^{*0}\overline{K}^{*0}$ decay is a pure $b \to s$ penguin. It can be used as a test of the SM since *CP*-violation is expected to be very small, and a nonzero measurement would be a clear signal of new physics. To estimate the SM result, the contribution due to the subleading penguin amplitude has to be considered. A method to constrain the error introduced by neglecting this contribution is described using the U-spin partner decay, $B^0 \to K^{*0}\overline{K}^{*0}$.[1] $B_{(s)}^0 \to VV'$ decays, where V and V' are light vector mesons provide a valuable additional source of information because the angular distributions give insight into the physics of hadronic B-meson decays and the interplay between the strong and weak interactions they involve. There are only two $B_{(s)}^0 \to VV'$ penguin modes that correspond to $b \to d$ loops: the $B^0 \to K^{*0}\overline{K}^{*0}$ and the $B_s^0 \to \phi\overline{K}^{*0}$ decays.

In Chapter 2.1 a brief introduction of the SM is presented, concentrating on the electroweak sector and in the structure of the flavour dynamics. Chapter 2.2 includes a more detailed explanation of the discrete symmetries C, P, T and CP, the violation of CP within the SM and the relation with the neutral meson system, finally particularising in the B^0- and B_s^0-meson systems. In Chapter 2.3, the importance of the $B_s^0 \to K^{*0}\overline{K}^{*0}$ decay as a benchmark of the SM and the relevance of the $B^0 \to K^{*0}\overline{K}^{*0}$ decay to control the errors induced due to the neglection of the subleading penguin amplitudes is analyzed. Lastly, in Chapter 2.4, the amplitudes and observables obtained in an amplitude analysis are described.

2.1 The Standard Model of Particle Physics

The Standard Model of Particle Physics [11–14] is a spontaneously broken non-abelian (Yang-Mills [15]) gauge quantum field theory obtained formulating the most general renor-

[1] The diagrams describing both processes, the $B^0 \to K^{*0}\overline{K}^{*0}$ decay and the $B_s^0 \to K^{*0}\overline{K}^{*0}$ decay, are identical with a $d \leftrightarrow s$ exchange.

Table 2.1: Left-handed doublets and right-handed singlets in the SM for the first (top row), second (middle row) and third (bottom row) fermion generations.

$\begin{pmatrix} \nu_e \\ e^- \end{pmatrix}_L$,	$\begin{pmatrix} u \\ d \end{pmatrix}_L$,	e_R^-,	u_R,	d_R,
$\begin{pmatrix} \nu_\mu \\ \mu^- \end{pmatrix}_L$,	$\begin{pmatrix} c \\ s \end{pmatrix}_L$,	μ_R^-,	c_R,	s_R,
$\begin{pmatrix} \nu_\tau \\ \tau^- \end{pmatrix}_L$,	$\begin{pmatrix} t \\ b \end{pmatrix}_L$,	τ_R^-,	t_R,	b_R,

malisable Lagrangian which is local invariant under the symmetry group

$$G_{\text{SM}} = SU(3)_C \otimes SU(2)_L \otimes U(1)_Y. \tag{2.1}$$

The strong interaction is described by $SU(3)_C$, where C represents the colour charge, while the electroweak interaction is described by $SU(2)_L \otimes U(1)_Y$, where Y is the weak hypercharge and L means that the $SU(2)$ part only affects to left-handed fields. The interactions are mediated by the corresponding spin-1 gauge fields, eight massless gluons and one massless photon, respectively, for the strong and electromagnetic interactions, and three massive bosons, $W^\pm$ and Z, for the weak interaction. The fermionic matter content of the SM is given by the leptons and quarks, which are represented as Dirac spinors, organised in three families with identical properties (gauge interactions), only differing by their mass and their flavour quantum number. Each fermion generation has five representations of the symmetry group,

$$\begin{pmatrix} \nu_\ell \\ \ell^- \end{pmatrix}_L, \quad \begin{pmatrix} q_u \\ q_d \end{pmatrix}_L, \quad \ell_R^-, \quad q_{uR}, \quad q_{dR}, \tag{2.2}$$

plus the corresponding antiparticles. Each quark appears in three different colours. In Table 2.1, the SM fermions are summarised.

The $SU(3)_C \otimes SU(2)_L \otimes U(1)_Y$ group is spontaneously broken into $SU(3)_C \otimes U(1)_{EM}$ by the vacuum expectation value (VEV) of (the neutral component of) a scalar isospin doublet, with hypercharge $1/2$, named after Higgs. The Spontaneous Symmetry Breaking (SSB) mechanism generates the masses of the weak gauge bosons and also the fermion masses and mixings.

2.1.1 Electroweak theory

This brief introduction of the SM is focused on the electroweak sector following Ref. [16]. Considering a single family of quarks for simplicity,

$$\psi_1(x) = \begin{pmatrix} u \\ d \end{pmatrix}_L, \quad \psi_2(x) = u_R, \quad \psi_3(x) = d_R, \tag{2.3}$$

and imposing that the free Lagrangian is gauge invariant under local transformations of the group $SU(2)_L \otimes U(1)_Y$, the next Lagrangian is obtained

$$\mathcal{L} = \sum_{j=1}^{3} i\overline{\psi}_j(x)\gamma^\mu D_\mu \psi_j(x), \tag{2.4}$$

with

$$\begin{aligned} D_\mu\psi_1(x) &\equiv [\partial_\mu + ig\widetilde{W}_\mu(x) + ig' y_1 B_\mu(x)]\psi_1(x), \\ D_\mu\psi_2(x) &\equiv [\partial_\mu + ig' y_2 B_\mu(x)]\psi_2(x), \\ D_\mu\psi_3(x) &\equiv [\partial_\mu + ig' y_3 B_\mu(x)]\psi_3(x), \end{aligned} \tag{2.5}$$

where

$$\widetilde{W}_\mu(x) \equiv \frac{\sigma_i}{2} W^i_\mu(x) \tag{2.6}$$

denotes a $SU(2)_L$ matrix field and σ_i are the Pauli matrices. The y_i terms are called hypercharges and B_μ and $\widetilde{W}^i_\mu$ are four gauge fields, related to the $W^\pm$, Z^0 and γ bosons.

The Lagrangian in Eq. 2.4 contains charged-current interactions of the fermion fields with the boson field $W_\mu \equiv (W^1_\mu + iW^2_\mu)/\sqrt{2}$ and its complex-conjugate $W^\dagger_\mu \equiv (W^1_\mu - iW^2_\mu)/\sqrt{2}$,

$$\mathcal{L}_{\mathrm{CC}} = -\frac{g}{2\sqrt{2}} \left\{ W^\dagger_\mu \left[\overline{u}\gamma^\mu (1-\gamma_5) d \right] + \mathrm{h.c.} \right\}. \tag{2.7}$$

Eq. 2.4 also contains interactions with the neutral gauge fields W^3_μ and B_μ. Trying an arbitrary combination of them,

$$\begin{pmatrix} W^3_\mu \\ B_\mu \end{pmatrix} \equiv \begin{pmatrix} \cos\theta_{\mathrm{W}} & \sin\theta_{\mathrm{W}} \\ -\sin\theta_{\mathrm{W}} & \cos\theta_{\mathrm{W}} \end{pmatrix} \begin{pmatrix} Z_\mu \\ A_\mu \end{pmatrix}, \tag{2.8}$$

the neutral-current Lagrangian is given by

$$\mathcal{L}_{\mathrm{NC}} = -\sum_j \overline{\psi}_j \gamma^\mu \left\{ A_\mu \left[g\frac{\sigma_3}{2}\sin\theta_{\mathrm{W}} + g' y_j \cos\theta_{\mathrm{W}} \right] + Z_\mu \left[g\frac{\sigma_3}{2}\cos\theta_{\mathrm{W}} - g' y_j \sin\theta_{\mathrm{W}} \right] \right\} \psi_j. \tag{2.9}$$

The conditions

$$g\sin\theta_{\mathrm{W}} = g'\cos\theta_{\mathrm{W}} = e, \quad Y = Q - T_3 \tag{2.10}$$

are imposed to get QED from the A_μ piece, where $T_3 \equiv \sigma_3/2$ and Q denotes the charge operator

$$Q_1 \equiv \begin{pmatrix} Q_u & 0 \\ 0 & Q_d \end{pmatrix}, \quad Q_2 = Q_u, \quad Q_3 = Q_d. \tag{2.11}$$

The neutral-current Lagrangian can be written as,

$$\mathcal{L}_{\mathrm{NC}} = \mathcal{L}_{\mathrm{QED}} + \mathcal{L}^{\mathrm{Z}}_{\mathrm{NC}}, \tag{2.12}$$

where

$$\mathcal{L}_{\mathrm{QED}} = -eA_\mu \sum_j \overline{\psi}_j \gamma^\mu Q_j \psi_j, \tag{2.13}$$

and

$$\mathcal{L}^{\mathrm{Z}}_{\mathrm{NC}} = -\frac{e}{2\sin\theta_{\mathrm{W}}\cos\theta_{\mathrm{W}}} Z_\mu \sum_j \overline{\psi}_j \gamma^\mu \left(\sigma_3 - 2\sin^2\theta_{\mathrm{W}} Q_j \right) \psi_j. \tag{2.14}$$

In addition, the gauge-invariant kinetic term for the gauge fields is given by

$$\mathcal{L}_{Kin} = -\frac{1}{4}B_{\mu\nu}B^{\mu\nu} - \frac{1}{2}\mathrm{Tr}\left[\widetilde{W}_{\mu\nu}\widetilde{W}^{\mu\nu}\right] = -\frac{1}{4}B_{\mu\nu}B^{\mu\nu} - \frac{1}{4}\widetilde{W}^{i}_{\mu\nu}\widetilde{W}^{\mu\nu}_{i}, \tag{2.15}$$

where

$$B_{\mu\nu} \equiv \partial_\mu B_\nu - \partial_\nu B_\mu, \tag{2.16}$$

$$\widetilde{W}_{\mu\nu} \equiv \frac{\sigma}{2}W^i_{\mu\nu}, \quad W^i_{\mu\nu} = \partial_\mu W^i_\nu - \partial_\nu W^i_\mu - g\epsilon^{ijk}W^j_\mu W^k_\nu, \tag{2.17}$$

which means that $\mathcal{L}_{Kin}$ gives rise to cubic and quartic self-interactions among the gauge fields.

2.1.2 Spontaneous Symmetry Breaking

The gauge invariance forbids the writing of a mass term for the gauge bosons. Neither are fermionic masses allowed, because they would communicate the left- and right-handed fields, which have different transformation properties, and therefore would produce an explicit breaking of the gauge symmetry. However, the physical $W^\pm$ and Z bosons are quite heavy objects.

As shown by Weinberg in 1967 [13], there is a way to overcome the problem, through the Higgs mechanism [17–19].[1] The gauged scalar lagrangian, which is invariant under $SU(2)_L \otimes U(1)_Y$ transformations is introduced,

$$\mathcal{L}_S = (D_\mu\phi)^\dagger D^\mu\phi - \mu^2\phi^\dagger\phi - \lambda\left(\phi^\dagger\phi\right)^2, \tag{2.18}$$

where $\lambda > 0$ and $\mu^2 < 0$,

$$\phi(x) = \begin{pmatrix} \phi^+(x) \\ \phi^0(x) \end{pmatrix} \tag{2.19}$$

is a $SU(2)_L$ doublet of complex scalar fields and

$$D^\mu\phi = \left[\partial^\mu + ig\widetilde{W}^\mu + ig'y_\phi B^\mu\right]\phi, \tag{2.20}$$

with $y_\phi = \frac{1}{2}$.

The Higgs potential,

$$V(\phi) = \mu^2\phi^\dagger\phi - \lambda\left(\phi^\dagger\phi\right)^2 \tag{2.21}$$

has an infinite set of degenerate states with minimum energy (Fig. 2.1), satisfying

$$\langle\phi\rangle_0 = \frac{1}{\sqrt{2}}\begin{pmatrix} 0 \\ v \end{pmatrix}, \tag{2.22}$$

with $v = \sqrt{-\mu^2/\lambda}$. Since the electric charge is conserved, the vacuum expectation value (VEV) of ϕ^+ must vanish. Once a particular ground state is chosen, the Spontaneous Symmetry Breaking occurs and the $SU(2)_L \otimes U(1)_Y$ symmetry is spontaneously broken to the electromagnetic subgroup $U(1)_{EM}$.

[1] The mechanism is known with several names since it was published almost simultaneously by three independent groups (https://en.wikipedia.org/wiki/1964_PRL_symmetry_breaking_papers). The most complete name is the ABEGHHK'tH mechanism (for Anderson, Brout, Englert, Guralnik, Hagen, Higgs, Kibble and 't Hooft) coined by Peter Higgs.

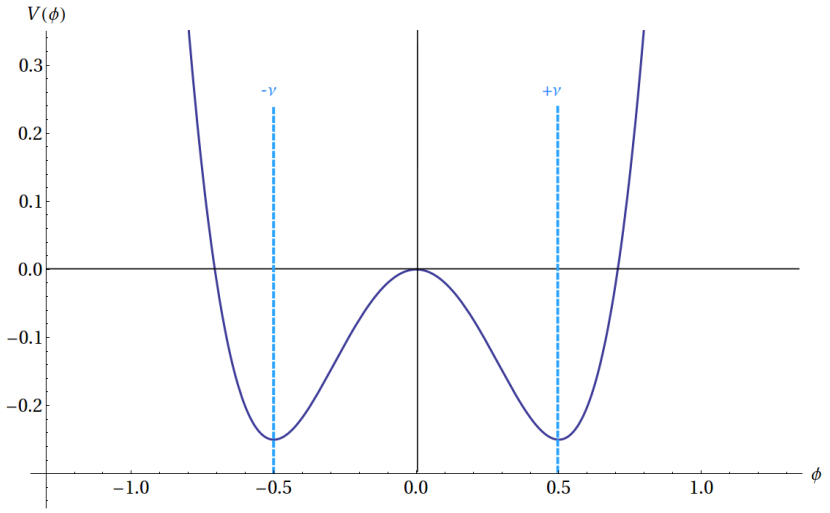

Figure 2.1: Higgs-like potential. The minimum is not at 0, and therefore the potential has a VEV.

The scalar doublet can be parametrised as

$$\phi(x) = exp\left\{i\frac{\sigma_i}{2}\theta^i(x)\right\}\frac{1}{\sqrt{2}}\begin{pmatrix} 0 \\ v + H(x) \end{pmatrix}, \tag{2.23}$$

with the real fields $\theta^i(x)$, which are arbitrary $SU(2)$ gauge transformations, and $H(x)$, a fluctuating real field with $\langle H(x)\rangle = 0$, which is the Higgs boson itself. The crucial point is that the local $SU(2)_L$ invariance of the Lagrangian allows to rotate away any dependence on θ^i. If one takes the physical (unitary) gauge $\theta^i(x) = 0$, the kinetic piece of the scalar Lagrangian (Eq. 2.18) takes the form

$$(D_\mu\phi)^\dagger D^\mu\phi \xrightarrow{\theta^i=0} \frac{1}{2}\partial_\mu H\partial_\mu H + (v+H)^2\left\{\frac{g^2}{4}W_\mu^\dagger W^\mu + \frac{g^2}{8\cos^2\theta_W}Z_\mu Z^\mu\right\}. \tag{2.24}$$

The vacuum expectation value of the neutral scalar has generated a quadratic term for the $W^\pm$ and the Z, *i.e.*, the gauge bosons have acquired masses,

$$M_Z\cos\theta_W = M_W = \frac{1}{2}vg. \tag{2.25}$$

Apart from that, the scalar Lagrangian in Eq. 2.18 includes a term for the Higgs mass, given by

$$M_H = \sqrt{-2\mu^2} = \sqrt{2\lambda}v, \tag{2.26}$$

and the interactions between the Higgs and the gauge bosons. These interactions are always proportional to the mass (squared) of the coupled boson. All Higgs couplings are determined by M_H, M_W, M_Z and the vacuum expectation value v.

The Higgs mechanism also allows to obtain masses for the fermions. The following gauge-invariant fermion-scalar coupling can be written,

$$\mathcal{L}_Y = -\lambda_d\left(\overline{u},\overline{d}\right)_L\begin{pmatrix}\phi^+\\ \phi^0\end{pmatrix}d_R - \lambda_u\left(\overline{u},\overline{d}\right)_L\begin{pmatrix}\phi^{0*}\\ -\phi^-\end{pmatrix}u_R - \lambda_e\left(\overline{\nu}_e,\overline{e}\right)_L\begin{pmatrix}\phi^+\\ \phi^0\end{pmatrix}e_R + \text{h.c.}, \tag{2.27}$$

where the second term involves the $\mathcal{C}$-conjugate scalar field $\phi^c \equiv i\sigma_2\phi^*$. In the unitary gauge (after SSB), this Yukawa-type Lagrangian takes the simpler form

$$\mathcal{L}_Y = -\left(1+\frac{H}{v}\right)\{m_d d\overline{d} + m_u u\overline{u} + m_e e\overline{e}\}, \tag{2.28}$$

where the SSB mechanism has generated also fermion masses,

$$m_d = \lambda_d \frac{v}{\sqrt{2}}, \quad m_u = \lambda_u \frac{v}{\sqrt{2}}, \quad m_e = \lambda_e \frac{v}{\sqrt{2}}, \tag{2.29}$$

and all Yukawa couplings are fixed in terms of the fermion masses. But this is not the end, as it has been previously mentioned, fermions are organised in three families, and therefore a more general Yukawa Lagrangian can be written, allowing interactions among quarks of different generations, as it is shown below.

2.1.3 Flavour dynamics

In the general case of N_G generations of fermions, additional fermion-scalar couplings mixing quarks of different generations are allowed by the gauge symmetry. The most general Yukawa Lagrangian has the form,

$$\begin{aligned}\mathcal{L}_Y = -\sum_{jk}\Bigg\{&\left(\overline{u}'_j, \overline{d}'_j\right)_L \left[c^{(d)}_{jk}\begin{pmatrix}\phi^+\\ \phi^0\end{pmatrix} d'_{kR} + c^{(u)}_{jk}\begin{pmatrix}\phi^{0*}\\ -\phi^-\end{pmatrix} u'_{kR}\right]\\ &+\left(\overline{\nu}'_j, \overline{\ell}'_j\right)_L c^{(\ell)}_{jk}\begin{pmatrix}\phi^+\\ \phi^0\end{pmatrix}\ell'_{kR}\Bigg\} + \text{h.c.},\end{aligned} \tag{2.30}$$

where ν'_j, ℓ'_j, u'_j and d'_j denote the members of the weak family j ($j = 1, ..., N_G$) and $c^{(d)}_{jk}$, $c^{(u)}_{jk}$ and $c^{(\ell)}_{jk}$ are arbitrary coupling constants.

After SSB, the Yukawa Lagrangian can be written as

$$\mathcal{L}_Y = -\left(1+\frac{H}{v}\right)\left\{\overline{\boldsymbol{d}}'_L M'_d \boldsymbol{d}'_R + \overline{\boldsymbol{u}}'_L M'_u \boldsymbol{u}'_R + \overline{\boldsymbol{\ell}}'_L M'_\ell \boldsymbol{\ell}'_R + \text{h.c.}\right\}. \tag{2.31}$$

Here, $\boldsymbol{d}'$, $\boldsymbol{u}'$ and $\boldsymbol{\ell}'$ denote vectors in the N_G-dimensional flavour space. The corresponding mass matrices are given by

$$(M'_f)_{ij} \equiv c^{(f)}_{ij}\frac{v}{\sqrt{2}}, \tag{2.32}$$

with $f = \{d, u, \ell\}$. The diagonalisation of these mass matrices determines the mass eigenstates d_j, u_j and ℓ_j, which are linear combinations of the corresponding weak eigenstates d'_j, u'_j and ℓ'_j, respectively. There can always be found unitary matrices V_{fL} and V_{fR} such that[1]

$$V_{fL} M'_f V^\dagger_{fR} = \mathcal{M}_f \equiv \lambda_f \frac{v}{\sqrt{2}}, \tag{2.33}$$

where $\mathcal{M}_d = \text{diag}(m_d, m_s, m_b)$, $\mathcal{M}_u = \text{diag}(m_u, m_c, m_t)$ and $\mathcal{M}_\ell = \text{diag}(m_e, m_\mu, m_\tau)$ are diagonal and real matrices. The quark mass eigenstates are then defined as

$$f_{Li} = (V_{fL})_{ij} f'_{Lj}, \quad f_{Ri} = (V_{fR})_{ij} f'_{Rj}, \tag{2.34}$$

[1] A unitary matrix accomplishes $V^\dagger V = \mathbb{I}$.

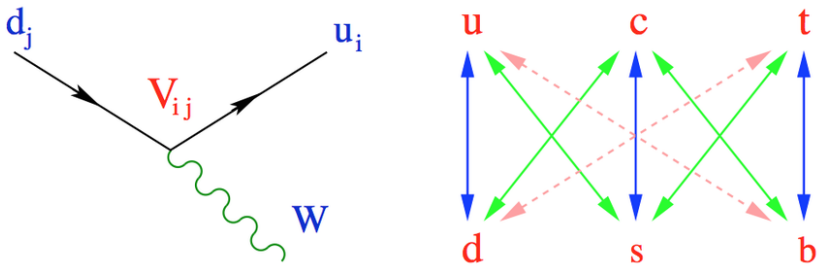

Figure 2.2: Flavour-changing transitions through the charged-current couplings of the $W^{\pm}$ bosons

Since $\overline{f}'_L f'_L = \overline{f}_L f_L$ and $\overline{f}'_R f'_R = \overline{f}_R f_R$, the form of the neutral-current part of the $SU(2)_L \otimes U(1)_Y$ Lagrangian, Eq. 2.12, does not change when expressed in terms of mass eigenstates. Flavour-changing neutral-currents are forbidden at tree level in the SM.

On the other hand, since $\overline{\boldsymbol{u}}'_L \boldsymbol{d}'_L \neq \overline{\boldsymbol{u}}_L \boldsymbol{d}_L$, the charged-current interaction of Eq. 2.7 is generalised in the mass basis as

$$\mathcal{L}_{CC} = -\frac{g}{2\sqrt{2}} \left\{ W^{\dagger}_{\mu} \left[\sum_{ij} \overline{u}_i \gamma^{\mu} (1-\gamma_5) [V_{uL} V^{\dagger}_{dL}]_{ij} d_j + \sum_{l} \overline{\nu}_l \gamma^{\mu} (1-\gamma_5) \ell \right] + \text{h.c.} \right\}, \tag{2.35}$$

where the matrix $V_{uL} V^{\dagger}_{dL} = V_{CKM}$, is the Cabibbo-Kobayashi-Maskawa (CKM) matrix [4, 20]. By convention, the interaction eigenstates and the mass eigenstates are chosen to be equal for the 'up-type' quarks, whereas the 'down-type' quarks are chosen to be rotated (the CKM matrix couples any 'up-type' quark with all 'down-type' quarks). Thanks to the CKM matrix elements, weak decays involving charged-currents may change the quark flavours not only within families, but also across families, as schematically shown in Fig. 2.2. Since the CKM matrix lies at the core of *CP*-violation within the SM, a detailed explanation is given below.

If neutrinos are assumed to be massless, the neutrino flavours can always be redefined in such a way as to eliminate the analogous mixing in the lepton sector: $\overline{\boldsymbol{\nu}}'_L \ell'_L = \overline{\boldsymbol{\nu}}_L \ell_L$ Thus, there is lepton-flavour conservation in the minimal SM without right-handed neutrinos.

2.2 *CP*-violation in the Standard Model

Whereas electromagnetic (QED) and strong (QCD) interactions are *C*- and *P*-symmetric, both symmetries are maximally violated in the charged-current weak interactions [21–23]. Still, the combined *CP*-symmetry was thought to be an exact symmetry of the system. However in 1964 it was demonstrated that *CP* is also violated in nature at the 10^{-3} level by the $K^0_S - K^0_L$ system [5]. Once *CP* is violated, even if so slightly, then an absolute, convention-independent definition of matter with respect to antimatter can be made.

Even though a mechanism to produce *CP*-violation is included in the SM, via the Kobayashi-Maskawa (KM) mechanism, the predicted amount of *CP*-violation is known to be insufficient to generate the matter-antimatter asymmetry observed in the universe today [24]. Hence new sources of *CP*-violation must exist in nature, and understanding

CP-violation is then a key aspect to find them. Moreover, many extensions of the SM provide new sources of *CP*-violation, so the study of *CP*-violating processes is intimately related to the search of new physics.

The following paragraphs have been written following Ref. [25–27]. Before moving on to the description of the CKM matrix and its importance to *CP*-violation, and to the discussion of the most relevant *CP*-violating processes, in the neutral meson systems, a brief comment on the discrete symmetries and the meaning of the *CP*-symmetry is included.

2.2.1 Discrete symmetries

Discrete symmetries describe non-continuous changes in a physical system. Among the discrete symmetries, spatial parity (P), charge conjugation (C) and time reversal (T) are of singular importance in flavour physics. Consider a particle of momentum $\vec{p}$, spin $\vec{s}$ and internal quantum numbers χ, represented by the state $|\vec{p}, h, \chi\rangle$, where $h = \vec{s}\cdot\vec{p}/|\vec{p}|$ is its helicity:[1]

- Parity is defined as the simultaneous inversion of the spatial coordinates, while the time component is conserved, $P : (x, y, z, t) \to (-x, -y, -z, t)$. The parity transformation can be viewed as a mirroring with respect to a plane, followed by a rotation around an axis perpendicular to the plane. The particle transforms as $P|\vec{p}, h, \chi\rangle \to |-\vec{p}, -h, \chi\rangle$. P transforms left-handed particles into right-handed particles, and inversely. The eigenvalues of P can only be complex phases, since the application of the operators twice must return the original state (up to an unobservable phase). For elementary particles or fields an intrinsic parity can also be defined.

- Charge conjugation inverts the quantum numbers of the particle, effectively interchanging the particle for its antiparticle, $C|\vec{p}, h, \chi\rangle \to |\vec{p}, h, \overline{\chi}\rangle$. Only completely neutral particles, with $\chi = 0$, are eigenstates of C. In this case, the particle coincides with its antiparticle.

- Time reversal means the inversion of the time coordinate, $T : t \to -t$. The particle transforms as $T|\vec{p}, h, \chi\rangle \to |-\vec{p}, h, \chi\rangle^*$. The T operator is antiunitary.

The Lagrangians of the electromagnetic and strong interaction are invariant under C, P and T (and consequently to any combination of them), whereas the weak interaction maximally violates C and P [22, 23]: the charged W bosons couple to left-handed electrons, e_L^-, but to neither their C-conjugate left-handed positrons, e_L^+, nor their P-conjugate right-handed electrons, e_R^-. Additionally, a first direct observation of T-violation by the weak interaction has been obtained [28].

It was thought that the product of the C and P operators, denoted CP, was conserved by the weak interaction [29], since the charged W bosons couple also to the CP-conjugate of the left-handed electrons, right-handed positrons, e_R^+. The discovery of the $K_L^0 \to \pi^+\pi^-$ decay in 1964 [5] demonstrated that *CP*-symmetry is violated in weak interactions.

[1] The helicity of a particle is right-handed if the direction of its spin is the same as the direction of its motion and it is left-handed if the directions of spin and motion are opposite.

The product of the three symmetries, *CPT*, is known to be a fundamental symmetry of any Lorentz invariant local quantum field theory [30, 31], such as the SM. It is, by definition, an exact symmetry of the theory, and so far searches for *CPT*-violation have not found any significant violation [32].One of the consequences of the *CPT* symmetry is that any observation of *CP*-violation results in a violation of T. Assuming *CPT* invariance, time-reversal symmetry violation has been detected [33]. Another consequence is that a particle and its antiparticle have identical mass and lifetime.

2.2.2 CKM matrix

To produce *CP*-violation, several conditions have to be required. There have to be three fermion generations; with only two generations *CP*-violation is not possible (the unitarity condition imposes that the complex phases can be removed without affecting any observables). In addition, all CKM matrix elements must be non-zero and the quarks of a given charge must be non-degenerate in mass. Finally, there must be a phase in the Lagrangian. It turns out that the only existing phase in the SM is the complex phase that appears in the CKM matrix. Therefore this phase is the sole source of *CP*-violation within the SM and the predictions for *CP*-violating phenomena are quite constrained.

The CKM matrix has the general form

$$\mathrm{V_{CKM}} = \begin{pmatrix} V_{ud} & V_{us} & V_{ub} \\ V_{cd} & V_{cs} & V_{cb} \\ V_{td} & V_{ts} & V_{tb} \end{pmatrix}. \tag{2.36}$$

The matrix elements are complex and there are in general 18 parameters. Since the matrix is unitary, $\mathrm{V_{CKM}V_{CKM}^{\dagger}} = 1$, the number of independent parameters is reduced to 9.[1] Of these, five can be absorbed in the redefinition of the quark fields. This leaves four independent parameters, three rotation angles, the quark mixing angles θ_{ij}, and one complex phase. The value of the coefficients can be found in Ref. [1].

Several parametrisations of the CKM matrix have been proposed. The 'standard' parametrisation [34], in which the matrix is written as an Euler rotation around three axes is given by

$$\mathrm{V_{CKM}} = \begin{pmatrix} c_{12}c_{13} & s_{12}c_{13} & s_{13}e^{-i\delta} \\ -s_{12}c_{23} - c_{12}s_{23}s_{13}e^{i\delta} & c_{12}c_{23} - s_{12}s_{23}s_{13}e^{i\delta} & s_{23}c_{13} \\ s_{12}s_{23} - c_{12}c_{23}s_{13}e^{i\delta} & -s_{23}c_{12} - s_{12}c_{23}s_{13}e^{i\delta} & c_{23}c_{13} \end{pmatrix}, \tag{2.37}$$

where δ is a complex phase, $c_{ij} = \cos\theta_{ij}$, $s_{ij} = \sin\theta_{ij}$ and c_{ij} and s_{ij} can all be chosen to be positive. Another parametrisation, which has the nice feature of clearly showing the hierarchical pattern of the CKM matrix is the Wolfenstein parametrisation [35],

$$\mathrm{V_{CKM}} = \begin{pmatrix} 1 - \frac{\lambda^2}{2} & \lambda & A\lambda^3(\rho - i\eta) \\ -\lambda & 1 - \frac{\lambda^2}{2} & A\lambda^2 \\ A\lambda^3(1 - \rho - i\eta) & -A\lambda^2 & 1 \end{pmatrix} + \mathcal{O}(\lambda^4), \tag{2.38}$$

[1] A $n \times n$ complex matrix contains $2n^2$ parameters. If the matrix is unitary, the number of independent parameters decreases to n^2.

where $\lambda = |V_{us}| \approx 0.22$ and A, η and ρ are numbers of order unity. From this parametrisation it is easy to see that the interactions between members of the same family are more favourable than the cross-family interactions.

Several relations can be obtained from the unitarity of the CKM matrix,

$$\sum_{k=1}^{3} V_{ki}^{*} V_{kj} = \delta_{ij}. \tag{2.39}$$

The three equations with $i = j$ express the *weak universality*, because they show that the sum of all couplings of the up-type quarks to all the down-type quarks is the same for all generations. Theoretically it is a consequence of the fact that all $SU(2)$ doublets couple with the same strength to the vector bosons of weak interactions. Besides the sum adds up to one, meaning that they do not couple to a fourth down-type quark. The other six equations with $i \neq j$ are known as the orthogonality conditions. As these are sums of three complex numbers that must yield zero they can be viewed as triangles in the complex plane. All of the triangles have equal surface area, related to the Jarlskog invariant [36], defined as the imaginary part of the product of the diagonal elements with the complex conjugate of the non-diagonal elements of the CKM matrix after removing one row and one column,

$$\mathcal{J} = \mathcal{I}m(V_{11}V_{22}V_{12}^{*}V_{21}^{*}) = \mathcal{I}m(V_{22}V_{33}V_{23}^{*}V_{32}^{*}) = \ldots = 2 \times \text{area}. \tag{2.40}$$

In the Wolfenstein parametrisation,

$$\mathcal{J} = A^2 \lambda^6 \eta, \tag{2.41}$$

and in the standard parametrisation,

$$\mathcal{J} = c_{12} c_{13}^2 c_{23} s_{12} s_{13} s_{23} \sin\delta. \tag{2.42}$$

The Jarlskog invariant has to be different from zero so that *CP*-violation can exist, because if any of the mixing angles is zero, the CKM matrix would essentially be reduced to a 2×2 matrix allowing the removal of the phase, and if the complex phase is zero no *CP*-violation is possible. This means that there can be *CP*-violation only if the triangles have finite area. Besides, any *CP*-violation observable involves the product $\mathcal{J}$ [36]. Thus, violations of the *CP*-symmetry are necessarily small, since $\mathcal{J} < 10^{-4}$.

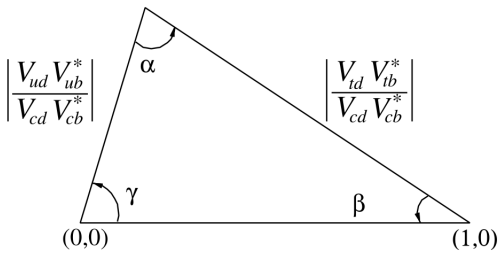

Figure 2.3: Unitarity triangle defined in Eq. 2.43.

Among these triangles, the one defined by the equation

$$V_{ud}V_{ub}^{*} + V_{cd}V_{cb}^{*} + V_{td}V_{tb}^{*} = 0 \tag{2.43}$$

is of great interest since all the terms of the sum are of the same order in λ, $\mathcal{O}(\lambda^3)$, and therefore all the angles have sizeable values. It is known as the *unitarity triangle*. By dividing the three sides of the unitarity triangle by $V_{cd}V_{cb}^{*}$ and subsequently rotating it, a triangle in the complex $(\overline{\rho}, \overline{\eta})$ plane, where

$$\overline{\rho} = \rho\left(1 - \frac{\lambda^2}{2}\right), \quad \overline{\eta} = \eta\left(1 - \frac{\lambda^2}{2}\right), \tag{2.44}$$

is obtained, as shown in Fig. 2.3. One side now has unit length and points along the real axis. The apex of the triangle is located by definition at

$$\overline{\rho} + i\overline{\eta} \equiv \frac{V_{ud}V_{ub}^{*}}{V_{cd}V_{cb}^{*}}. \tag{2.45}$$

The three angles of the triangle are related to the CKM elements by

$$\alpha = \arg\left(-\frac{V_{td}V_{tb}^{*}}{V_{ud}V_{ub}^{*}}\right), \tag{2.46}$$

$$\beta = \arg\left(-\frac{V_{cd}V_{cb}^{*}}{V_{td}V_{tb}^{*}}\right), \tag{2.47}$$

$$\gamma = \arg\left(-\frac{V_{ud}V_{ub}^{*}}{V_{cd}V_{cb}^{*}},\right). \tag{2.48}$$

Experimentally, the sides and the angles of the triangle can be determined by measuring the decay rates and *CP*-violating asymmetries of processes involving those CKM elements. These measurements have intensively been performed by the *B*-factories [37], with an important contribution by LHCb to the precision in γ. The current experimental situation of the unitarity triangle is shown in Fig. 2.4, from Ref. [38].

Apart from the unitarity triangle defined previously, other five triangles can be constructed. There is another one with the three sides of the same order, defined by: $V_{td}V_{ud}^{*} + V_{ts}V_{us}^{*} + V_{tb}V_{ub}^{*} = 0$, but the angles of this triangle are equal to (α, β, γ) up to corrections of $\mathcal{O}(\lambda^2)$. A different kind of triangles include sides of unequal orders in λ, therefore corresponding to almost flat triangles. Among them, the one represented by

$$V_{us}V_{ub}^{*} + V_{cs}V_{cb}^{*} + V_{ts}V_{tb}^{*} = 0, \tag{2.49}$$

is increasingly gaining importance since the start of the operation of the LHCb experiment. This triangle is crucial for testing the Kobayashi-Maskawa theory of *CP*-violation in the B_s^0 sector, only accesible to hadron colliders, which has not been studied as precisely as the B^0 sector. The huge amount of B_s^0 mesons produced at the LHC makes LHCb the perfect place to study this triangle. The side described by $V_{us}V_{ub}^{*}$ is much smaller than the other two, and then the angle defined by

$$\beta_s = \arg\left(-\frac{V_{ts}V_{tb}^{*}}{V_{cs}V_{cb}^{*}}\right), \tag{2.50}$$

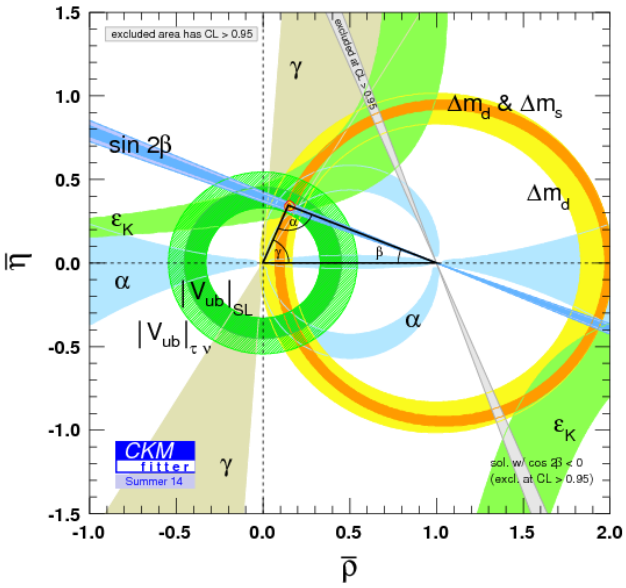

Figure 2.4: Current experimental status of the unitarity triangle defined in Eq. 2.43.

is very small. Any deviation from this SM prediction would thus mean NP. The other triangles are not as useful for now, but some of them should play a role when the data on rare and *CP* violating decays improve.

Finally, it is very convenient to write the CKM matrix using the Wolfenstein parametrisation with the weak phases explicitly shown,

$$V_{CKM} = \begin{pmatrix} |V_{ud}| & |V_{us}| & |V_{ub}|e^{-i\gamma} \\ -|V_{cd}| & |V_{cs}| & |V_{cb}| \\ |V_{td}|e^{-i\beta} & -|V_{ts}|e^{i\beta_s} & |V_{tb}| \end{pmatrix} + \mathcal{O}(\lambda^5). \tag{2.51}$$

2.2.3 Neutral meson system

The K^0, D^0, B^0 and B_s^0 neutral meson systems are an important environment for investigating *CP*-violating phenomena. Each of these is the lightest neutral meson with a particular combination of flavours of quarks. Since the strong and electromagnetic interactions conserve flavour, the only available decay modes are via the weak interaction. Apart from the decay, these mesons can experience particle-antiparticle conversions, in a process called oscillation or mixing, through the Feynman diagrams shown in Fig. 2.5 (only shown for the B^0 and B_s^0 mesons, diagrams for the K^0 and D^0 mesons are similar replacing the appropriate quarks), often referred to as box diagrams. This second-order weak coupling 'mixes' the particle and the antiparticle, playing a crucial role in providing a second transition amplitude from the initial state to a given final state, which gives rise to three different types of *CP*-violating processes: *CP*-violation in the decay, *CP*-violation in the oscillation and *CP*-violation in the interference between the decay and the mixing. *CP*-violating effects have also been observed in decays of charged particles. In the next

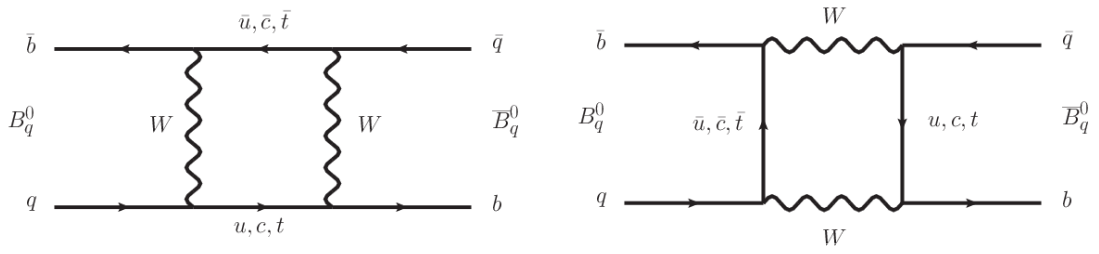

Figure 2.5: Leading order Feynman diagrams contributing to the B-meson oscillations ($q = \{s, d\}$).

lines, the oscillation in the neutral meson system along with the types of CP-violation that can be observed are explained.

Consider a neutral meson P^0 (any of the weakly decaying neutral mesons: K^0, D^0, B^0 and B_s^0) and its CP conjugate, $\bar{P}^0$, which are eigenstates of the strong and electromagnetic interaction with common mass and opposite flavour content. A state that is initially a superposition of P^0 and $\bar{P}^0$,

$$|\psi(0)\rangle = a(0)|P^0\rangle + b(0)|\bar{P}^0\rangle, \tag{2.52}$$

will evolve in time following,

$$|\psi(t)\rangle = a(t)|P^0\rangle + b(t)|\bar{P}^0\rangle + \sum_n c_n(t)|n\rangle, \tag{2.53}$$

where $|n\rangle$ are the different decay modes of the original mesons. If only the values of $a(t)$ and $b(t)$ are of interest and the considered times t are much larger than the typical strong-interaction scale, the problem can be simplified. Under these assumptions, known as the Weisskopf-Wigner approximation [39], the evolution of the system is determined by an effective Hamiltonian,

$$i\frac{\mathrm{d}|\psi(t)\rangle}{\mathrm{d}t} = \boldsymbol{H}_{eff}|\psi(t)\rangle. \tag{2.54}$$

Since the mesons have to decay, $\boldsymbol{H}_{eff}$ is non hermitian, but it can always be written in terms of the two-by-two hermitian matrices $\boldsymbol{M}$ and $\boldsymbol{\Gamma}$,

$$\boldsymbol{H}_{eff} = \boldsymbol{M} - \frac{i}{2}\boldsymbol{\Gamma}, \tag{2.55}$$

with $\boldsymbol{M}$ and $\boldsymbol{\Gamma}$ representing the masses and lifetimes of the states. Assuming CPT invariance ensures that the diagonal elements of these matrices are equal,

$$M_{11} = M_{22} = M, \quad \Gamma_{11} = \Gamma_{22} = \Gamma, \tag{2.56}$$

meaning that mass and total decay width of particle and antiparticle are identical. The off-diagonal terms,

$$M_{21} = M_{12}^*, \quad \Gamma_{21} = \Gamma_{12}^*, \tag{2.57}$$

are responsible for the mixing between the meson and antimeson. The dispersive part, M_{12} corresponds to virtual $\Delta F = 2$ transitions dominated by heavy internal particles (top

quarks in the SM) while the absorptive part Γ_{12} arises from on-shell transitions due to decay modes common to P^0 and $\bar{P}^0$ mesons. In general there can be a relative phase between Γ_{12} and M_{12},

$$\phi = arg\left(-\frac{M_{12}}{\Gamma_{12}}\right). \tag{2.58}$$

The flavour eigenstates differ from the mass eigenstates, but are related through a basis rotation. The mass basis is defined by the eigenstates that diagonalise H_{eff} in Eq.2.54. The eigenvalues of the mass-decay matrix are,

$$\mu_{H,L} = M - \frac{i}{2}\Gamma \pm F, \tag{2.59}$$

where

$$F = \sqrt{(M_{12} - \frac{i}{2}\Gamma_{12})(M^*_{12} - \frac{i}{2}\Gamma^*_{12})}. \tag{2.60}$$

Defining $\mu_{H,L} = M_{H,L} - \frac{i}{2}\Gamma_{H,L}$, the following expressions are obtained,

$$\begin{aligned} \Delta m &\equiv M_H - M_L = 2\mathcal{R}eF, \\ \Delta\Gamma &\equiv \Gamma_L - \Gamma_H = 4\mathcal{I}mF. \end{aligned} \tag{2.61}$$

where the subindices L and H refer respectively to the light- and heavy-mass eigenstates. By definition $\Delta m > 0$, and the sign of $\Delta\Gamma$ has to be measured experimentally (with the convention used $\Delta\Gamma$ is positive in the SM for B^0 and B^0_s mesons). The next relations can be obtained using $\mu_H - \mu_L = \Delta M + \frac{i}{2}\Delta\Gamma = 2F$,

$$\begin{aligned} \Delta M^2 - \frac{1}{4}\Delta\Gamma^2 &= 4|M_{12}|^2 - |\Gamma_{12}|^2, \\ \Delta M\Delta\Gamma &= -4\mathcal{R}e\left[M_{12}\Gamma^*_{12}\right]. \end{aligned} \tag{2.62}$$

The mass eigenstates are expressed in the flavour basis,

$$\begin{aligned} |P_H\rangle &= p|P^0\rangle + q|\bar{P}^0\rangle, \\ |P_L\rangle &= p|P^0\rangle - q|\bar{P}^0\rangle, \end{aligned} \tag{2.63}$$

where the complex parameters p and q are normalised,

$$|p|^2 + |q|^2 = 1, \tag{2.64}$$

and related through

$$\frac{q}{p} = \sqrt{\frac{M^*_{12} - \frac{i}{2}\Gamma^*_{12}}{M_{12} - \frac{i}{2}\Gamma_{12}}}. \tag{2.65}$$

The time evolution of the mass eigenstates is given by the simple expression

$$|P_{H,L}(t)\rangle = e^{-i(M_{H,L} - \frac{i}{2}\Gamma_{H,L})}|P_{H,L}(0)\rangle. \tag{2.66}$$

Recovering Eq. 2.63, the time evolution of the flavour eigenstates is described by

$$\begin{aligned} |P^0(t)\rangle &= g_+(t)|P^0\rangle + \frac{q}{p}g_-(t)|\bar{P}^0\rangle, \\ |\bar{P}^0(t)\rangle &= \frac{p}{q}g_-(t)|P^0\rangle + g_+(t)|\bar{P}^0\rangle, \end{aligned} \tag{2.67}$$

where

$$g_{\pm} = \frac{1}{2}\left(e^{-i(M_H - \frac{i}{2}\Gamma_H)t} \pm e^{-i(M_L - \frac{i}{2}\Gamma_L)t}\right). \tag{2.68}$$

Once the formalism of neutral meson oscillations is defined, the subsequent decay of the meson to a final state f is considered. Defining the decay amplitudes of P^0 and $\overline{P}^0$ to f and to its CP conjugate $\overline{f}$ as

$$\begin{aligned} A_f &= \langle f|H|P^0\rangle, \quad \overline{A}_f = \langle f|H|\overline{P}^0\rangle, \\ A_{\overline{f}} &= \langle \overline{f}|H|P^0\rangle, \quad \overline{A}_{\overline{f}} = \langle \overline{f}|H|\overline{P}^0\rangle, \end{aligned} \tag{2.69}$$

the general expressions for the time-dependent decay rates are thus calculated as

$$\begin{aligned} \Gamma(P^0 \to f) \;&\propto |A_f|^2 \frac{e^{-\Gamma t}}{2}\Bigg[(1+|\lambda_f|^2)\cosh\left(\frac{\Delta\Gamma t}{2}\right) - 2\mathcal{R}e[\lambda_f]\sinh\left(\frac{\Delta\Gamma t}{2}\right) \\ &\quad + (1-|\lambda_f|^2)\cos(\Delta m t) - 2\mathcal{I}m[\lambda_f]\sin(\Delta m t)\Bigg], \\ \Gamma(P^0 \to \overline{f}) \;&\propto |\overline{A}_{\overline{f}}|^2 \frac{e^{-\Gamma t}}{2}\left|\frac{q}{p}\right|^2\Bigg[(1+|\overline{\lambda}_{\overline{f}}|^2)\cosh\left(\frac{\Delta\Gamma t}{2}\right) - 2\mathcal{R}e[\overline{\lambda}_{\overline{f}}]\sinh\left(\frac{\Delta\Gamma t}{2}\right) \\ &\quad - (1-|\overline{\lambda}_{\overline{f}}|^2)\cos(\Delta m t) + 2\mathcal{I}m[\overline{\lambda}_{\overline{f}}]\sin(\Delta m t)\Bigg], \\ \Gamma(\overline{P}^0 \to f) \;&\propto |A_f|^2 \frac{e^{-\Gamma t}}{2}\left|\frac{p}{q}\right|^2\Bigg[(1+|\lambda_f|^2)\cosh\left(\frac{\Delta\Gamma t}{2}\right) - 2\mathcal{R}e[\lambda_f]\sinh\left(\frac{\Delta\Gamma t}{2}\right) \\ &\quad - (1-|\lambda_f|^2)\cos(\Delta m t) + 2\mathcal{I}m[\lambda_f]\sin(\Delta m t)\Bigg], \\ \Gamma(\overline{P}^0 \to \overline{f}) \;&\propto |\overline{A}_{\overline{f}}|^2 \frac{e^{-\Gamma t}}{2}\Bigg[(1+|\overline{\lambda}_{\overline{f}}|^2)\cosh\left(\frac{\Delta\Gamma t}{2}\right) - 2\mathcal{R}e[\overline{\lambda}_{\overline{f}}]\sinh\left(\frac{\Delta\Gamma t}{2}\right) \\ &\quad + (1-|\overline{\lambda}_{\overline{f}}|^2)\cos(\Delta m t) - 2\mathcal{I}m[\overline{\lambda}_{\overline{f}}]\sin(\Delta m t)\Bigg], \end{aligned} \tag{2.70}$$

where the complex quantities λ_f and $\overline{\lambda}_{\overline{f}}$ are defined as:

$$\lambda_f = \frac{q}{p}\frac{\overline{A}_f}{A_f}, \quad \overline{\lambda}_{\overline{f}} = \frac{p}{q}\frac{A_{\overline{f}}}{\overline{A}_f}, \tag{2.71}$$

and also

$$\Gamma = \frac{\Gamma_L + \Gamma_H}{2}, \quad \Delta\Gamma = \Gamma_L - \Gamma_H, \quad \Delta m = M_H - M_L. \tag{2.72}$$

Three types of CP-violation can be distinguished considering the master formulae for the decay rates of neutral mesons, Eq. 2.70:

- CP-**violation in decay**, when the decay rates of $P^0 \to f$ and $\overline{P}^0 \to \overline{f}$ are different. In a case where there is no oscillation,

$$\begin{aligned} \Gamma(P^0(t) \to f) &\propto \frac{e^{-\Gamma t}}{2}|A_f|^2, \\ \Gamma(\overline{P}^0(t) \to \overline{f}) &\propto \frac{e^{-\Gamma t}}{2}|\overline{A}_{\overline{f}}|^2, \end{aligned} \tag{2.73}$$

and therefore *CP* is violated if

$$\left|\frac{\overline{A}_{\overline{f}}}{A_f}\right| \neq 1. \tag{2.74}$$

This type of *CP*-violation is the only possible in charged meson decays.

- *CP*-**violation in mixing**, when the decay rate of the oscillation $P^0 \to \bar{P}^0$ is different from $\bar{P}^0 \to P^0$. Considering a *flavour specific* decay, in which the final state f is only accessible to P^0, and its *CP* analogue, that is

$$A_{\overline{f}} = \overline{A}_f = \lambda_f = \overline{\lambda}_{\overline{f}} = 0, \tag{2.75}$$

then the transitions $P^0 \to \overline{f}$ and $\bar{P}^0 \to f$ can only procceed through mixing,

$$\begin{aligned}
\Gamma(P^0(t) \to \overline{f}) &\propto |\overline{A}_{\overline{f}}|^2 \frac{e^{-\Gamma t}}{2} \left|\frac{q}{p}\right|^2 \left[\cosh\left(\frac{\Delta\Gamma t}{2}\right) - \cos(\Delta m t)\right], \\
\Gamma(\bar{P}^0(t) \to f) &\propto |A_f|^2 \frac{e^{-\Gamma t}}{2} \left|\frac{p}{q}\right|^2 \left[\cosh\left(\frac{\Delta\Gamma t}{2}\right) - \cos(\Delta m t)\right].
\end{aligned} \tag{2.76}$$

Considering also that there is not *CP*-violation in the decay ($|A_f| = |\overline{A}_{\overline{f}}|$), *CP* can still be violated in the mixing if

$$\left|\frac{q}{p}\right| \neq 1. \tag{2.77}$$

- *CP*-**violation in the interference between mixing and decay**, when the final state is accesible from P^0 and $\bar{P}^0$. In particular if the final state f is a *CP* eigenstate, $f = \overline{f} \equiv f_{CP}$, the neutral meson can either decay to the final state directly or first oscillate and then decay,

$$A(P^0(t) \to f_{CP}) \sim A(P^0 \to f_{CP}) + A(P^0 \to \bar{P}^0 \to f_{CP}). \tag{2.78}$$

Even if there is no direct or indirect *CP*-violation, the interference between these two decays can induce *CP*-violation,

$$\begin{aligned}
\Gamma(P^0(t) \to f_{CP}) \;\propto\; & |A_{f_{CP}}|^2 e^{-\Gamma t}\Big[(1 + |\lambda_{f_{CP}}|^2)\cosh\left(\frac{\Delta\Gamma t}{2}\right) \\
& - 2\mathcal{R}e[\lambda_{f_{CP}}]\sinh\left(\frac{\Delta\Gamma t}{2}\right) + (1 - |\lambda_{f_{CP}}|^2)\cos(\Delta m t) \\
& - 2\mathcal{I}m[\lambda_{f_{CP}}]\sin(\Delta m t)\Big],
\end{aligned} \tag{2.79}$$

$$\begin{aligned}
\Gamma(\bar{P}^0(t) \to f_{CP}) \;\propto\; & |A_{f_{CP}}|^2 e^{-\Gamma t}\left|\frac{p}{q}\right|^2\Big[(1 + |\lambda_{f_{CP}}|^2)\cosh\left(\frac{\Delta\Gamma t}{2}\right) \\
& - 2\mathcal{R}e[\lambda_{f_{CP}}]\sinh\left(\frac{\Delta\Gamma t}{2}\right) - (1 - |\lambda_{f_{CP}}|^2)\cos(\Delta m t) \\
& + 2\mathcal{I}m[\lambda_{f_{CP}}]\sin(\Delta m t)\Big],
\end{aligned} \tag{2.80}$$

and the following time-dependent *CP*-asymmetry can be defined

$$\begin{aligned}
\mathcal{A}^{CP}(t) =& \frac{\Gamma(\bar{P}^0(t) \to f_{CP}) - \Gamma(P^0(t) \to f_{CP})}{\Gamma(\bar{P}^0(t) \to f_{CP}) + \Gamma(P^0(t) \to f_{CP})} = \\
& \frac{(|\lambda_{f_{CP}}|^2 - 1)\cos(\Delta m t) + 2\mathcal{I}m[\lambda_{f_{CP}}]\sin(\Delta m t)}{(1 + |\lambda_{f_{CP}}|^2)\cosh\left(\frac{\Delta\Gamma t}{2}\right) - 2\mathcal{R}e[\lambda_{f_{CP}}]\sinh\left(\frac{\Delta\Gamma t}{2}\right)},
\end{aligned} \tag{2.81}$$

where it is clear that even though $|\lambda_{f_{CP}}| = 1$ (meaning not *CP*-violation neither in the decay nor in the mixing), *CP*-violation can arise from the interference, if

$$\mathcal{I}m[\lambda_{f_{CP}}] \neq 0, \tag{2.82}$$

and only if there is $P^0 - \bar{P}^0$ oscillation ($\Delta m \neq 0$). Since in this case $\lambda_{f_{CP}}$ is a pure phase, it can be defined as

$$\lambda_{f_{CP}} = e^{-i(\phi_M + \phi_D)}, \tag{2.83}$$

where

$$\phi_M \equiv arg\left(\frac{p}{q}\right) \quad \text{and} \quad \phi_D \equiv arg\left(\frac{A_f}{\overline{A}_f}\right) \tag{2.84}$$

are the mixing and the decay angle, respectively. These two phases are convention dependent, being $arg(\lambda_{f_{CP}})$ the only measurable phase.

2.2.4 *B*-meson systems

The different properties of the K^0, D^0, B^0 and B_s^0 mesons, namely the difference in mass (and thus available phase space for the final state) and coupling strength (CKM-elements), confer striking variations in the ways in which the four meson systems behave, resulting in dramatically different phenomenology. For instance, the large lifetime difference in the K^0 system allows to clearly separate the K_S^0 and the K_L^0, whereas this is not possible for the other mesons. Only the particularities of the B^0 and B_s^0 mesons are described here, with the details of the K^0 and D^0 meson systems reviewed in many other places, for example Ref. [40].

The oscillations of neutral B^0-mesons were first observed at DESY with the ARGUS experiment in 1987 [41]. Measurements of $B^0 - \bar{B}^0$ mixing have been performed by several experiments. The most recent value of the mass difference is obtained fitting the time dependent mixing asymmetry in flavour specific B^0 decays to $D^{(*)-}\mu^+\nu_\mu X$ [42],

$$\Delta m_d = 505.0 \pm 2.1\,(\text{stat}) \pm 1.0\,(\text{syst})\,\text{ns}^{-1}. \tag{2.85}$$

The $B_s^0 - \bar{B}_s^0$ oscillations were first observed at the Tevatron $p\bar{p}$ collider at Fermilab by the CDF and D0 experiments [43]. The most recent result by the LHCb collaboration uses the flavour specific $B_s^0 \to D_s^-\pi^+$ decay [44],

$$\Delta m_s = 17.768 \pm 0.023\,(\text{stat}) \pm 0.006\,(\text{syst})\,\text{ps}^{-1}, \tag{2.86}$$

and represents the most precise measurement to date of such quantity. The B_s^0-meson therefore oscillates much faster than the B^0-meson, with 25 oscillations before the decay, on average, whereas the B^0-meson oscillates slowly, as seen in Fig. 2.6.

The SM predicts a very small width difference for the B^0 meson. This is confirmed by the analyses performed by the *B*-factories and by the LHCb experiment. The most precise measurement of this parameter is reported by the ATLAS collaboration comparing the decay-time distributions of $B^0 \to J/\psi K_S^0$ and $B^0 \to J/\psi K^{*0}(892)$ decays [45],

$$\frac{\Delta\Gamma_d}{\Gamma_d} = (-0.1 \pm 1.1\,(\text{stat}) \pm 0.9\,(\text{syst})) \times 10^{-2}. \tag{2.87}$$

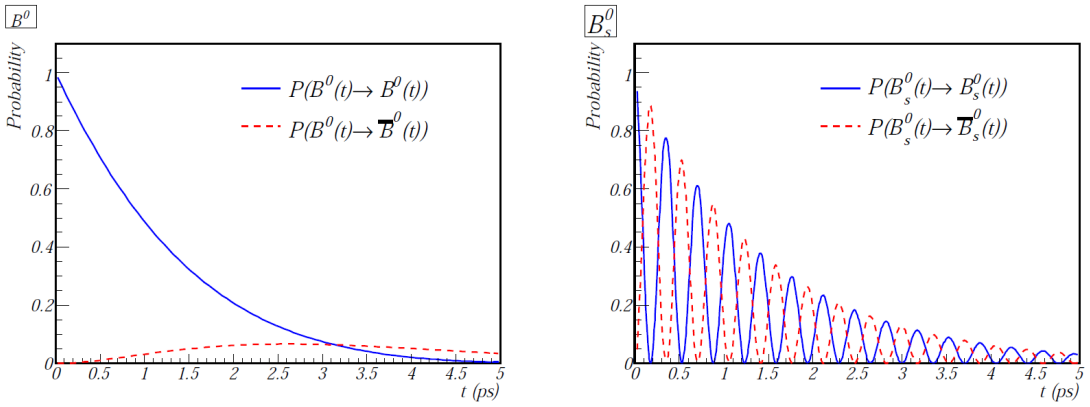

Figure 2.6: Left (Right): Starting from a pure B^0 (B_s^0) beam, the thick blue line corresponds to the probability of observing a B^0 (B_s^0) meson and the dashed red line to the probability of observing a $\bar{B}^0$ ($\bar{B}_s^0$) meson at time t.

For the B_s^0 system, on the other hand, the width difference has a sizeable value and therefore it has to be taken into account. $\Delta\Gamma_s$ has been measured by several experiments, D0, CDF, ATLAS, CMS and LHCb, using $B_s^0 \to J/\psi\,\phi$ decays. The most precise measurement, performed by the LHCb collaboration using $B_s^0 \to J/\psi\,K^+K^-$ decays, gives [46],

$$\begin{aligned} \Gamma_s &= 0.6603 \pm 0.0027\,(\text{stat}) \pm 0.0015\,(\text{syst})\,\text{ps}^{-1}, \\ \Delta\Gamma_s &= 0.0805 \pm 0.0091\,(\text{stat}) \pm 0.0032\,(\text{syst})\,\text{ps}^{-1}. \end{aligned} \tag{2.88}$$

CP-violation in mixing has been previously explained, with the parameter $|q/p|$ determining wheter there is *CP*-violation or not. The SM predicts that there is no *CP*-violation in mixing in the B-meson systems. In both B-meson systems, $\Delta M \gg \Delta\Gamma$, and since $|\Gamma_{12}| \ll \Delta M$ is firmly established from a SM calculation (the possible impact of new physics on $|\Gamma_{12}|$ is small), it can be deduced from Eq. 2.62 that $\Delta M \approx 2|M_{12}|$ and then $|\Gamma_{12}| \ll |M_{12}|$. Therefore,

$$\frac{q}{p} = \sqrt{\frac{M_{12}^* - \frac{i}{2}\Gamma_{12}^*}{M_{12} - \frac{i}{2}\Gamma_{12}}} \simeq \sqrt{\frac{M_{12}^*}{M_{12}}} \equiv e^{-i\phi_M}, \tag{2.89}$$

and

$$\left|\frac{q}{p}\right| = 1, \tag{2.90}$$

meaning no *CP*-violation in mixing. The phase of q/p is essentially given by the phase of the $B^0 - \bar{B}^0$ or $B_s^0 - \bar{B}_s^0$ box diagrams in Fig. 2.5. Since $B - \bar{B}$ mixing is dominated by the box diagram with internal top quarks,

$$\left(\frac{q}{p}\right)_Q = \frac{V_{tb}^* V_{tQ}}{V_{tb} V_{tQ}^*}, \tag{2.91}$$

where $Q = \{d, s\}$, and therefore

$$\phi_M^Q = 2\arg(V_{tb}V_{tQ}^*). \tag{2.92}$$

From Eq. 2.51, it can be seen that V_{tb} is real and that V_{ts} and V_{td} acquire a phase, therefore,

$$\begin{aligned} \phi_d &= 2\beta + \mathcal{O}(\lambda^5), \\ \phi_s &= -2\beta_s + \mathcal{O}(\lambda^5). \end{aligned} \tag{2.93}$$

This is the way in which the mixing angles are related to the angles of the unitarity triangles in the Standard Model.

Experimentally, *CP*-violation in mixing can be measured using semileptonic decays. The b-quarks decay as $b \to \ell^- \overline{\nu} X$, whereas the $\overline{b}$-quarks decay as $\overline{b} \to \ell^+ \nu X$. At the B-factories, B and $\overline{B}$ mesons are produced simultaneously through $e^- e^+ \to \Upsilon(4S) \to B\overline{B}$. Two same-sign leptons in the final state characterise the events where mixing has taken place, so the following asymmetry can be determined,

$$\mathcal{A}_{sl} = \frac{N^{++} - N^{--}}{N^{++} + N^{--}} = \frac{\Gamma(P^0 \to \overline{P}^0) - \Gamma(\overline{P}^0 \to P^0)}{\Gamma(P^0 \to \overline{P}^0) + \Gamma(\overline{P}^0 \to P^0)} = \frac{1 - |q/p|^4}{1 + |q/p|^4}. \tag{2.94}$$

Furthermore, LHCb has recently measured $\mathcal{A}_{sl}$ using $B^0 \to D^{(*)-} \mu^+ \nu_\mu X$ decays [47]. Combining the result by the B-factories, LHCb and other experiments gives [48]

$$\left| \frac{q}{p} \right|_d = 1.0010 \pm 0.0008. \tag{2.95}$$

In the B_s^0 meson case, the Tevatron experiments, CDF and D0, have measured linear combinations of $\mathcal{A}_{sl}^d$ and $\mathcal{A}_{sl}^s$ using inclusive semileptonic decays of b hadrons. The D0 result [49] differs by 3.6 standard deviations from the SM expectation. Direct measurements of $\mathcal{A}_{sl}^s$ have been also obtained by D0 and LHCb, using the time-integrated charge asymmetry of untagged $B_s^0 \to D_s^- \mu^+ \nu_\mu X$ decays [50]. These results are in agreement with the SM calculation, even though they are not precise enough to solve the issue. The average result is [48]

$$\left| \frac{q}{p} \right|_s = 1.0003 \pm 0.0014. \tag{2.96}$$

Both values, $|q/p|_d$ and $|q/p|_s$ are compatible with *CP* conservation in mixing of B^0 and B_s^0 and in agreement with the SM prediction.

2.3 $B_s^0 \to K^{*0}\overline{K}^{*0}$ and $B^0 \to K^{*0}\overline{K}^{*0}$ decays

Both $B^0 \to K^{*0}\overline{K}^{*0}$ and $B_s^0 \to K^{*0}\overline{K}^{*0}$ decays formally proceed through Flavour Changing Neutral Currents. In the SM these processes are forbidden at tree level, since the couplings of the quarks to the Z^0 boson are flavour diagonal, but they can still occur at first order through a loop penguin diagram, as seen in Fig. 2.7. Penguin diagrams are very interesting processes since contributions mediated by heavy particles contemplated in new physics models may enter into the loop of the diagram or mediate in additional amplitudes which could produce detectable effects in experimentally observed magnitudes, thus modifying the predictions of the SM.

The $B_s^0 \to K^{*0}\overline{K}^{*0}$ decay is a pure $\overline{b} \to \overline{s}$ penguin, dominated in the SM by a single contributing amplitude. Therefore all *CP*-violation observables are predicted to be small,

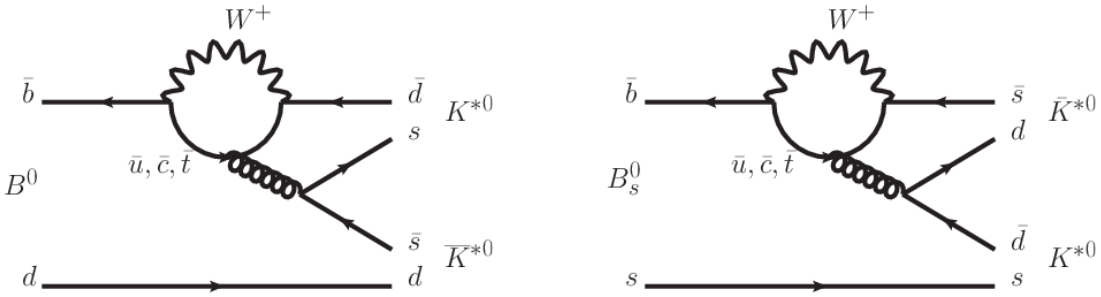

Figure 2.7: Leading order Feynman diagrams for the $B^0 \to K^{*0}\overline{K}^{*0}$ decay (left) and $B_s^0 \to K^{*0}\overline{K}^{*0}$ decay (right). Both diagrams are identical exchanging the s-quarks and the d-quarks (U-spin symmetry).

and the presence of NP would then clearly be indicated by the measurement of a sizeable *CP*-violating observable. Some authors consider this decay as a *golden channel* to search for new physics [51]. The subleading penguin amplitude is strongly CKM suppressed ($\mathcal{O}(\lambda^4)$), and if it is neglected *CP*-violation asymmetry is actually cancelled between the mixing and the decay. The measurement of *CP*-violation in this decay would therefore be a null test of the SM. This assumption may not be well justified [52, 53], but in any case this channel is still very interesting, because the contribution of the subleading amplitude can be handled in a model independent way by means of the mirror decay $B^0 \to K^{*0}\overline{K}^{*0}$ [51, 52, 54, 55]. In the next paragraphs these ideas are developed.

The $B_s^0 \to K^{*0}\overline{K}^{*0}$ amplitude receives contributions only from gluonic and electroweak penguin diagrams, and it can be expressed as the sum of the three contributing amplitudes, one for each of the internal quarks, u-, c- and t-quark [51–53, 55–57],

$$\begin{aligned} A(B_s^0 \to K^{*0}\overline{K}^{*0}) &= V_{ub}^* V_{us} P'_u + V_{cb}^* V_{cs} P'_c + V_{tb}^* V_{ts} P'_t \\ &= V_{tb}^* V_{ts} P'_{tc} + V_{ub}^* V_{us} P'_{uc} = |V_{tb}^* V_{ts}| e^{-i\phi_s/2} P'_{tc} + |V_{ub}^* V_{us}| e^{i\gamma} P'_{uc}, \end{aligned} \tag{2.97}$$

where P'_q contains penguin contractions of charmed current-current operators containing quarks q, together with the matrix elements of $b \to s$ penguin operators (the diagrams are written with primes because it is a $\overline{b} \to \overline{s}$ transition), in the second line the unitarity of the CKM matrix ($V_{ub}^* V_{us} + V_{cb}^* V_{cs} + V_{tb}^* V_{ts} = 0$) is used to eliminate the c-quark contribution: $P'_{tc} \equiv P'_t - P'_c$, $P'_{uc} \equiv P'_u - P'_c$, γ is one of the angles of the unitarity triangle and ϕ_s is the mixing angle in the $B_s^0 - \overline{B}_s^0$ system ($\phi_s = -2\beta_s$ in the SM). The second contribution to the amplitude of the $B_s^0 \to K^{*0}\overline{K}^{*0}$ decay is strongly CKM suppressed ($V_{ub}^* V_{us} \sim \lambda^4$) with respect to the first ($V_{tb} V_{ts} \sim \lambda^2$), and therefore it may be neglected [51].

With this assumption there cannot be direct *CP*-violation, because the decay is mediated by a single amplitude, and since the *CP*-violation in mixing is expected to be negligible, the only *CP*-violating phenomena that could exist in this decay according to the SM is the interference between mixing and decay. The indirect *CP*-violating asymmetry is defined in Eq. 2.81, where the parameter that defines the *CP*-violation is,

$$\lambda_{CP}(B_s^0 \to K^{*0}\overline{K}^{*0}) = \left(\frac{q}{p}\right)_s \frac{A(\overline{B}_s^0 \to K^{*0}\overline{K}^{*0})}{A(B_s^0 \to K^{*0}\overline{K}^{*0})}. \tag{2.98}$$

As already pointed out in Chapter 2.2.4, $|q/p|_s = 1$, and with a single amplitude contributing to the decay, $|A(\overline{B}^0_s \to K^{*0}\overline{K}^{*0})/A(B^0_s \to K^{*0}\overline{K}^{*0})| = 1$. With Eq. 2.91 and Eq. 2.97,

$$\lambda_{CP}(B^0_s \to K^{*0}\overline{K}^{*0}) = \frac{V^*_{tb}V_{ts}}{V_{tb}V^*_{ts}}\frac{V_{tb}V^*_{ts}}{V^*_{tb}V_{ts}} = 1, \tag{2.99}$$

and therefore the study of time-dependent *CP*-violating asymmetries in the $B^0_s \to K^{*0}\overline{K}^{*0}$ decay would be a null test of the SM [51].

Other authors [53] have pointed out that even though the final result of a vanishing indirect *CP*-violation is valid, the argument leading to it is not. It can be seen easily if instead of eliminating the c-quark contribution in Eq. 2.97, the t-quark contribution is removed,

$$A(B^0_s \to K^{*0}\overline{K}^{*0}) = V^*_{cb}V_{cs}P'_{ct} + V^*_{ub}V_{us}P'_{ut}\,. \tag{2.100}$$

Now if the second term is neglected, there is no cancellation of the mixing and the decay, and the indirect CPA is (apparently) nonzero. What is really happening is that if the terms of $\mathcal{O}(\lambda^4)$ are neglected, ϕ_s also vanishes in that limit, and the result of a vanishing indirect CPA is then recovered. Therefore the subleading amplitude has to be kept in order to generate a weak phase in $A(B^0_s \to K^{*0}\overline{K}^{*0})$.

Assuming that the CKM values in Eq. 2.97 are taken from independent measurements, there are four unknowns: both penguin amplitudes $|P'_{uc}|$ and $|P'_{tc}|$, their relative strong phase δ' and ϕ_s. However, there are three measurements which can be made in $B^0_s \to K^{*0}\overline{K}^{*0}$ decays: the branching ratio ($\mathcal{B}$), and the direct ($A_{\rm dir}$) and mixing-induced ($A_{\rm mix}$) *CP*-violating asymmetries [52]:

$$\begin{aligned}
\mathcal{B} &= g_{\rm ps}\frac{|A_s|^2 + |\overline{A}_s|^2}{2},\\
A_{\rm dir} &= \frac{|A_s|^2 - |\overline{A}_s|^2}{|A_s|^2 + |\overline{A}_s|^2},\\
A_{\rm mix} &= 2\frac{\mathcal{I}m\left(e^{-i\phi_s}A^*_s\overline{A}_s\right)}{|A_s|^2 + |\overline{A}_s|^2},\\
A_{\Delta\Gamma} &= 2\frac{\mathcal{R}e\left(e^{-i\phi_s}A^*_s\overline{A}_s\right)}{|A_s|^2 + |\overline{A}_s|^2},
\end{aligned} \tag{2.101}$$

where $g_{\rm ps}$ is a phase space factor, $A_s = A(B^0_s \to K^{*0}\overline{K}^{*0})$ and $A_{\Delta\Gamma}$ is not an independent measurement since $|A_{\rm dir}|^2 + |A_{\rm mix}|^2 + |A_{\Delta\Gamma}|^2 = 1$. There are more unknown parameters than observables, and therefore additional input is needed to determine the unknowns. Several methods have been developed to handle the size of the subleading penguin amplitude: using theoretical input and using the $B^0 \to K^{*0}\overline{K}^{*0}$ decay.

Theoretically, the parameter $\Delta = P'_{tc} - P'_{uc}$ can be computed in a well-controled way leading to safe predictions and small uncertainties [56]. For penguin mediated decays, both contributions share the same long-distance dynamics, the difference coming from the quark running in the loops. Some predictions of the value of ϕ_s can be made taking as input this theoretical value and several of the measurements previously mentioned [55, 56]. In Fig 2.8 (left), an example of the possible values of ϕ_s depending on the values of $A_{\rm mix}$ and $A_{\Delta\Gamma}$ to be measured in $B^0_s \to K^{*0}\overline{K}^{*0}$ decays is shown.

Another way to control the contribution of the subleading amplitude has been studied by different authors [51, 52, 54]. It is based on the use of the $B^0 \to K^{*0}\overline{K}^{*0}$ decay, related

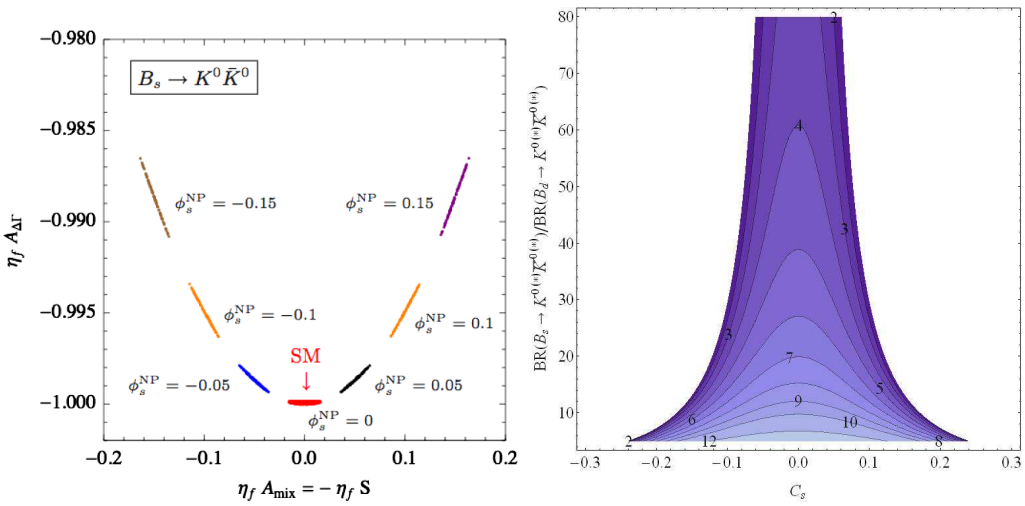

Figure 2.8: Left: A_{mix} vs $A_{\Delta\Gamma}$ in $B_s^0 \to K^{*0}\overline{K}^{*0}$ for several values of the mixing angle ϕ_s^{NP}, from Ref. [55]. Right: β_s^{eff} predictions as a function of the direct *CP*-asymmetry in $B_s^0 \to K^{*0}\overline{K}^{*0}$ and the ratio of branching ratios $(\mathcal{B}(B_s^0)/\mathcal{B}(B^0))$, from Ref. [52].

to the $B_s^0 \to K^{*0}\overline{K}^{*0}$ decay through the *U*-spin flavour symmetry of strong interactions. For $B^0 \to K^{*0}\overline{K}^{*0}$ decays, the amplitude reads,

$$A(B^0 \to K^{*0}\overline{K}^{*0}) = V_{tb}^* V_{td} P_{tc} + V_{ub}^* V_{ud} P_{uc} = |V_{tb}^* V_{td}| e^{-i\beta} P_{tc} + |V_{ub}^* V_{ud}| e^{i\gamma} P_{uc}, \quad (2.102)$$

where now the second amplitude not only cannot be neglected, but the situation is that both amplitudes have equal order contributions, $V_{tb}^* V_{td} \sim V_{ub}^* V_{ud} \sim \lambda^3$, and as a consequence the sensitivity to P_{uc} is maximal. In this case, there are only three unknowns, the penguin amplitudes (P_{tc} and P_{uc}) and the strong phase (δ), since the B^0 mixing angle, β, has been measured in other experiments. And as in the B_s^0 case there are three measurements that can be made of $B^0 \to K^{*0}\overline{K}^{*0}$. Therefore the magnitude of the penguin amplitudes and the strong phase can be calculated. The key point is that $|P_{uc}|$ and $|P'_{uc}|$ are equal under flavour $SU(3)$ symmetry. Thus, given a value of $|P_{uc}|$, obtained with the study of the $B^0 \to K^{*0}\overline{K}^{*0}$ decays, and with a value (or range) for the $SU(3)$-breaking, one obtains the value (or range) of $|P'_{uc}|$, and with this one can extract the true value (or range) of ϕ_s from the $B_s^0 \to K^{*0}\overline{K}^{*0}$ experimental data.

As shown, the $B^0 \to K^{*0}\overline{K}^{*0}$ decay provides an excellent tool to evaluate the magnitude of the P'_{uc} pollution to the B_s^0 case, under convenient use of the U-spin conservation hypothesis. Allowing for a 100% $SU(3)$-breaking, much larger than any known breaking effect, in Ref. [51] an error of 0.8° on $\arg(\lambda_{CP}(B_s^0 \to K^{*0}\overline{K}^{*0}))$ induced by neglecting the subleading penguin amplitude is obtained. When that study was published in 2007, there were no experimental measurements of $B_{(s)}^0 \to K^{*0}\overline{K}^{*0}$ decays yet, and some values based on QCD factorisation calculations were chosen. They found that the value of $|P_{uc}|$ is such that, even allowing for 100% $SU(3)$-breaking, $|V_{ub}^* V_{us} P'_{uc}|$ is indeed small. In Ref. [52] a revision of the method is performed including a large range of experimental input values. In Fig. 2.8 (right), the $\arg(\lambda_{CP}(B_s^0 \to K^{*0}\overline{K}^{*0}))$ prediction as a function of the direct *CP*-asymmetry in $B_s^0 \to K^{*0}\overline{K}^{*0}$ and the ratio of branching ratios $(\mathcal{B}(B_s^0)/\mathcal{B}(B^0))$ is shown. Considering the worst-case scenario (the largest possible value of $|P'_{uc}|$ within

100% breaking), the value of $\arg(\lambda_{CP}(B_s^0 \to K^{*0}\overline{K}^{*0}))$ predicted by the SM can be as large as 18°. Still, it is interesting to mention that a small theoretical error ($< 5°$) is found for a non-negligible subset of input numbers.

The previous results are obtained assuming a worst-case scenario, including a 100% $SU(3)$-breaking, but they can be ameliorated with a better determination of the size of the breaking factor. The precise knowledge of the $SU(3)$-breaking between $|P_{uc}|$ and $|P'_{uc}|$ would therefore considerably reduce the theoretical uncertainty . Several ways, experimental and theoretical, to determine the magnitude of the $SU(3)$-breaking have been proposed [52, 56].

2.4 Polarisation in B decays

B-meson decays provide an abundant source of information on CP-violation and flavour-changing processes [37]. When the B-meson decays to two vector mesons, the study of the angular distributions of the final-state particles also provides insight into the spin structure of the flavour-changing interaction. The decays studied in this thesis correspond to a B-meson (pseudoscalar particle) decaying to two light vector mesons (K^{*0}, $\overline{K}^{*0}$ or ϕ), which subsequently decay to a pair of pseudoscalars ($K^{\pm}$ or $\pi^{\pm}$). This type of processes, $B \to V_1(\to P_{11}P_{12})V_2(\to P_{21}P_{22})$, are sensitive to spin correlations and reveal properties of the particles and their interactions.

In general, in the sequential process $ab \to X \to P_1P_2 \to (p_{11}p_{12})(p_{21}p_{22})$, both the production and the decay of the particle X are of interest. In Fig. 2.9 [1], the angular observables in the process are shown: the two production angles, θ^* and Ψ are defined in the X frame, where Ψ is the angle between the production plane and the average of the two decay planes; and the three helicity angles, θ_1, θ_2 and ϕ, where θ_1 and θ_2 are defined in the rest frame of the two daughters P_1 and P_2 and ϕ is defined in the X frame as the angle between the two decay planes. In the case of a spin-zero particle, such as a B-meson, there are no spin correlations in the production mechanism and therefore the interest is in the decay chain. Because the final-state particles are vector mesons, this decay involves in fact three separate decay amplitudes, one for each polarisation of the vector mesons. To disentangle the fraction corresponding to the different contributions, an amplitude analysis is needed.

Consider a B^0 or a B_s^0 meson with four-momentum p and mass m_B decaying into two vector mesons, V_1 and V_2. The decay amplitude for $B^0_{(s)}(p) \to V_1(k_1, \epsilon_1) + V_2(k_2, \epsilon_2)$ may be written in terms of angular momentum amplitudes [57–59],

$$M = \boldsymbol{a}\epsilon_1^* \cdot \epsilon_2^* + \frac{\boldsymbol{b}}{m_B^2}(p \cdot \epsilon_1^*)(p \cdot \epsilon_2^*) + i\frac{\boldsymbol{c}}{m_B^2}\epsilon_{\mu\nu\rho\sigma}p^\mu q^\nu \epsilon_1^{*\rho}\epsilon_2^{*\sigma}, \tag{2.103}$$

where $k_{1,2}$ are the momenta of the vector meson 1 and 2, $\epsilon_{1,2}$ are their polarisations and $q \equiv k_1 - k_2$. The amplitudes **a** and **b** are linear combinations of the amplitudes describing final states with relative angular momentum between V_1 and V_2 of $L = 0, 2$, and **c** corresponds to $L = 1$. It is customary to use transversity amplitudes, where the decay amplitude is decomposed into components in which the polarisations of the final-state vector meson fields are either longitudinal (A_0), or transverse to their directions of motion and parallel ($A_\parallel$) or perpendicular ($A_\perp$) to each other [60],

$$M = A_0\epsilon_1^{*L} \cdot \epsilon_2^{*L} + \frac{1}{\sqrt{2}}A_\parallel \epsilon_1^{*T} \cdot \epsilon_2^{*T} - \frac{i}{\sqrt{2}}A_\perp \epsilon_1^{*T}\epsilon_2^{*T} \cdot \hat{p}, \tag{2.104}$$

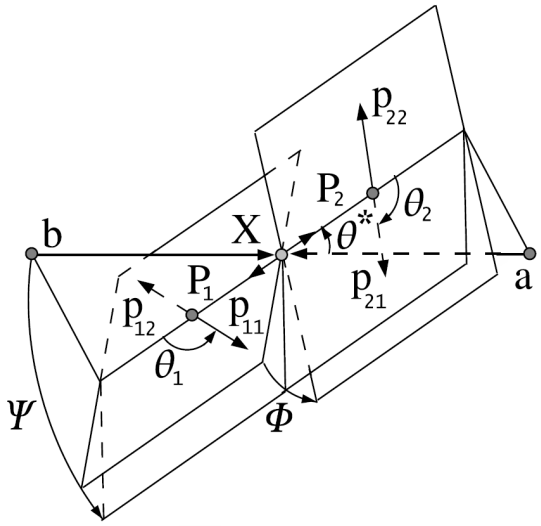

Figure 2.9: Definition of the production and helicity angles in the sequential process $ab \to X \to P_1P_2 \to (p_{11}p_{12})(p_{21}p_{22})$. The helicity angles and the production angles are defined in the text.

where $\hat{p}$ is the unit vector along the direction of motion of V_2 in the rest frame of V_1, $\epsilon_i^{*L} = \epsilon_i \cdot \hat{p}$, and $\epsilon_i^{*T} = \epsilon_i^* - \epsilon_i^{*L}\hat{p}$. A_0, $A_\parallel$ and $A_\perp$ are related to the angular momentum amplitudes through the following relations,

$$A_\parallel = \sqrt{2}\boldsymbol{a}, \quad A_0 = -\boldsymbol{a}x - \frac{m_1 m_2}{m_B^2}\boldsymbol{b}(x^2-1), \quad A_\perp = 2\sqrt{2}\frac{m_1 m_2}{m_B^2}\boldsymbol{c}\sqrt{x^2-1}, \quad (2.105)$$

where $x \equiv (k_1 \cdot k_2)/(m_1 m_2)$, m_1 and m_2 are the masses of V_1 and V_2. An alternative basis is to express the decay amplitude in terms of helicity amplitudes A_λ, where $\lambda = 1, 0, -1$. The helicity amplitudes can be written in terms of the linear polarisation amplitudes via $A_{\pm 1} = (A_\parallel \pm A_\perp)/\sqrt{2}$, with A_0 the same in both bases [61]. The transversity amplitudes have definite *CP* transformation properties, A_0 and $A_\parallel$ correspond to *CP*-even final-state configurations and $A_\perp$ describes a *CP*-odd final-state configuration, *i.e.*, to the *CP* eigenvalues $+1$ and -1, respectively.

The decay rate of the process is obtained squaring the amplitude, and can be written as

$$\frac{\mathrm{d}\Gamma}{\mathrm{d}\Omega} \propto |A_0 F_0(\Omega) + A_\parallel F_\parallel(\Omega) + A_\perp F_\perp(\Omega)|^2, \quad (2.106)$$

where $F_{0,\parallel,\perp}$ are functions describing the angular observables of the decay, with the exact form of these distributions depending on the spins of the decay products of V_1 and V_2. The amplitudes A_i and the *CP*-conjugate $\overline{A}_i$ are the sum of all the channels that contribute to the total decay, and can be expressed as,

$$\begin{aligned} A_i &= \sum_j |A_j| e^{i\delta_j} e^{i\phi_j}, \\ \overline{A}_i &= \sum_j |A_j| e^{i\delta_j} e^{-i\phi_j}, \end{aligned} \quad (2.107)$$

where ϕ_j are often called *weak phases*, which arise from the *CP*-violating terms in the Lagrangian and correspond to the contributions to the amplitude that appear in complex conjugate form in the *CP*-conjugate amplitude, in the Standard Model these phases occur only in the couplings of the $W^{\pm}$ bosons and encode inside the amount of *CP* violation. A second type of phases appear, δ_j, often called *strong phases*, which are *CP*-conserving and do not change sign in the *CP*-conjugate amplitude, their origin is the possible contribution from intermediate on-shell states in the decay process. The effect of the *CP* symmetry can only induce a difference in phase, not magnitude, in each channel taken separately. Besides, both weak and strong phases of any single term are convention dependent, but the difference between phases in two different terms in the amplitude is convention independent and therefore physically meaningful.

Additionaly, some modifications must be made to the angular analysis when an indistinguishable background coming from the decay of a scalar resonance $S \to PP'$ (P and P' are pseudoscalars), or from the scalar nonresonant PP' production exists [62]. It is therefore necessary to add one or more (scalar) helicities to the angular analysis (the number depends on whether the final state contains identical particles or not and whether the scalar-scalar contribution is included). In the general case, $B \to V_1/S_1(\to P_{11}P_{12})V_2/S_2(\to P_{21}P_{22})$, there are six helicities: $h = VV$ (three), VS, SV and SS, constructed as follows [53],

$$\begin{aligned}
\mathcal{A}_{VV} &= N \sum_{j=-1}^{1} A_j^{VV} Y_1^{-j}(\theta_1, -\phi) Y_1^j(\pi - \theta_2, 0), \\
\mathcal{A}_{VS} &= N A_0^{VS} Y_1^0(\theta_1, -\phi) Y_0^0(\pi - \theta_2, 0), \\
\mathcal{A}_{SV} &= N A_0^{SV} Y_0^0(\theta_1, -\phi) Y_1^0(\pi - \theta_2, 0), \\
\mathcal{A}_{SS} &= N A_0^{SS} Y_0^0(\theta_1, -\phi) Y_0^0(\pi - \theta_2, 0),
\end{aligned} \tag{2.108}$$

where N is a normalisation constant and Y_l^m are the spherical harmonics. Shifting from the helicity basis to the transversity basis, $A_{\parallel} = \frac{A_+ + A_-}{\sqrt{2}}$ and $A_{\perp} = \frac{A_+ - A_-}{\sqrt{2}}$, and making explicit the Y_j^m expressions, the following equation is obtained,

$$\begin{aligned}
\mathcal{A}_{VV} + \mathcal{A}_{VS} + \mathcal{A}_{SV} + \mathcal{A}_{SS} = -\frac{3N}{4\pi} \Bigg[& A_0 \cos\theta_1 \cos\theta_2 + \frac{A_{\parallel}}{\sqrt{2}} \sin\theta_1 \sin\theta_2 \cos\phi \\
& + i \frac{A_{\perp}}{\sqrt{2}} \sin\theta_1 \sin\theta_2 \sin\phi - \frac{A_{VS}}{\sqrt{3}} \cos\theta_1 + \frac{A_{SV}}{\sqrt{3}} \cos\theta_2 - \frac{A_{SS}}{3} \Bigg].
\end{aligned} \tag{2.109}$$

And the magnitudes and relative phases can therefore be extracted experimentally from the analysis of the angular distributions of the vector resonances decay products.

The $B^0_{(s)} \to VV'$ decays can be described by models based on perturbative QCD, or QCD factorisation and $SU(3)$ flavour symmetries. From the V−A structure of the weak interaction and helicity conservation in the strong interaction, the final state of these decays is expected to be highly longitudinally polarised. This applies to both tree and penguin decays. Whilst some authors predict a longitudinal polarisation fraction $f_0 \sim 0.9$ for tree-dominated and ~ 0.75 for penguin decays [63], other studies have proposed different mechanisms such as penguin annihilation [64, 65] and QCD rescattering [66] to accommodate smaller longitudinal polarisation fractions ~ 0.5, although the predictions have large uncertainties.

It has been experimentally confirmed that longitudinal polarisation dominates in $b \to u$ tree processes such as $B^0 \to \rho^+\rho^-$ [67], $B^+ \to \rho^0\rho^+$ [68] and $B^+ \to \omega\rho^+$ [69]. However, measurements of the polarisation in decays with both tree and penguin contributions, such as $B^0 \to \rho^0 K^{*0}$ and $B^0 \to \rho^- K^{*+}$ [70] and in $b \to s$ penguin decays, $B^0 \to \phi K^{*0}$ [71–73], $B_s^0 \to K^{*0}\overline{K}^{*0}$ [74] and $B_s^0 \to \phi\phi$ [75], indicate a low value of the longitudinal polarisation fraction comparable with, or even smaller than, the transverse fraction.

USC UNIVERSIDADE DE SANTIAGO DE COMPOSTELA

3 The LHCb experiment

The LHCb (Large Hadron Collider beauty) experiment [76] is one of the four main particle detectors (Fig. 3.1) placed in the 27 km long tunnel of the LHC (Large Hadron Collider) [77], at CERN (European Organization for Nuclear Research)[1] in Geneva, Switzerland.

The LHCb collaboration is composed nowadays of about 1200 members, from 69 institutes in 16 countries.[2] It was initially created in 1995 [78], as the result of the association of three alternative proposals for a b-dedicated experiment at the LHC.[3] In December 1998, the Technical Proposal was approved [79]. After some modifications to the original design of the detector introduced in 2003 [80], mainly concerning the tracking system (reducing the material budget) and the trigger schema (improving its performance), the detector was assembled and ready to start taking data in 2008. In September that year an electrical fault led to a loss of approximately six tonnes of liquid helium from the LHC bending magnets, which was leaked into the tunnel, damaging over 50 superconducting magnets, and contaminating the vacuum pipe. Due to this incident, the beginning of the proton-proton collisions had to be delayed until 2010, year that was used for the commisioning of the accelerator, being 2011 the first complete year of data taking.

The main goal of the LHCb experiment is the study of Heavy Flavour physics, looking for indirect evidences of NP in *CP* violation and rare decays of beauty and charm hadrons. The key channels to be studied were summarised in Ref. [81], being the first observation of the $B_s^0 \to \mu^+\mu^-$ decay [82], the measurement of several discrepancies with the SM in the angular analysis of the $B^0 \to K^{*0}\mu^+\mu^-$ decay [83] or the first observation of *CP* violation in B_s^0 mesons decays [84] some examples of the most relevant results. Apart from the analysis collected in that document, the LHCb experiment is able to study a broader spectrum of physics proccesses, such as the observation of exotic four- and five-quarks resonances [85–88], probe Lepton Universality Violation [89] or obtain the most precise value of the effective weak mixing angle ($\sin^2\theta_W^{\text{eff}}$) at the LHC [90].[4] Even more recently, LHCb took part in the heavy-ions runs, where Pb-Pb collisions and p-Pb collisions are produced [91].

[1] http://home.cern/

[2] http://lhcb.web.cern.ch/lhcb/

[3] More details about the creation of LHCb can be found in the slides presented in 2015 celebrating the 20th anniversary: https://indico.cern.ch/event/434085/timetable/

[4] For a full list of the publications by the LHCb collaboration: http://lhcbproject.web.cern.ch/lhcbproject/CDS/cgi-bin/index.php

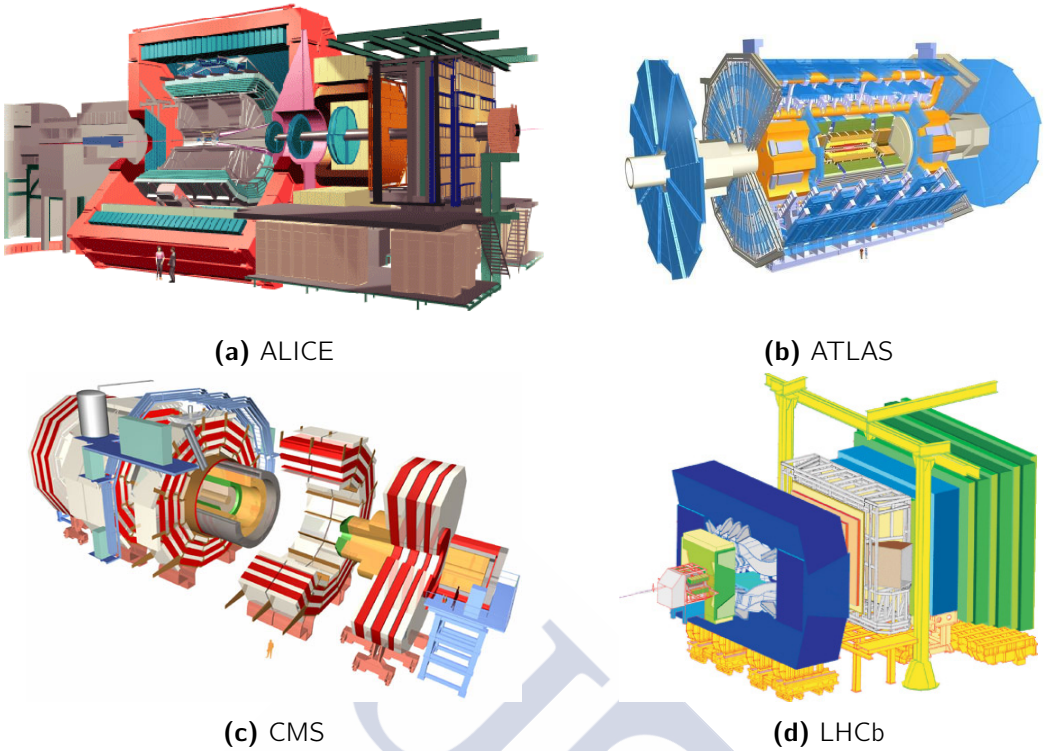

(a) ALICE **(b)** ATLAS

(c) CMS **(d)** LHCb

Figure 3.1: The four main experiments at the LHC.

3.1 The Large Hadron Collider

The LHC accelerator complex is a set of several machines in which protons are progressively accelerated up to 7 TeV. Prior to being injected into the main accelerator, the particles are prepared by a series of accelerators that successively increase their energy. The trip of the protons begins in a simple bottle of hydrogen gas. An electric field is used to strip the hydrogen atoms of their electrons. The first accelerator in the chain, LINAC2, accelerates the protons to the energy of 50 MeV, which feed the Proton Synchrotron Booster (PSB), where they reach 1.4 GeV. In the next step, the Proton Synchrotron (PS), the protons are accelerated up to 25 GeV. Finally, the Super Proton Synchrotron (SPS) is used to further increase their energy to 450 GeV, before they are at last injected into the main ring.

The LHC collider is housed in a circular tunnel, with a circumference of 26.7 kilometres, at a depth ranging from 50 to 175 metres underground. The tunnel was constructed between 1984 and 1989 to house the Large Electron-Positron Collider (LEP). The tunnel has eight straight sections and eight arcs. It contains two adjacent parallel beam pipes, each containing a beam, which travel in opposite direction around the ring. To keep the beams in their circular path, there are 1232 superconducting Nb-Ti dipole magnets that bend the trajectory of the particles. Each of the dipoles generates a magnetic field of 8.33 T (at the 7 TeV nominal energy). To set the magnets to their operating temperature of 1.9 K superfluid He is used. To focus the particles 392 quadrupole magnets are located around the ring. Magnets of higher multipole orders are used to correct smaller imperfections.

Along the tunnel there are four crossing points, called interaction points, where the protons in one direction collide with the protons in the opposite direction, causing p-p collisions with a nominal center-of-mass energy of $\sqrt{s} = 14\,\text{TeV}$. As of the end of 2017, this energy was still not reached, although it is expected that this will occur after the long shutdown scheduled in 2019 (LS2). In 2011, the first complete year of operation, the machine was run at a center-of-mass energy of $\sqrt{s} = 7\,\text{TeV}$ and in 2012, it was risen to $\sqrt{s} = 8\,\text{TeV}$. The statistics collected in these two years, known as Run I, correspond to $3\,\text{fb}^{-1}$ ($1\,\text{fb}^{-1}$ in 2011 and $2\,\text{fb}^{-1}$ in 2012). After Run I was finished, the collisions of the particles were paused to permit the complete repair of the different problems that had appeared in the previous years, and to allow the implementation of some upgrades in the experiments. These operations were performed in 2013 and 2014. The collisions were resumed in 2015, with a center-of-mass-energy of $\sqrt{s} = 13\,\text{TeV}$, the same energy with wich the machine was run in 2016 and 2018. As mentioned, it is foreseen that the nominal center-of-mass energy of $\sqrt{s} = 14\,\text{TeV}$ will be finally reached after the LS2, in 2021.

Four main spectrometers are placed at each of the four interactions points, where they are able to detect and measure the properties of the particles coming out of the collisions. The ATLAS (A Toroidal LHC ApparatuS) [92, 93] and CMS (Compact Muon Solenoid) [94, 95] experiments were designed as General Purpose Detectors (GPDs), trying to maximise the physics processes that can be studied with them and to measure the

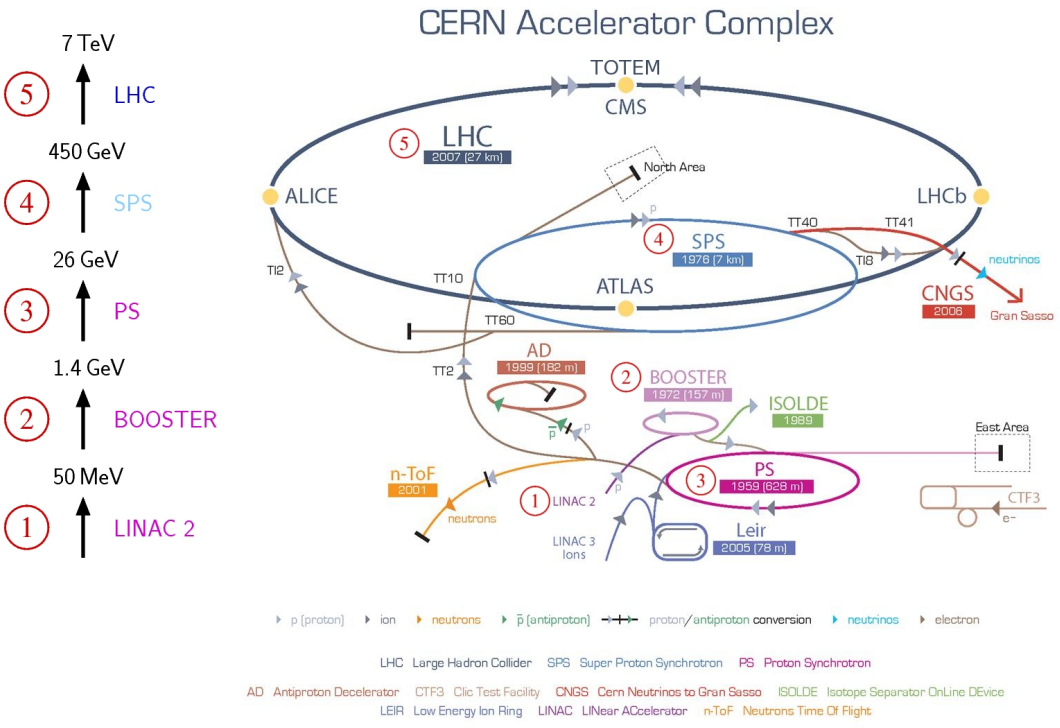

Figure 3.2: CERN accelerator complex, with a schema of the accelerator chain applied to the particles.

broadest possible range of signals. They are built in layers like an onion surrounding the interaction point, to detect all the particles that are produced in the collisions. They are designed for direct detection of new physics, with the fundamental objective of the detection of the Higgs boson achieved in 2012 [96, 97]. After that, with the way towards the new physics still unknown, a plethora of analyses are being carried on trying to find the elusive new particles. On the other side, ALICE (A Large Ion Collider Experiment) [98, 99] was built to study heavy-ion physics. For that, lead-lead collisions are also produced in the LHC, which allow to investigate the nature of the quark-gluon plasma, believed to have filled the universe a few microseconds after the Big Bang. And finally the LHCb experiment, already mentioned, and detailed below.

Apart from the four main detectors, there are other three experiments being operated at the LHC: TOTEM (TOTal Elastic and diffractive cross-section Measurement) [100], MoEDAL (Monopole and Exotics Detector at the LHC) [101] and LHCf (Large Hadron Collider forward) [102].

Fig. 3.2 shows a schematic view of the CERN accelerator complex with the location of the experiments indicated.

3.2 The LHCb detector

The LHCb experiment was initially designed to focus on the study of b-physics, the decays of hadrons containing a b-quark. At high energies, both the b- and $\overline{b}$-hadrons are mainly produced in the same forward or backward cones, as shown in Fig.3.3. Due to this property, the LHCb detector was designed as a single-arm spectrometer with a forward angular coverage from approximately 10 mrad to 300 (250) mrad in the bending (non-bending) plane, with respect to the beam axis. In terms of pseudorapidity, the LHCb acceptance is in the $2 < \eta < 5$ interval. Another key point for the LHCb experiment is the ability to estimate the point where the p-p collision took place (primary vertex or PV) and the point where the short-lived but flying particles decayed (secondary vertex or SV).

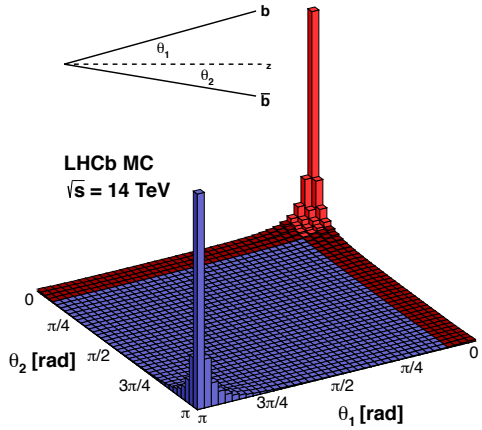

Figure 3.3: Angular distribution of the $b\overline{b}$ pairs produced in p-p collisions at $\sqrt{s} = 14$.

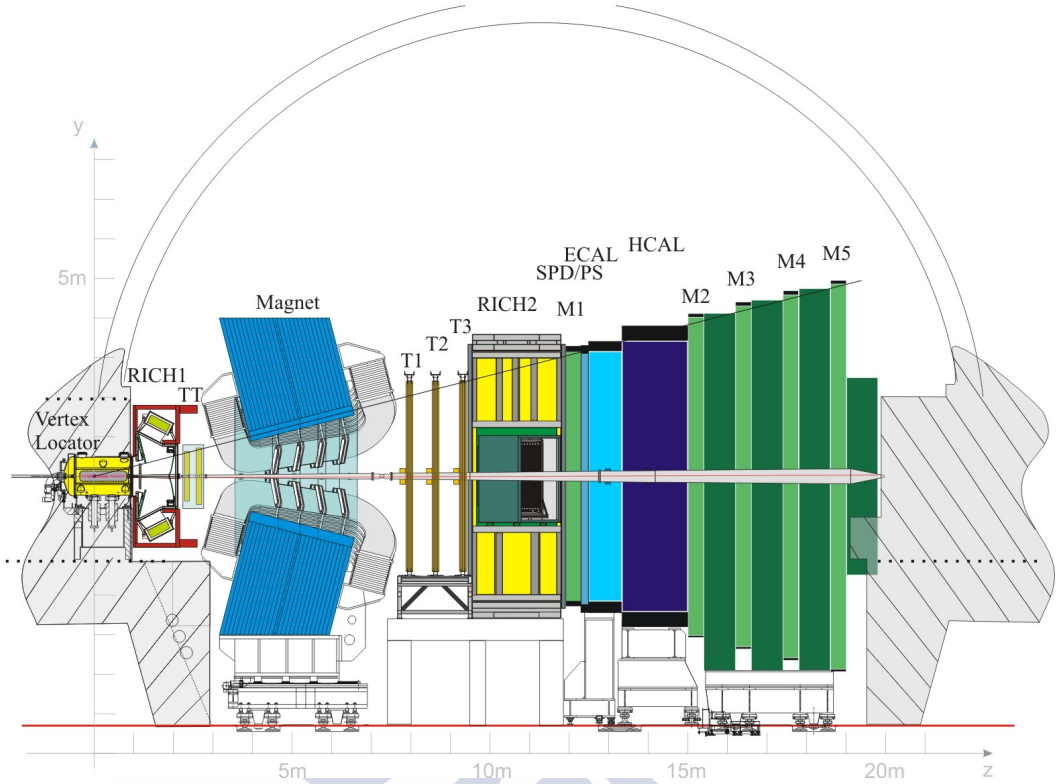

Figure 3.4: General layout of the LHCb detector.

If operated at the nominal LHC instantaneous luminosity, $10^{34}\,\mathrm{cm}^{-2}\,\mathrm{s}^{-1}$, an average of 23 PV's would be produced, making very difficult the PV-SV separation. To facilitate this task LHCb operates at an instantaneous luminosity in the range $2 - 5 \times 10^{32}\,\mathrm{cm}^{-2}\,\mathrm{s}^{-1}$. This is achieved using larger β^*values[1] than other LHC detectors, therefore less focusing of the beam. Due to this lower luminosity events are dominated by a single p-p interaction per bunch crossing, enabling the analysis. Low luminosity also helps to reduce the higher radiation damage at low angle. With this luminosity, an amount of 10^{12} $b\bar{b}$ pairs are produced in a nominal year of data taking.

The LHCb spectrometer is located at IP8, one of the LHC interaction points. The cavern where the detector is located was used during the LEP times to host the DELPHI experiment. In Fig. 3.4, the layout of the spectrometer is shown. The right-handed coordinate system adopted has the z-axis along the beam and the y-axis almost along the vertical (since there exists a $\sim 3.7\,\mathrm{mrad}$ tilt compared to the actual geometrical vertical). The detector has an overall dimension of approximately $6\,\mathrm{m} \times 5\,\mathrm{m} \times 20\,\mathrm{m}$. Since the collision point of LHCb is not at the centre of the detector, but instead at one of its ends, the LHC optics had to be modified to displace the interaction point by 11.25 m.

To separate the decays of interest from the background, both displaced vertex and high transverse momentum signatures are exploited. Excellent vertex resolution is required to measure impact parameters and to achieve a good decay time resolution, which is essen-

[1] $\beta^*$is the amplitude modulation of the beam in the interaction point, directly related to the size of the beam.

tial to resolve B_s^0 flavour oscillations and to reject various sources of background. Good momentum and invariant mass resolution are important to minimise combinatorial background and resolve heavy-flavour decays with kinematically similar topologies. Charged particle identification is essential in any flavour physics programme, for instance to isolate suppressed decays and for b-quark flavour tagging. Detection of photons, in addition to charged particles, allows the reconstruction of rare radiative decays and more common decays with a π^0 or an η meson in the final state. Finally, to benefit from the high event rate at the LHC, a high-bandwidth data acquisition system and a robust and selective trigger system are required. Taking these considerations into account, the main elements of the detector are:

- the magnet: warm dipole magnet to measure the momentum of the charged particles, described in Chapter 3.2.1;
- the vertex locator (VELO): uses silicon microstrips detectors that give information about the track coordinates close to the interaction region. Described in Chapter 3.2.2;
- the tracking system: composed of the Tracker Turicensis (TT), a silicon microstrip detector situated upstream the magnet, and of three Tracking Stations (T1, T2 and T3) downstream the magnet, made of silicon microstrips in the regions close to the beam pipe (Inner Tracker or IT) and of straw-tubes in the outer region (Outer Tracker or OT). The TT and the IT were developed in a common project called the Silicon Tracker (ST). The tracking system is described in Chapter 3.2.3;
- two RICH detectors (Ring Imaging CHerenkov): the upstream detector, RICH1, uses aerogel and C_4F_{10} radiators to cover the low moment range, while the downstream detector, RICH2, covers the high momentum range using a CF_4 radiator. In combination they can achieve an excellent particle identification in the momentum range from 2 to 100 GeV/c. Both are described in Chapter 3.2.4;
- the calorimeter system: composed of a Scintillator Pad Detector (SPD), a Preshower (PS), an Electromagnetic Calorimeter (ECAL) and a Hadronic Calorimeter (HCAL). The calorimeter system is described in Chapter 3.2.5;
- the muon detection system: composed of Multi Wire Proportional Chamber (MWPC), except in the region with the highest rate, where Gas Electron Multipliers (GEM) are used. The system is described in Chapter 3.2.6.

Before entering into the details of each subdetector description it is worth mentioning that, besides technical reports and other bibliography, referenced in the text, several LHCb theses have been used to collect information to write this chapter. Since these works are not followed in specific parts, but rather used as guidelines, they are referenced here [103–109].

3.2.1 Magnet

In order to measure the momentum of the charged particles produced in the collisions, the experiment uses a warm dipole magnet [110–112] that bends the charged particle

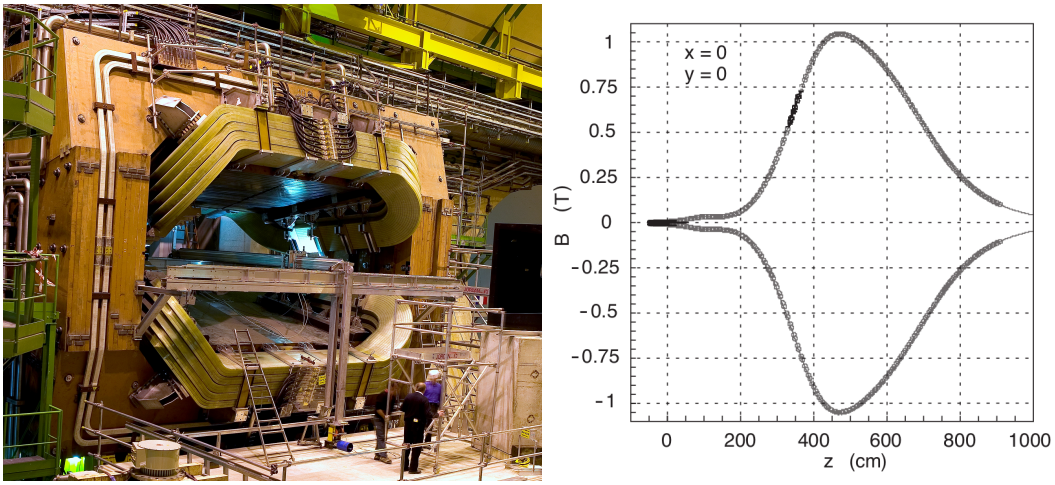

Figure 3.5: Left: Dipole magnet installed at the LHCb experimental site. Right: Magnetic field in the B_y direction along the z-axis.

trajectories in the horizontal plane (xz plane). The magnet covers an acceptance of ± 300 mrad horizontally and ± 250 mrad vertically. The dipole is composed of two identical coils of conical saddle shape placed mirror-symmetrically to each other in a window-frame iron magnet yoke. Each coil consists of fifteen pancakes arranged in five triplets and produced of pure Al-99.7 hollow conductor in an annealed state. A picture of the magnet installed at the LHCb experimental site can be seen in Fig. 3.5 (left).

The dipole provides a magnetic field of 4 Tm for tracks originating near the primary interaction point. To achieve the required momentum resolution, the magnetic field is known with a precision of 4×10^{-4}. In Fig. 3.5 (right), the B_y component of the magnetic field (the most relevant), is shown as a function of the z coordinate. To control the systematic uncertainties introduced by the detector in the measurement of CP asymmetries, the direction of the magnetic field is inverted periodically [113].

3.2.2 VELO

The main goal of the Vertex Locator (VELO) [114] is to precisely separate the proton-proton interaction point (primary vertex, PV) and the point where the b- or c-hadron decays (secondary vertex, SV).

The VELO is made of 21 stations surrounding the interaction point region arranged along the beam axis and perpendicular to it. Each station contains two semicircular silicon strip sensors mounted back-to-back. One of them measures the r coordinate, whereas the other measures the ϕ coordinate. The r-sensors are made of concentric semicircular strips (4×512 strips) centered on the nominal LHC beam position. To minimise the occupancy, each strip is subdivided into four 45° regions. The minimum pitch at the innermost radius is of 32 µm, increasing linearly to 101.6 µm at the outer radius. The ϕ-sensors are subdivided into two regions, inner and outer, with 683 and 1365 strips, respectively. This avoids unacceptably high strip occupancies in the innermost edge and too large strip pitch at the outer edge of the sensor. A skew of 20° (10°) is introduced

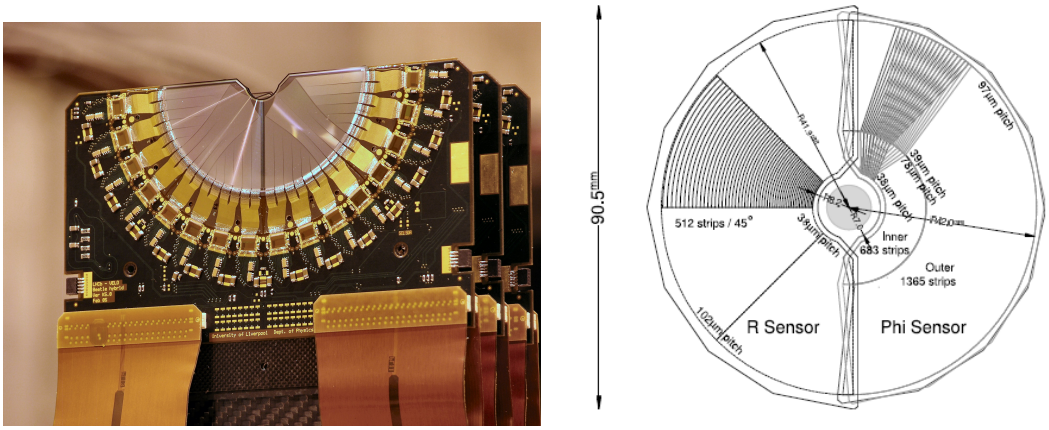

Figure 3.6: Left: One of the r-sensors of the VELO. Right: Schema of the $r\phi$ geometry of the VELO sensors. In the ϕ-sensor, the strips on two adjacent modules are indicated, to highlight the stereo angle.

in the inner (outer) region to improve pattern recognition, with reversed skew between the inner and the outer regions. Furthermore, the modules are placed so that adjacent ϕ-sensors have opposite skew with respect to each other, achieving a traditional stereo configuration. In Fig. 3.6, a picture of one of the r-sensors (left) and the schema of the $r\phi$-sensors (right) are shown.

In order to have the first measurement of the tracks as close to the primary vertex as possible, therefore improving the resolution, the sensitive area of the sensors starts at 8 mm from the beam axis, distance which is much smaller than the aperture required by the LHC during the injection. Due to this, the VELO was designed so that the two halves of the detector can be shifted from the beam axis in the horizontal direction, keeping the detector safe from the radiation during the stabilisation of the LHC beams. In Fig. 3.7, a partial view of the VELO is shown.

The VELO acceptance covers a pseudo–rapidity range of $1.6 < \eta < 4.9$ for particles coming from primary vertices in the range $-10.6 < z < 10.6$ cm. A spatial cluster resolution of about 4 μm is achieved for 100 mrad tracks (corresponding to the smallest strip pitch region). To minimise the material traversed by a charged particle, the detectors are mounted in a vessel that maintains vacuum around the sensors and the geometry is such that it allows the two halves of the VELO to overlap when in the closed position.

3.2.3 TT and tracking stations

The tracking system can be divided in two different parts taking into account the materials used for its construction: the ST and the OT.

The ST comprises two detectors: the TT [80,115], placed right upstream the magnet, and the IT [116], which corresponds to the region close to the beam of the three tracking stations. Both TT and IT use silicon microstrip sensors with a strip pitch of about 200 μm, which gives a single hit resolution of 50 μm.

Each of the four ST stations has four detection layers in an $(x-u-v-x)$ arrangement with vertical strips in the first and the last layer and strips rotated by a stereo angle of

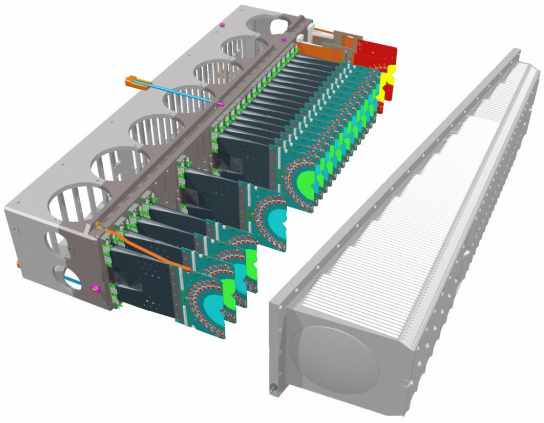

Figure 3.7: Layout of one half of the VELO.

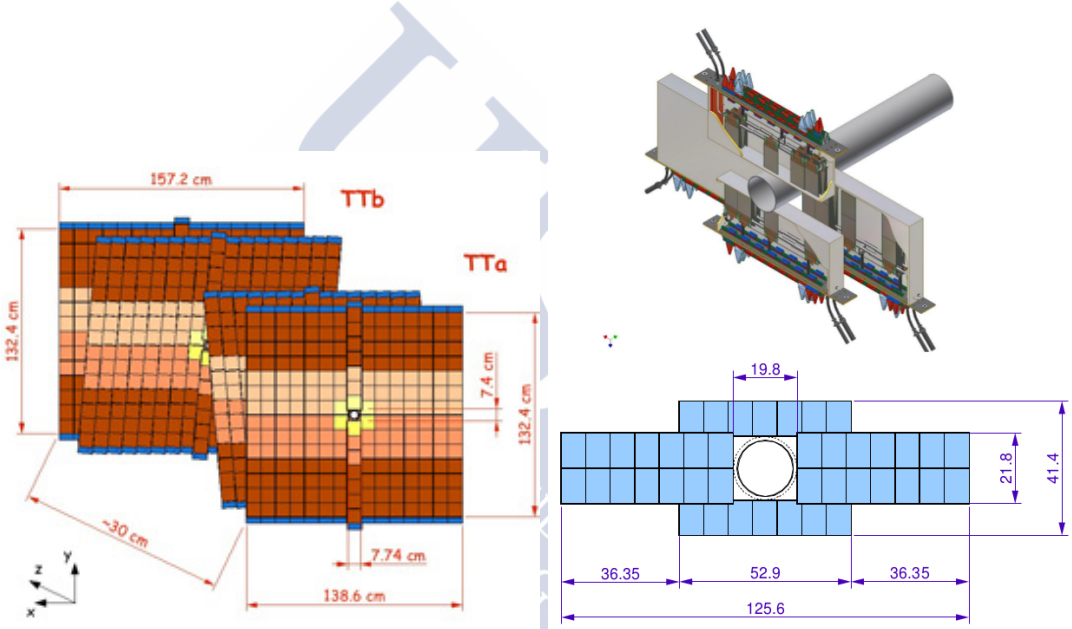

Figure 3.8: Left: Layout of the four TT layers. Right: View of one of the three IT stations (top) and schematic layout (bottom).

$-5°$ and $+5°$ in the second and the third layer, respectively. The TT is a 150 cm wide and 130 cm high planar tracking station with a total active area of around $8\,m^2$, wich covers the full acceptance of the experiment. The IT covers a 120 cm wide and 40 cm high cross-shaped region around the beam pipe. Fig. 3.8 shows pictures of both TT and IT. The total active area of the IT is approximately $4\,m^2$. Even though it constitutes only 1.3% of a tracking station, approximately 20% of the charged tracks produced close to the interaction point and traversing the tracking stations pass through it. For instance, roughly 60% of the four-body decays of B-mesons, of interest in this thesis, require the IT system.

The OT [117] is a drift-tube gas detector consisting of approximately 200 gas-tight

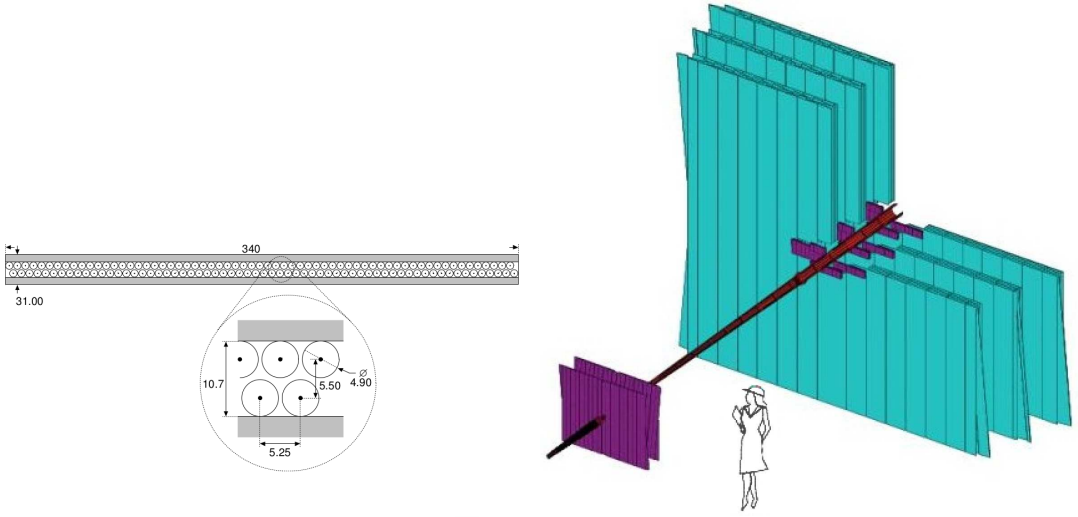

Figure 3.9: Left: Cross-section of one OT module. Right: OT (blue), TT, IT (purple) stations.

straw-tube modules with drift-time read-out. The modules are arranged in three stations, each one consisting of four detection layers. As in the case of the ST, the first and the last layers are oriented vertically, while those in the center are rotated by $\pm 5^{\circ}$ with respect to the others. A mixture of Argon (70%), CO_2 (28.5%) and O_2 (1.5%) is chosen as counting gas. It provides a drift-time below 50 ns and a spacial resolution of 200 µm. The total active area of a station is about 6 m $\times$ 5 m. Fig. 3.9 shows pictures of the OT.

3.2.4 RICH detectors

As previously mentioned, the identification of charged particles is essential for the LHCb experiment, mainly to separate pions from kaons in selected b-hadrons decays. To achieve a particle identification that covers the full momentum range LHCb has two RICH detectors.

RICH1 [80, 118] is situated upstream the magnet, between the VELO and the Trigger Tracker, covers the low momentum range, $1 - 60\,\mathrm{GeV}/c$ and uses aerogel and C_4F_{10} radiators. It covers the full LHCb acceptance from ± 25 mrad to ± 300 mrad (horizontal) and ± 250 mrad (vertical). RICH2 [119, 120] is located downstream the magnet, between the last tracking station and the first muon station, and is used to identify charged particles in the high momentum range, from 15 GeV/c up to and beyond 100 GeV/c using a CF_4 radiator. RICH2 has a limited angular acceptance, from ± 15 mrad to ± 120 mrad (horizontal) and 100 mrad (vertical) covering the region where high momentum particles pass. In Fig. 3.10, a picture of both RICH1 and RICH2 is shown.

To detect the Cherenkov photons, produced in the wavelength range $200 - 600$ nm, HPDs (Hybrid Photon Detectors) are used. The HPDs are located out of the spectrometer acceptance. Therefore, to focus the Cherenkov light, a combination of spherical and planar mirrors is needed. In RICH1 the optical layout is vertical, whereas in RICH2 is horizontal. Since the detectors are under the action of magnetic fields up to 50 mT, the

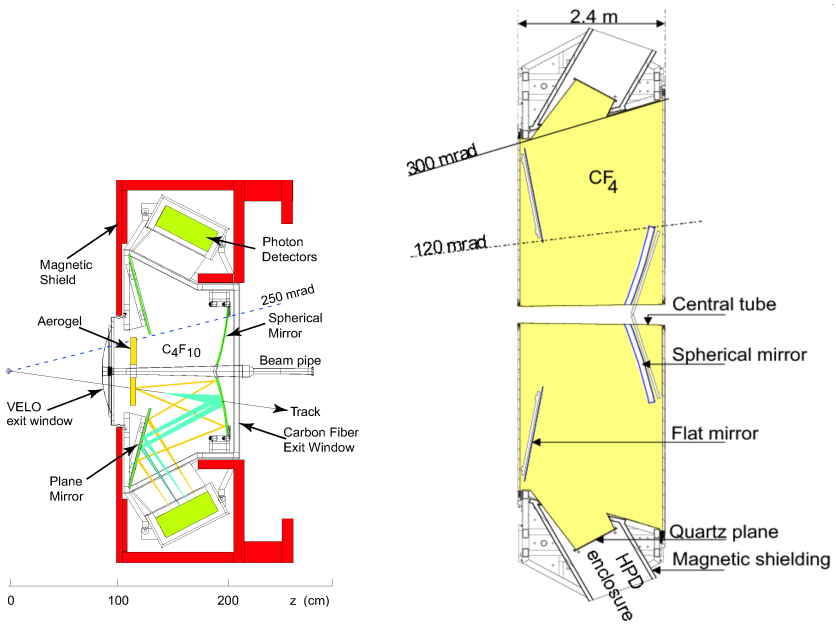

Figure 3.10: Layout of the RICH detectors. Left: RICH1. Right: RICH2.

HPDs are surrounded by external iron shields, as can be seen in Fig. 3.10.

3.2.5 Calorimeter system

The calorimeter system [121] of LHCb is used to identify electrons, photons and hadrons as well as to measure their energies and positions, and participates in the first trigger level (L0), selecting hadron, electron and photon candidates with high transverse energy (E_T).

The general structure is that of an Electromagnetic Calorimeter (ECAL) followed by a Hadron Calorimeter (HCAL). To reject the high background of charged pions, it is required the longitudinal segmentation of the electromagnetic shower detection. This is achieved with the introduction of a Pre-Shower (PS) detector. The distinction between charged pions and electrons is done measuring the dispersion of this electromagnetic shower in the PS. To separate photons from electrons, a Scintillator Pad Detector (SPD) is introduced in front of the PS, which gives information about the charge of the particle. Additionally, the SPD hit multiplicity information is used in the hardware trigger since it is correlated with the multiplicity of the event.

All the LHCb calorimeters follow the same principle, a sampling scintillator/absorber structure where the scintillation light is transmitted to a Photo-Multiplier (PMT) by wavelength-shifting (WLS) fibres. The single fibres for the SPD/PS cells are read out using multianode photomultiplier tubes (MAPMT), while the fibre bunches in the ECAL and HCAL modules require individual phototubes. Since the hit density varies by two orders of magnitude over the calorimeter surface, the SPD/PS/ECAL lateral segmentation is divided in three regions, whereas the HCAL is divided in two zones with larger cell sizes, as can be seen in Fig. 3.11.

The SPD/PS detector consists of a 15 mm lead converter with a thickness of 2.5

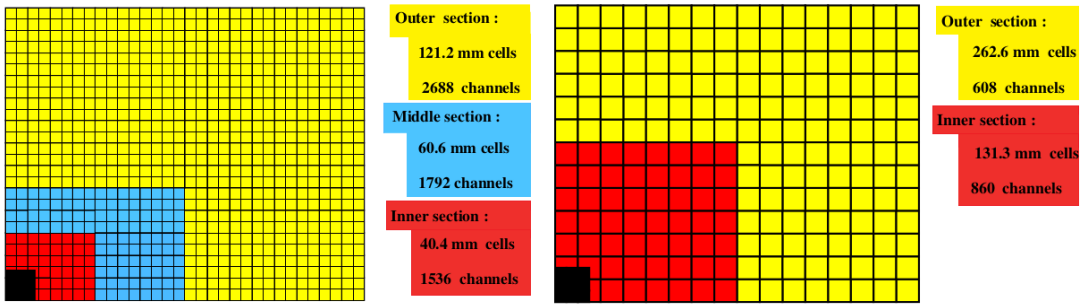

Figure 3.11: Lateral segmentation of the SPD/PS and ECAL (left) and HCAL (right). One quarter of the detectors front face is shown.

radiation lengths (X_0), that is sandwiched between two almost identical planes of rectangular scintillator pads of high granularity. The sensitive area of the detector is 7.6 m wide and 6.2 m high. Due to the projectivity requirements all dimensions of the SPD plane are smaller than those of the PS by $\sim 0.45\%$. The distance along the beam axis between the centres of the PS and the SPD scintillator planes is 56 mm.

The ECAL is placed at 12.5 m from the interaction point. The outer dimensions of the ECAL match projectively those of the tracking system, $\theta_x < 300$ mrad and $\theta_y < 250$ mrad; the inner acceptance is mainly limited by $\theta_{x,y} > 25$ mrad around the beampipe due to the substantial radiation dose level. In depth the 66 Pb and scintillator layers form a 42 cm stack corresponding to 25 radiation lengths.

The HCAL is a sampling device made from iron and scintillating tiles, as absorber and active material respectively. The special feature of this sampling structure is the orientation of the scintillating tiles which run parallel to the beam axis. The overall HCAL structure is built as a wall, positioned at a distance from the interaction point of 13.33 m with dimensions of 8.4 m in height, 6.8 m in width and 1.65 m in depth. The HCAL thickness is limited to 5.6 nuclear interaction lenghts (λ_i) due to space constraints.

3.2.6 Muon system

The muon system [122–124] is the last subdetector of the LHCb spectrometer. Since the amount of material that the particles have to go through to reach this subdetector is very high, only muons are expected to reach the muon chambers. The goal of this system is to identify muons and to measure their transverse momentum. This information is used in the trigger and in the offline analysis.

The muon system is composed of five stations of rectangular shape, placed along the beam axis. M1 is placed in front of the calorimeters, improving the p_T measurement in the trigger. M2 to M5 are placed downstream the calorimeters, interleaved with iron absorbers 80 cm thick to select penetrating muons. The minimum momentum that a muon must have to traverse the five stations is approximately 6 GeV/c. The geometry of the five stations is projective, meaning that all their transverse dimensions scale with the distance from the interaction point. The inner and outer angular acceptances of the muon system are 20 (16) mrad and 306 (258) mrad in the bending (non-bending) plane respectively. In Fig. 3.12 (left), the schematic cross-section of the muon system can be

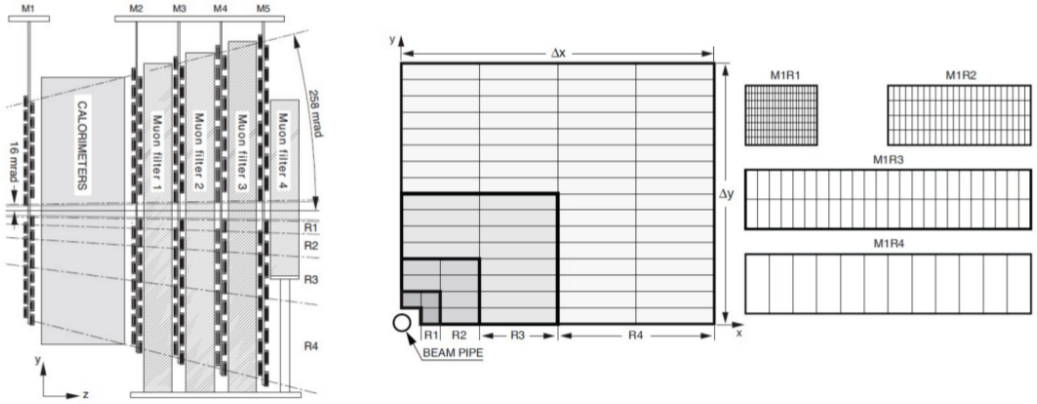

Figure 3.12: Left: Side view of the muon system. Center: Front view of a quadrant of a muon station. Right: Division into logical pads of four chambers belonging to the four regions of station M1.

seen.

To detect the particles, Multi-Wire Proportional Chambers (MWPC) are used for all regions, except the inner region of station M1, where the expected particle rate exceeds safety limits for ageing. In this region triple-GEM (Gas Electron Multiplier) detectors are employed. The detectors provide space point measurements of the tracks. The information is obtained by partitioning the detector into rectangular logical pads. Each Muon Station is divided into four regions, R1 to R4 with increasing distance from the beam axis. The linear dimensions of the regions R1, R2, R3, R4, and their segmentations scale in the ratio $1 : 2 : 4 : 8$. With this geometry, the particle flux and channel occupancy are expected to be roughly the same over the four regions of a given station. In Fig. 3.12 (center and right), the division of a muon station can be seen.

3.3 LHCb operation in Run I

Previously, the different components that constitute the LHCb detector have been summarised describing their fundamental features. In the following, the combined operation of all of them will be explained, focusing on how the subdetectors work together to produce the dataset that will be afterwards studied and on the performance of the detector in the data already recorded [125].

The sequence followed by the data until they are analised is performed using several tools and algorithms, grouped in different software projects. The package which serves as framework for all these projects in LHCb is called Gaudi [126].[1] It is an object-oriented framework written in C++ which consists of services that allow sharing of basic functionality, such as job steering, message logging, data access, and data analysis. Gaudi applications are composed of algorithms which exploit these services.

The first step in the data workflow is performed by the trigger (Chapter 3.3.1). Since

[1] The Gaudi project: http://proj-gaudi.web.cern.ch/proj-gaudi/

not all the events can be stored due to the available resources, a fast and efficient selection of the most interesting ones must be accomplished. The trigger reduces the several millions of events that are produced per second to just a few thousand. This is done at the same time that the data are being recorded by the detector and therefore it is considered an online process. The online system is described in Chapter 3.3.2 and it is in charge of the correct transfer of data from the front-end electronics to the permanent storage.

Once the raw data has been triggered and stored, the electronic signals produced by the different subdetectors are converted into physical quantities in the reconstruction. In LHCb it is performed with the use of a group of C++ libraries with the relevant tools collected in the Brunel project.[1] Two different procedures can be clearly separated in the reconstruction. The first one, tracking and vertexing (Chapter 3.3.3), refers to the reconstruction of the trajectories of the charged particles and the search for the vertices in which the pp collisions are produced and in which the particles decay. The second one is particle identification (Chapter 3.3.4), where the output of several subdetectors is used to determine the identities of the different particles that are produced in the event. One key point for the correct reconstruction of the events is the accuracy of the detector alignment. Organised under the Alignment project there are a set of C++ libraries and tools for the alignment of each subdetector.[2] The reconstruction program makes use of calibration and alignment constants to correct for any temporal changes in the response of the detector and its electronics. The calibration and alignment data as well as the necessary detector information (detector conditions) are stored in a database.

After their reconstruction the events are separated and filtered in streams according to their physics content in a procedure called stripping. A loose pre-selection algorithm, known as stripping line, is provided for each channel of interest with the aim of reducing to a manageable size the datasets that have to be manipulated. Thus avoiding the use of the whole triggered dataset by each analyst. Since these algorithms use tools that are common to many different physics analyses they are executed in a centralised production-mode. The stripped data are then ready to be analyzed offline. The relevant tools for the stripping and the offline analysis are contained in a set of C++ LHCb libraries in the DaVinci project.[3]

The final tool needed to produce physics results is the use of simulated events. A full simulation of the pp collisions, the formation and decay of the subsequent particles, their propagation through the LHCb spectrometer and the detector reaction are reproduced in order to understand the experimental conditions and characterise the detector response to the signal events. The analytical derivation of such processes is impossible to obtain due to the complex detector geometries and the numerous effects that need to be accounted for. Therefore, numerical results that use algorithms involving random sampling are exploited. These methods are collectively known as Monte Carlo (MC) simulation. In order to be profitable, the simulation must be as realistic as possible. However, it is usual that real and simulated data show some discrepancies. In Chapter 3.3.5, the MC simulation at LHCb is explained, with the differences found between the simulation and the data mentioned as well.

[1] The Brunel project: http://lhcb-release-area.web.cern.ch/LHCb-release-area/DOC/brunel/
[2] The Alignment project: http://lhcb-release-area.web.cern.ch/LHCb-release-area/DOC/alignment/
[3] The DaVinci project: http://lhcb-release-area.web.cern.ch/LHCb-release-area/DOC/davinci/

In charge of the long term storage of the real and simulated LHCb data is the offline system [127]. It is based on a computing model in which data are distributed and stored in different locations (called Tiers). The raw data obtained from the detector are transferred and kept in its entirety at the CERN Tier-0 centre. Another copy is distributed across the seven Tier-1 centres (IN2P3 in France, GRIDKA in Germany, CNAF in Italy, NIKHEF in the Netherlands, PIC in Spain, RAL in the United Kingdom and CERN, which also takes on the role of a Tier-1 centre), where the full offline reconstruction and the stripping are performed. The offline reconstruction is executed with a more accurate alignment and calibration of the subdetectors, and with reconstruction software that is more elaborate and allows for more redundancy than is possible in the trigger. Both the reconstruction and the stripping are repeated as many times as needed once the relevant algorithms are improved. Usually the reconstruction is applied once per year, after the end of data taking for that year, and the stripping is run two or three times each year. Moreover, the Tier-1 centres are in charge of storing these reconstructed and stripped data. Finally, placed at the different LHCb institutes, there are more than 100 Tier-2 centres responsible for the production of simulated events. The process of distributing the data has a double intention. On the one hand, it ensures that data cannot be lost, regardless any possible technical problem appearing. On the other, it allows physicists an easy access to a distributed computing system of huge power. This distributed system is called GRID [128][1] and it is managed via the Dirac framework [129],[2] interfaced to the LHCb software using Ganga [130].[3]

3.3.1 Trigger

As previously mentioned, the operating luminosity for the LHCb experiment is about $2 \times 10^{32}\,\mathrm{cm}^{-2}\,\mathrm{s}^{-1}$. This implies that the multiplicities per bunch crossing are dominated by single interaction events, which facilitates the triggering and reconstruction by ensuring low channel occupancy. With these conditions, a rate of about 100 kHz of $b\bar{b}$-pairs are produced. However, only about 15% of these events include at least one B-meson with all its decay products in the spectrometer acceptance. Furhtermore, the branching ratios of interesting B decays are typically less than 10^{-3}.

Due to the available resources not all the collected information can be written to storage and, therefore, a mechanism is needed to efficiently select events suitable for LHCb physics analyses. The trigger system [80, 131] is in charge of this task, reducing the 10 MHz of visible interactions[4] to the few kHz that are finally stored. To reject uninteresting background events as strongly as possible, the trigger uses the distinctive features of the b- and c-hadron decays, *i.e.*, tracks with significant non-zero impact parameter with respect to the primary vertex and high transverse momentum (p_{T}) with respect to the beam axis.

The LHCb trigger is divided in two levels, the Level-0 (L0) trigger, implemented using custom made electronics, operating synchronously with the bunch crossing frequency of

[1] Worldwide LHC computing GRID: http://wlcg-public.web.cern.ch/

[2] The Dirac interware: http://diracgrid.org/

[3] The Ganga project: http://ganga.web.cern.ch/ganga/

[4] An interaction is defined to be visible if it produces at least two charged particles with sufficient hits in the VELO and T1-T3 to allow them to be reconstructible.

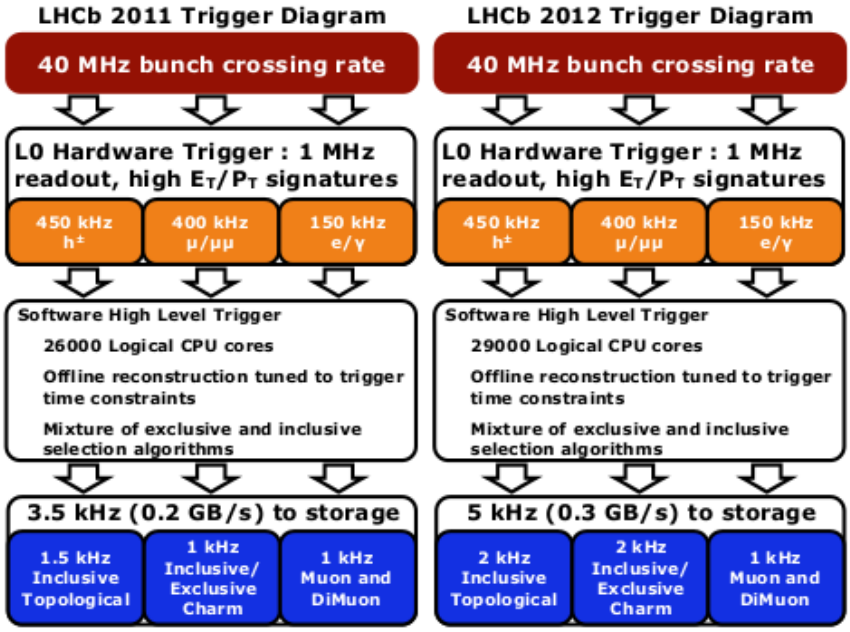

Figure 3.13: Schema of the event flow in the LHCb trigger system for 2011 (left) and 2012 (right).

40 MHz and the High Level Trigger (HLT), executed asynchronously on a processor farm. A sketch of the complete LHCb trigger chain is shown in Fig. 3.13.

3.3.1.1 L0 trigger

The L0 trigger reduces the input data rate to 1 MHz, rate at which the entire detector can be read out. It is a hardware trigger implemented in custom electronics boards. L0 uses the information from the calorimeters (L0Calo) and the muon system (L0Muon) to reconstruct the particles with the highest E_T and p_T.

The L0Calo trigger [132, 133] computes the transverse energy deposited in clusters of 4 cells (2×2) and saves those with the highest E_T. From these elementary clusters, three types of candidates are built depending on the information from the different subdetectors: hadron candidates (`L0Hadron`), for the highest E_T HCAL cluster, which also contains the energy of the matching ECAL cluster; photon candidates (`L0Photon`) for the highest E_T ECAL cluster with 1 or 2 PS hits in front of the ECAL cluster and no hit in the SPD cells corresponding to the PS cells; and electron candidates (`L0Electron`), which have the same requirements as for a photon candidate, with in addition more than one SPD cell hit in front of the PS cells. Events with at least one candidate with E_T over the thresholds shown in Table 3.1 are accepted by L0. Moreover, the number of hits in the SPD is used to reject busy events, which would then saturate the HLT (Table 3.1 also shows the SPD multiplicity thresholds implemented).

The L0Muon trigger [134] uses a fast stand-alone muon reconstruction which searches for hits that define a straight line through the five muon stations and that points towards the interaction point. Either the single muon (`L0Muon`) or a muon pair (`L0DiMuon`) with

Table 3.1: L0 thresholds in 2011 and 2012.

	2011	2012	SPD multiplicity
`L0Muon`	$p_T > 1.48\,\text{GeV}/c$	$p_T > 1.76\,\text{GeV}/c$	< 600
`L0DiMuon`	$\sqrt{p_{T1} \times p_{T2}} > 1.296\,\text{GeV}/c$	$\sqrt{p_{T1} \times p_{T2}} > 1.6\,\text{GeV}/c$	< 900
`L0Hadron`	$E_T > 3.5\,\text{GeV}$	$E_T > 3.7\,\text{GeV}$	< 600
`L0Electron`	$E_T > 2.5\,\text{GeV}$	$E_T > 3\,\text{GeV}$	< 600
`L0Photon`	$E_T > 2.5\,\text{GeV}$	$E_T > 3\,\text{GeV}$	< 600

transverse momentum above the thresholds shown in Table 3.1 are selected by the trigger. The transverse momentum is reconstructed with a precision of roughly 25%.

Finally, the information from these subdetectors is passed to the Decision Unit (L0DU), which is able to perform simple arithmetic to combine all signatures into one decision, to accept the event or to reject it. This decision is transferred to the Readout Supervisor (RS) which transmits the ultimate decision (depending on the status of the different detector components in order to prevent overflows) to the front-end electronics of all subdetectors. The system latency is fixed to 4 μs, which includes the time of flight of the particles as well as cables and electronic delays, meaning that 2 μs are left in the end for the L0 data processing.[1]

3.3.1.2 High Level Trigger

The data accepted by the L0 is transmitted to the Event Filter Farm (EFF), a farm of multiprocessor PCs, where the HLT is executed. The HLT consists of a C++ application which runs on every CPU of the EFF.[2] It reduces the rate from 1 MHz to a few kHz (3 kHz in 2011 [135] and 5 kHz in 2012 [136]). The HLT performs a full event reconstruction using the entire detector information in order to discriminate signal events. Due to the output rate of L0 and the CPU power limitations, the algorithms executed at the HLT are simplified with respect to the ones executed offline. The HLT is divided in two levels, HLT1 and HLT2.

The HLT1 uses the information from the VELO to perform a 3D reconstruction of the primary vertex and to make a fast reconstruction of the tracks associating the VELO information with the T-stations. For `L0Muon` candidates, a fast muon identification is carried out to confirm the event. For `L0Hadron` candidates the energy depositions are associated with tracks. The impact parameter, the total momentum, the transverse momentum and the quality of the tracks are used to further reduce the rate.

For the HLT2, a full reconstruction of the event is possible. This level is formed of a combination of inclusive trigger algorithms, where the B decay is partially reconstructed, and exclusive trigger algorithms that fully reconstruct the B-hadron final states. Tracks with very loose cuts on momentum and IP are combined to form composite particles ($J/\psi \to \mu^+\mu^-$, $K^{*0} \to K^+\pi^-$, $\phi \to K^+K^-$, *etc.*) and cuts on the invariant masses or on the pointing of the B momentum towards the primary vertex are used.

[1] The system latency is the time between a proton-proton interaction and the moment when the L0 delivers its decision to the front-end electronics.

[2] More information on the EFF: http://lbonupgrade.cern.ch/doku.php?id=outreach:the_lhcb_eventfilterfarm

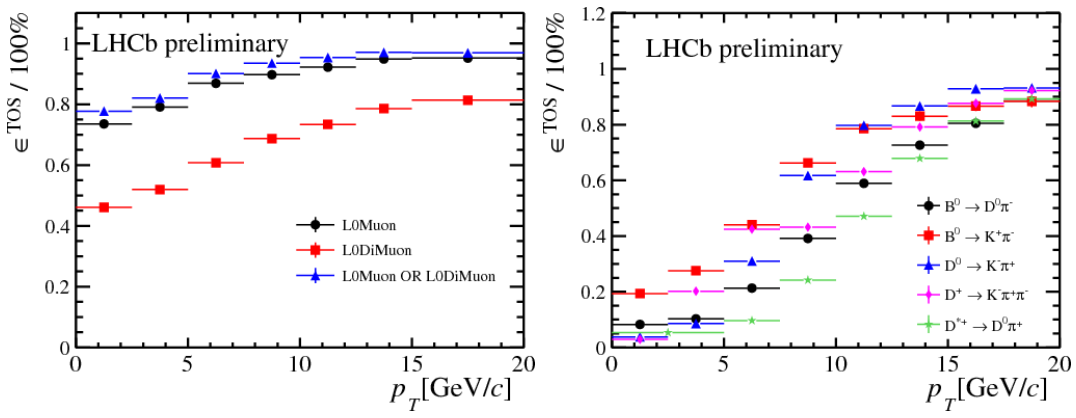

Figure 3.14: Left: L0 muon trigger performance: TOS trigger efficiency for selected $B^+ \to J/\psi K^+$ candidates as a function of the B p_T. Right: L0 hadron trigger performance: TOS trigger efficiency for different beauty and charm decay modes as a function of the B or D p_T.

The fact that the HLT is software implemented makes it very flexible, with the capacity of evolving and adapting to the different running conditions. To preserve the relation of the event with the trigger lines that selected it a Trigger Configuration Key (TCK) is defined. The TCK is an hexadecimal label pointing to a database that contains the parameters that configure the trigger lines for a given run. The TCK is stored for every event, together with the information on which trigger lines accepted the event. The group of C++ libraries in which the trigger algorithms are gathered is the Moore project.[1]

3.3.1.3 Trigger performance

To evaluate the trigger efficiency a data-driven method is used, where the efficiency of the trigger is computed with respect to the offline reconstruction. An event is classified as TOS (Trigger On Signal) if the spectrometer response associated with the signal candidate is sufficient to select the event. An event is classified as TIS (Trigger Independent of Signal) if it has been selected by the response of the spectrometer not associated with the signal. A number of events can be classified as TIS and TOS simultaneously, which allows the extraction of the trigger efficiency relative to the offline reconstructed events from data [137]. Therefore, the trigger efficiency contains only the additional inefficiency due to simplifications used in the trigger, possible alignment inaccuracies, worse resolution than the offline reconstruction or harder cuts imposed by rate and/or processing time limitations. Some representative channels of the LHCb physics are chosen.

The output rate of L0 consists of approximately 400 kHz of muon triggers, 500 kHz of hadron triggers and 150 kHz of electron and photon triggers. In Fig. 3.14, the efficiencies of the L0 muon triggers evaluated on $B^+ \to J/\psi K^+$ events (left) and the efficiencies of the L0 hadron trigger evaluated on different B and D decays (right) as a function of the B or D p_T are shown.

The most relevant HLT1 line for this work is the inclusive track trigger line [138], where tracks with good quality, significant IP with respect to all PVs and large transverse

[1] The Moore project: http://lhcb-release-area.web.cern.ch/LHCb-release-area/DOC/moore/

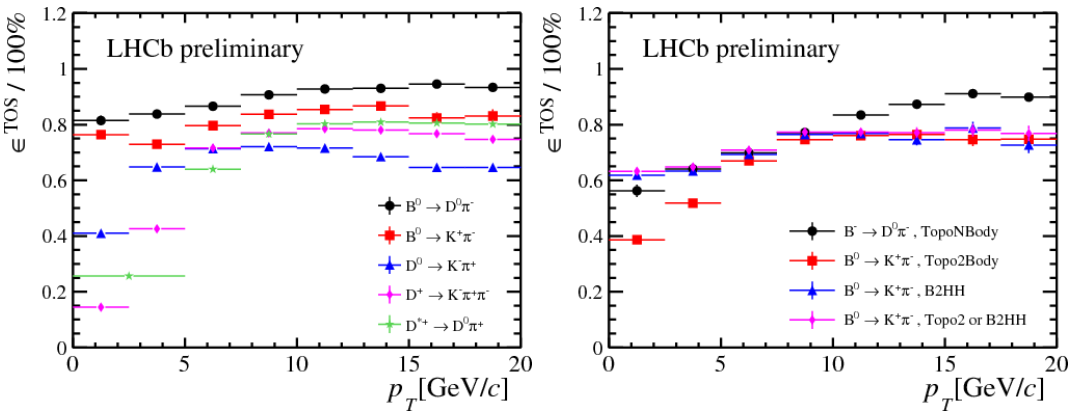

Figure 3.15: Left: HLT1 inclusive track trigger performance: TOS efficiency for various channels as a function of B or D p_T. Right: HLT2 inclusive beauty trigger performance as a function of B p_T. The efficiency for the exclusive $B^0 \to K^+\pi^-$ trigger line is also given.

momentum are selected. In Fig. 3.15 (left) the efficiencies of this line evaluated on different decays as a function of the B and D p_T are shown. This trigger line produces around 58 kHz of output in 2012 (43 kHz in 2011), which is the largest contribution to the allocated HLT1 bandwidth. For HLT2, the so-called topological trigger lines [139] are the most relevant for the analyses in this thesis. Designed to cover all b-hadron decays with at least two charged particles in the final state and a displaced decay vertex. Several variables of the candidates are combined using a Bonsai Boosted Decision Tree (BBDT). The output rate of the topological trigger is 2 kHz in 2012 (1 kHz in 2011). In Fig. 3.15 (right), the efficiency for the topological trigger lines for $B^0 \to K^+\pi^-$ and $B^0 \to D^+\pi^-$ events as well as the additional efficiency that can be gained by an exclusive selection for $B^0 \to K^+\pi^-$ are shown.

3.3.2 Online system

The online system [140, 141] is in charge of the data transfer from the front-end electronics to permanent storage. This includes not only the movement of data, but also the configuration and monitoring of the operational and environmental parameters. The general architecture of the online system is shown in Fig. 3.16. It is composed of three components:

- the Data Acquisition (DAQ) system [142], which receives the data from the detector electronics and transfer it to the EFF where the HLT runs. Data from the front-end electronics are collected in LHCb-wide standardised readout boards, TELL1 [143].[1] The boards have four pre-processing Field Programmable Gate Array (FPGA) where common-mode processing, zero-suppression or data compression is performed depending on the needs of the different subdetectors. The resulting data packets are collected by a fifth FPGA (SyncLink) which formats it into a format acceptable by

[1] The RICH detectors use a specific board, UKL1, which are functionally identical to TELL1 from the data acquisition point of view.

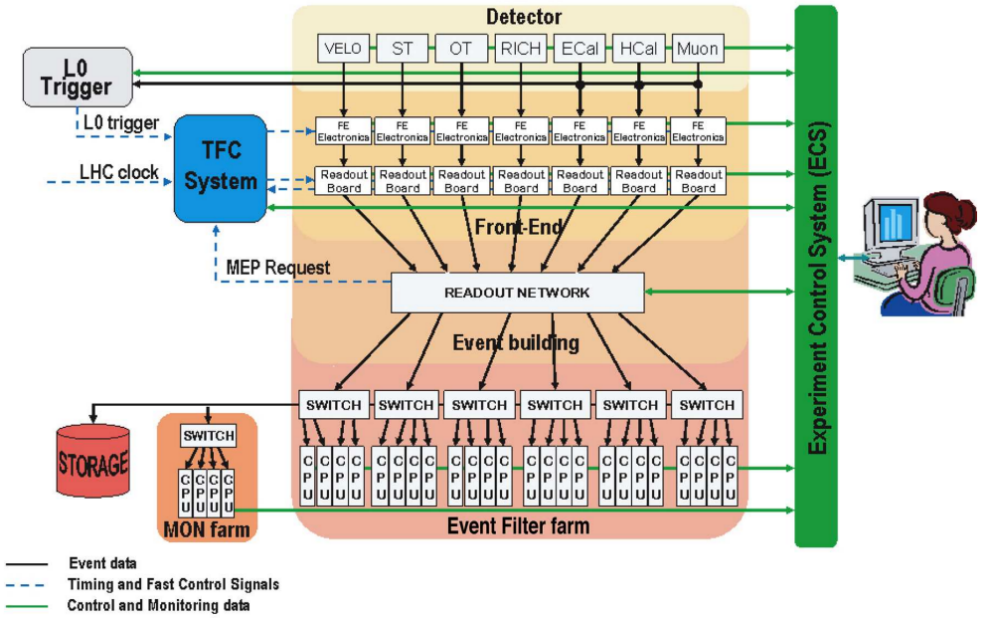

Figure 3.16: General architecture of the LHCb online system with its three major components: TFC, DAQ and ECS.

the Event Builder computing farm, using Gigabit-Ethernet links. The Event Builder collates information from the subdetector for a single event and sends it to the HLT for filtering and this in turn sends the data into permanent storage. The DAQ is also in charge of monitoring the quality of data and trigger in a separate monitoring farm.

- the Timing and Fast Control (TFC), which synchronises the data readout stages between the front-end electronics and the EFF by distributing the beam-synchronous clock, the L0 trigger, the synchronous resets and the fast control commands. The heart of the system is the Readout Supervisor, which implements the interface between the LHCb trigger system and the readout chain, synchronizing trigger decisions and beam-synchronous commands to the LHC clock and orbit signal provided by the LHC. The Readout Supervisor can also perform load balancing among the nodes in the EFF by dynamically selecting the destination node for the incoming events, and can produce a variety of auto-triggers for sub-detector calibration and tests.

- the Experiment Control System (ECS), which ensures the control and monitoring of the operational state of the entire LHCb detector. Apart from the traditional detector control domains, such as high and low voltages, temperatures, gas flows or pressures, it also encompasses the control and monitoring of the Trigger, TFC and DAQ systems.

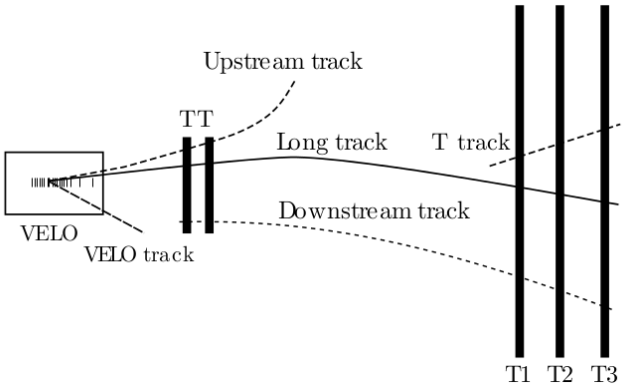

Figure 3.17: Illustration of the different types of tracks according to their trajectories.

3.3.3 Tracking and vertexing

Tracking consists in identifying and reconstructing the trajectories (tracks) followed by the different charged particles when they go through the detector [144]. The tracking detectors in LHCb are the the VELO, the TT and the T-stations. The passage of charged particles produces hits in the individual elements that form these subdetectors. Combining these hits with a mathematical algorithm, the full track can be deduced for each particle. Depending on the subdetectors in which the particles have produced hits (Fig. 3.17), the tracks can be classified as:

- Long tracks: contain hits in the VELO and in the tracking stations. Hits in the TT are added when possible, improving the resolution. Since these tracks combine information upstream and downstream the magnetic field, they have the most precise momentum estimate and therefore are the ones used for most of the LHCb analyses.
- Upstream tracks: contain hits in the VELO and in the TT. Mainly tracks with low momentum that are bent out of the acceptance by the magnetic field.
- Downstream tracks: contain hits in the TT and in the tracking stations. Mainly due to particles with a large lifetime which decay outside the VELO acceptance, such as K^0_S and Λ.
- Velo tracks: contain hits only in the VELO. Backward tracks or with a large angle, used for the PV reconstruction.
- T tracks: contain hits only in the tracking stations. Typically produced by secondary interactions.

The reconstruction of the tracks starts with a search for complementary hits in the VELO [145, 146]. Since this detector is outside the magnetic field, charged particle tracks are approximated by straight line segments. VELO tracks must have at least three hits in the r-sensors and three in the ϕ-sensors. These VELO tracks are then combined with the information given by the tracking stations, extrapolating their trajectories through

the magnetic field. Two complementary algorithms are used. The first one, called forward tracking [147], prolongs the VELO track into the T-stations by using a "thin lens" approximation of the dipole field, and finds the best possible combination of the VELO track and the hits in the tracking stations. The second method, called track matching [148, 149], uses a standalone algorithm [150] to create track segments in the tracking stations, and then match the VELO and the T-stations segments to produce long tracks. The candidate tracks found by each algorithm are then combined, removing duplicates, to form the final set of long tracks used for analysis. Finally, hits in the TT consistent with the extrapolated trajectories are included to improve the momentum determination. Since the tracking reconstruction is affected by scattering effects and by energy loss due to ionisation, the tracks are estimated using a Kalman Filter [151, 152]. Moreover, the quality of each track can be derived mathematically with the obtention of a χ^2 per degree of freedom for each track. The χ^2 accounts for the probability of the track being produced by a real particle or by a mixture of hits from different particles (a ghost). There is also the possibility of reconstructing the same track through different algorithms (clones). Only the best-χ^2 track is kept in these cases.

The tracking efficiency is defined as the probability that the trajectory of a charged particle that has passed through the full tracking system is reconstructed. It is measured using a tag-and-probe technique [153, 154] with $J/\psi \to \mu^+\mu^-$ decays. The overall efficiency depends on the kinematics of the track and on the number of charged particles in an event. In Fig. 3.18, the tracking efficiency as a function of the momentum and the pseudorapidity of the track and the number of tracks in the event is shown. The average track reconstruction efficiency for long tracks is found to be $(97.78 \pm 0.07)\%$ for 2011 data and $(96.99 \pm 0.05)\%$ for 2012 data [154].

With an accurate knowledge of the trajectories obtained from the tracking and using the measured value of the magnetic field, the momentum of the particles can be obtained. Since the momentum is one of the most important magnitudes entering in the invariant mass which, in turn, is one of the key parameters to select the signal events, a good momentum resolution is very important. In Fig. 3.19, the momentum resolution as a function of the momentum itself is shown. The momentum resolution is $\delta p/p \simeq 0.5\%$ for particles below 20 GeV/c, rising to $\delta p/p \simeq 0.8\%$ for particles around 100 GeV/c. This results in a mass resolution of $\sim 22\,\text{MeV}/c^2$ ($\sim 15\,\text{MeV}/c^2$) at the B-meson mass for two-body (four-body) B decays.

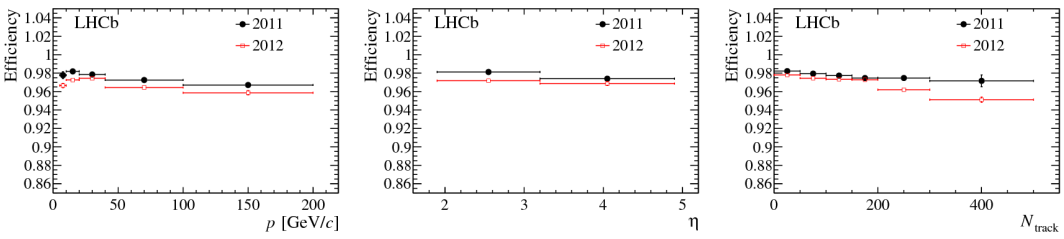

Figure 3.18: Tracking efficiency as a function of the momentum, p (left), the pseudorapidity, η (center) and the total number of tracks in the event, N_{tracks} (right), for 2011 and 2012 data.

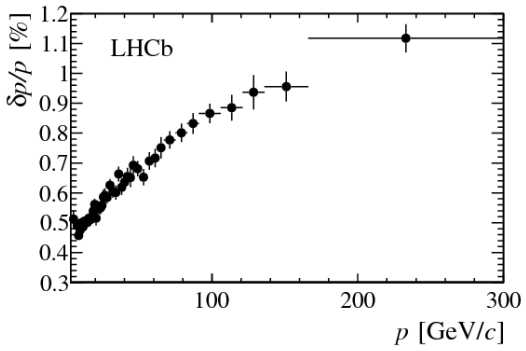

Figure 3.19: Left: Relative momentum resolution versus momentum for long tracks in data obtained using J/ψ decays.

Vertexing is another key ingredient of LHCb. It is the ability to accurately reconstruct vertex positions and resolve between primary and secondary vertices. The high spacial resolution of the VELO enables a precise determination of the particle's flight direction close to the primary interaction point, resulting in a good vertex resolution.

To reconstruct the PV [155], VELO tracks are used. A minimum of 5 VELO tracks is required in a distribution that can go as far as 150 tracks per PV. The PV resolution depends on the number of tracks used to reconstruct the vertex, as can be seen in Fig. 3.20 (left). Associated with the reconstruction of the PV and with a good tracking is the impact parameter (IP). The IP of a track is defined as its distance from the primary vertex at its point of closest approach to the primary vertex. Particles originating from the decays of long lived b- or c-hadrons tend to have larger IP than those particles produced at the PV. The IP and the IP significance, defined as the ratio of the IP/χ^2 of the track, are then variables used to reduce the background. A good resolution of the IP is needed for LHCb. In Fig. 3.20 (right), the IP resolution in the x coordinate is shown as a function of $1/p_{\mathrm{T}}$.

The reconstruction of the SV is of great importance for the determination of the decay time of the particles, used for lifetime measurements and for time-dependent CP violation measurements. The proper-time resolution is at the level of $\sim 50\,\mathrm{fs}$ allowing to resolve the fast B_s^0-$\overline{B}_s^0$ oscillation, which has a frequency of $\Delta m_s = (17.768 \pm 0.023\,(\mathrm{stat}) \pm 0.006\,(\mathrm{syst}))\,\mathrm{ps}^{-1}$ as measured by LHCb [156].

3.3.4 Particle identification

The identification of the different particles produced in the events of interest is needed in LHCb to discriminate between signal and background with identical topologies. The particle identification is performed by the two RICH detectors, the calorimeter system and the muon stations. The relevant subdetector for the identification depends on the particle properties:

- RICH PID [157]: the main role of the RICH detectors is the identification of charged hadrons ($\pi^{\pm}$, $K^{\pm}$ and p ($\overline{p}$)). When these particles traverse the radiating medium with high enough momentum, Cherenkov photons are produced and focused into

ring images, as shown in Fig. 3.21 (left). Based on the difference of the expected Cherenkov emission angle among the various species, the particles can be identified. In Fig. 3.21 (right), the reconstructed Cherenkov angles are shown and, as expected, the events populate distinct bands according to their mass. For the particle identification an overall event log-likelihood algorithm is employed. Since the most abundant particles in pp collisions are pions, the likelihood minimisation procedure starts by assuming that all particles are pions and compares the log-likelihood of this hypothesis with the electron, muon, kaon and proton hypotheses. The final results of the particle identification are then differences in the log-likelihood values for the different hypotheses, $\Delta\log\mathcal{L}$. The efficiency of the kaon identification and the pion misidentification rate (probability of identifying a kaon as a pion) are shown in Fig. 3.22 (left) as a function of the momentum and for different requirements in $\Delta\log\mathcal{L}_{K/\pi}$. In Fig. 3.22 (right), the efficiencies of proton identification and kaon misidentification are shown. In addition, the RICH system can contribute to the identification of charged leptons (e, μ), complementing information from the calorimeter and muon systems, respectively.

- CALO PID [158,159]: the main role of the LHCb calorimeters regarding the particle identification is the recognition of photon, electron and π^0 candidates. The information of the energy deposited in the different regions of the calorimeters is combined to achieve the separation. For the identification of electrons, the clusters in the PS, the ECAL and the HCAL are used. A log-likelihood difference between electrons and hadrons is built for each of these subdetectors based on reference histograms correlating the energy measurement with the particle momentum. In addition, for the ECAL likelihood, another estimator that matches the tracks produced in the tracking system with the energy deposits is included. The final $\Delta\log\mathcal{L}^{\mathrm{CALO}}(e-h)$, is the sum of each subdetector $\Delta\log\mathcal{L}$ ($\Delta\log\mathcal{L}^{\mathrm{PS}}(e-h)+\Delta\log\mathcal{L}^{\mathrm{ECAL}}(e-h)+\Delta\log\mathcal{L}^{\mathrm{HCAL}}(e-h)$). Fig. 3.23 shows the dependence of the electron identification (left) and misidentification as hadrons (right) with respect to the momentum for various cuts in $\Delta\log\mathcal{L}_{e/h}$.

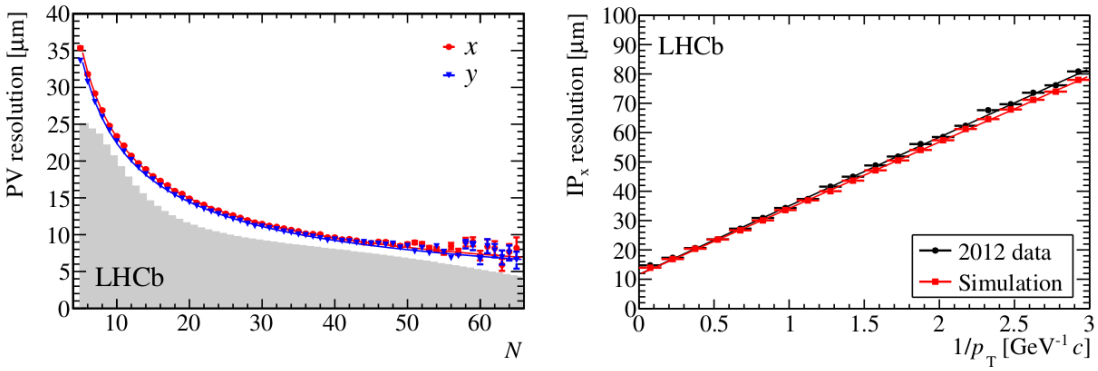

Figure 3.20: Left: Primary vertex resolution, for events with one reconstructed primary vertex, as a function of track multiplicity. The x (red) and y (blue) resolutions are separately shown and the superimposed histogram shows the distribution of the number of tracks per reconstructed primary vertex for all events that pass the HLT. Right: Impact parameter in x resolution as a function of $1/p_{\mathrm{T}}$. Both plots were prepared using data collected in 2012.

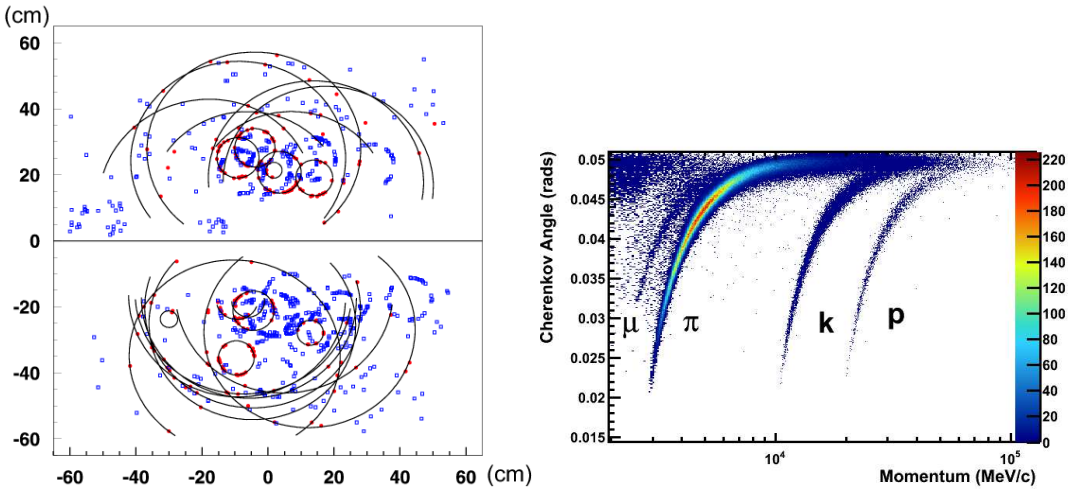

Figure 3.21: Left: Display of a simulated LHCb event in RICH1. Right: Reconstructed Cherenkov angle for isolated tracks, as a function of track momentum in the C_4F_{10} radiator.

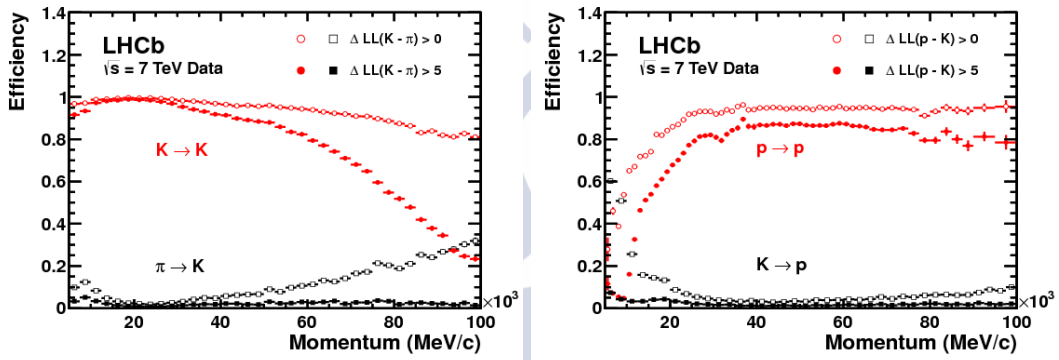

Figure 3.22: Left: kaon identification efficiency and pion misidentification rate measured on data as a function of track momentum, with two different cuts in $\Delta\log\mathcal{L}_{K/\pi}$. Right: proton efficiency and kaon misidentification fraction as a function of momentum with two different cuts in $\Delta\log\mathcal{L}_{p/K}$.

These figures are obtained using 2011 data of $B^{\pm} \to J/\psi(e^+e^-)K^{\pm}$ decays.

For the identification of γ and π^0, the absence of tracks matching the energy deposits in the ECAL is considered. The cluster shape is used to separate between single γ and double γ events from π^0 decays.

- Muon PID [160]: the muon identification is based on the fact that almost all the particles punching through the calorimeters and reaching the muon stations are muons. An association of hits in the muon system around the extrapolated trajectories reconstructed in the tracking system is used to build the muon likelihood. The muon identification performance is obtained using data from $J/\psi \to \mu^+\mu^-$ decays, selected without using PID information. Fig. 3.24 shows, as a function of the track momentum and for different requirements in the muon likelihood, the muon

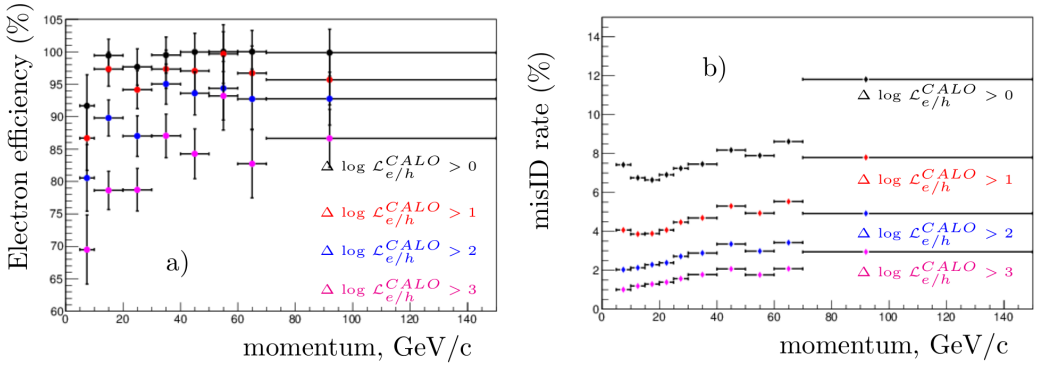

Figure 3.23: Performance of the electron PID efficiency (left) and misidentification rate (right) as a function of the momentum for different $\Delta\log\mathcal{L}^{\mathrm{CALO}}(e-h)$ cuts.

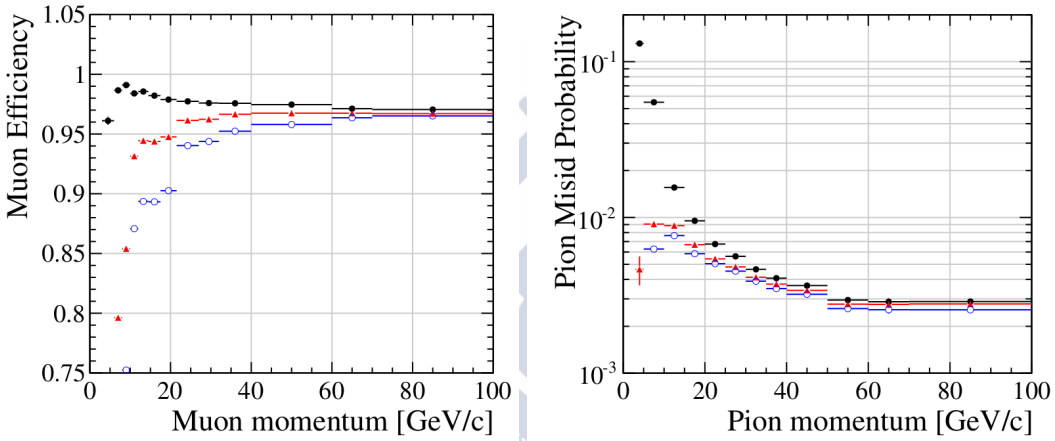

Figure 3.24: Muon identification performance as a function of the track momentum and for different cuts in the muon likelihood. Left: Muon identification efficiency. Right: Pion misidentification rate.

identification efficiency (left) and the pion misidentification rate (right).

- Combined PID: the information given by the different subdetectors, as previously explained, is combined to give a global log-likelihood difference between two hypotheses,

$$\Delta\log\mathcal{L}_{a/b} = log(\mathcal{L}_a) - log(\mathcal{L}_b) = log\left[\frac{\mathcal{L}_a}{\mathcal{L}_b}\right]. \tag{3.1}$$

3.3.5 Simulation

The importance of a detailed MC simulation arises for several reasons, both in the design and construction phase of an experiment and during its operation. On the one hand, it permits to train the tools that are later used on data, but with the advantage of having a full knowledge in advance of the process being studied. On the other, it is useful to

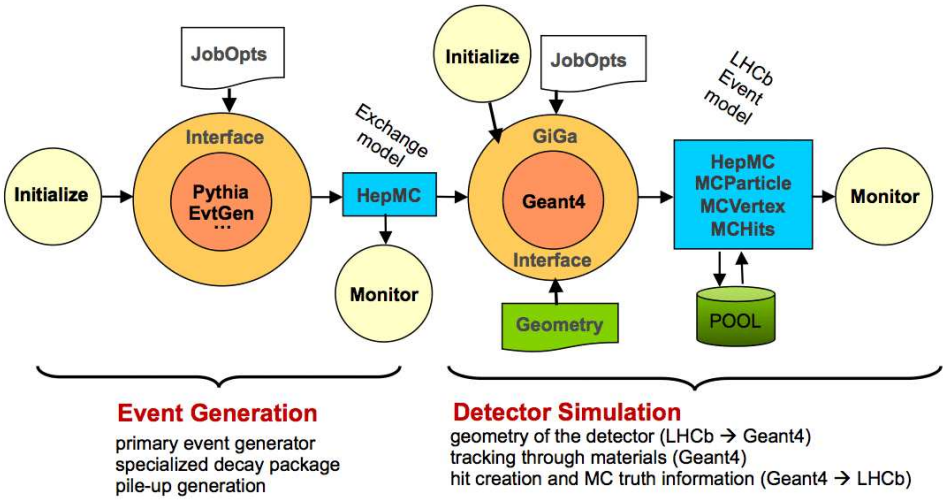

Figure 3.25: Structure of the Gauss application.

obtain certain parameters needed for the physics results but very difficult to be extracted from data itself.

At LHCb, the task of modeling the behaviour of the spectrometer for the different type of events occurring in the experiment is carried out by two separate applications called Gauss [161][1] and Boole.[2] Gauss generates the initial particles and simulates their transport through the LHCb detector, whilst Boole reproduces the different subdetectors responses and their digitisation converting the data in the same format provided by the experiment electronics and the DAQ system [152].

The simulation of the physics events can be divided in two parts that can be run together or separately. This division is shown in Fig. 3.25, where a schematic view of the structure of the Gauss application can be seen.

The first phase consists of the event generation of pp collisions using Pythia [162], with a specific LHCb configuration [163], and the decay and time evolution of hadronic particles, described by EvtGen [164], in which final-state radiation is generated using Photos [165]. The generator phase of Gauss also handles the simulation of the running conditions, the smearing of the interaction region due to the transverse and longitudinal sizes of the proton bunches and the change of luminosity during a fill due to the finite beam lifetime. Single and multiple pp-collisions are produced according to the chosen running luminosity. Other event generator engines can be interfaced in this phase if required.

The second phase consists of the interaction of the generated particles with the material inside the detector, the tracking of the charged particles in the magnetic field and the decay of the remaining unstable particles. The simulation of the physics processes which the particles undergo when travelling through the experimental setup is implemented using the Geant4 toolkit [166].

The behaviour of the generator phase and the detector response is regularly studied using reference decay channels. As the second phase is the most CPU-intensive, it is

[1] The Gauss project: http://lhcb-release-area.web.cern.ch/LHCb-release-area/DOC/gauss/
[2] The Boole project: http://lhcb-release-area.web.cern.ch/LHCb-release-area/DOC/boole/

possible to specify a set of requirements to the first phase (generator-level cuts) in order to veto out events that have no chance to be reconstructed by LHCb, for instance, a signal event with a charged track outside the LHCb acceptance.

The final stage of the LHCb simulation is the digitisation and the building of the raw dataset, modelled by the Boole package. Boole applies the detector response to hits previously generated in sensitive detectors by the Gauss simulation. This response can typically be divided into a physical process of signal collection, such as electrons drifting to a wire, and the specific behaviour of the electronics. The digitisation step includes simulation of the detector response and of the read-out electronics, as well as of the L0. The output of Boole has the same format as the real data (except that the generator-level information from the simulated particles is retained, known as MC "truth"), and it is used as input for trigger decision, reconstruction, stripping and offline analysis, which are performed as on real data, to obtain the final simulated MC samples.

3.3.5.1 Data/MC discrepancies

In general, the overall performance of the LHCb simulation is excellent and there is good agreement between data and MC. However, this simulation, as exhaustive as it is, can not include all effects playing a role in the data taking, and there are several variables for which the MC does not perfectly match the data. One example of these discrepancies is the track multiplicity of each event.

Due to our limited knowledge of the strong interaction and the hadron physics, the simulation of the underlying event in pp collisions is only an approximation.[1] Therefore, the kinematical spectrum of the products of pp interactions and the number of these products is different in MC and data. The response of the RICH detectors and of the calorimeters is correlated with the kinematics of the particle and with the occupancy of the detectors, which may be different from event to event and is sensitive to the beam conditions. Besides, the simulation of the RICH is difficult because the refractive index of their radiator highly depends on the temperature and gas pressure, which may vary from run to run. These variations throughout the year are impossible to simulate. Another complicated issue is the simulation of the `L0Hadron` trigger response. Due to the imperfect simulation of the E_{T} deposited in the calorimeters, the trigger appears to be more efficient on simulation than what it is on real data.

In order to surpass these obstacles, some data-driven approaches have been developed inside the collaboration. Several of these methods will be used in this thesis, and therefore they will be explained with detail in the pertinant chapters.

3.4 Run I experimental conditions

The period of the LHC operation known as Run I comprises years 2011 and 2012. The operating conditions at both years are described here, since the analysis performed in this work corresponds to these data taking periods. For completeness, a brief summary of the conditions in 2009 and 2010 are also included.

[1] The underlying event (UE) is all what is seen in a hadron collider event which is not coming from the primary hard scattering process.

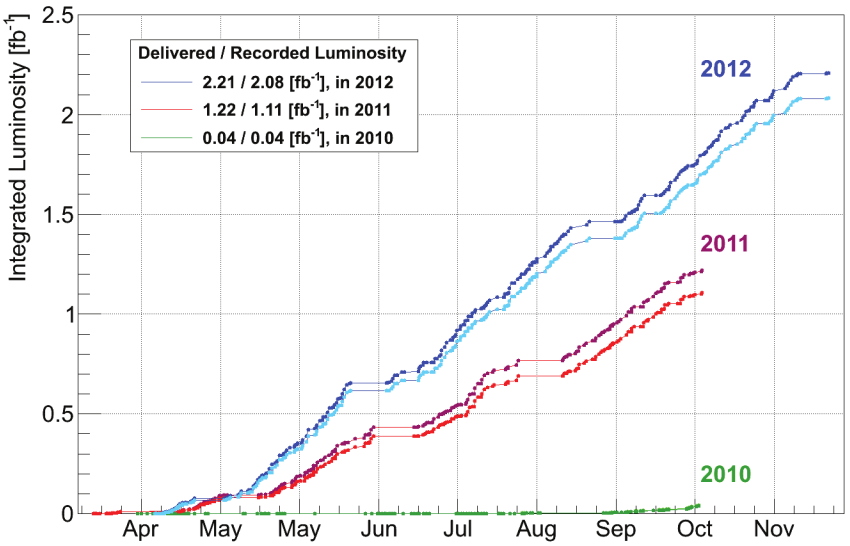

Figure 3.26: Integrated luminosity in LHCb during the three years of LHC Run I. Delivered (dark lines) and recorded (light lines) are displayed.

At the end of 2009 the first pp collisions were recorded at the LHC injection energy of $\sqrt{s} = 0.9\,\text{TeV}$. These data were used to finalise the commissioning of the detector and the reconstruction software. During 2010 the LHC luminosity was ramped-up, starting with luminosities $\sim 10^{28}\,\text{cm}^{-2}\,\text{s}^{-1}$ and almost no pile-up ($\mu_{\text{vis}} \simeq 1$),[1] and reaching $10^{32}\,\text{cm}^{-2}\,\text{s}^{-1}$ with $\mu_{\text{vis}} \approx 2.5$. Although the pile-up for this year was much larger than the design value due to the low number of bunches in the machine, the trigger and reconstruction worked efficiently, demonstrating the capabilities of the detector under such harsh conditions. The LHC beam energy in 2010 was $\sqrt{s} = 3.5\,\text{TeV}$ and the integrated luminosity recorded was $38\,\text{pb}^{-1}$.

In the first part of the 2011 data taking the number of bunches in the machine was increased to about 1300, the maximum possible with 50 ns bunch spacing. Due to this larger number, the pile-up was reduced to $\mu_{\text{vis}} \simeq 1.5$. The majority of data were taken at a luminosity of $3.5 \times 10^{32}\,\text{cm}^{-2}\,\text{s}^{-1}$, 1.75 times more than the design luminosity. In 2011 a levelling procedure was introduced at the LHCb interaction point [167]. This system displaces the beams allowing LHCb to maintain an approximately constant luminosity throughout each LHC fill. The levelling permits to maintain the same trigger configuration during a fill and reduce systematic uncertainties due to changes in the detector occupancy.

In 2012 the LHCb beam energy was increased to 4 TeV. LHCb took data at a luminosity of $4 \times 10^{32}\,\text{cm}^{-2}\,\text{s}^{-1}$. A deferred triggering system was developed for the 2012 data taking to use more efficiently the processing power available [168]. Since $\sim 70\%$ of the available time the EFF would be idle (LHC delivers stable beams $\sim 30\%$ of the available time), the L0 accepted events are temporarily saved on the EFF node local disks and these events are subsequently processed by the HLT during the inter-fill periods. This method allowed LHCb to increase the data sample available for physics analysis.

The integrated luminosity recorded by LHCb in 2011 and 2012 was $1.11\,\text{fb}^{-1}$ and

[1] The pile-up is defined as the average number of visible interactions per beam-beam crossing.

$2.08\,\text{fb}^{-1}$, respectively. The evolution of the integrated luminosity for years 2010 to 2012 is shown in Fig. 3.26. The average operational efficiency (defined as the ratio of recorded over delivered luminosity) was 93%. The main inefficiency sources are the detector-safety procedure for the VELO closing (0.9%) and the non-conformities in the implementation of the read-out protocol of some subdetectors (2.4%). Short technical problems with the subdetector electronics or the central read-out system are responsible for the remaining 3.6%.

To reach the LHCb design sensitivity in *CP* violation measurements, the difference in performance of the left and right sides of the detector must be under control. These differences would lead to charge detection asymmetries. The polarity of the LHCb magnet is inverted about twice per month to cancel the asymmetries [113].

USC UNIVERSIDADE DE SANTIAGO DE COMPOSTELA

4

First observation of the $B_s^0 \to \phi \overline{K}^{*0}$ decay

In this Chapter the first observation of the $B_s^0 \to \phi \overline{K}^{*0}$ decay, with $\phi \to K^+K^-$ and $\overline{K}^{*0} \to K^-\pi^+$, is reported and the determination of its branching ratio and polarisations are presented.

4.1 Introduction

The mode $B_s^0 \to \phi \overline{K}^{*0}$ is the only $b \to d$ penguin decay into vector mesons that has not previously been observed. This decay is closely linked to $B^0 \to \phi K^{*0}$, differing in the spectator quark and the final quark in the loop, as shown in Fig. 4.1.[1] From the relation between $b \to s$ and $b \to d$ transitions, their relative branching ratios should scale as $|V_{td}|^2/|V_{ts}|^2$ and their polarisation fractions are expected to be very similar. Moreover, since both decays share the same final state, except for charge conjugation, $B^0 \to \phi K^{*0}$ is the ideal normalisation channel for the determination of the $B_s^0 \to \phi \overline{K}^{*0}$ branching ratio. The $B_s^0 \to \phi \overline{K}^{*0}$ decay is also related to $B^0 \to K^{*0}\overline{K}^{*0}$, since their loop diagrams only differ in the spectator quark (s instead of d), although it has been suggested that S-wave interference effects might break the $SU(3)$ symmetry relating the two channels [169]. Finally, it is also interesting to explore the relation of the $B_s^0 \to \phi \overline{K}^{*0}$ decay with the $B^0 \to \rho^0 K^{*0}$ mode since the penguin loop diagrams of these modes are related by the $d \leftrightarrow s$ exchange. The $B^0 \to \rho^0 K^{*0}$ decay also has a $b \to u$ tree diagram, but it is expected that the penguin contribution is dominant, since the branching ratio is comparable to that of the pure penguin $B^0 \to \phi K^{*0}$ decay.

The most stringent previous experimental limit on the $B_s^0 \to \phi \overline{K}^{*0}$ branching ratio is $\mathcal{B}(B_s^0 \to \phi \overline{K}^{*0}) < 1.0 \times 10^{-3}$ at the 90% confidence level [170]. Calculations based on the QCD factorisation framework predict a value of $(0.4^{+0.5}_{-0.3}) \times 10^{-6}$ [64], while in perturbative QCD a value of $(0.65^{+0.33}_{-0.23}) \times 10^{-6}$ [171] is obtained. The precise determination of the branching ratio tests these models and provides a probe for physics beyond the SM.

Its branching ratio is measured using the mode $B^0 \to \phi K^{*0}$ as a reference. Very little difference in the efficiency of both the trigger and the selection of these two channels is expected based on their very similar topology. This strategy minimises the impact of systematic effects.

[1] Both the decays $B_s^0 \to \phi \overline{K}^{*0}$ and $B^0 \to \phi K^{*0}$ could also have contributions from QCD singlet-penguin amplitudes [64].

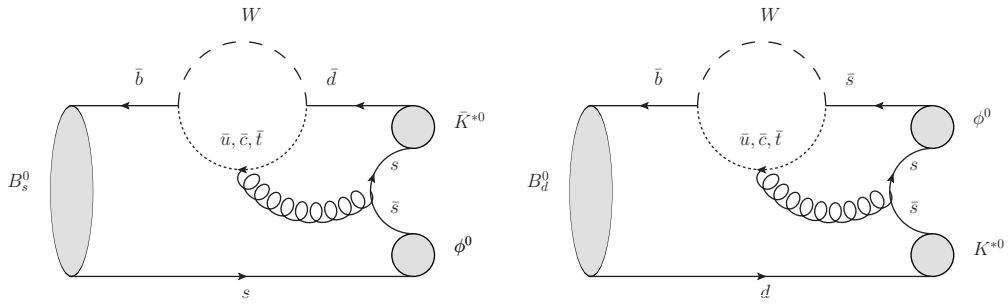

Figure 4.1: Feynman diagrams for the $B_s^0 \to \phi\overline{K}^{*0}$ (left) and the $B^0 \to \phi K^{*0}$ (right) decays.

The study of the angular distributions in the $B_s^0 \to \phi\overline{K}^{*0}$ channel provides a measurement of its polarisation. In Ref. [171], a prediction of $f_L = 0.712^{+0.042}_{-0.048}$ is made for the longitudinal polarisation fraction, using the perturbative QCD approach, that can be compared to the experimental result.

4.2 Selection

A total of 1 fb^{-1} of LHCb data collected in 2011 at $\sqrt{s} = 7$ TeV are analyzed to search for $B_s^0 \to \phi(K^+K^-)\overline{K}^{*0}(K^-\pi^+)$ decays.[1] All the physics triggers are considered. The data is stripped with DaVinci `v29r1` (Reco12, Stripping 17) using the Dirac production management system. The events passing the `StrippingBs2PhiKst0` stripping line are considered. The cuts at the stripping level are shown in Table 4.1. After the stripping, a first data reduction is performed applying the set of rectangular offline cuts shown in Table 4.2. Most of this selection follows the path opened in the $B_s^0 \to K^{*0}\overline{K}^{*0}$ analysis [172].

4.2.1 Charmless backgrounds

Additional selection requirements are implemented to remove contamination from $B_s^0 \to \phi\phi$ decays where one of the kaons from the ϕ is misidentified as a pion. The $B_s^0 \to \phi\phi$ branching ratio is $(1.4 \pm 0.8) \times 10^{-5}$ [173], an order of magnitude larger than the expected branching ratio for the $B_s^0 \to \phi\overline{K}^{*0}$, therefore, as the probability of misidentifying a kaon as pion is small but not negligible, these events could produce some contamination, mostly in the $B^0 \to \phi K^{*0}$ peak but also in the signal region. In order to recognise such events the mass hypothesis has been switched from a pion into a kaon in the sole pion of the four-body decay: the one emerging from the $\overline{K}^{*0}$ candidate. The reconstruction of the invariant mass of the new K^+K^- pair shows a little peak around the mass of the ϕ. The four-body invariant mass of these events also shows a clear peak around the B_s^0 mass. The two dimensional distribution of these events is displayed in Fig. 4.2.

To clean this background the following condition is imposed on the data selection:

$$|M_{K^+K^-K^+K^-}[\text{MeV}/c^2] - 5374.| > 50. \;\; \text{OR} \;\; |M_{K^+K^-}[\text{MeV}/c^2] - 1019.4| > 7.$$

[1] Charge conjugated modes are implied in this Chapter, unless otherwise stated.

Table 4.1: Stripping cuts for $B_s^0 \to \phi \overline{K}^{*0}$.

Variable	Stripping cut
K/π p_{T}	$> 500\,\mathrm{MeV}/c$
K/π χ^2_{IP}	> 9
K $\mathrm{DLL}_{K\pi}$	> 0
π $\mathrm{DLL}_{K\pi}$	< 10
K^{*0} mass window	$\pm 150\,\mathrm{MeV}/c^2$
K^{*0} p_{T}	$> 900\,\mathrm{MeV}/c$
K^{*0} vertex χ^2/ndf	< 9
ϕ mass window	$\pm 25\,\mathrm{MeV}/c^2$
ϕ p_{T}	$> 900\,\mathrm{MeV}/c$
ϕ vertex χ^2/ndf	< 9
B_s^0 mass window	$\pm 500\,\mathrm{MeV}/c^2$
B_s^0 DOCA	$< 0.3\,\mathrm{mm}$
B_s^0 vertex χ^2/ndf	< 15

Table 4.2: Offline cuts to select $B_s^0 \to \phi \overline{K}^{*0}$ events.

Variable	Offline selection
K/π p_{T}	$> 500\,\mathrm{MeV}/c$
K/π χ^2_{IP}	> 36
K from ϕ, $\mathrm{DLL}_{K\pi}$	> 0
K from K^{*0}, $\mathrm{DLL}_{K\pi}$	> 2
π $\mathrm{DLL}_{K\pi}$	< 0
K^{*0} mass window	$\pm 150\,\mathrm{MeV}/c^2$
K^{*0} p_{T}	$> 900\,\mathrm{MeV}/c$
K^{*0} vertex χ^2	< 9
K^{*0} DIRA	> 0
ϕ mass window	$\pm 25\,\mathrm{MeV}/c^2$
ϕ p_{T}	$> 900\,\mathrm{MeV}/c$
ϕ vertex χ^2	< 9
ϕ DIRA	> 0
B_s^0 mass window	$\pm 500\,\mathrm{MeV}/c^2$
B_s^0 DOCA	$< 0.3\,\mathrm{mm}$
B_s^0 vertex χ^2/ndf	< 15
B_s^0 flight distance χ^2	> 22
B_s^0 χ^2_{IP}	< 5

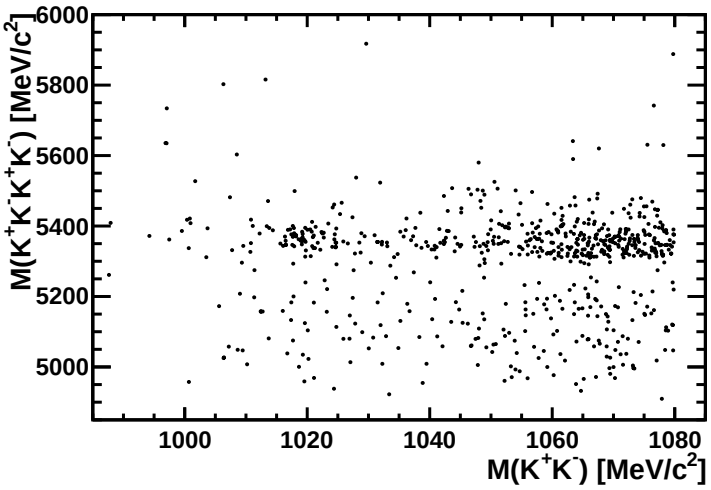

Figure 4.2: K^+K^- mass versus the four-body mass in the hypothesis of the pion from the K^{*0} decay being a kaon. This reveals a little contamination of $B_s^0 \to \phi(K^+K^-)\phi(K^+K^-)$.

This cut suppresses very few legitimate signal events. When applied to $B_s^0 \to \phi\overline{K}^{*0}$ simulated events, only 1.2 per mile of them are lost. None events are suppressed in the $B^0 \to \phi K^{*0}$ Monte Carlo sample with this selection.

Additionally, two and three body decay resonances that could pollute the ϕK^{*0} final state have been searched for. First, the effect of possible kaon-proton misidentifications in the quasi-two bodies has been studied by assigning the mass of a proton to one of the three kaons in the event. The kaon with the highest probability of being mistaken as a proton has been chosen, that is to say the kaon with the highest value of the difference in the log-likelihoods between the proton and kaon hypotheses, $\Delta\log\mathcal{L}(p-K)$, or DLL_{pK} for short. Next, this proton has been combined with each other particle in the event trying to check for the presence of resonances, in particular $\Lambda \to p\pi$ decays. No contribution is found since the invariant mass of such pairs is above the Λ mass.

4.2.2 Charmed backgrounds

Moreover, a small pollution of $B_s^0 \to D_s K$ decays has been identified, shown in Fig. 4.3. This has been possible by reconstructing three body invariant masses where the pion pronging from the K^{*0} candidate is combined with the two kaons that are produced in the ϕ decay. This suggests a $D_s^+ \to \phi\pi^+$ decay that has a large branching ratio of $2.34 \pm 0.14\%$ [173]. To veto this contamination, an additional cut on the invariant mass of the three $KK\pi$ body system is applied, $|M_{KK\pi} - (1968.5 + 4.8)| > 15\,\mathrm{MeV}/c^2$, where the additional $4.8\,\mathrm{MeV}/c^2$ shift in the mass is deduced from the result of the global fit of the four-body invariant mass, summarised in Chapter 4.3.

Three-body searches are also made switching the kaon with largest DLL_{pK}. This has allowed to identify some Λ_c^+ decays into $pK\pi$. However, these events do not contaminate the signal since the narrow K^+K^- invariant mass window around the ϕ mass strongly suppresses them and the few that survive the cut fall far from the B_s^0 mass when the

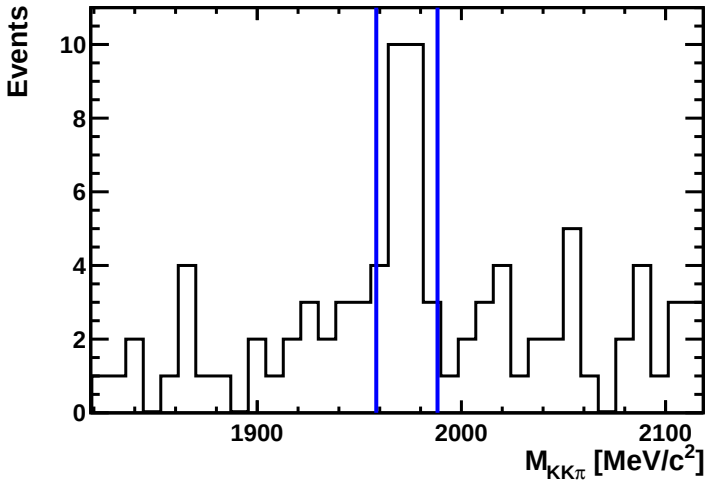

Figure 4.3: Events excluded by the cut in the $KK\pi$ mass.

four-body mass is reconstructed.

4.3 Fit model for the four-body mass spectrum

For the parametrisation of the invariant mass shape of the signal events a data sample of $B^0 \to J/\psi K^{*0}$ events reconstructed in 2011 has been used. For these events the four-body mass is reconstructed without the usual constraint of the muon pair to the J/ψ mass. These events constitute a large sample of B^0 decays and are parametrised as a Crystal-Ball function [174] plus a concentric Gaussian for both the $B^0 \to J/\psi K^{*0}$ and the $B_s^0 \to J/\psi \overline{K}^{*0}$ decays. Both distributions are shifted by the mass difference between the B^0 and the B_s^0 mesons. Additionally an exponential decreasing distribution is added to account for the combinatorial background. The results of the fit are shown in Table 4.3 and Fig. 4.4. The small contamination of $B_s^0 \to J/\psi \overline{K}^{*0}$ and combinatorial background can be appreciated if a logarithmic scale is applied, Fig. 4.4 (bottom).

The parameter f reflects the percentage of events in the distribution containing the bulk of the events, since the distributions are combined according to: $f \times CB + (1-f) \times G$. Therefore the Crystal-Ball contains most of the statistics and the Gaussian parametrises events reconstructed with lower resolution. These events contain particles that have most likely suffered a hard collision in one of the detectors. They constitute a small fraction of the total sample but produce a little tail of $B^0 \to \phi K^{*0}$ decays contaminating the $B_s^0 \to \phi \overline{K}^{*0}$ peak.

For completeness the parametrisation of the Crystal-Ball distribution is shown,

$$f(x;\alpha,n,\bar{x},\sigma) = N \cdot \begin{cases} \exp(-\frac{(x-\bar{x})^2}{2\sigma^2}), & \text{for } \frac{x-\bar{x}}{\sigma} > -\alpha, \\ A \cdot (B - \frac{x-\bar{x}}{\sigma})^{-n}, & \text{for } \frac{x-\bar{x}}{\sigma} \leqslant -\alpha, \end{cases} \tag{4.1}$$

where

$$A = \left(\frac{n}{|\alpha|}\right)^n \cdot \exp\left(-\frac{|\alpha|^2}{2}\right), \quad B = \frac{n}{|\alpha|} - |\alpha|\,,$$

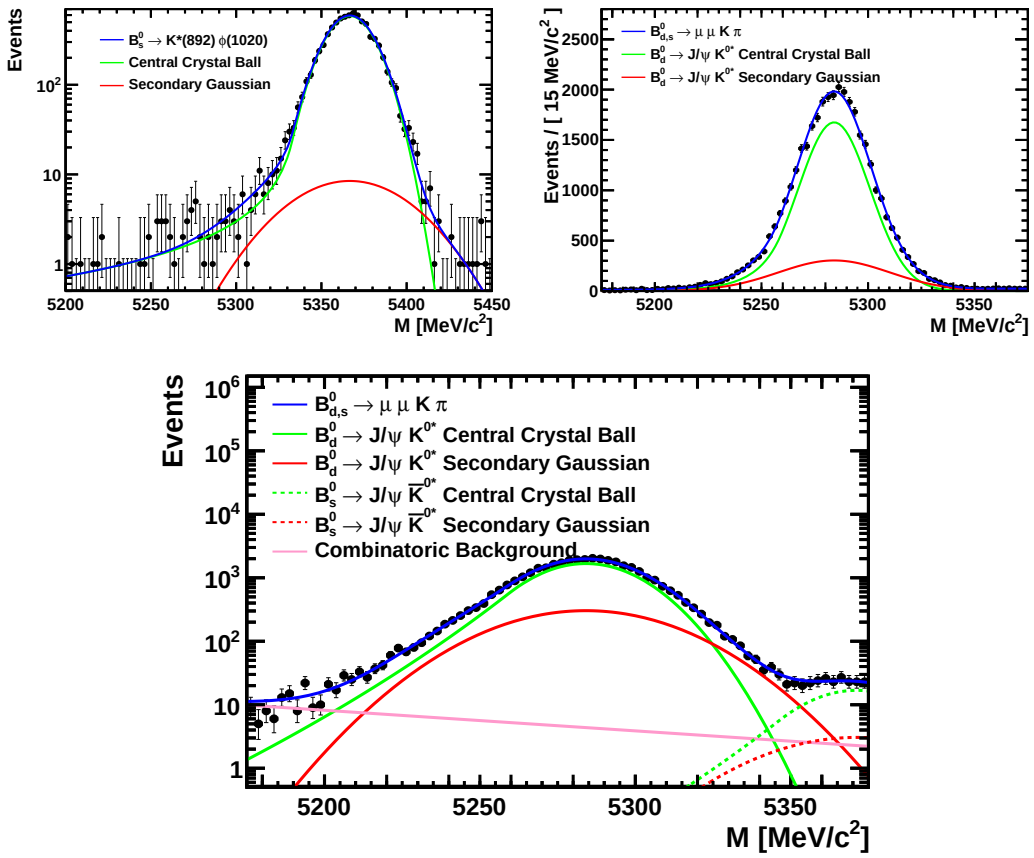

Figure 4.4: Fit to the four-body invariant mass using a Crystal-Ball plus a Gaussian distribution. Top left: Monte-Carlo $B_s^0 \to \phi\overline{K}^{*0}$ decays. Top right: Real data $B_{d,s}^0 \to \mu\mu K\pi$ decays. Bottom: Real data $B_{d,s}^0 \to \mu\mu K\pi$ decays in logarithmic scale.

and the parameters α and n describe the radiative tail. Very large values for either α or n imply that the radiative tail is negligible.

As a cross-check the same parametrisation of a Crystal-Ball plus a little Gaussian has been applied to $B_s^0 \to \phi\overline{K}^{*0}$ Monte Carlo signal events. This is a sample of 500000 events of MC11 generated with the 13104021 vector file, that simulates the $B_s^0 \to \phi\overline{K}^{*0}$ decay, also stripped with the Stripping17 `StrippingBs2PhiKst0` line. This approach has the disadvantage that, for the simulated data, a matching between the reconstructed and truth particles is applied. This is aimed at filtering events where particles from the underlying event would replace some of the legitimate grand-daughters of the B_s^0 decay. The matching between the truth and reconstructed events is sensitive to the emitted photons and the radiative tail is often underestimated. This effect is minimised by relaxing some of the matching cuts.

Applying the rectangular cuts of Table 4.2 to the referred MC sample the fit parameters shown in Table 4.3 are obtained. The results are not very far from those obtained with the $B^0 \to J/\psi\,K^{*0}$ data sample and could be used when fitting the data sample, however the parameters obtained from data are finally used. The fit quality is given by a χ^2/ndf

Table 4.3: Results of the $B^0 \to J/\psi K^{*0}$ data and of the $B_s^0 \to \phi \overline{K}^{*0}$ Monte Carlo signal fit to a Crystal Ball plus a Gaussian. The distributions are combined according to: $f \times CB + (1-f) \times Gauss$.

	$B^0 \to J/\psi K^{*0}$ Data	$B_s^0 \to \phi \overline{K}^{*0}$ MC
$\bar{x}$ [MeV/c^2]	5283.48 ± 0.13	5366.6 ± 0.2
α	2.03 ± 0.08	2.52 ± 0.16
n	1.41 ± 0.19	1.11 ± 0.27
σ [MeV/c^2]	15.62 ± 0.23	13.32 ± 0.24
σ_2 [MeV/c^2]	29.26 ± 0.53	23.67 ± 7.23
f	0.783 ± 0.019	0.97 ± 0.03

of 0.808.

Equipped with this parametrisation the data has been fitted using the cuts displayed in Table 4.2. For that it has been considered that the B^0 events and the B_s^0 events are described by the same Crystal-Ball+Gaussian distribution. Of course, a shift of 87.13 MeV/c^2 is applied accounting for the mass difference between the two mesons. The number of events corresponding to each decay (N_d and N_s) are considered independent, therefore proposing an extended fit strategy. Three parameters have been fixed in the distribution according to the results of the Monte Carlo fit. One is the relative amount of events in the Crystal-Ball and the Gaussian, given by the parameter f of Table 4.3, another is the ratio between the widths of the Gaussian and the Crystal-Ball, that can be easily calculated with the data in the same Table 4.3, and the last one is the parameter n, which provides the power law exponent of the CB function tail.

On top of the B-meson signals two additional ingredients have been added. One is a physical background that is described with a modified ARGUS shape. This is a convolution of the ARGUS distribution [175] and a Gaussian. This contribution accounts for partially reconstructed decays and is parametrised as,

$$f_P(m) \propto m' \left(1 - \frac{m'^2}{m_0^2}\right) \Theta(m_{PhysBkg} - m') e^{-k_{PhysBkg} \cdot m'} \otimes G(m - m'; \sigma_{PhysBkg}), \quad (4.2)$$

where Θ is the Heaviside-step function, $\otimes$ stands for the convolution product, m' is the variable over which the convolution integral is calculated, $G(m-m';\sigma_P)$ is a Gaussian PDF with standard deviation $\sigma_{PhysBkg}$ representing the experimental resolution and $m_{PhysBkg}$ is a free parameter. The origin of partially reconstructed events can be in B^0 or $B^{\pm}$ decays into ϕ and K or K^* excited states ($K_i^{(*)}$). The excited kaon will subsequently decay into a K^* and a pion that is either lost or not included in the four-body invariant mass computation. In addition to this contribution a decreasing exponential is included to account for combinatorial background,

$$f_C(m) \propto e^{-r_{Comb} \times m}. \quad (4.3)$$

The results of the fit performed on the data using the rectangular cuts are shown in Fig. 4.5 and the parameters in Table 4.4. This fit gives a total of 35.0 ± 8.4 B_s^0 decays and a statistical significance of 4.91σ calculated as twice the difference between the likelihood logarithms without and with signal hypothesis.

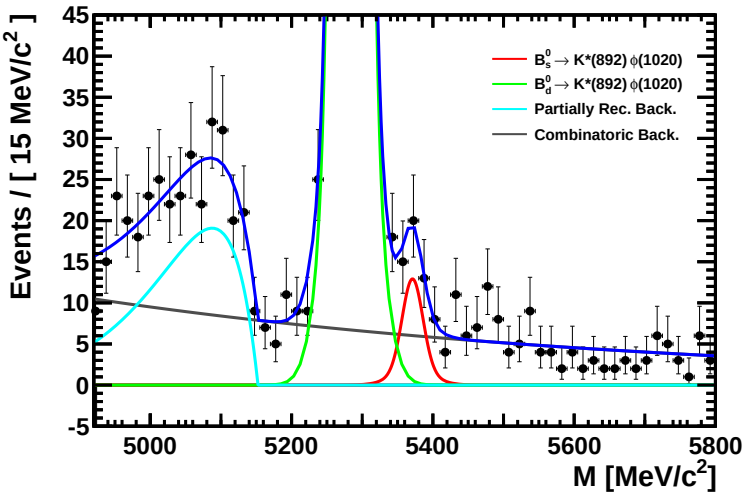

Figure 4.5: Fit to the $KKK\pi$ mass distribution for the data sample with the rectangular cuts of Table 4.2.

4.4 Initial MVA selection

To improve the result obtained with the simple rectangular cuts, several multivariate methods have been implemented. In particular all of the methods in the TMVA package [176] and a Geometrical Likelihood that has already been proposed in a previous analysis [172] are tested. For the sake of simplicity only two of the tested methods are reported, the Boosted Decision Tree (BDT) and the Geometrical Likelihood (GL).

The six variables that are used in the multivariate selection are:

- the B-meson candidate impact parameter with respect to the closest primary vertex,
- the distance of closest approach between the K^{*0} and the ϕ trajectories reconstructed from the pion and the kaon tracks,
- the lifetime of the B-meson candidate, calculated using the distance between the primary and secondary vertexes,
- the transverse momentum of the B-meson,
- the minimum impact parameter χ^2 of the tracks of the ϕ candidate daughters with respect to all primary vertexes in the event. The χ^2_{IP} is defined as $(\text{IP}/\sigma_{IP})^2$, where σ_{IP} is the IP error,
- the minimum impact parameter χ^2 of the tracks of the K^{*0} candidate daughters.

The training of the multivariate methods requires the use of a signal and a background sample. As the signal Monte Carlo events already reported in the description of the signal shape have been used. For the background, real data is used, selecting events that fulfill the conditions, $|M_\phi - 1019.455| > 7.\,\text{MeV}/c^2$ AND ($M_B < 5225.75\,\text{MeV}/c^2$ OR $M_B > 5412.88\,\text{MeV}/c^2$), where M_ϕ is the mass of the K^+K^- pair that constitutes the ϕ candidate and M_B is the four-body mass ($KKK\pi$) under study and, therefore, the

Table 4.4: Results of the fit to the data selected with the rectangular cuts of Table 4.2.

Parameter	Result
N_s	35.0 ± 8.4
N_d	1309 ± 37
α	4.4 ± 1.5
σ [MeV/c^2]	14.49 ± 0.46
$\bar{x}$ [MeV/c^2]	5284.05 ± 0.50
N_{Comb}	383 ± 40
r_{Comb} [MeV/c^2]$^{-1}$	$(1.228 \pm 0.035) \times 10^{-3}$
$N_{PhysBkg}$	197 ± 30
m' [MeV/c^2]	5152.4 ± 4.3
$\sigma_{PhysBkg}$ [MeV/c^2]	$0. \pm 31.$
$k_{PhysBkg}$ [MeV/c^2]$^{-1}$	0.0151 ± 0.0023

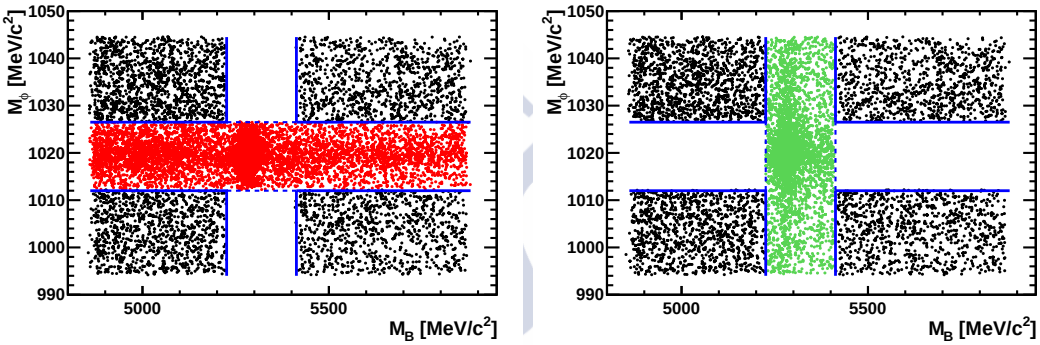

Figure 4.6: Regions used in the analysis. In black the sidebands used as the background in the multivariate methods training. In red, the data used in the analysis of the four-body spectrum. In green the data used for the analysis of the ϕ candidates spectrum.

B-meson candidate. In Fig. 4.6 the different data samples are displayed. The choice of sidebands that do not overlap with the mass window containing the B^0 and B_s^0 mesons aims at keeping the sidebands of the ϕ as wide as the stripping cut allows. This is necessary in order to do the analysis of non-resonant contributions that is discussed in Chapter 4.6.

The selection is optimised for a final amount of 500 background and 40 signal events maximising the significance $S/\sqrt{S+B}$. These figures are obtained from roughly rounding the results of the rectangular cuts analysis of Table 4.4. Nevertheless the cut value is quite insensitive to 20% variations of these two numbers. The resulting optimal cut in the GL is GL>0.185 as shown in Fig. 4.7. For the BDT the cut optimisation resulted in a value of 0.0703 for the discriminating variable. The distribution of this variable is also shown in Fig. 4.7.

The mass spectrum of this selection is fitted using the same parametrisation explained previously, resulting in an enriched signal sample. The results of the fit are shown in Figs. 4.8 and Table 4.5.

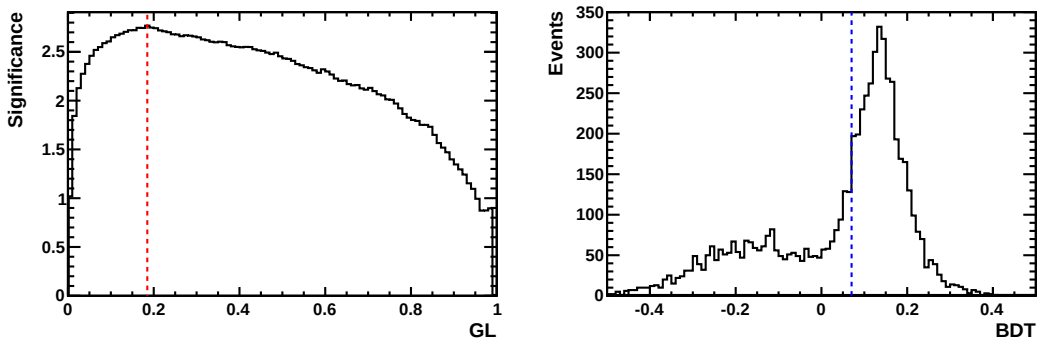

Figure 4.7: Left: GL cut optimisation under the hypothesis of 500 background and 40 signal events. Right: BDT distribution and selection cut.

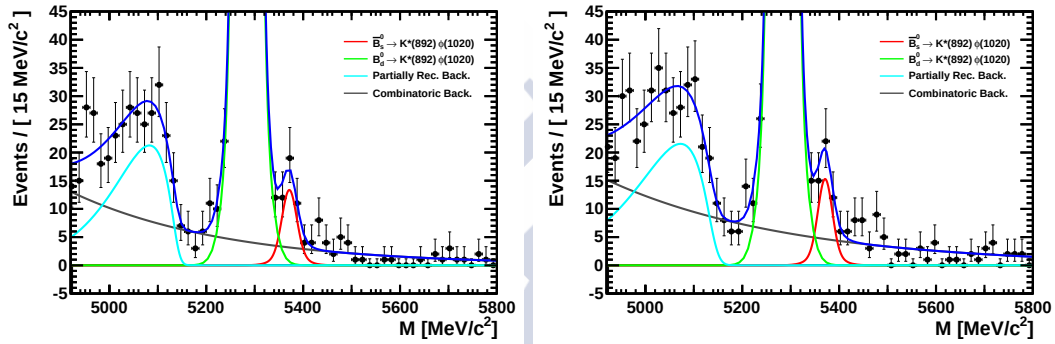

Figure 4.8: Fit to the $KKK\pi$ mass distribution for the data sample with Geometrical Likelihood selection (left) and with Boosted Decision Tree selection (right).

As a cross-check of the selection method, and trying to quantify systematic effects, a second optimisation of the multivariate techniques has been implemented using the $B^0 \to \phi K^{*0}$ as the signal. This is motivated by the possible differences in the events topology originated by the mass difference between the B^0_s and the B^0. This change produces very little deviation from the original result. The result obtained with this optimisation is shown in the last column in Table 4.5.

4.5 Final selection

In addition to the application of the multivariate methods mentioned above, several improvements have been found during the development of the analysis, both in the selection and in the model of the fit, that lead to the final four-body invariant mass result described below.

Table 4.5: Results of the fit to the data selected with the multivariate methods explained in the text. The χ^2/ndf is calculated for a binning of 60 elements.

Selection method	BDT	B_s^0 GL	B^0 GL
N_s	41.6 ± 8.4	37.4 ± 7.1	37.0 ± 7.7
N_d	1511 ± 43	1350 ± 37	1343 ± 38
α	4.3 ± 3.7	4.6 ± 3.7	4.1 ± 6.6
σ [MeV/c^2]	14.51 ± 0.43	14.98 ± 0.45	14.96 ± 0.45
$\bar{x}$ [MeV/c^2]	5283.92 ± 0.47	5284.32 ± 0.50	5284.27 ± 0.50
N_{Comb}	354 ± 71	266 ± 48	266 ± 49
r_{Comb} [MeV/c^2]$^{-1}$	$(2.62 \pm 0.55) \times 10^{-3}$	$(3.14 \pm 0.49) \times 10^{-3}$	$(3.00 \pm 0.55) \times 10^{-3}$
$N_{PhysBkg}$	234 ± 52	204 ± 34	201 ± 41
m' [MeV/c^2]	5145 ± 11	5142.1 ± 3.8	5144.0 ± 8.3
$\sigma_{PhysBkg}$ [MeV/c^2]	13 ± 10	8.8 ± 4.3	7.5 ± 9.9
$k_{PhysBkg}$ [MeV/c^2]$^{-1}$	0.0139 ± 0.0039	0.0169 ± 0.0033	14.95 ± 0.45
Significance/σ	6.30	6.41	6.30
χ^2/ndf	0.713	0.647	0.685

4.5.1 Removing the four-body high mass background

To explain the existence of a little excess in the four-body mass spectrum in the $5420\,\text{MeV}/c^2 < M < 5500\,\text{MeV}/c^2$ range several hypothesis have been tested:

- Λ_b^0 decays where one proton is misidentified as a kaon. This would lead into a wrong calculation of the Λ_b^0 mass ($5620\,\text{MeV}/c^2$) that would be shifted to smaller values, consequently in the range where this excess is observed. Such events can be identified by two methods. One is checking the distribution of the DLL_{pK}, other is trying to reconstruct the Λ_b^0 invariant mass by assigning the proton mass to one of the kaons. Whereas, if existing the amount of these events is very small, the first test did not succeed in identifying the Λ_b^0 in the analyzed region. On the other hand some $\Lambda_b^0 \to p\pi\phi$ events are seen reconstructing these four-body invariant mass. These events are shown in Fig. 4.9 (top). An explanation of how this background is almost suppressed is given below.

- The possibility of misidentifying the pion with a proton is also considered. This pursues the identification of $\Lambda_b^0 \to \phi\Lambda^*$ decays, where Λ^* stands for excited states of the Λ baryon. In the high region of the invariant-mass spectrum ($M_{3K\pi} > 5410\,\text{MeV}/c^2$) a clear excess of these events is seen as shown in Fig. 4.9 (bottom) in both the hypothesis of a proton substituting the pion around the Λ_b^0 mass simultaneous with the excited Λ states ($1520\,\text{MeV}/c^2$ and above).

- Another explored possibility is the pollution by $B_s^0 \to K^{*0}(K^+\pi^-)\overline{K}^{*0}(K^-\pi^+)$ where one of the pions is misidentified as a kaon. This is a frequent decay with very similar topology. Nevertheless this excess would be expected at higher masses $\sim 5720\,\text{MeV}/c^2 = M_{B_s^0} + M_{K^\pm} - M_{\pi^\pm}$. Anyhow, such events could be suppressed by increasing the cut in the kaon likelihood in the RICH. This is done without obtaining a stronger suppression in the commented region as compared to the signal.

Having this in mind several selections to reduce potential contamination by events containing protons are tested. A broad cut in the Λ_b^0 mass would kill the signal. Therefore,

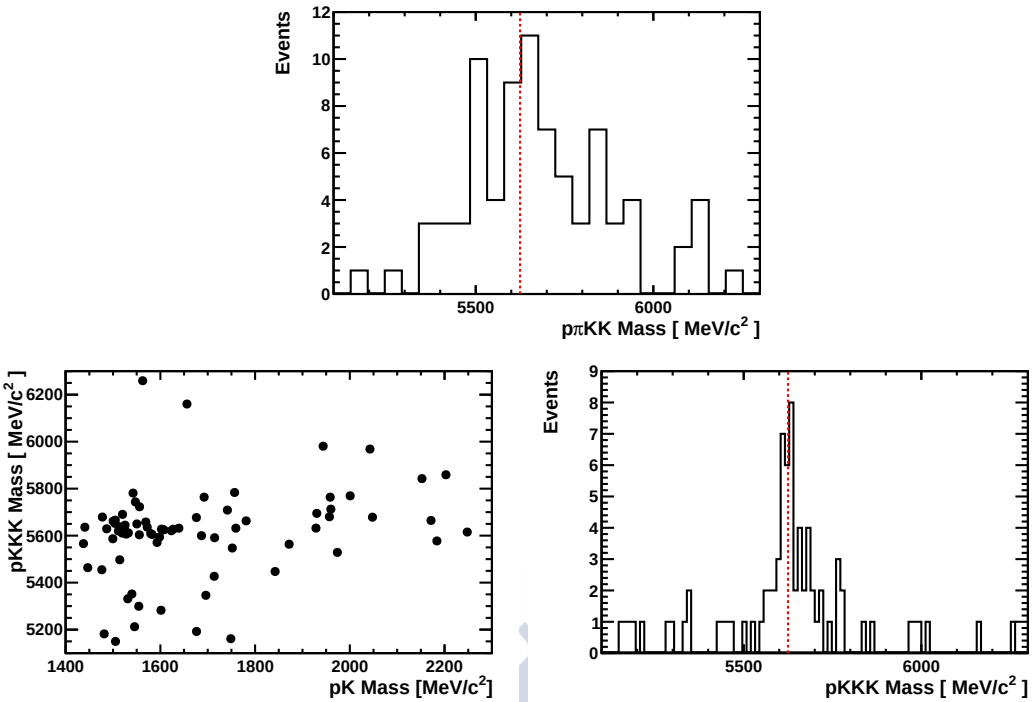

Figure 4.9: Top: $\Lambda_b^0 \to p\pi\phi$ polluting events where the proton is misidentified as a kaon. Bottom: Λ_b^0 polluting events where the proton is misidentified as a pion. The bottom left figure shows the four-body and two-body invariant mass where the latter spans in the region of the excited stats of the Λ. The bottom right figure shows the four-body mass peaking at the Λ_b^0.

as an alternative, different combinations between the mass and the DLL proton ID are tested. Additionally a cut in the pion candidate momentum, selecting only particles with momentum below 100 GeV is considered. These combinations decreased the amount of background (and signal too) but substantially kept the structures on the four-body high mass. The final study lead to choose a selection on the DLL differences of the proton and pion hypothesis $\mathrm{DLL}_{p\pi} < 0$. In order to further suppress this background the cut $\mathrm{DLL}_{pK} < 0$ is also implemented. This almost eliminates the possibility of the kaon from the K^{*0} decay to be confused with a proton. The consequence of these cuts is an almost complete suppression of the high-mass structured background in the four-body high mass region at the price of, as will be seen, a reduction $\sim 20\%$ in the signal.

In addition to the previous cuts, and also pursuing the high-mass background suppression, the multivariate methods are trained considering only the high-mass sideband background, where the four-body mass is above $M_B > 5412.88\,\mathrm{MeV}/c^2$, see Fig. 4.6. This is intended to be more efficient at the time of suppressing combinatorial background whereas the partially reconstructed background is well parametrised and does not pollute the signal region. The new Geometrical Likelihood optimisation results in a new GL requirement above 0.225.

4.5.2 Final fit model

As an improvement to the fit proposed in Chapter 4.3, one degree of freedom is removed by making equal the resolution of the signal to the resolution of the partially reconstructed background ($\sigma_{PhysBkg} = \sigma$). This is based on the small dependence of the resolution as a function of the invariant mass and motivated by the small amount of partially reconstructed background that produced large uncertainties in this parameter when left free in the fit.

Additionally, as the suppression of background containing protons results in a sample free of combinatorial background the parameters f and n have been unlocked in the spectrum model. Remember that f is the percentage of events in the Gaussian tail whereas n is one of the Crystal-Ball tail parameters, see Eq. 4.1.

The result of the four-body mass fit including both the new selection, equalising $\sigma_{PhysBkg} = \sigma$ and leaving f and n free is shown in the last column of Table 4.6 and in Fig. 4.10. It is clearly seen that the application of the additional cuts is at the cost of hurting both the B^0 and B_s^0 signals. However, the background is so efficiently suppressed that the statistical significance rises to 7.04σ. Additionally it can be seen that the hypothesis of $f = 0.783$ was quite reasonable since the fit gives $f = 0.735 \pm 0.069$ whereas for n it had been assumed $n = 1.41$ and the fit gives $n = 4.01 \pm 2.99$. The signal results are quite insensitive to this last parameter.

For the sake of understanding systematic effects, some additional tests have been implemented. In the case that some background is still present in the signal region an additional fit is performed that would reduce its effect regardless of whether it is a statistical fluctuation or not. For that the cut in the GL has been relaxed to GL$>$ 0.025 allowing a considerably larger amount of combinatorial background. The mass spectrum of this sample is fitted to the above proposed spectrum shape and extracted from it the value of the slope of the exponent of the decreasing exponential ($r_{Comb} = 0.001342[\,\mathrm{MeV}/c^2]^{-1}$). This parameter is afterwards blocked while fitting the standard selection. This fit results in an increase of the statistical significance (8.04σ) and the number of events in the signal peak. Also, favored by the use of one less parameter, a similar $\chi^2/\mathrm{ndf} = 0.521$ is obtained. The complete results are shown in the first column of Table 4.6.

Finally, a last fit is performed in which the combinatorial background is parametrised as a first degree polynomial. The result is also highly compatible with the previous models and helps to estimate systematic effects. This result can be seen in the second column of Table 4.6.

The result of the final model fit shows a good behaviour when a profile in the likelihood is made as a function of the number of B_s^0 and B^0 events. These profiles are shown in Fig. 4.11.

4.5.3 Significance

The estimation of the significance of the signal does not consider potential systematic effects. The strategy to account for such effects is to estimate a fluctuation in the signal of 1.7 events. This is calculated as the difference in the signal result with two different parametrisation of the combinatorial background (linear and exponential) that are shown in the last two columns of Table 4.6. It is not straightforward to combine the statistical

Table 4.6: Results of the fit to the data selected with the final selection explained in the text. The χ^2/ndf is calculated for a binning of 60 elements. In boldface the column of what is considered the final result. The parameters with no error quoted are blocked in the fit. In the column labeled Linear, a linear parametrisation of the combinatorial background is assumed, the dependence being: $1 + r_{Comb} M_{KK K\pi}$. In the column labeled Blocked, the parameter of the exponential is fixed to the value obtained with a fit with a relaxed GL cut.

Fit model	Blocked	Linear	**Exponential**
N_s	31.6 ± 6.3	31.6 ± 6.4	**29.9 ± 6.4**
N_d	1005 ± 32	1005 ± 33	**1000.4 ± 32.3**
α	2.36 ± 0.27	2.34 ± 0.31	**3.61 ± 2.12**
n	1.41	1.41	**4.01 ± 2.99**
σ $[MeV/c^2]$	15.11 ± 0.59	15.1 ± 0.6	**14.52 ± 0.98**
$\bar{x}$ $[MeV/c^2]$	5284.03 ± 0.61	5284.04 ± 0.62	**5283.97 ± 0.58**
N_{Comb}	28 ± 10	25.4 ± 14.6	**95 ± 42**
r_{Comb} $[MeV/c^2]^{-1}$	locked	$(-1.58 \pm 0.27) \times 10^{-4}$	**(4.46 ± 1.23) × 10^{-3}**
$N_{PhysBkg}$	213 ± 16	215 ± 17	**95 ± 42**
m' $[MeV/c^2]$	5157.4 ± 7.8	5157.5 ± 7.8	**5151.4 ± 9.5**
$\sigma_{PhysBkg}$ $[MeV/c^2]$	$= \sigma$	$= \sigma$	$= \sigma$
$k_{PhysBkg}$ $[MeV/c^2]^{-1}$	0.0102 ± 0.0017	0.0101 ± 0.007	**0.0135 ± 0.0041**
f	0.783	0.783	**0.735 ± 0.069**
Significance/σ	8.04	7.36	**7.04**
χ^2/ndf	0.521	0.524	**0.537**

and systematical fluctuations of the signal to produce a figure for the significance. This is caused for how the significance is calculated as twice the difference of the likelihoods of the fit with and without a signal hypothesis. In order to obtain a result it has been proceeded as follows:

- first the ratio between the number of signal events and the significance is calculated: $29.9/7.04 = 4.25$,
- then that number is added in quadrature to the systematical error: $\sigma_{eff} = \sqrt{(4.25^2 + 1.7^2)} = 4.6$,
- finally the significance is computed as: $\text{Significance} = N_s/\sigma_{eff} = 6.5$.

4.6 K^{*0} and ϕ purity in the signal

To determine the branching ratio of the decays $B_{s(d)} \to \phi(K^+K^-)\overline{K}^{*0}(K^-\pi^+)$, the amount of non-resonant contributions present in the KK and $K\pi$ final state systems must be subtracted. Due to the much larger statistics available, the S-wave component is evaluated for the $B^0 \to \phi K^{*0}$ channel and assumed to be of the same size in the $B_s^0 \to \phi\overline{K}^{*0}$ decay. A possible deviation from this assumption is treated as a systematic uncertainty. Furthermore, the hypothesis of having the same amount of S-wave for both channels is tested by looking at the χ^2/ndf of the KK and $K\pi$ mass fits for selected $B_s^0 \to \phi\overline{K}^{*0}$ decays.

The resonant $K\pi$ pairs (from the K^{*0} decays) are described with a relativistic spin-1

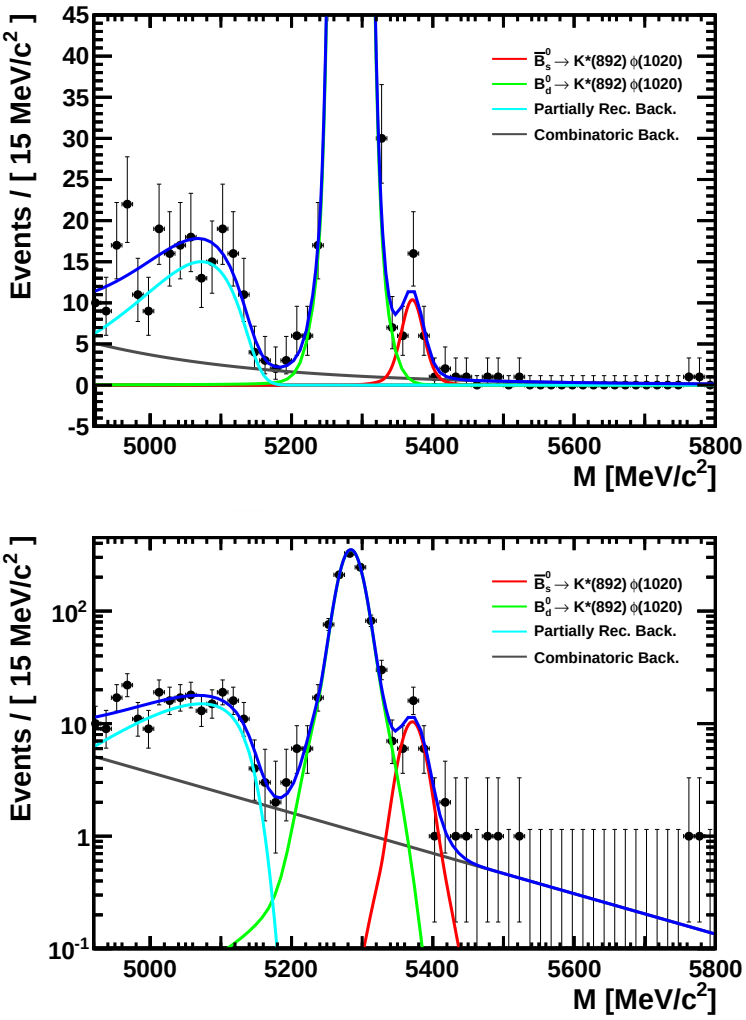

Figure 4.10: Fit to the $KKK\pi$ mass distribution for the data sample with the final model.

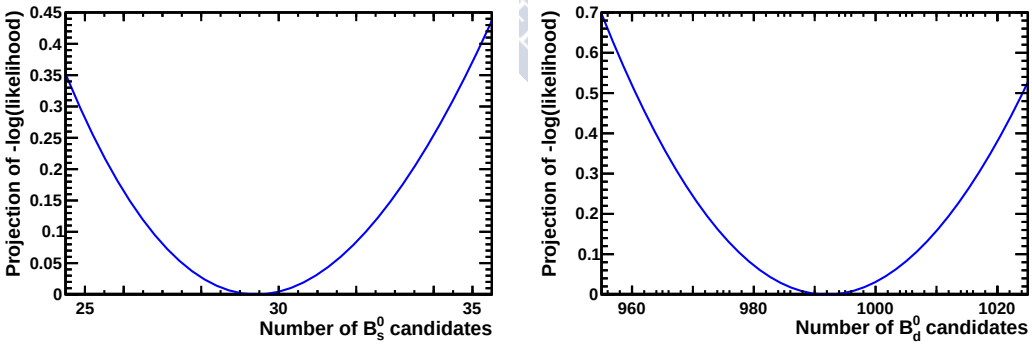

Figure 4.11: Likelihood profile in the number of B_s^0 (left) and B^0 (right) candidates.

Breit-Wigner amplitude [1] as in Ref. [72],

$$M_1^{K\pi}(m) \propto \frac{m_1\Gamma_1(m)}{m_1^2 - m^2 - im_1\Gamma_1(m)}, \tag{4.4}$$

with

$$\Gamma_1(m) = \Gamma_1\left(\frac{m_1}{m}\right)\left(\frac{q}{q_1}\right)^{2L+1} B_L^2(q, q_1), \tag{4.5}$$

where Γ_1 is the K^{*0} width (50.3 MeV/c^2) and m_1 its nominal mass (896 MeV/c^2). The value of L is the spin of the resonance ($L = 1$ in this case) and q is the momentum of the kaon in the K^{*0} rest frame, given by

$$q(m, m_A, m_B) = \frac{\sqrt{(m^2 - (m_A + m_B)^2)(m^2 - (m_A - m_B)^2)}}{2m}, \tag{4.6}$$

where $m_A = M_K$, $m_B = M_\pi$ and $q_0 = q$ when $m = m_1$. The functions $B_L(q, q_1)$ are the Blatt-Weisskopf barrier factors. For $L = 1$,

$$B_1(q, q_1) = \sqrt{\frac{1 + z_0}{1 + z}}, \tag{4.7}$$

with $z = (rq)^2$, $z_0 = (rq_1)^2$ and $r = 3.4\,\text{GeV}^{-1}$ being the interaction radius.

The S-wave component of the $K\pi$ spectrum is described by a modified Breit-Wigner distribution that takes into account both the resonant, $K_0^{*0}(1430)$, and non-resonant components [72, 177],

$$M_0^{K\pi}(m) \propto \frac{m}{q\cot\Delta B - iq} + e^{2i\Delta B}\frac{\Gamma_0 {m_0}^2/q_0}{({m_0}^2 - m^2) - im_0\Gamma_0(m)}, \tag{4.8}$$

where

$$\cot\Delta B = \frac{1}{aq} + \frac{1}{2}bq. \tag{4.9}$$

In these formulas m_0 is the nominal mass of the resonance (1435 MeV/c^2), a is the scattering length, b is the effective range, and $\Gamma_0(m)$ is defined as

$$\Gamma_0(m) = \Gamma_0\frac{m_0}{m}\left(\frac{q}{q_0}\right). \tag{4.10}$$

The term $e^{2i\Delta B}$ is needed for the conservation of unitarity. The values for all these parameters are shown in Table 4.7.

As in Ref. [178], the ϕ component in the KK mass spectrum is fitted to the Breit-Wigner amplitude given by

$$M_1^{KK}(m) \propto \frac{\sqrt{m\Gamma_1(m)}}{m_1^2 - m^2 - im_1\Gamma_1(m)}, \tag{4.11}$$

where $\Gamma_1(m)$ is

$$\Gamma_1(m) = \Gamma_1\frac{m_1}{m}\left(\frac{q}{q_0}\right)^3, \tag{4.12}$$

[1] The subscript in some of the variables, like m_1, Γ_1 and q_1, stands for the spin of the resonance or the angular momentum of the partial wave.

Table 4.7: Values for the spin dependent resonances used in the analysis. The mass of the resonance is m_J, Γ_J is the width, r the interaction radius, a the scattering length and b is the effective range.

	$(K\pi)_0^{*0}$ $J=0$	$K^{*0}(892)$ $J=1$
m_J(MeV)	$1435 \pm 5 \pm 5$	896.00 ± 0.25
Γ_J(MeV)	$279 \pm 6 \pm 21$	50.3 ± 0.6
r(GeV^{-1})	-	3.4 ± 0.7
a(GeV^{-1})	$1.95 \pm 0.09 \pm 0.06$	-
b(GeV^{-1})	$1.76 \pm 0.36 \pm 0.67$	-

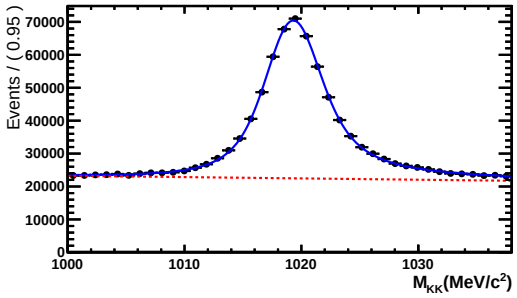

Figure 4.12: Invariant K^+K^- mass after the stripping, without applying any further cut, for $B^0 \to \phi K^{*0}$ candidates. The data have been fitted with a Breit-Wigner function convoluted with a Gaussian, as described in the text, and a linear background (red-dotted line). The χ^2/ndf of the fit is 2.2.

with $\Gamma_1 = 4.26\,\text{MeV}/c^2$ the width of the ϕ resonance and $m_1 = 1019.45\,\text{MeV}/c^2$ its mass. The momentum of a kaon in the KK rest frame is denoted by q and can be expressed as

$$q(m, m_A, m_B) = \frac{\sqrt{(m^2 - m_A^2 - m_B^2)^2 - 4m_A^2 m_B^2}}{2m}, \tag{4.13}$$

where $m_A = m_B = m_K$.

Since the width of the ϕ resonance ($4.26\,\text{MeV}/c^2$) is comparable to the experimental resolution ($\sim 1\,\text{MeV}/c^2$), the Breit-Wigner is convoluted with a Gaussian distribution in this case. The experimental resolution is measured using $B_{s,d} \to \phi K^{*0}$ data without applying any cut apart from those implemented at the stripping level. This is done in order to maximise the available statistics and, at the same time, check the validity of the Breit-Wigner function to fit the data. The fit has a χ^2/ndf of 2.2 and is shown in Fig. 4.12. The resolution is found to be $1.394 \pm 0.014\,\text{MeV}/c^2$.

The $K\pi$ mass spectra is fitted to $|M_0^{K\pi}(m)|^2 + |M_1^{K\pi}(m)|^2$, being $M_1^{K\pi}(m)$ and $M_0^{K\pi}(m)$ described in Eq. 4.4 and Eq. 4.8, respectively. The K^+K^- mass spectra is fitted to $|M_1^{KK}(m)|^2$, described in Eq. 4.11, plus a constant line that parametrises the S-wave contribution.

The fits of the $K\pi$ and K^+K^- mass distributions for the selected $B^0 \to \phi K^{*0}$ candidates are shown in Fig. 4.13 (top). The purity for the K^{*0} and ϕ is found to be

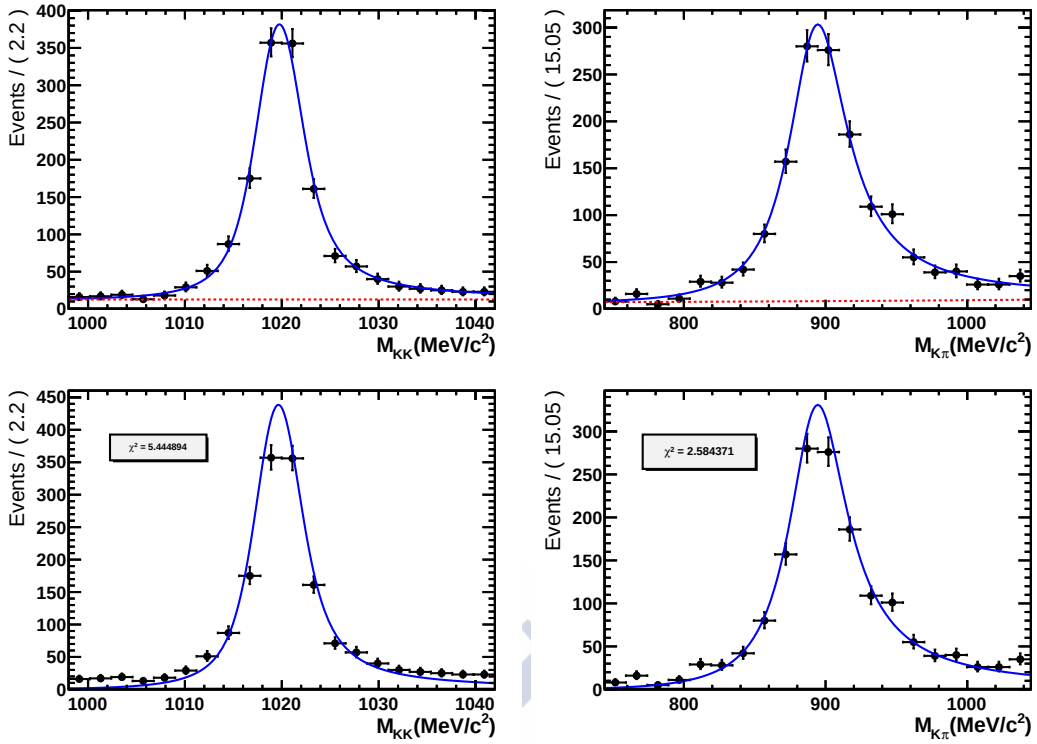

Figure 4.13: Invariant K^+K^- (left) and $K\pi$ (right) mass for the B^0 decays after the selection cuts in a window of $\pm 30\,\mathrm{MeV}/c^2$ around the B^0 mass. The data have been fitted with a Breit-Wigner function, as described in the text. Top: The S-wave component (red-dotted line) is given by a modified Breit-Wigner (Eq. 4.8) in the case of the $K\pi$ system and a constant line for the K^+K^-. The χ^2/ndf are 0.80 and 1.23 for the K^+K^- and $K\pi$ invariant masses, respectively. Bottom: The S-wave component is removed from the fit. The χ^2 values can be compared with those shown above.

0.89 ± 0.02 (in a $\pm 150\,\mathrm{MeV}/c^2$ window around the K^{*0} nominal mass) and 0.950 ± 0.005 (in a $\pm 7\,\mathrm{MeV}/c^2$ window around the ϕ mass) respectively, which means a total purity of 0.84 ± 0.02. In other words, 84% of the reconstructed $B \to K^+K^-K^+\pi^-$ candidates are legitimate $B^0 \to \phi K^{*0}$ decays. This factor will be used to scale down the number of $B_s^0 \to \phi \overline{K}^{*0}$ candidates when computing the branching ratio.

When fitting the $B_s^0 \to \phi \overline{K}^{*0}$ mass distribution, special care must be taken to account for contamination from the $B^0 \to \phi K^{*0}$ peak and the combinatorial background. A window of $\pm 2\sigma = \pm 30\,\mathrm{MeV}/c^2$ around the B_s^0 mass is used to select $B_s^0 \to \phi \overline{K}^{*0}$ candidates. In this region, the yields shown in Table 4.8 are obtained. The signal to background ratios are used as fixed parameters in the mass fit. The combinatorial background is studied in the sidebands removing the cut in the geometrical lihelihood, as is explained in Chapter 4.8.2. The signal, together with the two backgrounds, is shown in Fig. 4.14. The χ^2/ndf of the fit is 0.84 and 0.67 for the $K\pi$ and K^+K^- invariant mass distributions, respectively. No indication that the underlying hypothesis is wrong is therefore found. For illustration about the importance of the S-wave in the analysis, in Fig. 4.13 (bottom), the S-wave contribution is removed from the fit, showing the bad fit quality in both $K\pi$ and K^+K^-

Table 4.8: Number of events in a $\pm 2\sigma = 30\,\text{MeV}/c^2$ window around the fitted B_s^0 mass.

Contribution	Number of events
N_s	26.38 ± 5.67
N_d	5.44 ± 0.18
N_{Comb}	2.75 ± 1.36

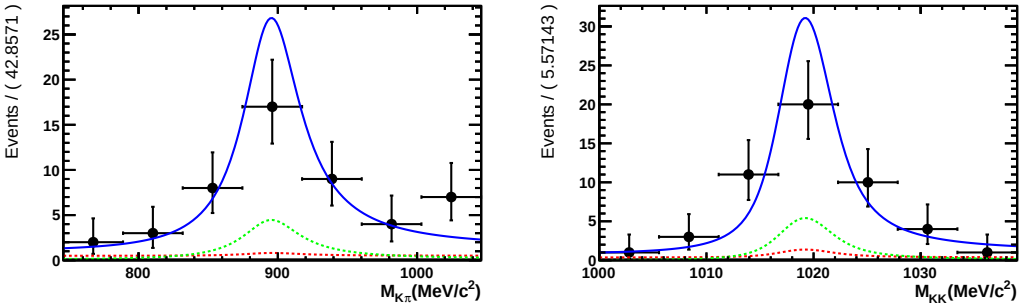

Figure 4.14: Invariant K^+K^- (left) and $K\pi$ (right) mass distributions for $B_s^0 \to \phi \overline{K}^{*0}$ decays. In the fit the amount of S-wave component is fixed to the value measured in the $B^0 \to \phi K^{*0}$ channel. The green line describes the amount of $B^0 \to \phi K^{*0}$ candidates in the B_s^0 mass region ($\pm 30\,\text{MeV}/c^2$ around the B_s^0 mass). The red line is the combinatorial background in the same region, which is introduced after a dedicated study of the sidebands.

mass distributions.

4.7 Measurement of the $B_s^0 \to \phi \overline{K}^{*0}$ branching ratio

The method for the measurement of $\mathcal{B}(B_s^0 \to \phi \overline{K}^{*0})$ is based upon the use of $B^0 \to \phi K^{*0}$ as normalisation channel, which has a branching ratio of $(9.8 \pm 0.6) \times 10^{-6}$ [173]. Both channels share the same stripping line and are obviously very similar from the kinematical point of view. The value of $\mathcal{B}(B_s^0 \to \phi \overline{K}^{*0})$ is computed with,

$$\mathcal{B}(B_s^0 \to \phi \overline{K}^{*0}) = \lambda_{f_L} \times \lambda_{Eff} \times \lambda_P \times \frac{f_d}{f_s} \times \mathcal{B}(B^0 \to \phi K^{*0}) \times \frac{N_s}{N_d},$$

where N_s and N_d stand for the number of B_s^0 and B^0 candidates, 29.9 ± 6.4 and 1000.4 ± 32.3; $\frac{f_d}{f_s} = 3.75 \pm 0.29$ is the ratio of hadronisation factors needed to account for the different yields of B^0 and B_s^0 mesons, which is taken from Ref. [179]; λ_{Eff} and λ_P are correction factors to account for the different efficiency and purity of the two channels, which are set to one in the calculation (differences from this hypotheses are taken as sources of systematic error); and λ_{f_L} is a correction factor taking into account the different detection efficiencies for the two channels due to the different polarisations, calculated in Chapter 4.9.2 to be 0.989 ± 0.037. With this numbers the branching ratio is measured to be,

$$\mathcal{B}(B_s^0 \to \phi \overline{K}^{*0}) = (1.09 \pm 0.24\,(\text{stat})) \times 10^{-6}. \tag{4.14}$$

where only the statistical uncertainty due to N_d and N_s is quoted.

4.8 Angular analysis: measurement of the f_L polarisation fraction

The $\mathcal{B}(B_s^0 \to \phi\overline{K}^{*0})$ depends on the polarisation fractions of $B_s^0 \to \phi\overline{K}^{*0}$ decays. This is because the efficiency, calculated using simulation, depends on the longitudinal polarisation, f_L, specified in the vector file used for the generation of events. Since the value measured for f_L differs from the one used in the simulation, a correction factor needs to be applied to the branching ratio.

The differential decay width as a function of the polarisation angles $\Omega = \{\theta_1, \theta_2, \varphi\}$, shown in Fig. 4.15, is given by,

$$\frac{\mathrm{d}^3\Gamma}{\mathrm{d}\Omega} \propto \left|\left(\mathcal{A}_0 F_0(\Omega) + \mathcal{A}_\parallel F_\parallel(\Omega) + \mathcal{A}_\perp F_\perp(\Omega)\right)\right|^2 . \tag{4.15}$$

Assuming no *CP*-violation, and summing over B_s^0 and $\overline{B}_s^0$ the total PDF can be written as [180],

$$\frac{\mathrm{d}^3\Gamma}{\mathrm{d}\Omega} \propto |A_0|^2 f_1 + |A_\parallel|^2 f_2 + |A_\perp|^2 f_3 + |A_0||A_\parallel| \cos(\delta_\parallel) f_5, \tag{4.16}$$

where the angular functions f_i are,

$$\begin{aligned} f_1 &= \cos^2\theta_1 \cos^2\theta_2, \\ f_2 &= \frac{1}{2}\sin^2\theta_1 \sin^2\theta_2 \cos^2\varphi, \\ f_3 &= \frac{1}{2}\sin^2\theta_1 \sin^2\theta_2 \sin^2\varphi, \\ f_5 &= \frac{1}{2\sqrt{2}}\sin 2\theta_1 \sin 2\theta_2 \cos\varphi. \end{aligned} \tag{4.17}$$

4.8.1 Angular acceptance

The acceptance function is computed using simulated $B^0 \to \phi K^{*0}$ decays with the following helicities,

$$\begin{aligned} |H_0| &= 0.72, \quad \delta_0 = 0, \\ |H_+| &= 0.69, \quad \delta_+ = 1.39, \\ |H_-| &= 0.03, \quad \delta_- = -0.74, \end{aligned} \tag{4.18}$$

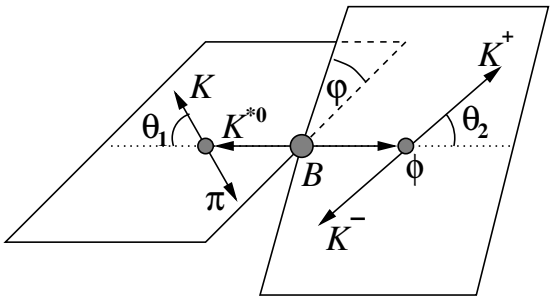

Figure 4.15: Definition of the angles in the decay.

Table 4.9: Values of the modules of the longitudinal ($|A_0|$), parallel ($|A_\parallel|$) and perpendicular ($|A_\perp|$) amplitudes and the corresponding polarisation fractions ($f_{L,\parallel,\perp} = |A_{0,\parallel,\perp}|^2$), together with the phase difference between the parallel an perpendicular amplitudes with the longitudinal one (which is defined to be zero). These values are used as input in the generation of the $B^0 \to \phi K^{*0}$ simulated events.

Parameter	Generated value
$\lvert A_0 \rvert$	0.72
$\lvert A_\parallel \rvert$	0.48
$\lvert A_\perp \rvert$	0.50
f_L	0.52
$f_\parallel$	0.23
$f_\perp$	0.25
$\delta_\parallel$	1.35
$\delta_\perp$	1.43

where $|H_0|$, $|H_+|$ and $|H_-|$ are the magnitudes of the longitudinal polarisation and, right-handed and left-handed helicities respectively, and δ_0, δ_+ and δ_- are the corresponding phases. The polarisation amplitudes in the transversity basis, A_0, $A_\parallel$ and $A_\perp$ can be determined using the relations,

$$\begin{aligned} A_0 &= H_0, \\ A_\parallel &= \frac{1}{\sqrt{2}}(H_+ + H_-), \\ A_\perp &= \frac{1}{\sqrt{2}}(H_+ - H_-). \end{aligned} \tag{4.19}$$

In Table 4.9 the values of A_0, $A_\parallel$ and $A_\perp$ are shown, and those of $f_L = |A_0|^2$, $f_\parallel = |A_\parallel|^2$ and $f_\perp = |A_\perp|^2$.

The acceptance function can be determined from,

$$\epsilon(\cos\theta_1, \cos\theta_2) = \frac{F'(\cos\theta_1, \cos\theta_2)}{F(\cos\theta_1, \cos\theta_2)}, \tag{4.20}$$

where $F(\cos\theta_1, \cos\theta_2)$ and $F'(\cos\theta_1, \cos\theta_2)$ are the angular distributions at the generator level, and after reconstruction and selection, respectively. The φ angle is not present in the relation since the φ acceptance is found to be uniform. The acceptance in $\cos\theta_1$ is also found to be constant, as shown in Fig. 4.16. On the other hand, the acceptance in $\cos\theta_2$ is described by a fourth order polynomial. The result from the fit is shown in Fig. 4.16 and is taken to describe the acceptance function in the likelihood of the angular analysis.

Several corrections to the acceptance are found to be needed due to differences in the transverse momentum between the data and the simulation and to the effect of the trigger categories. In Fig. 4.17 the acceptance reweighted taking into account these effects and the acceptance before the reweighting are shown.

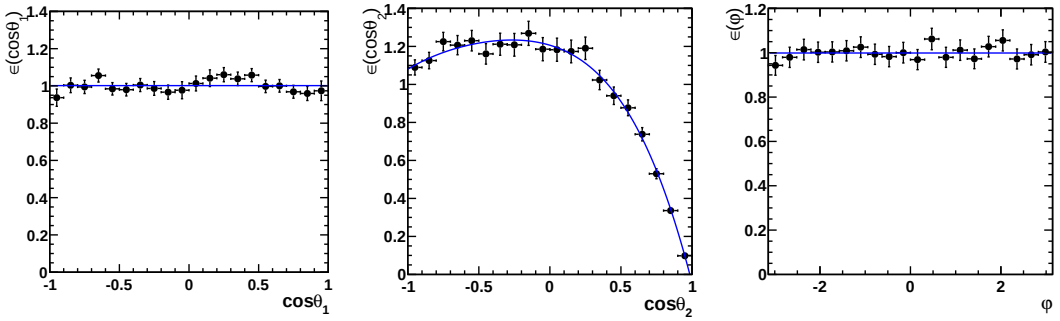

Figure 4.16: Acceptance function for $\cos\theta_1$ (left), $\cos\theta_2$ (center) and φ (right). The acceptance as a function of φ and $\cos\theta_1$ is compatible with being a flat distribution.

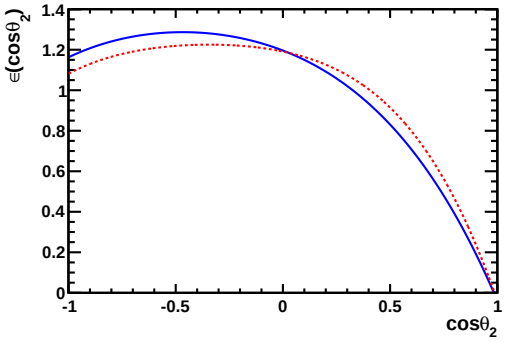

Figure 4.17: Comparison of the acceptance functions in $\cos\theta_2$ before (red dashed line) and after (blue line) the weighting of the Monte Carlo.

4.8.1.1 Correction to the acceptance due to the pion p_T

In Fig. 4.18 it is shown the ratio between data and Monte Carlo in function of the pion transverse momentum p_T for the $B^0 \to K^+K^-K^+\pi^-$ and $\bar{B}^0 \to K^+K^-K^-\pi^+$. Then, a straight line is used to fit the distributions. The results from the two fits are used to weight the Monte Carlo and re-calculate the angular acceptance for the B^0 and $\bar{B}^0$ separately.

4.8.1.2 Acceptance dependence on the TIS and TOS triggers

The acceptance response depends very much on the trigger category, in particular on whether the event is accepted by the TOS (Trigger On Signal) or the TIS (Trigger Independent of Signal) categories. For this study the data is divided in three categories: TIS and not TOS, TOS and not TIS, and TIS and TOS. Then, the Monte Carlo is weighted according to the ratios observed in the data.

In Fig. 4.19 the acceptance function, calculated by Monte Carlo, is shown for TIS (left) and TOS (right), showing the big differences between them. For $\cos\theta_1$ and φ the acceptance is uniform regardless of the TIS or TOS nature of the trigger.

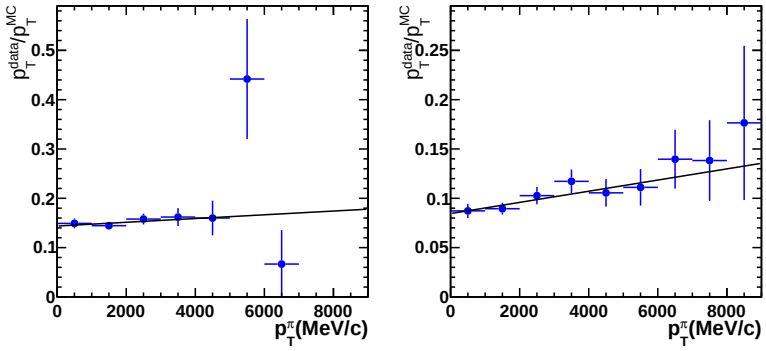

Figure 4.18: Data over Monte Carlo ratio in function of the pion transverse momentum for B^0 (left) and $\overline{B}^0$ (right). The ratio is fitted with a straight line and the function is applied as a weight to the Monte Carlo.

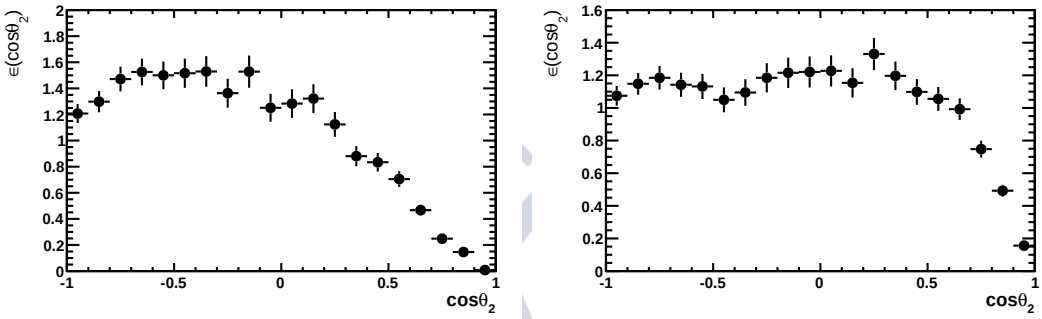

Figure 4.19: Dependence of the acceptance function with $\cos\theta_2$ for the TIS (left) and TOS (right) triggers.

4.8.2 f_L determination

The data in a 2σ window around the B_s^0 mass ($\pm 30\,\text{MeV}/c^2$) is fitted to the angular distribution given by Eq. 4.16, after proper parametrisation of the observed backgrounds. The amount of events in a $\pm 2\sigma$ window is shown in Table 4.8.

To study the combinatorial background, the geometrical likelihood cut is removed, and the data in the four-body invariant mass $M(KKK\pi)$ in the range $[5450, 5840]\,\text{MeV}/c^2$ is fitted using a non-correlated model,

$$F(\cos\theta_1, \cos\theta_2, \varphi) = F_{\theta_1}(\cos\theta_1) F_{\theta_2}(\cos\theta_2) F_{\varphi}(\varphi), \tag{4.21}$$

where F are second-order polynomials describing the angular distribution. The results of the fit are shown in Fig. 4.20. This distribution is used to describe the amount of background under the B_s^0 signal, fixing the parameters to those obtained from the fit to the sidebands. There is yet another contamination under the B_s^0 signal, corresponding to the B^0 events decaying to ϕK^{*0}. The polarisation for the B^0 is taken from Ref. [72] and is fixed in the minimisation.

The likelihood used is the following,

$$\begin{aligned}\mathcal{L} = &(1 - \alpha_d - \alpha_b)\epsilon_{\theta_1}(\cos\theta_1)\epsilon_{\theta_2}(\cos\theta_2) I(\cos\theta_1, \cos\theta_2, \varphi) \\ &+ \alpha_d \epsilon_{\theta_1}(\cos\theta_1)\epsilon_{\theta_2}(\cos\theta_2) I_d(\cos\theta_1, \cos\theta_2, \varphi) + \alpha_b I_b(\cos\theta_1, \cos\theta_2, \varphi),\end{aligned} \tag{4.22}$$

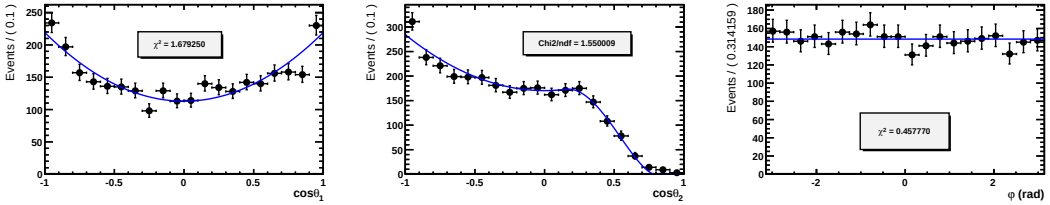

Figure 4.20: Angular distributions of the combinatorial background.

Table 4.10: Fit results. There are three parameters, namely the longitudinal polarisation f_L, the parallel polarisation $f_{\|}$ and the relative phase between the longitudinal and parallel waves $\delta_{\|}$.

Parameter	Result
f_L	0.46 ± 0.11
$f_{\|}$	0.27 ± 0.10
$\delta_{\|}$	2.38 ± 0.48

where $I(\cos\theta_1, \cos\theta_2, \varphi)$ and $I_d(\cos\theta_1, \cos\theta_2, \varphi)$ are the physical angular distributions given by Eq. 4.16 for the B_s^0 and B^0, respectively, and $I_b(\cos\theta_1, \cos\theta_2, \varphi)$ is the combinatorial background, described by Eq. 4.21. The coefficients α_d and α_b are the percentage of B^0 and combinatorial background in our sample, which are fixed in the fit minimisation to the values obtained in Table 4.8. The results are shown in Fig. 4.21 and Table 4.10.

4.8.3 Systematic errors of the angular analysis

4.8.3.1 Systematic error due to the S-wave

A toy Monte Carlo including the $K\pi$ and K^+K^- S-waves is used. The Monte Carlo is generated with a S-wave of the 11% and 5% for the $K\pi$ and K^+K^- respectively. Then, the events are fitted with the hypothesis of no S-wave. The differences between the generated values and the result of the fit without S-wave are taken as the systematic error. The results are,

$$\begin{aligned} \Delta f_L &= 0.07, \\ \Delta f_{\|} &= 0.03, \\ \Delta \delta_{\|} &= 0.23. \end{aligned} \tag{4.23}$$

4.8.3.2 Systematic error due to the GL

The angular fit shown previously is repeated after removing the GL cut and introducing the rectangular cuts shown in Table 4.2. The results from this fit provide a systematic effect due to the utilisation of the GL. Those systematic errors are,

$$\begin{aligned} \Delta f_L &= 0.02, \\ \Delta f_{\|} &= 0.04, \\ \Delta \delta_{\|} &= 0.17. \end{aligned} \tag{4.24}$$

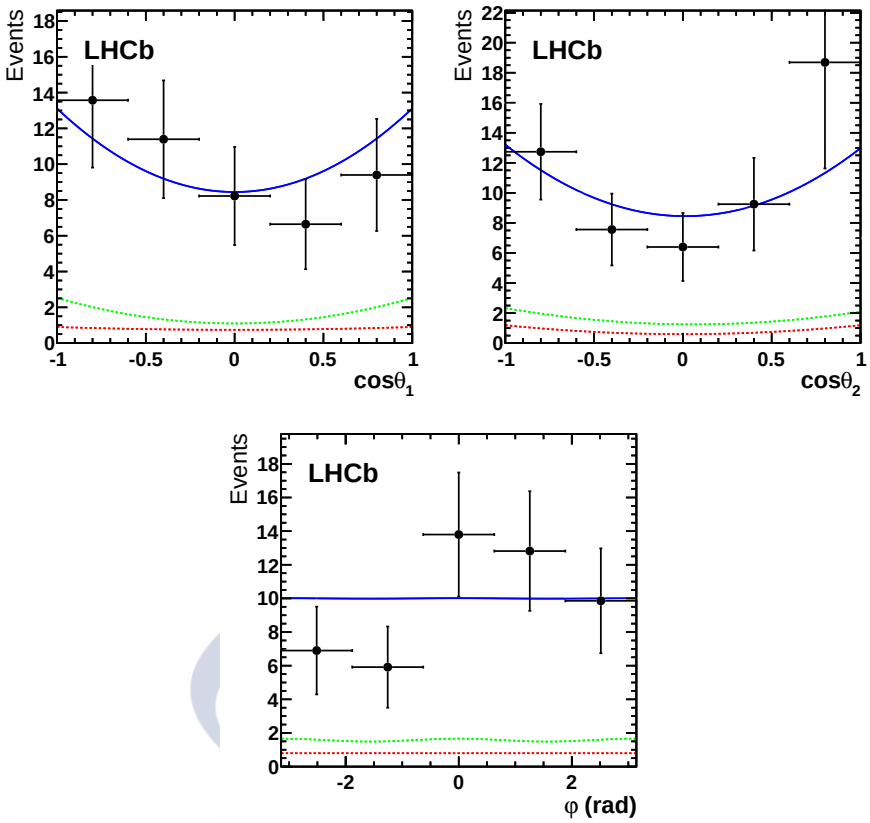

Figure 4.21: Angular distribution for the $B_s^0 \to \phi \overline{K}^{*0}$ in $\cos\theta_1$ (top left), $\cos\theta_2$ (top right) and φ (bottom). The red dashed line corresponds to the combinatorial background under the B_s^0 signal, and the green line is the $B^0 \to \phi K^{*0}$ signal in the B_s^0 region.

4.8.3.3 Systematic error due to the angular acceptance

In Chapter 4.8.1, the angular acceptance is calculated using the Monte Carlo. In Fig. 4.17, the acceptance before and after introducing the weights in the pion p_T and ratio between TIS and TOS is shown. The angular fit is performed with both acceptances, taken the weighted one as reference, and the differences found in the fit parameters are taken as the systematic error due to the angular acceptance,

$$\begin{aligned} \Delta f_L &= 0.007, \\ \Delta f_{\parallel} &= 0.005, \\ \Delta \delta_{\parallel} &= 0.000. \end{aligned} \tag{4.25}$$

4.8.3.4 Systematic error due to the combinatorial background

The angular distribution of the combinatorial background, taken from the sidebands is modified in order to calculate the systematic error due to the knowledge of its angular distribution. The distributions in $\cos\theta_{1,2}$ and φ are taken as flat, before passing through the detector acceptance. The differences in the fit results respect to the results using the

Table 4.11: Summary of systematic errors in the angular analysis.

Effect	Δf_L	$\Delta f_{\parallel}$	$\Delta \delta_{\parallel}$
S-wave	0.07	0.03	0.23
GL	0.02	0.04	0.17
Acceptance	0.007	0.005	0.000
Combinatorial Background	0.02	0.01	0.01
Total	0.08	0.05	0.29

model described in Eq. 4.21 are taken as the systematic errors. The results are,

$$\begin{aligned} \Delta f_L &= 0.02, \\ \Delta f_{\parallel} &= 0.01, \\ \Delta \delta_{\parallel} &= 0.01. \end{aligned} \tag{4.26}$$

4.8.3.5 Total systematic error

The total systematic error is obtained adding quadratically the errors calculated previously. A summary is shown in Table 4.11.

4.9 Systematic errors of the branching ratio

4.9.1 Systematic error due to the four-body spectra fit model

In Chapter 4.5, three methods in the fitting procedure are compared. In the first method the combinatorial background is fitted with an exponential function whose slope is left free. In the second one, the cut in the GL is relaxed, the combinatorial background is fitted with an exponential and then, the value of its slope is fixed after activating again the cut in the GL. The third method assumes a linear parametrisation for the combinatorial background. Both the second and third methods give 1.7 additional signal events, see Table 4.6. This difference in the number of events is taken as the main systematic error in the determination of the $B_s^0 \to \phi \overline{K}^{*0}$ signal.

The variation of 1.7 events in the signal changes the branching ratio in,

$$\Delta \mathcal{B}(B_s^0 \to \phi \overline{K}^{*0}) = 0.062 \times 10^{-6}, \tag{4.27}$$

which is identified as the systematic error associated with the fit model in the branching ratio measurement.

4.9.2 Systematic error due to the longitudinal polarisation

Since the $B_s^0 \to \phi \overline{K}^{*0}$ and the $B^0 \to \phi K^{*0}$ have different polarisations, their angular distributions differ. The different polarisations seen in both channels have associated different overall efficiencies. This effect can be corrected. For that, the relation between

the overall efficiency and f_L is needed, which can be calculated as,

$$\epsilon(f_L) = \int_{-1}^{1} \epsilon(\cos\theta_1, \cos\theta_2) \left[f_L \cos^2\theta_1 \cos^2\theta_2 + \frac{1}{4}(1 - f_L) \sin^2\theta_1 \sin^2\theta_2 \right] \mathrm{d}\cos\theta_1 \mathrm{d}\cos\theta_2. \tag{4.28}$$

The odd terms in φ vanish because of the symmetry of the physical distribution, and $\epsilon(\cos\theta_1, \cos\theta_2)$ is given by Eq. 4.20. So the correction factor is given by,

$$\epsilon(f_L) \propto 0.5277 - 0.1505 f_L, \tag{4.29}$$

$$\lambda_{f_L} = \frac{\epsilon_{B^0}}{\epsilon_{B_s^0}} = \frac{0.5277 - 0.1505 f_L^{B^0}}{0.5277 - 0.1505 f_L^{B_s^0}} = \frac{1 - 0.2852 f_L^{B^0}}{1 - 0.2852 f_L^{B_s^0}}. \tag{4.30}$$

The f_L for the $B^0 \to \phi K^{*0}$ is $f_L^{B^0} = 0.494 \pm 0.034 \pm 0.013$ [72], and the f_L measured for the $B_s^0 \to \phi \overline{K}^{*0}$ is $f_L^{B_s^0} = 0.46 \pm 0.11$. With this, the correction obtained is

$$\lambda_{f_L} = 0.989 \pm 0.037, \tag{4.31}$$

which is applied to the branching ratio measurement.

The statistical error in the measurement of λ_{f_L} is used as a systematic error to the branching ratio, with a value,

$$\Delta\mathcal{B}(B_s^0 \to \phi \overline{K}^{*0}) = 0.041 \times 10^{-6}. \tag{4.32}$$

4.9.3 Systematic error due to the purity

In Chapter 4.6 a purity for the $B^0 \to \phi K^{*0}$ of 0.84 ± 0.02 is found, which means an impurity of 0.16 ± 0.02. A systematic error is proposed due to the purity for the $B_s^0 \to \phi \overline{K}^{*0}$ equal to the 50% of the impurity in the $B^0 \to \phi K^{*0}$. This means a variation of 8% in the purity resulting in a systematic error contribution of the branching ratio,

$$\Delta\mathcal{B}(B_s^0 \to \phi \overline{K}^{*0}) = 0.087 \times 10^{-6}. \tag{4.33}$$

4.9.4 Systematic error due to the efficiency

The method for measuring the $\mathcal{B}(B_s^0 \to \phi \overline{K}^{*0})$ is based on the use of the $B^0 \to \phi K^{*0}$ as reference channel. This channel passes the same stripping line as the $B_s^0 \to \phi \overline{K}^{*0}$, and the only difference is given by the difference in the B^0 and B_s^0 masses ($\sim 80\,\mathrm{MeV}/c^2$). So, the correction is expected to be very small.

The detection efficiency is factorised into ϵ^{sel} (selection efficiency), and $\epsilon^{trig/sel}$ (trigger efficiency on selected events). The selection efficiency is computed as product of two factors: on one hand, the generation efficiency ϵ^{gen} due to the selection cuts applied to the simulation generator and the LHCb angular coverage acceptance, on the other hand, $\epsilon^{sel/gen}$, the product of the track reconstruction efficiency and the specific efficiency caused by the selection criteria in each case. Note that the measurement is only sensitive to the efficiency ratios between the signal and the control channels.

The generator level efficiency is found by generating simulated signal events and then counting how many of them have all their final state particles falling within the LHCb geometric acceptance. The results are given in Table 4.12.

Table 4.12: Generation efficiencies for the $B_s^0 \to \phi\overline{K}^{*0}$ and $B^0 \to \phi K^{*0}$ decays.

	%
$\epsilon^{gen}_{B_s^0 \to \phi\overline{K}^{*0}}$	17.51 ± 0.06
$\epsilon^{gen}_{B^0 \to \phi K^{*0}}$	17.54 ± 0.06

Table 4.13: Selection efficiencies for the $B_s^0 \to \phi\overline{K}^{*0}$ and $B^0 \to \phi K^{*0}$ decays calculated using simulation.

	%
$\epsilon^{sel}_{B_s^0 \to \phi\overline{K}^{*0}}$	2.563 ± 0.025
$\epsilon^{sel}_{B^0 \to \phi K^{*0}}$	2.568 ± 0.018

Table 4.13 shows the values for ϵ^{sel} obtained for the signal and normalisation channels using simulated samples. This efficiency accounts for the reconstruction and selection cuts applied to the sample.

The calculation of the trigger efficiencies for the signal and normalisation channels has been determined using simulation. The results are shown in Table 4.14.

The branching ratio has to be corrected by the ratio,

$$\lambda_{Eff} = \frac{\epsilon^{gen}_{B^0 \to \phi K^{*0}}}{\epsilon^{gen}_{B_s^0 \to \phi\overline{K}^{*0}}} \times \frac{\epsilon^{sel}_{B^0 \to \phi K^{*0}}}{\epsilon^{sel}_{B_s^0 \to \phi\overline{K}^{*0}}} \times \frac{\epsilon^{trig}_{B^0 \to \phi K^{*0}}}{\epsilon^{trig}_{B_s^0 \to \phi\overline{K}^{*0}}}, \tag{4.34}$$

which is found to be,

$$\lambda_{Eff} = \frac{17.54}{17.51} \times \frac{2.568}{2.563} \times \frac{40.312}{40.273} = 1.005. \tag{4.35}$$

The deviation from the unity is taken as a systematic error, so,

$$\Delta\mathcal{B}(B_s^0 \to \phi\overline{K}^{*0}) = 0.005 \times 10^{-6}. \tag{4.36}$$

4.9.5 Systematic error due to the PID

Since both $B_s^0 \to \phi\overline{K}^{*0}$ and $B^0 \to \phi K^{*0}$ channels pass the same stripping line, and the masses are very close ($\sim 80\,\mathrm{MeV}/c^2$), the only difference between the decay products is a slightly different transverse momentum p_T. Some changes in the $\mathrm{DLL}_{K\pi}(K^\pm)$ particle ID cut from 0 to 2 gives no significant changes in the N_s/N_d ratio, and consequently in the branching ratio. For this reason, the systematic error due to the cut in the particle ID can be considered negligible.

4.9.6 Summary on systematic errors

In Table 4.15, a summary of the sources of systematic error and the associated systematic uncertainties are shown. Finally, in the last row of the table their sum in quadrature is shown, which is considered as the total systematic error.

Table 4.14: Trigger efficiencies for $B_s^0 \to \phi \overline{K}^{*0}$ and $B^0 \to \phi K^{*0}$ decays determined using simulation.

	%
$\epsilon^{trig}_{B_s^0 \to \phi K^{*0}}$	40.273 ± 0.882
$\epsilon^{trig}_{B^0 \to \phi K^{*0}}$	40.312 ± 0.645

Table 4.15: Source of systematic errors in the branching ratio measurement. The total item is the squared sum of the individual systematic errors.

Source	Error in $\mathcal{B}$ (10^{-6})
Fit model	0.062
f_L	0.041
Purity	0.087
Efficiency	0.005
PID	0.0
Total	0.11

4.10 Significance tests

Some checks have been made in order to test the strength of the signal. One can test the strength of this signal with different methods. In particular the Feldman-Cousins test [181] is a good choice in the case of small or negligible uncertainties in the components of the sample. If the uncertainty of the total background (8.19 ± 1.37) is considered to fulfil such a requirement, it is obtained an interval $(13.92, 36.92)$ with a confidence level of 95% for the signal. Thus, with 95% probability more than 13 signal events have been observed. A better approximation is using the Rolke test [182]. This test computes confidence levels considering an uncertainty in the background. In particular, if a Gaussian behaviour is chosen for this uncertainty, an interval of $(14.07, 36.67)$ is obtained for the 95% confidence level of the signal.

4.11 Summary

Data taken in 2011 at an energy $\sqrt{s} = 7\,\text{TeV}$ by the LHCb experiment corresponding to an integrated luminosity of $1\,\text{fb}^{-1}$ are studied to report the first observation of the $B_s^0 \to \phi \overline{K}^{*0}$ decay.

The selection and the fit model are described in Chapter 4.5. The result of the four-body invariant mass fit is shown in Table 4.6 and in Fig. 4.10. A total of 29.9 ± 6.4 candidates of $B_s^0 \to (K^+K^-)(K^\pm\pi^\mp)$ are found within mass windows $746\,\text{MeV}/c^2 < M(K^\pm\pi^\mp) < 1046\,\text{MeV}/c^2$ and $1012.5\,\text{MeV}/c^2 < M(K^+K^-) < 1026.5\,\text{MeV}/c^2$, giving a significance of 6.5σ. The amount of resonant contributions present in the KK and $K\pi$ final state systems is obtained in Chapter 4.6. Within this sample, $(84 \pm 2)\%$ of the candidates correspond to resonant ϕ and K^{*0} decays. The statistical tests in a 2σ window around the B_s^0 peak show that with 95% confidence level the sample contains more than 14 signal events confirming the discovery.

The branching ratio $\mathcal{B}(B_s^0 \to \phi\overline{K}^{*0})$ is determined in Chapter 4.7 and the systematic uncertainties in Chapter 4.9. The $B_s^0 \to \phi\overline{K}^{*0}$ decay is used as the normalisation channel. The final result is,

$$\mathcal{B}(B_s^0 \to \phi\overline{K}^{*0}) = \left(1.09 \pm 0.24\,(\text{stat}) \pm 0.11\,(\text{syst}) \pm 0.08\left(\frac{f_d}{f_s}\right)\right) \times 10^{-6},$$

where the contribution to the uncertainty due to the f_d/f_s ratio is displayed separately. The result is larger than the predicted values, $(0.4^{+0.5}_{-0.3}) \times 10^{-6}$ [64] and $(0.65^{+0.33}_{-0.23}) \times 10^{-6}$ [171], although compatible within 1σ.

With this signal, an angular analysis is performed in Chapter 4.8, finding the following polarisations,

$$\begin{aligned} f_L &= 0.46 \pm 0.11\,(\text{stat}) \pm 0.08\,(\text{syst}), \\ f_\parallel &= 0.27 \pm 0.10\,(\text{stat}) \pm 0.05\,(\text{syst}), \\ \delta_\parallel &= 2.38 \pm 0.48\,(\text{stat}) \pm 0.29\,(\text{syst}). \end{aligned}$$

The result of the longitudinal polarisation is smaller than the prediction of perturbative QCD, $f_L = 0.712^{+0.042}_{-0.048}$ [171].

USC UNIVERSIDADE DE SANTIAGO DE COMPOSTELA

5

Study of the decays $B^0 \to K^{*0}\overline{K}^{*0}$ and $B_s^0 \to K^{*0}\overline{K}^{*0}$

In this Chapter the polarisation fractions of the $B^0 \to K^{*0}\overline{K}^{*0}$ and $B_s^0 \to K^{*0}\overline{K}^{*0}$ decays are reported and the ratio of branching ratios between the two modes is presented.

5.1 Introduction

The BaBar collaboration reported the discovery of the $B^0 \to K^{*0}\overline{K}^{*0}$ channel with 6σ significance and a measurement of its branching ratio $\mathcal{B}(B^0 \to K^{*0}\overline{K}^{*0}) = (1.28^{+0.35}_{-0.30} \pm 0.11) \times 10^{-6}$ [183]. This is in tension with the results of the Belle collaboration that published an upper limit of $\mathcal{B}(B^0 \to K^{*0}\overline{K}^{*0}) < 0.8 \times 10^{-6}$ at the 90% confidence level [184]. The BaBar publication also reported a measurement of the longitudinal polarisation $f_L = 0.80^{+0.12}_{-0.13}$ [183], which is large compared to those from $B^0 \to \phi K^{*0}$ ($f_L = 0.497 \pm 0.019$ [73]), $B_s^0 \to \phi\phi$ ($f_L = 0.364 \pm 0.012$ [75]) and $B_s^0 \to K^{*0}\overline{K}^{*0}$ ($f_L = 0.201 \pm 0.057$ [74]). The difference with this last channel is specially intriguing, since the diagrams describing both decays are the same exchanging the s-quarks and the d-quarks.

In the framework of QCD factorisation, the branching ratio of the $B^0 \to K^{*0}\overline{K}^{*0}$ decay is predicted to be $(0.6^{+0.1+0.3}_{-0.1-0.2}) \times 10^{-6}$, and the longitudinal polarisation fraction, $f_L = 0.69 \pm 0.01^{+0.16}_{-0.20}$ [64]. In Ref. [55], a prediction for the ratio of the longitudinal branching ratios of the $B_s^0 \to K^{*0}\overline{K}^{*0}$ and $B^0 \to K^{*0}\overline{K}^{*0}$ decays, $\mathcal{B}^{\text{long}}(B_s^0 \to K^{*0}\overline{K}^{*0})/\mathcal{B}^{\text{long}}(B^0 \to K^{*0}\overline{K}^{*0})$, is included, with a value 16.4 ± 5.2.

The measurement of the polarisation fractions is presented, with an untagged and time-integrated amplitude analysis of the $B^0 \to K^+\pi^-K^-\pi^+$ decay in a mass window of $\pm 150\,\text{MeV}/c^2$ around the K^{*0} mass. In addition to the three helicity angles, the two $K^\pm\pi^\mp$ invariant masses are also included. Following the $B_s^0 \to K^{*0}\overline{K}^{*0}$ decay analysis [74], only the P- and S-wave contributions are considered. Special attention is paid to the measurement of the longitudinal polarisation fraction, trying to confirm the high value obtained by BaBar. Additionally, an update of the $B_s^0 \to K^{*0}\overline{K}^{*0}$ untagged time-integrated amplitude analysis shown in Ref. [74] is performed with the 2011 and 2012 data, and a direct comparison between the $B^0 \to K^{*0}\overline{K}^{*0}$ and the $B_s^0 \to K^{*0}\overline{K}^{*0}$ decays is presented. Finally, the BR of the $B^0 \to K^{*0}\overline{K}^{*0}$ decay is measured with respect to the $B_s^0 \to K^{*0}\overline{K}^{*0}$ decay.

Table 5.1: Simulated decay modes employed with the event type and the number of generated events.

Decay mode	Event type	Number of events			
		MC2011		MC2012	
		MagDown	MagUp	MagDown	MagUp
$B^0 \to K^{*0}\overline{K}^{*0}$	11104003	1026627	1018418	2036193	2039791
$B_s^0 \to K^{*0}\overline{K}^{*0}$	13104002	1004743	1014489	2013957	2020489
$B^0 \to \phi K^{*0}$	11104021	1017500	1018999	2007492	2020493
$B^0 \to \rho K^{*0}$	11104041	1021997	1027000	2010995	2010491
$\Lambda_b^0 \to K^{*0} p\pi$	15104030	1056085	1003189	2044496	2003144

5.2 Dataset, Monte Carlo, trigger and stripping

The data sample used to perform the analysis corresponds to $1\,\text{fb}^{-1}$ of pp collisions taken by LHCb during 2011 with a center-of-mass energy of $\sqrt{s} = 7\,\text{TeV}$ and $2\,\text{fb}^{-1}$ during 2012 with $\sqrt{s} = 8\,\text{TeV}$.

The Monte Carlo samples used for the analysis correspond to the Sim08 production, generated at a center-of-mass energy of $\sqrt{s} = 7\,\text{TeV}$ for MC2011 and $\sqrt{s} = 8\,\text{TeV}$ for MC2012. The decay modes used in the analysis are specified in Table 5.1, with the event type and the number of generated events for each of them.

5.2.1 Stripping

Both data and Monte Carlo samples correspond to the LHCb `Reco14-Stripping20` campaign. The candidates have to pass the `StrippingBetaSBs2KstKstNominalLine`. This line is dedicated to select four particles, a $K^+\pi^-$ pair and a $K^-\pi^+$ pair, both in a window around the known K^{*0} mass, coming from the same common vertex. The cuts applied by the stripping line are explained in the next paragraphs and summarised in Table 5.2.

All the tracks are required to have transverse momentum (p_T) greater than $500\,\text{MeV}/c$. To exclude particles coming from the interaction point, the impact parameter χ^2 of all tracks with respect to the primary vertex (χ^2_IP) has to be larger than 9. Ghost tracks are removed setting the Ghost Probability to be less than 0.8. To separate between kaons and pions a cut in the difference of the log-likelihoods of the K and π hypothesis ($\text{DLL}_{K\pi}$) is applied. For the kaons, the $\text{DLL}_{K\pi}$ has to be greater than -5 and for pions it has to be less than 10.

To select the intermediate resonances, a window of $\pm 150\,\text{MeV}/c^2$ around the nominal K^{*0} mass for the $K^+\pi^-$ and $K^-\pi^+$ pairs reconstructed mass is applied. The K^{*0} and $\overline{K}^{*0}$ candidates must have a transverse momentum greater than $900\,\text{MeV}/c$ and the quality of the vertex is ensured by requiring that the vertex χ^2 over the number of degrees of freedom (K^{*0} vertex χ^2/ndf) is less than 9.

For the B candidate, a window of $500\,\text{MeV}/c^2$ around the B_s^0 mass is selected. The distance of closest approach between the K^{*0} and the $\overline{K}^{*0}$ trajectories (DOCA) has to be less than 0.3 mm and the vertex χ^2/ndf has to be less than 15, ensuring with these two cuts that the four particles originate from a common vertex identified with good quality. To guarantee that the B^0 comes from the interaction point, the cosine of the

Table 5.2: Set of cuts applied by the stripping line. The variables are defined in the text.

Variable	Stripping cut
K/π p_{T}	> 500 MeV/c
K/π χ^2_{IP}	> 9
K/π Ghost Prob	< 0.8
K $\mathrm{DLL}_{K\pi}$	> -5
π $\mathrm{DLL}_{K\pi}$	< 10
K^{*0} mass window	± 150 MeV/c^2
K^{*0} p_{T}	> 900 MeV/c
K^{*0} vertex χ^2/ndf	< 9
B mass window	± 500 MeV/c^2
B min χ^2_{IP}	< 25
B DOCA	< 0.3 mm
B DIRA	> 0.99
B vertex χ^2/ndf	< 15

angle between the B momentum and the direction of flight from the primary vertex to the decay vertex (DIRA) is required to be larger than 0.99 and the impact parameter χ^2 with respect to the primary vertex has to be less than 25.

The stripping cuts are also applied to the Monte Carlo samples shown previously, with the exception of the PID cuts. It is known that the Monte Carlo does not fully reproduce the distributions of the particle identification variables from data. Therefore, to estimate the efficiencies of the PID cuts, a data driven method, that is explained in Chapter 5.6.5, has to be used. To get the best performance of the method, the Monte Carlo samples are produced without including cuts in the PID variables.

5.2.2 Trigger

The trigger lines used are the standard choice for multibody hadronic decays. For the Level-0, the candidates have to pass either the `L0HadronDecision_TOS` or the `L0Global_TIS`. At HLT1, the line `Hlt1TrackAllL0Decision_TOS` is required and for HLT2, the candidates have to fire any of the 2-, 3- or 4-body topological trigger lines, `Hlt2Topo2BodyBBDTDecision_TOS`, `Hlt2Topo3BodyBBDTDecision_TOS` or `Hlt2Topo4BodyBBDTDecision_TOS`. The lines are summarised in Table 5.3. The efficiency of each trigger line is shown in Table 5.14 for $B^0 \to K^{*0}\overline{K}^{*0}$ simulated events.

Table 5.3: Trigger lines required at each step of the trigger.

Trigger level	Trigger lines
L0	`L0HadronDecision_TOS` or `L0Global_TIS`
HLT1	`Hlt1TrackAllL0_TOS`
HLT2	`Hlt2Topo2BodyBBDTDecision_TOS` or `Hlt2Topo3BodyBBDTDecision_TOS` or `Hlt2Topo4BodyBBDTDecision_TOS`

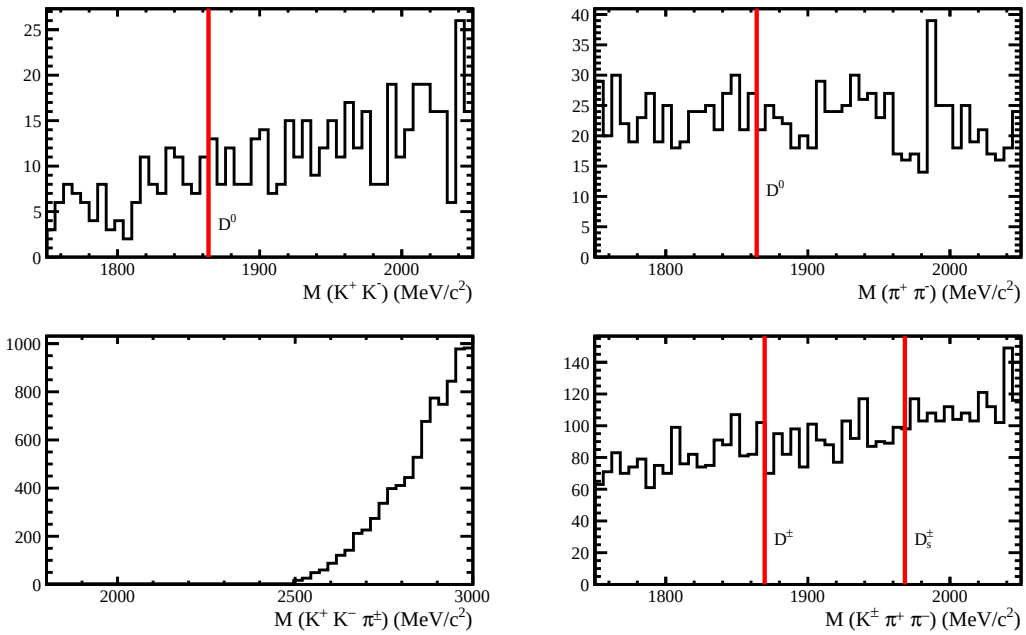

Figure 5.1: Different reconstructed invariant masses from data after the trigger and stripping selection. K^+K^- (top left) and $\pi^+\pi^-$ (top right) invariant masses in a window of $\pm 50\,\mathrm{MeV}/c^2$ around the B^0 mass. $K^+K^-\pi^\pm$ (bottom left) and $K^\pm\pi^+\pi^-$ (bottom right) invariant masses.

5.3 Background studies

After the stripping and trigger cuts, some studies are carried out to try to identify the main sources of background that can pollute the signal.

5.3.1 Peaking backgrounds with charm

Events of the type $B \to K^+\pi^-K^-\pi^+$ correctly reconstructed but decaying via an intermediate charm resonance may appear in the sample. Charm resonances decaying into $K\pi$ pairs are excluded by the cut in the mass window of the K^{*0}, but some pollution could exist from K^+K^- or $\pi^+\pi^-$ combinations. Events from the $B^0 \to D^0(K^+K^-)\pi^+\pi^-$ ($\mathcal{B} \sim 3 \times 10^{-6}$) and $B^0 \to D^0(\pi^+\pi^-)K^+K^-$ ($\mathcal{B} \sim 6 \times 10^{-8}$) decays are investigated. Nothing is found as can be seen in the top row of Fig. 5.1. Resonances in three body combinations $K^+K^-\pi^\pm$ and $K^\pm\pi^+\pi^-$ have also been searched for. In the former case, the three body invariant mass in the data sample is above all known charm resonances (bottom left in Fig. 5.1). In the latter, events coming from the $B \to D^\mp K^\pm$ and $B \to D_s^\mp K^\pm$ decays could appear with $\mathcal{B} \sim 10^{-7}$, or from the $B_s^0 \to D_s^\mp K^\pm$ decay with $\mathcal{B} \sim 10^{-6}$. There is no evidence for them in data (bottom right in Fig. 5.1).

Moreover, three body combinations with one K-π misidentification have also been reconstructed. Among all the possible combinations, the one that has the largest branching ratio corresponds to the $B^0 \to D^-(2\pi^-K^+)\pi^+$ decay ($\mathcal{B} = 2.45 \times 10^{-4}$), where a π is misidentified as a K. To search for this background, the K in the decay with the highest probability of being mistaken as a π, i.e. with the smallest $\mathrm{DLL}_{K\pi}$, is selected, and its

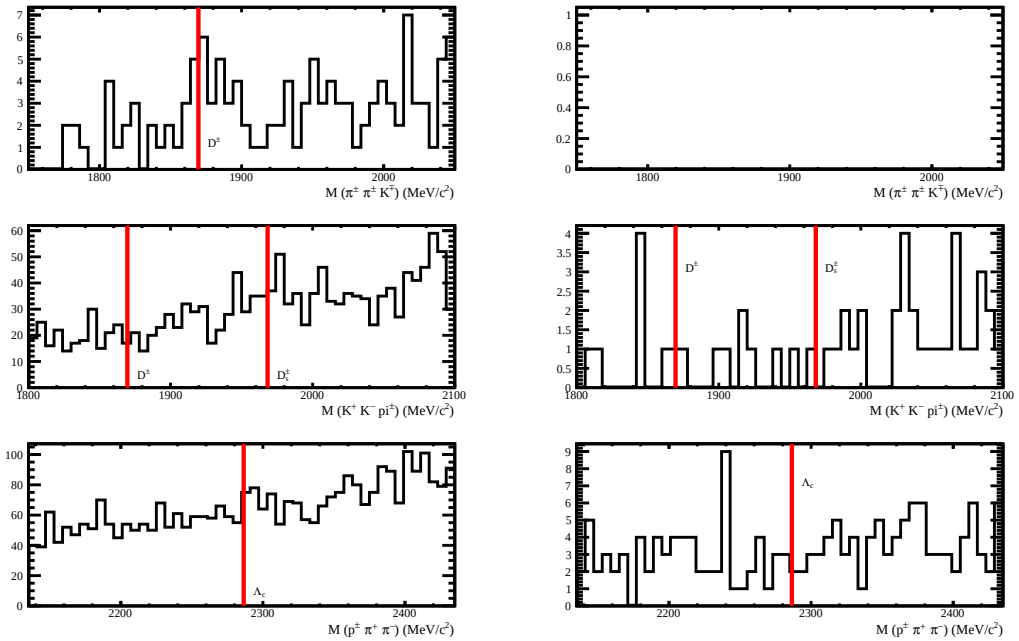

Figure 5.2: Different reconstructed invariant masses from data with one misidentified particle. Left: After the trigger and stripping selection. Right: With the final selection applied (Chapter 5.5). Top: $2\pi^{\pm}K^{\mp}$ invariant mass in which a π is misidentified as a K. Middle: $K^+K^-\pi^{\pm}$ invariant mass in which a K is misidentified as a π. Bottom: $p\pi^+\pi^-$ invariant mass in which the p is misidentified as a K.

mass is switched into the π mass. It is then combined with the pion of the same sign in the decay and with the remaining kaon. In the top row of Fig. 5.2 this reconstructed invariant mass is shown. Even though it seems that a peak exists in the distribution of the data sample after the trigger and the stripping selections, no events remain when the full selection is applied (Chapter 5.5), mainly due to the PID cuts that are used. Another possible combination is the $K^+K^-\pi^+$, in which a K is misidentified as a π. There are several decays that can contribute to this final state, $B_s^0 \to D_s^{\pm}K^{\mp}$ ($\mathcal{B} \sim 10^{-5}$), $B^0 \to D^-K^+$ and $B^0 \to D_s^-K^+$ ($\mathcal{B} \sim 10^{-6}$). In this case, the π with more probabilities of being a K, i.e. with the largest $\mathrm{DLL}_{K\pi}$, is chosen and its mass is switched into the K mass. As in the previous case, these peaks are suppressed after applying the full selection (middle row in Fig. 5.2).

The search for three body combinations with a proton has also been performed trying to identify contributions from decays with a Λ_c^+ baryon. The kaon with the highest probability of being mistaken as a proton, that is to say the kaon with the highest value of DLL_{pK}, is chosen and the proton mass hypothesis is imposed. For the $pK^-\pi^+$ case, the reconstructed invariant mass is above the Λ_c^+ mass, and for the $p\pi^+\pi^-$ combination (bottom row in Fig. 5.2), the possible peak that may exist after the trigger and the stripping vanishes after applying the final selection.

As it has been shown, the potential peaking backgrounds with charm that can pollute the signal are negligible when the final selection is imposed. Because of this, no explicit vetoes are applied.

5.3.2 Reflections or cross-feed backgrounds

These correspond to backgrounds in which one of the final particle candidates, a K or a π, is a misidentification of another particle. Since these events appear in the $K^+\pi^-K^-\pi^+$ invariant mass, which is used to discriminate between signal and background, it is needed to keep them under control to obtain a pure signal sample. The location of these backgrounds in the four-body invariant mass spectrum is obtained with MC events in Fig. 5.3. There are three main cases which have to be taken into account in the analysis:

- $B^0 \to K^+K^-K^{*0}(K^+\pi^-)$ decays ($B^0 \to \phi K^{*0}$ and non resonant K^+K^- pairs), in which one of the kaons is misidentified as a π. As shown in Fig. 5.3, this background appears in the low mass sideband. To reduce and subtract its contribution, cuts in the PID variables are used (Chapter 5.5.5) and the sWeights [185] are calculated when performing the four-body invariant mass fit.

- $B^0 \to \pi^+\pi^-K^{*0}(K^+\pi^-)$ decays (mainly $B^0 \to \rho^0 K^{*0}$), in which one of the pions is misidentified as a kaon. This decay is the most resilient, because it appears in the region between the $B^0 \to K^{*0}\overline{K}^{*0}$ and $B_s^0 \to K^{*0}\overline{K}^{*0}$ peaks and overlaps with them (Fig. 5.3). Therefore, its contribution cannot be precisely determined with the four-body invariant mass fit. As explained in Chapter 5.5.5, cuts in the PID variables are applied to reduce the yield. Afterwards, the expected number of events from this background is calculated using simulation and negative weights are applied subsequently in the four-body invariant mass fit to remove its contribution, as shown in Chapter 5.7.1.

- $\Lambda_b^0 \to p\pi K^{*0}(K^+\pi^-)$ decays, in which the p is misidentified as a K. In Fig. 5.3, it can be seen that this background pollutes the upper sideband of the four-body invariant mass. It has a long tail that overlaps with the B^0 peak. The expected yields of this decay are calculated from data, as explained in Chapter 5.7.2. Its contribution in the four-body invariant mass fit is then fixed to the values obtained, and the sWeight calculation is modified accordingly to deal with fixed yields in the fit [186].

5.3.3 Partially reconstructed and combinatorial backgrounds

The partially reconstructed background is composed of events coming from multibody b-hadron decays in which one of the particles is not reconstructed. The main contributions to this background are B^0 and B_s^0 decays in which π^0 or γ are produced. Because of the missing particle the measured four-body invariant mass of these events lies at the lower mass sideband of the four-body mass spectrum. As shown in Chapter 5.4.3, all the contributions to this background are parametrised together, and no special effort is put into separating them.

Candidates composed by charged tracks not originating from the same decay chain from the combinatorial background. To remove this background, a Multivariate Analysis is used, as shown in Chapter 5.5.3.

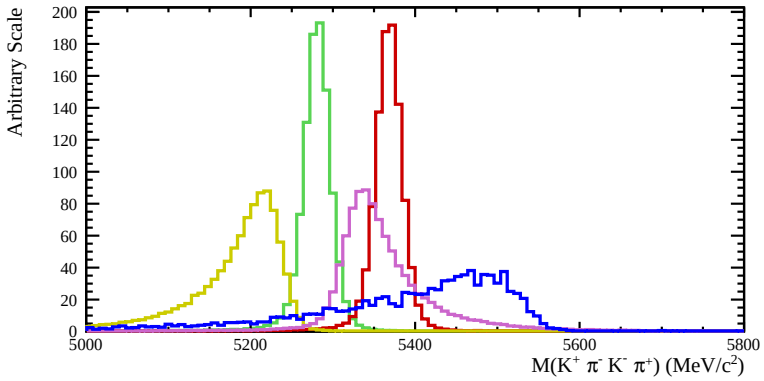

Figure 5.3: Distribution of the four-body invariant mass of simulated events from the main cross-feed backgrounds with the $K^+\pi^-K^-\pi^+$ hypothesis. In yellow, $B^0 \to \phi K^{*0}$ decays, in blue, decays from $\Lambda_b^0 \to K^{*0}p\pi$ and in pink, $B^0 \to \rho^0 K^{*0}$ events. For comparison $B_s^0 \to K^{*0}\overline{K}^{*0}$ decays are shown in red and decays from $B^0 \to K^{*0}\overline{K}^{*0}$ in green.

5.4 Four-body mass fit model

To discriminate between signal and background, the experimental four-body mass spectrum is fitted simultaneously for the 2011 and 2012 samples. The probability density functions (PDF) used to parametrise the different contributions entering into the fit are discussed in the next paragraphs.

5.4.1 Signal model

For the parametrisation of the lineshape of the $B^0 \to K^{*0}\overline{K}^{*0}$ decay, a double-sided Hypatia distribution [187] is chosen,

$$I(m,\mu,\sigma,\lambda,\zeta,\beta,a_1,a_2,n_1,n_2) \propto \begin{cases} \frac{A}{(B+m-\mu)^{n_1}} & \text{if } m-\mu < -a_1\sigma\,, \\ \frac{C}{(D+m-\mu)^{n_2}} & \text{if } m-\mu > a_2\sigma\,, \\ \left((m-\mu)^2+\delta^2\right)^{\frac{1}{2}\lambda-\frac{1}{4}} e^{\beta(m-\mu)} K_{\lambda-\frac{1}{2}}\left(\alpha\sqrt{(m-\mu)^2+\delta^2}\right) & \text{otherwise}\,, \end{cases} \tag{5.1}$$

where $K_\nu(z)$ is the modified Bessel function of the second kind, $\delta \equiv \sigma\sqrt{\frac{\zeta K_\lambda(\zeta)}{K_{\lambda+1}(\zeta)}}$, $\alpha \equiv \frac{1}{\sigma}\sqrt{\frac{\zeta K_{\lambda+1}(\zeta)}{K_\lambda(\zeta)}}$, and A, B, C, D are obtained by imposing continuity and differentiability. The core of the Hypatia models the resolution effects in which the per event variance is not constant, but rather an unknown quantity with certain prior probability. In addition, it allows to include extra (Crystal-Ball, CB [174]) tails in order to (phenomenologically) accommodate effects other than resolution.

In general it has been shown that ζ and β can be fixed to 0 [187]. The parameters λ, a_1 and n_1, a_2 and n_2 [1] are obtained from a fit of the $B^0 \to K^{*0}\overline{K}^{*0}$ truth matched Monte

[1] The parameter λ is one of the per-event variance density parameters $\rho(v) \propto v^{\lambda-1}e^{-b/v}$, whereas a_1

Carlo, sharing a common value between the 2011 and 2012 samples. The mean and the resolution are free to float in the data fit, with the mean fixed to have a common value in the 2011 and 2012 samples and the resolution left independent for both samples.

The $B_s^0 \to K^{*0}\overline{K}^{*0}$ signal is modeled with the same lineshape and parameters as the $B^0 \to K^{*0}\overline{K}^{*0}$, but with the mean value of the B_s^0 shifted by the difference of the masses given in Ref. [1], 87.13 MeV/c^2. Moreover, the resolution of the B_s^0 signal is constrained to the resolution of the B^0. The ratio of resolutions is given by the ratio of the Q-values between the modes.[1]

5.4.2 Reflections

As explained in Chapter 5.3.2, three different species of cross-feed backgrounds have to be taken into account when performing the four-body invariant mass fit. Below, the chosen parametrisation for each of them is described:

- $B^0 \to \rho^0 K^{*0}$: a double-sided Hypatia function is used to parametrise this background. The procedure is the same followed with the $B^0 \to K^{*0}\overline{K}^{*0}$ decay: ζ and β are fixed to 0, the mean, λ, a_1 and n_1, a_2 and n_2 are obtained from Monte Carlo, with the same value for 2011 and 2012, whereas the resolution is independent for both years. In this case, all the parameters obtained from Monte Carlo are subsequently fixed in the data fit, including the values of the mean and the resolution.

- $B^0 \to \phi K^{*0}$: a Crystal-Ball function plus a Gaussian distribution are used. All the parameters are obtained from Monte Carlo. The mean is shared between the CB and the Gaussian, and it is common for 2011 and 2012. The resolutions and the fractions of events in the CB and in the Gaussian are left independent for 2011 and 2012. The other parameters of the CB are common between years. In the four-body invariant mass data fit, all the parameters are fixed to the values obtained with Monte Carlo.

- $\Lambda_b^0 \to K^{*0} p\pi$: for the Λ_b^0 contamination, a single Crystal-Ball is used. All the parameters are obtained from Monte Carlo, with all of them common between the two years except the resolution, that can take different values for the 2011 and 2012 samples. Since the MC events that pass the full selection are insufficient to precisely determine the parameters of the CB, a large sample of these decays is generated using the RapidSim fast simulation package [188]. This package includes a reliable simulation of the decay kinematics, track momentum resolution and kinematic cuts. More information about the technical details of the generated sample can be found in Appendix A.1.

Since the means of the $B^0 \to K^{*0}\overline{K}^{*0}$ obtained from data and from MC are slightly different, the mean of the cross-feed backgrounds is shifted with respect to the value from simulation in the same amount as the difference between the mean of the $B^0 \to K^{*0}\overline{K}^{*0}$ MC and the mean obtained from data.

and n_1, a_2 and n_2 are the parameters that rule the match between the Hypatia core and the lower and upper masses tails.

[1] Where the Q-value is given by the difference between the initial and the final masses of the process, $Q = (m_i - m_f)c^2$.

5.4.3 Partially reconstructed background

As previously mentioned, no attempt has been made to separate the different decays that can build this background. To model them, an ARGUS function [175] is used. To take into account the effects of the experimental resolution, the ARGUS is convolved with a Gaussian distribution whose width is set to be the same as for the B_s^0 signal. The ARGUS function depends on two parameters: m_t which is the end point of the distribution, and c, that gives the curvature. The formula of the ARGUS distribution reads:

$$A(m; m_t, c) = \frac{m}{m_t^2}\left(1 - \frac{m^2}{m_t^2}\right)^{\frac{1}{2}} \exp\Big[-\frac{1}{2}c^2(1 - \frac{m^2}{m_t^2})\Big]. \tag{5.2}$$

For the value of m_t, one constraint is imposed. It is assumed that the main contribution of the partially reconstructed background originates in B_s^0 decays in which one neutral pion is missing, and therefore the value of m_t is fixed to be the difference between the B_s^0 mass and the π^0 mass. The other parameter, c, is left unconstrained in the fit, with a common value for 2011 and 2012.

5.4.4 Combinatorial background

The last considered element of the four-body mass spectrum is the combinatorial background. This contribution is parametrised with a decreasing exponential. The exponential parameter is fitted independently for the 2011 and 2012 samples.

5.5 Selection

In order to further increase the signal to background separation, an offline selection has to be applied to the sample obtained after the trigger and the stripping cuts. In the next paragraphs the cuts and methods used to select the data are explained in detail.

5.5.1 Fiducial region

Firstly, the kinematic region which contains the final-state particles has to be unambiguously defined. These cuts are important in the calibration of the PID efficiencies in Chapter 5.6.5. The cuts that define the fiducial region are shown in Table 5.4.

Table 5.4: Cuts defining the fiducial region.

Variable	Cut
K/π momentum	$3 < p < 100\,\text{GeV}/c$
K/π pseudorapidity	$1.5 < \eta < 4.5$
Number of tracks in the event	$0 < nTracks < 600$

5.5.2 Preliminary cuts

After the trigger, the stripping selection and the choice of the fiducial region, the cut isMuon == 0 for all the tracks in the event is applied, to ensure that muons do not pollute the sample.

5.5.3 Multivariate analysis

To remove the combinatorial background, a Multivariate Analysis (MVA) is used. Several MVA methods from the TMVA package [176] are tried in order to search for the optimal performing solution: three different Boosted Decision Trees (BDT, BDTG and BDTD) and a Neural Network (MLP). The BDTG is finally chosen as the MVA method to be used in the analysis, since it gives the best performance with the least overtraining.

The events used as signal for the training are $B^0 \to K^{*0}\overline{K}^{*0}$ MC truth matched events, with the same trigger lines, the same stripping selection (including the PID cuts) and the same preliminary cuts applied to data. As background, the events from data with a four-body invariant mass above 5600 MeV/c^2 are used. With this selection, it is ensured that the background is purely combinatorial, since the Λ_b^0 reflection that appears in the high mass sideband has a mass below this value.

To train and apply the BDTG, the signal and background samples are splitted in two equal samples using random generated numbers. The first set of events from signal and background is used to train a BDTG, labelled BDTG1. This BDTG1 is tested on the second set of events and it is applied to this second sample. A second BDTG is trained using the second sample, BDTG2, and it is tested on and applied to the first sample.

Besides, data and MC are split according to the year. Therefore, there are 4 BDTGs, 2 for 2011 and 2 for 2012. In the next paragraphs, some figures of the performance of the MVA used are shown. These are for the 2012 BDTG1. The other MVA figures are very similar and can be seen in Appendix A.2

The variables chosen to train the BDTG are shown in Table 5.5. The MVA uses these variables to discriminate between signal and background. Variables with very different behaviour in signal and background give the best performance for the BDTG. In Fig. 5.4 the distributions of the considered variables can be seen. PID variables are not included in the MVA because the MC is known not to perfectly reproduce their distributions. Therefore they are treated separately.

In Fig. 5.5, the discriminant response can be seen. A comparison of the BDTG output between the training and testing samples, wich are compatible for signal and for

Table 5.5: Variables used to train the MVA.

Variable	Description
B_DOCA	Distance of Closest Approach
log10(1.0-|B_DIRA_OWNPV|)	B^0 pointing angle
log10(B_FDCHI2_OWNPV)	B^0 flight distance w.r.t. PV
log10(B_PT)	B^0 transverse momentum
B_MINIPCHI2	Minimum B^0 IP significance w.r.t. any PV
B_ENDVERTEX_CHI2/B_ENDVERTEX_NDOF	B^0 vertex fit
log10(min(Kplus_IPCHI2_OWNPV,piminus_IPCHI2_OWNPV))	Min K^{*0} tracks IP significance w.r.t. PV
log10(min(Kminus_IPCHI2_OWNPV,piplus_IPCHI2_OWNPV))	Min $\overline{K}^{*0}$ tracks IP significance w.r.t. PV

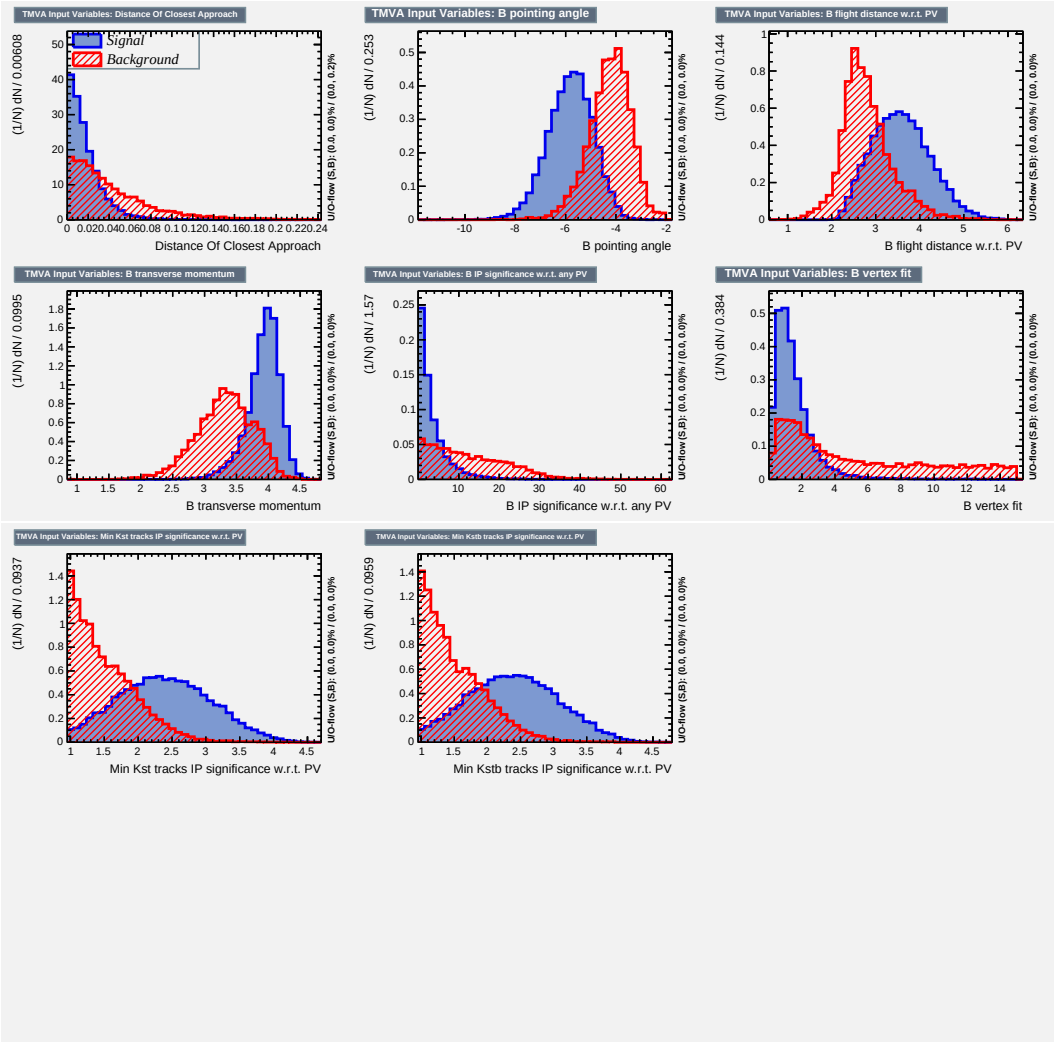

Figure 5.4: Distribution of the variables used to train the MVA. Their definitions are in Table 5.5. Events from the signal sample in blue and from the background sample in red. Only the plots for the 2012 BDTG1 are shown.

background, is displayed. Since the samples are independent, it is ensured that there is no obvious overtraining, *i.e.*, the BDTG output is not affected by possible random fluctuations in the samples used as input.

In Fig. 5.6 the linear correlations between the different variables for signal and background are shown. In Fig. 5.7, the signal efficiency vs background rejection for the MVA used can be seen. From this plot, it can be said that the BDTG performs well, with a very high signal efficiency, while rejecting most of the background.

Finally, to reject as much background as possible while keeping a high signal efficiency, a cut in the BDTG has to be applied. To find the optimal cut, a Figure of Merit (FoM) is chosen and optimised, as shown below.

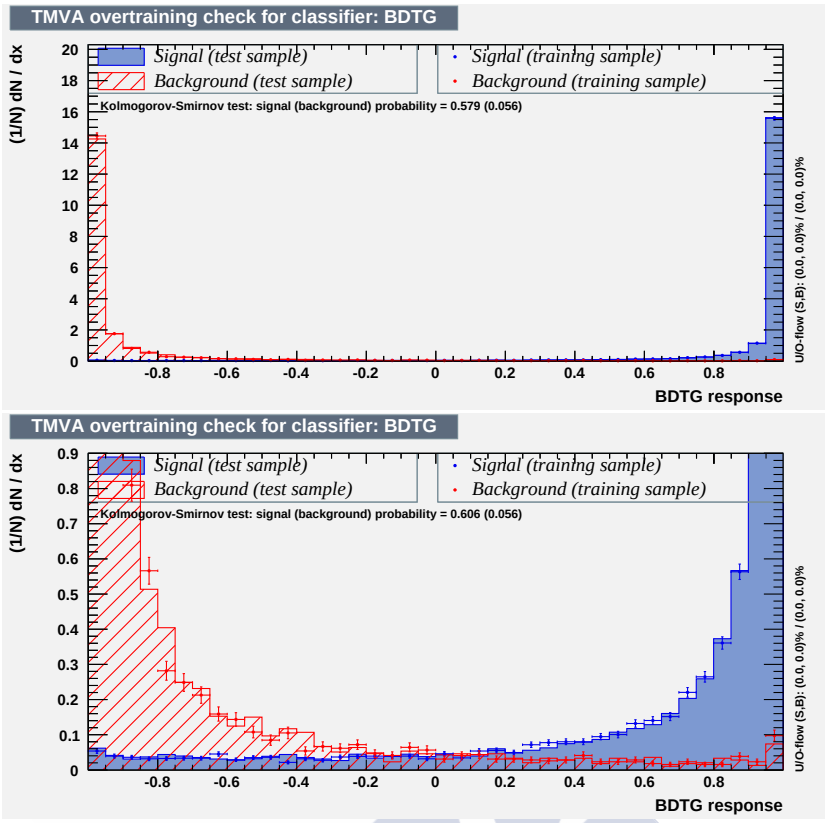

Figure 5.5: Top: BDTG response for training and testing samples. Signal events in blue and background events in red. The points correspond to the training samples and the solid histograms to the testing samples. Bottom: Zoom of the same plot. Only the plots for the 2012 BDTG1 are shown.

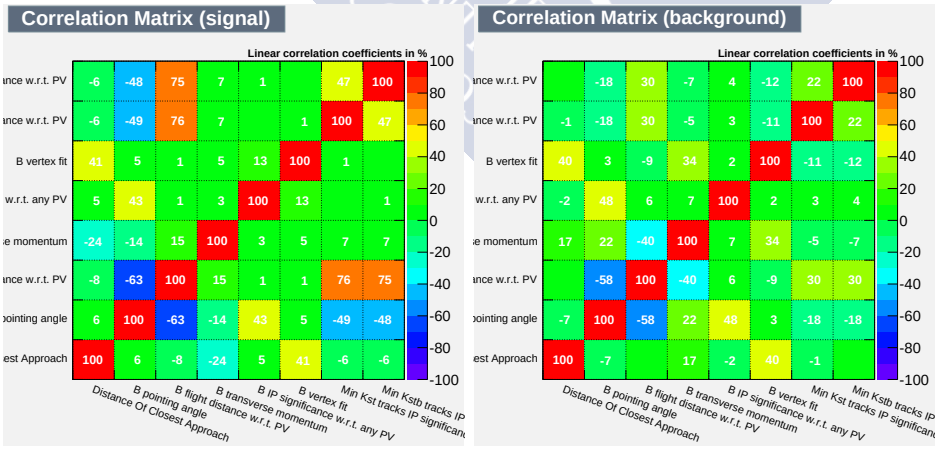

Figure 5.6: Linear correlations between the variables used to train the MVA. Left: Signal. Right: Background. Only the plots for the 2012 BDTG1 are shown.

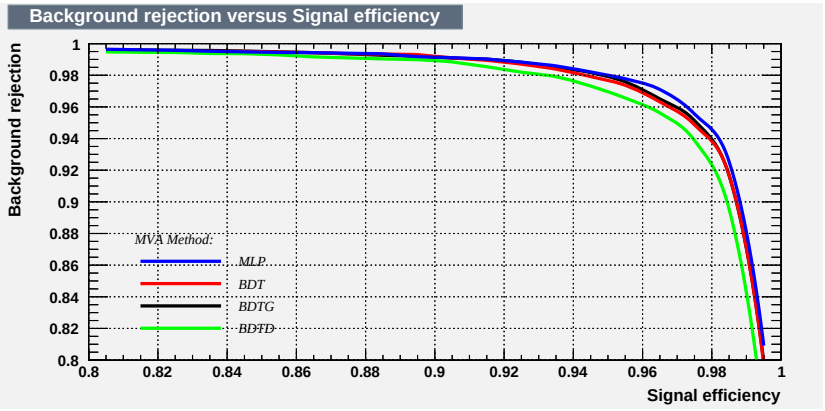

Figure 5.7: Signal efficiency and background rejection for the MVA methods analyzed. Red: BDT. Black: BDTG. Green: BDTD. Blue: MLP. Only the plot for the 2012 BDTG1 is shown.

5.5.4 FoM optimisation

The selected FOM is the significance, $S/\sqrt{S+B}$, where S and B are the expected number of signal and background events, respectively, after a given cut in the BDTG.

To calculate B, the number of events in the background region $5600 < M_{K\pi K\pi} < 5800\,\text{MeV}/c^2$ is obtained for each cut. To extrapolate it to the signal region ($\pm 30\,\text{MeV}/c^2$ around the B^0 mass), it has been supposed that the background distribution, dominated by combinatorial events, is flat. Then, by multiplying the number of background events by 60/200, the value of B is obtained.

To obtain the value of S, the yield of $B_s^0 \to K^{*0}\overline{K}^{*0}$ decays without specific selection cuts is obtained with a fit of the four-body invariant mass. For that purpose a simplification of the model described in Chapter 5.4 is considered. Since no cuts, other than stripping, are applied, the combinatorial background is the dominant contribution and some of the components with less statistics are disregarded. Only contributions from $B_s^0 \to K^{*0}\overline{K}^{*0}$ and $B^0 \to K^{*0}\overline{K}^{*0}$ decays, along with components from $B^0 \to \rho^0 K^{*0}$ and $B^0 \to \phi K^{*0}$ decays are considered, in addition to the dominating combinatorial background. The fit result can be seen in Fig. 5.8 and Table 5.6. Including contributions from the Λ_b^0 component or from the partially reconstructed background does not significantly modify the $B_s^0 \to K^{*0}\overline{K}^{*0}$ yield and, therefore, the FoM maximum does not vary either.

The number of $B^0 \to K^{*0}\overline{K}^{*0}$ events can be estimated by dividing the obtained B_s^0 yield by the ratio between the B_s^0 and B^0 yields from Ref. [189], which is 5.86. Once the signal yield in the sample without cuts is estimated, it is multiplied by the efficiency of each BDTG cut, obtained using Monte Carlo.

The value of the significance as a function of the BDTG cut is shown in Fig. 5.9. The optimal cuts found are in Table 5.7. In Table 5.8, the efficiencies of the BDTG cuts applied obtained from Monte Carlo are shown for different decay modes.

Table 5.6: Results of the four-body invariant mass fit without cuts, used to calculate the optimal cut in the Figure of Merit (Fig. 5.8).

Parameter	2011	2012
μ_{B^0}	5284.01 ± 0.66	
σ_{B^0}	17.3 ± 1.1	17.46 ± 0.89
$N_{B^0 \to K^{*0}\overline{K}^{*0}}$	85 ± 38	221 ± 69
$N_{B_s^0 \to K^{*0}\overline{K}^{*0}}$	1132 ± 76	2610 ± 130
$N_{B^0 \to \rho^0 K^{*0}}$	457 ± 89	800 ± 150
$N_{B^0 \to \phi K^{*0}}$	218 ± 54	722 ± 99
$k_{CombBkg}$	$(-0.610 \pm 0.089) \times 10^{-3}$	$(-0.025 \pm 0.049) \times 10^{-3}$
$N_{CombBkg}$	7950 ± 130	27510 ± 250

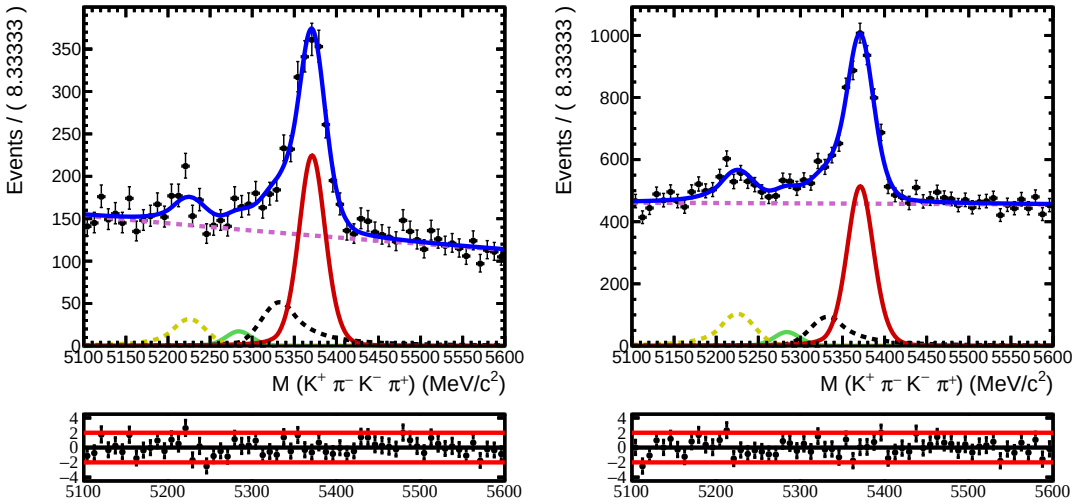

Figure 5.8: Fit of the four-body invariant mass used to calculate the optimal cut in the FoM, with the data sample obtained without cuts. The fit results are indicated in Table 5.6. In red, the $B_s^0 \to K^{*0}\overline{K}^{*0}$ component, in green, the $B^0 \to K^{*0}\overline{K}^{*0}$ decay, in black, the $B^0 \to \rho^0 K^{*0}$ contribution, in yellow, $B^0 \to \phi K^{*0}$ decays and the pink line corresponds to the combinatorial background. Left: 2011. Right: 2012.

5.5.5 PID cuts

As mentioned in Chapter 5.3, bbthe most important backgrounds for this analysis are those produced by the misidentification of one particle, particularly the resilient $B^0 \to \rho^0 K^{*0}$ contribution. To fight them, a set of cuts in the PID variables has to be included.

Different options to optimise the PID cuts were tried. In the end, quite tight selections are chosen using the approach described in the $B^0 \to \rho^0 K^{*0}$ analysis [190]. The selection combines the ProbNN variables as shown in Table 5.9. These cuts are also applied in the $B_s^0 \to K^+\pi^-K^-\pi^+$ time dependent analysis showing a good performance [191]. The efficiencies of the selected PID cuts are shown in Table 5.16.

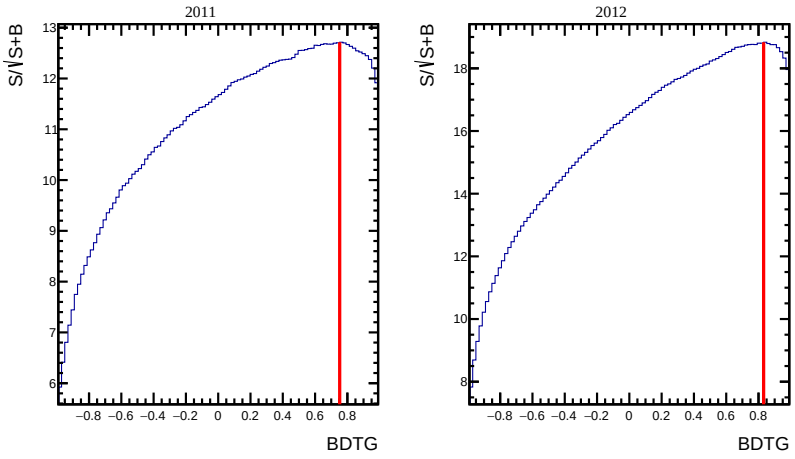

Figure 5.9: Significance obtained for each cut in the BDTG calculated as explained in the text, with the red line indicating the maximum. Left: 2011. Right: 2012.

Table 5.7: Optimal values of the BDTG cut obtained from the maximisation of the FoM as explained in the text.

Parameter	2011	2012
BDTG	> 0.7524	> 0.8316

Table 5.8: BDTG efficiencies from Monte Carlo simulated events. The efficiencies are in %.

Decay mode	2011		2012	
	MagUp	MagDown	MagUp	MagDown
$B^0 \to K^{*0}\overline{K}^{*0}$	92.85 ± 0.22	92.33 ± 0.22	90.26 ± 0.19	90.23 ± 0.19
$B_s^0 \to K^{*0}\overline{K}^{*0}$	91.87 ± 0.22	91.57 ± 0.22	90.01 ± 0.18	90.46 ± 0.17
$B^0 \to \rho^0 K^{*0}$	91.38 ± 0.29	91.60 ± 0.28	89.86 ± 0.23	90.14 ± 0.23
$B^0 \to \phi K^{*0}$	92.72 ± 0.25	92.24 ± 0.25	91.11 ± 0.20	90.77 ± 0.20
$\Lambda_b^0 \to K^{*0} p\pi$	90.9 ± 1.2	91.7 ± 1.1	88.43 ± 0.93	87.39 ± 0.98

Table 5.9: PID cuts imposed in the selection.

PID variable	Cut
K ProbNNk	> 0.2
K ProbNNk $\times$ (1 $-$ K ProbNNpi)	> 0.3
π ProbNNpi	> 0.2
π ProbNNpi $\times$ (1 $-$ π ProbNNk)	> 0.3

5.6 Efficiencies

In this Chapter, the calculation of the efficiencies is summarised. The total efficiency is calculated as a product of the efficiencies of the intermediate steps,

$$\varepsilon_{total} = \varepsilon_{gen} \cdot \varepsilon_{reco\ \&\ stripping} \cdot \varepsilon_{trigger} \cdot \varepsilon_{selection} \cdot \varepsilon_{PID}. \tag{5.3}$$

Each efficiency is calculated from the sample with the cuts of the previous steps applied. The selection efficiencies do not include the PID cuts, since the efficiencies of the particle identification are calculated separately. All efficiencies are obtained using Monte Carlo simulated events, except the PID efficiencies, which are obtained using a data-driven method, as explained in Chapter 5.6.5. All the quoted uncertainties are statistical. For the reconstruction and stripping efficiencies, the trigger efficiencies and the selection efficiencies, these uncertainties are obtained using the binomial formula,

$$\sigma(\varepsilon) = \sqrt{\frac{\varepsilon(1-\varepsilon)}{N}}, \tag{5.4}$$

where N is the total number of events before the cut is applied. The total efficiencies are summarised in Table 5.10.

5.6.1 Generator efficiencies

The generator level efficiency corresponds to the requirement that each of the charged tracks of a given decay must fall within the $10 < \theta < 400$ mrad acceptance of the LHCb detector. They are obtained generating simulated signal events and counting how many of them have all their final state particles within this geometric acceptance. The numerical values of the efficiencies for each decay used in the analysis can be found in Table 5.11.

5.6.2 Reconstruction and stripping efficiencies

In Table 5.12 the combined efficiencies of reconstruction and stripping are shown. The reconstruction efficiency accounts for the ability of the spectrometer to detect and correctly build the particles. The stripping efficiencies are obtained imposing the cuts shown in Table 5.2 to the reconstructed events. As already mentioned, the cuts in the PID variables are treated separately (Chapter 5.6.5) because the Monte Carlo does not fully reproduce them. In this category, the efficiency coming from the truth matching of the Monte Carlo is also included.

Table 5.10: Total efficiencies, obtained as the product of the different factors explained in the text. The efficiencies are in $\% \times 10^3$.

Decay mode	2011		2012	
	MagUp	MagDown	MagUp	MagDown
$\varepsilon(B^0 \to K^{*0}\overline{K}^{*0}) \times 10^3$	104.58 ± 0.92	106.57 ± 0.93	96.69 ± 0.66	98.33 ± 0.67
$\varepsilon(B_s^0 \to K^{*0}\overline{K}^{*0}) \times 10^3$	116.88 ± 0.98	116.89 ± 0.98	109.24 ± 0.70	108.53 ± 0.70
$\varepsilon(B^0 \to \rho^0 K^{*0}) \times 10^3$	0.972 ± 0.011	1.012 ± 0.011	1.0188 ± 0.0087	0.9159 ± 0.0078

Table 5.11: Generator efficiencies from the tables generated by the simulation group. The efficiencies are in %.

Decay mode	2011		2012	
	MagUp	MagDown	MagUp	MagDown
$B^0 \to K^{*0}\overline{K}^{*0}$	16.951 ± 0.028	17.000 ± 0.028	17.302 ± 0.031	17.290 ± 0.030
$B_s^0 \to K^{*0}\overline{K}^{*0}$	16.945 ± 0.029	16.964 ± 0.028	17.234 ± 0.030	17.178 ± 0.030
$B^0 \to \rho^0 K^{*0}$	16.716 ± 0.044	16.720 ± 0.043	17.050 ± 0.045	17.040 ± 0.045

Table 5.12: Reconstruction and stripping efficiencies from Monte Carlo simulated events. The efficiencies are in %.

Decay mode	2011		2012	
	MagUp	MagDown	MagUp	MagDown
$B^0 \to K^{*0}\overline{K}^{*0}$	5.301 ± 0.022	5.325 ± 0.022	4.856 ± 0.015	4.839 ± 0.015
$B_s^0 \to K^{*0}\overline{K}^{*0}$	6.082 ± 0.024	6.060 ± 0.024	5.585 ± 0.016	5.547 ± 0.016
$B^0 \to \rho^0 K^{*0}$	3.412 ± 0.018	3.414 ± 0.018	3.117 ± 0.012	3.079 ± 0.012

Table 5.13: Trigger efficiencies from Monte Carlo simulated events. The efficiencies are in %.

Decay mode	2011		2012	
	MagUp	MagDown	MagUp	MagDown
$B^0 \to K^{*0}\overline{K}^{*0}$	33.53 ± 0.20	33.61 ± 0.20	33.69 ± 0.15	33.93 ± 0.15
$B_s^0 \to K^{*0}\overline{K}^{*0}$	32.76 ± 0.19	32.66 ± 0.19	33.22 ± 0.14	32.95 ± 0.14
$B^0 \to \rho^0 K^{*0}$	33.99 ± 0.25	34.32 ± 0.25	34.60 ± 0.19	34.91 ± 0.19

5.6.3 Trigger efficiencies

The trigger efficiencies are obtained by counting how many events of the simulation sample obtained after the reconstruction and the stripping cuts pass the trigger lines shown in Table 5.3. The results can be seen in Table 5.13. The separated efficiency of each trigger line is shown in Table 5.14 for $B^0 \to K^{*0}\overline{K}^{*0}$ Monte Carlo events.

5.6.4 Selection efficiencies

The selection efficiencies correspond to the fiducial cuts applied in Table 5.4, and to the cut in the BDTG, reported in Table 5.7. The values of the efficiencies can be seen in Table 5.15.

5.6.5 PID efficiencies

The efficiencies of the PID cuts shown in Table 5.9 together with the preliminary condition isMuon == 0 are calculated here. Since the MC is known not to correctly reproduce the

Table 5.14: Efficiencies of the different trigger lines used in the analysis obtained with $B^0 \to K^{*0}\overline{K}^{*0}$ simulated events. Total L0 is the efficiency of passing one of the two L0 lines. The same for Total HLT2, which is the efficiency of passing one of the three HLT2 lines. HLT1 is calculated after applying the L0 trigger requirement, and the same for HLT2, which is obtained after the L0 and HLT1 trigger conditions are imposed to the sample. The efficiencies are in %.

Trigger line	2011		2012	
	MagUp	MagDown	MagUp	MagDown
L0HadronDecision_TOS	30.86 ± 0.20	31.22 ± 0.20	28.54 ± 0.14	28.70 ± 0.14
L0HadronDecision_TIS	29.08 ± 0.20	29.22 ± 0.19	27.58 ± 0.14	27.45 ± 0.14
Total L0	48.76 ± 0.22	48.97 ± 0.21	46.07 ± 0.16	46.26 ± 0.16
Hlt1TrackAllL0Decision_TOS	79.48 ± 0.25	79.59 ± 0.25	81.16 ± 0.18	80.98 ± 0.18
Hlt2Topo2BodyBBDDecision_TOS	74.68 ± 0.30	75.06 ± 0.30	76.73 ± 0.22	76.65 ± 0.22
Hlt2Topo3BodyBBDDecision_TOS	79.93 ± 0.28	79.98 ± 0.27	86.12 ± 0.18	86.83 ± 0.18
Hlt2Topo4BodyBBDDecision_TOS	58.30 ± 0.34	58.20 ± 0.34	67.92 ± 0.24	68.64 ± 0.24
Total HLT2	86.51 ± 0.24	86.23 ± 0.24	90.12 ± 0.16	90.57 ± 0.15
Total	33.53 ± 0.20	33.61 ± 0.20	33.69 ± 0.15	33.93 ± 0.15

Table 5.15: Selection efficiencies from Monte Carlo simulated events. The efficiencies are in %.

Decay mode	2011		2012	
	MagUp	MagDown	MagUp	MagDown
$B^0 \to K^{*0}\overline{K}^{*0}$	73.15 ± 0.33	72.75 ± 0.33	68.74 ± 0.25	68.66 ± 0.25
$B_s^0 \to K^{*0}\overline{K}^{*0}$	72.64 ± 0.32	72.30 ± 0.32	69.41 ± 0.24	69.30 ± 0.24
$B^0 \to \rho^0 K^{*0}$	73.31 ± 0.41	73.74 ± 0.40	69.66 ± 0.31	69.87 ± 0.31

behaviour of the PID variables in data, a data-driven approach is used to get the efficiency of the PID cuts with the PIDCalib package [192].

This package uses $D^* \to D^0(K\pi)\pi$ decays to calculate the efficiency of kaons and pions, where these particles can be well identified without using PID cuts, and samples from prompt $\Lambda \to p\pi$ and from inclusive $\Lambda_c^+ \to pK\pi$ decays to determine the efficiency of protons. To remove the background contamination, the *sPlot* technique [185] is used. Employing these calibration samples, the true efficiency for a given selection in the PID variables is obtained, as explained in the following paragraphs.

The PID response depends on the momentum of the particle through its relation with the emission angle of Cherenkov photons, on its pseudorapidity, since the two RICH detectors have different angular acceptances and are optimised for different momentum regions, and on the event occupancy.

The first step is to build a map of efficiencies for each set of PID cuts. The calibration samples are binned in these three variables (p, η and $nTracks$). The number of events passing a given set of cuts is obtained for each 3-D bin. Dividing by the number of events in that bin before the cuts are applied, a 3-D map of efficiencies is obtained. For the proton tracks, there are two calibration samples. The efficiency of the combination of the two samples is done by adding the number of events in each sample after the cut and dividing it by the sum of events before the cut.

The binning scheme has to be chosen in such a way that all the bins have enough statistics and that the efficiency does not vary much along consecutive bins. A non-uniform binning scheme is chosen:

- **Track momentum**: 1 bin for $3 < p < 8\,\text{GeV}/c$, 1 bin for $8 < p < 10.7\,\text{GeV}/c$ and 38 bins for $10.7 < p < 100\,\text{GeV}/c$
- **Track pseudorapidity**: 1 bin for $1.5 < \eta < 2.25$, 7 bins for $2.25 < \eta < 4$ and 1 bin for $4 < \eta < 4.5$
- **Number of tracks**: 4 bins for $0 < nTracks < 400$ and 1 bin for $400 < nTracks < 600$

The event occupancy is not well described in Monte Carlo but, since the number of tracks in the event and the kinematic of the track are independent quantities, the dependency on $nTracks$ can be integrated. If the analytic expression of the distribution of $nTracks$ in the data sample were known, the mathematical equation representing the integration would be

$$\bar{\varepsilon}(p,\eta) = \int \varepsilon(p,\eta,nT) f(nT) \mathrm{d}nT, \tag{5.5}$$

where $f(nT)$ is the distribution of the number of tracks in the data sample, $\varepsilon(p,\eta,nT)$ is the 3-D efficiency calculated as explained in the previous paragraphs and $\bar{\varepsilon}(p,\eta)$ is the efficiency depending on p and η in the same occupancy regime as in the data sample. The previous equation can be written for the situation in which the efficiencies are binned as,

$$\bar{\varepsilon}(p_i,\eta_j) = \frac{1}{N}\sum_{k=1}^{N} \varepsilon(p_i,\eta_j,nT_k), \tag{5.6}$$

where $\bar{\varepsilon}(p_i,\eta_j)$ is the final PID efficiency for the i-th bin in p and the j-th bin in η, $\varepsilon(p_i,\eta_j,nT_k)$ is the 3-D efficiency for the i-th bin in p, the j-th bin in η and the k-th bin in nT and N is a number large enough to avoid statistical fluctuation ($N = 200000$ is chosen). For each term of the sum, the value of nT is randomly extracted according to the distribution of nT in the data sample.

To get a distribution of the number of tracks in a data sample similar to the real $B^0 \to K^{*0}\overline{K}^{*0}$ distribution, the sWeighted $B_s^0 \to K^{*0}\overline{K}^{*0}$ data sample used for the FoM optimisation is chosen (Chapter 5.5.4, Fig. 5.8). In Fig. 5.10 (left), this distribution can be seen, compared to the one obtained from MC. The assumption that this distribution correctly describes the decay under study, $B^0 \to K^{*0}K^{*0}$ and the cross-feed backgrounds, $B^0 \to \rho^0 K^{*0}$, $B^0 \to \phi K^{*0}$ and $\Lambda_b^0 \to K^{*0}p\pi$ is used. In Fig. 5.10 (right), a comparison of the distribution of $nTracks$ for the MC of the mentioned decays is shown.

The efficiency of an event i is obtained as the product of the efficiencies of the four tracks entering into the event,

$$\varepsilon_{h_1,h_2,h_3,h_4}(p_1^i,\eta_1^i,p_2^i,\eta_2^i,p_3^i,\eta_3^i,p_4^i,\eta_4^i) = \bar{\varepsilon}_{h_1}(p_1^i,\eta_1^i)\cdot\bar{\varepsilon}_{h_2}(p_2^i,\eta_2^i)\cdot\bar{\varepsilon}_{h_3}(p_3^i,\eta_3^i)\cdot\bar{\varepsilon}_{h_4}(p_4^i,\eta_4^i), \tag{5.7}$$

where h_1, h_2, h_3 and h_4 are the four tracks that form the decay and $\bar{\varepsilon}_h(p,\eta)$ is the 2-D efficiency, calculated previously for the track h with momentum p and pseudorapidity η.

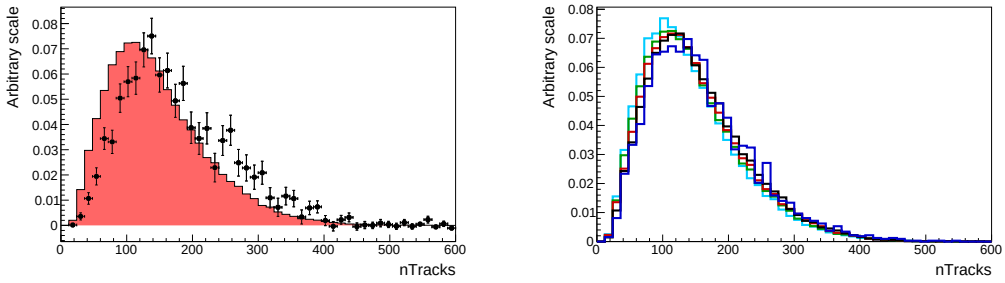

Figure 5.10: Left: Comparison between the distribution of the number of tracks in the $B_s^0 \to K^{*0}\overline{K}^{*0}$ data sample obtained as explained in the text (black points) and the $B^0 \to K^{*0}\overline{K}^{*0}$ MC (solid red histogram). Right: Comparison of the distribution of $nTracks$ for the MC of different decays: the $B_s^0 \to K^{*0}\overline{K}^{*0}$ decay is the light blue line, the $B^0 \to K^{*0}\overline{K}^{*0}$ decay is the green line, the $B^0 \to \rho^0 K^{*0}$ decay is the red line, the $B^0 \to \phi K^{*0}$ decay is the black line and the $\Lambda_b^0 \to K^{*0} p\pi$ decay is the dark blue line.

Table 5.16: PID efficiencies calculated as explained in the text. The efficiencies are in %.

Decay mode	2011		2012	
	MagUp	MagDown	MagUp	MagDown
$B^0 \to K^{*0}\overline{K}^{*0}$	47.4551 ± 0.0037	48.1521 ± 0.0025	49.6847 ± 0.0011	50.4489 ± 0.0011
$B_s^0 \to K^{*0}\overline{K}^{*0}$	47.6704 ± 0.0034	48.1513 ± 0.0025	49.2295 ± 0.0011	49.8752 ± 0.0011
$B^0 \to \rho^0 K^{*0}$	0.6843 ± 0.0010	0.70016 ± 0.00073	0.79538 ± 0.00039	0.71565 ± 0.00039

The final PID efficiency of a given decay is then calculated as the mean of the efficiencies of each event,

$$\varepsilon_{h_1,h_2,h_3,h_4} = \frac{1}{N}\sum_{i=1}^{N} \varepsilon_{h_1,h_2,h_3,h_4}(p_1^i, \eta_1^i, p_2^i, \eta_2^i, p_3^i, \eta_3^i, p_4^i, \eta_4^i). \tag{5.8}$$

The Monte Carlo distributions of p and η are used to calculate the efficiency. In Fig. 5.11, the distributions of the final efficiencies in bins of p and η are shown for kaons, pions and protons from the calibration samples. In the same figure, the distribution of the tracks in Monte Carlo is also shown, to compare the calibration samples with respect to the MC distributions.

In Table 5.16, the efficiencies of the cuts in the PID variables are shown.

5.7 Four-body invariant mass fit result

After the selection cuts are applied, an unbinned extended maximum likelihood fit of the four-body invariant mass, simultaneous for the 2011 and 2012 samples is performed to extract the sWeighted dataset with which to perform the amplitude analysis. Different approaches are followed to deal with the three cross-feed background components in the fit, $B^0 \to \phi K^{*0}$, $B^0 \to \rho^0 K^{*0}$ and $\Lambda_b^0 \to K^{*0} p\pi$ decays. Since the $B^0 \to \phi K^{*0}$ events appear in a location of the four-body mass where they are the main contribution, the sWeighting procedure is expected to perform accurately and completely subtract these

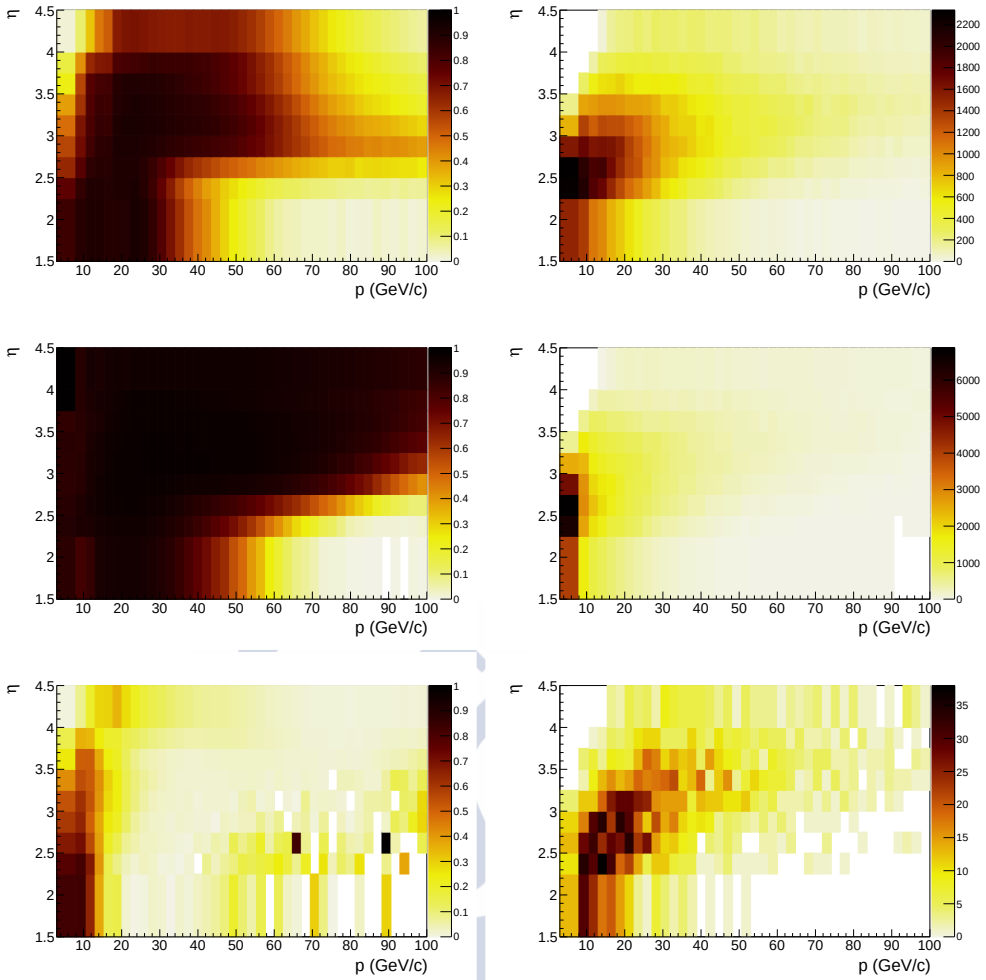

Figure 5.11: Left: Efficiencies in bins of p and η for kaons (top), pions (middle) and protons (bottom), obtained using the calibration samples as described in the text. Right: Distribution of p and η for kaons (top) and pions (middle) from $B^0 \to K^{*0}\overline{K}^{*0}$ MC and for protons (bottom) from $\Lambda_b^0 \to K^{*0}p\pi$ MC.

events. The other two modes need a special treatment, as it is explained in the next paragraphs.

5.7.1 Dealing with $B^0 \to \rho^0 K^{*0}$ decays

As shown in Fig. 5.3, the $B^0 \to \rho^0 K^{*0}$ decay sits below the $B^0 \to K^{*0}\overline{K}^{*0}$ and $B_s^0 \to K^{*0}\overline{K}^{*0}$ peaks. For this reason the sWeights cannot be efficiently obtained for its suppression. Unfortunately, the PID cuts applied do not remove all the background coming from this source and a way to extract its contribution is required. It is done by including negative weights. To apply this method, the number of $B^0 \to \rho^0 K^{*0}$ events that pass the

Table 5.17: Estimated number of events of the $B^0 \to \rho^0 K^{*0}$ decay entering into the final selection.

Decay	2011	2012
$B^0 \to \rho^0 K^{*0}$	6.0 ± 2.3	12.4 ± 4.4

complete selection is estimated using simulated events [1] with the equation

$$N(X \to Y) = 2 \times \mathcal{L} \times f_{d,s} \times \sigma_{b\bar{b}} \times \mathcal{B}(X \to Y) \times \varepsilon, \tag{5.9}$$

where $\mathcal{L}$ is the luminosity collected by LHCb, $\mathcal{L} = (1.017 \pm 0.0036)\,\text{fb}^{-1}$ in 2011 and $\mathcal{L} = (2.057 \pm 0.072)\,\text{fb}^{-1}$ in 2012; $\sigma_{b\bar{b}}$ is the pp cross-section for $b\bar{b}$ quarks production, $\sigma_{b\bar{b}} = (284 \pm 53)\,\mu\text{b}$ [193] at $\sqrt{s} = 7\,\text{TeV}$ and $\sigma_{b\bar{b}} = (298 \pm 36)\,\mu\text{b}$ [194] at $\sqrt{s} = 8\,\text{TeV}$; $f_{d,s}$ are the hadronisation fractions, $f_d = (40.1 \pm 0.8)\%$ and $f_s = (10.5 \pm 0.6)\%$ [1]; $\mathcal{B}(B^0 \to \rho^0 K^{*0})$ is the branching ratio of the decay, $(3.9 \pm 1.3) \times 10^{-6}$ [1]; and ε is the total efficiency, given in Table 5.10. The final number of events of this background that are estimated can be seen in Table. 5.17.

Once the estimated number of events is calculated, the contribution from the peaking background is cancelled out using negative weights. In order to do that, the same weight is applied to every MC event i, with the value,

$$\omega_i = -\frac{N^{data}}{N^{MC}} \tag{5.10}$$

where N^{MC} is the number of Monte Carlo events and N^{data} is the estimated number of events in data, previously calculated. These weighted MC events are then injected in the data sample, effectively supressing the contribution from $B^0 \to \rho^0 K^{*0}$ decays.

5.7.2 Estimation of the $\Lambda_b^0 \to K^{*0} p\pi$ events

For the case of $\Lambda_b^0 \to K^{*0} p\pi$ events, the problem is that if the yields are left free to float, the four-body invariant mass fit is unable to obtain consistent results between the 2011 and 2012 samples. Thus it was decided to fix them after estimating the expected $\Lambda_b^0 \to K^{*0} p\pi$ yield values and modify the sWeighting procedure accordingly to allow fixed yields following Ref. [186] and the Appendix 2 of Ref. [185].

The estimated yields are obtained from data. The proton mass hypothesis is imposed to the kaon with the highest proton likelihood value (DLL_{pK}) in each event. The resulting $p\pi K\pi$ four-body invariant mass is then fitted with three contributions: a Λ_b^0 component, described with a gaussian with the mean and the sigma floating; a component from the dominating $B_s^0 \to K^{*0}\overline{K}^{*0}$ events, whose lineshape is obtained from simulation, fitted with a Crystal-Ball, as shown in Fig. 5.12; and the rest of contributions, mainly $B^0 \to \phi K^{*0}$ and partially reconstructed events, with a small combinatorial background contribution, wich are parametrised with a decreasing exponential with a free decay constant. This shape has been checked to reasonably reproduce simulated events for any decay that in the original $K^+\pi^-K^-\pi^+$ spectrum is reconstructed at masses smaller than the B_s^0 mass.

[1] The $B^0 \to \rho^0 K^{*0}$ MC events are generated with a longitudinal polarisation of $f_L = 0.40$, following [70].

The result of the $p\pi K\pi$ invariant mass fit is shown in Table 5.18 and Fig. 5.13. The Λ_b^0 peaks are clearly visible and the yields obtained are used in the $K^+\pi^-K^-\pi^+$ four-body invariant mass fit.

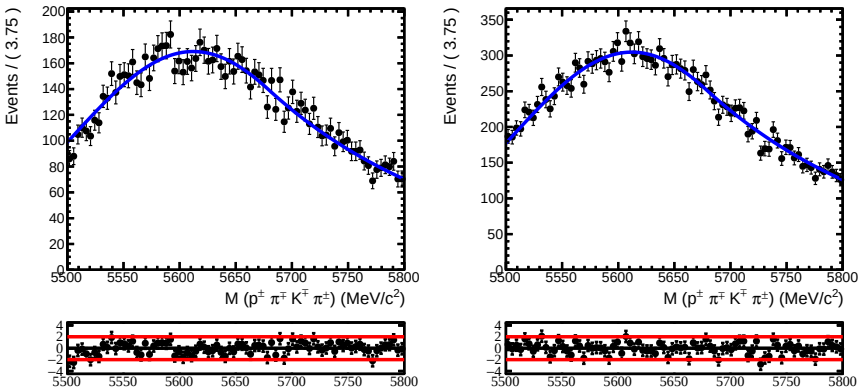

Figure 5.12: $p\pi K\pi$ invariant mass of $B_s^0 \to K^{*0}\overline{K}^{*0}$ Monte Carlo events fitted with a Crystal-Ball function. Left: 2011. Right: 2012.

Table 5.18: Result of the $p\pi K\pi$ mass spectrum fit (Fig. 5.13).

Parameters	2011	2012
$\mu_{\Lambda_b^0}$	5622.7 ± 3.2	
$\sigma_{\Lambda_b^0}$	14.7 ± 3.0	
$N_{\Lambda_b^0}$	36 ± 16	120 ± 28
$N_{B_s^0 \to K^{*0}\overline{K}^{*0}}$	494 ± 66	980 ± 160
k_{Bkg}	$(-8.1 \pm 2.9) \times 10^{-3}$	
N_{Bkg}	115 ± 59	350 ± 150

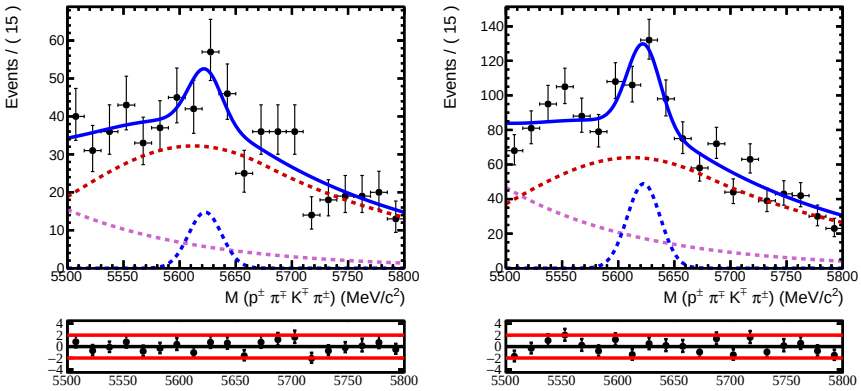

Figure 5.13: Results of the $p\pi K\pi$ mass spectrum fit (Table 5.18). The model consists of a $B_s^0 \to K^{*0}\overline{K}^{*0}$ decay contribution (red dotted line), a contribution of Λ_b^0 decays (blue dotted line) and the rest of contributions (pink dotted line). Left: 2011. Right: 2012.

5.7.3 $K^+\pi^-K^-\pi^+$ invariant mass fit result

The lineshapes chosen to parametrise the signal and the cross-feed backgrounds are described in Chapter 5.4. The parameters of these functions are obtained from simulation. Since the PID cuts modify the distribution of the four-body mass and the MC does not reproduce well the behaviour of the PID variables, a PID weight, extracted from Eq. 5.7, is assigned to each event.

In Table 5.19 and Fig. 5.14, the Hypatia parameters obtained for the signal with a fit of the $B^0 \to K^{*0}\overline{K}^{*0}$ Monte Carlo weighted to take into account the effects of the PID cuts are shown. All the parameters are fixed in the real data fit, except the mean and the resolution of the Hypatia.

In Table 5.20 and Fig. 5.15, the results of the fit of the $B^0 \to \phi K^{*0}$ PID corrected Monte Carlo can be seen. A Crystal-Ball plus a Gaussian concentric distributions are used.

In Table 5.21 and Fig. 5.16, the results of the fit to a Crystal-Ball distribution of the $\Lambda_b^0 \to K^{*0}p\pi$ PID weighted RapidSim generated events are shown.

Table 5.19: Parameters obtained in the fit of the $B^0 \to K^{*0}\overline{K}^{*0}$ Monte Carlo using an Hypatia function (Fig. 5.14).

Parameters	2011	2012
μ	5280.970 ± 0.084	
σ	15.28 ± 0.18	15.44 ± 0.17
λ	-5.12 ± 0.59	
a_1	2.197 ± 0.060	
n_1	1.261 ± 0.094	
a_2	2.705 ± 0.088	
n_2	1.69 ± 0.11	
N	12770 ± 110	23080 ± 150

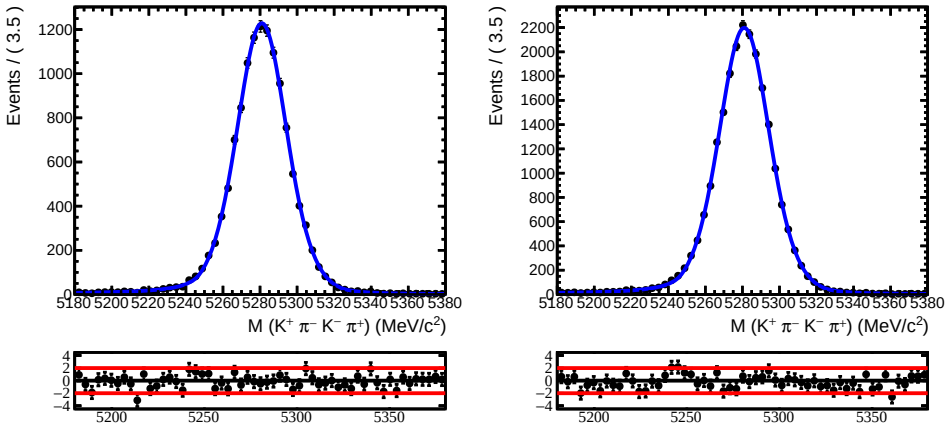

Figure 5.14: $B^0 \to K^{*0}\overline{K}^{*0}$ Monte Carlo events fitted with an Hypatia function (Table 5.19). Left: 2011. Right: 2012.

Table 5.20: Parameters obtained in the fit of the $B^0 \to \phi K^{*0}$ Monte Carlo using a Crystal-Ball plus a concentric Gaussian distributions (Fig. 5.15).

Parameters	2011	2012
μ	5221.99 ± 0.85	
σ_G	177 ± 45	113 ± 21
σ_{CB}	18.91 ± 0.79	18.64 ± 0.69
a_{CB}	0.763 ± 0.091	
f_{CB}	2.80 ± 0.84	
fraction	0.9859 ± 0.0060	0.9818 ± 0.0062
N	1146 ± 34	1988 ± 45

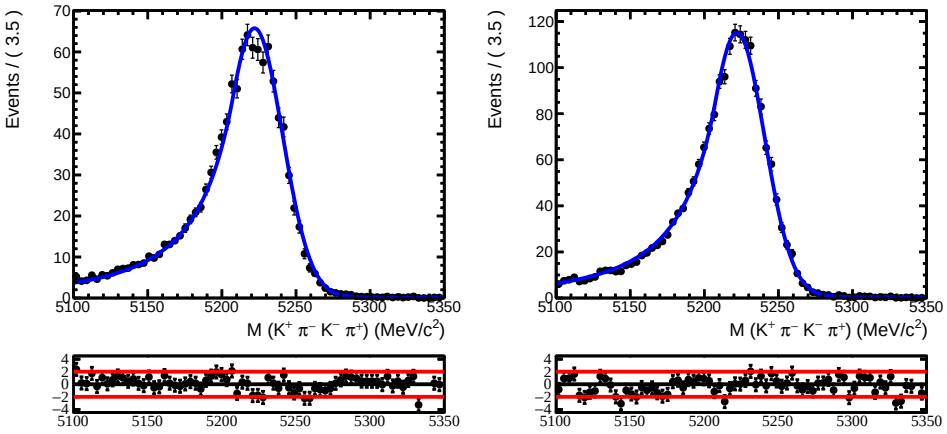

Figure 5.15: $B^0 \to \phi K^{*0}$ Monte Carlo events fitted with a Crystal-Ball plus a concentric Gaussian (Table 5.20). Left: 2011. Right: 2012.

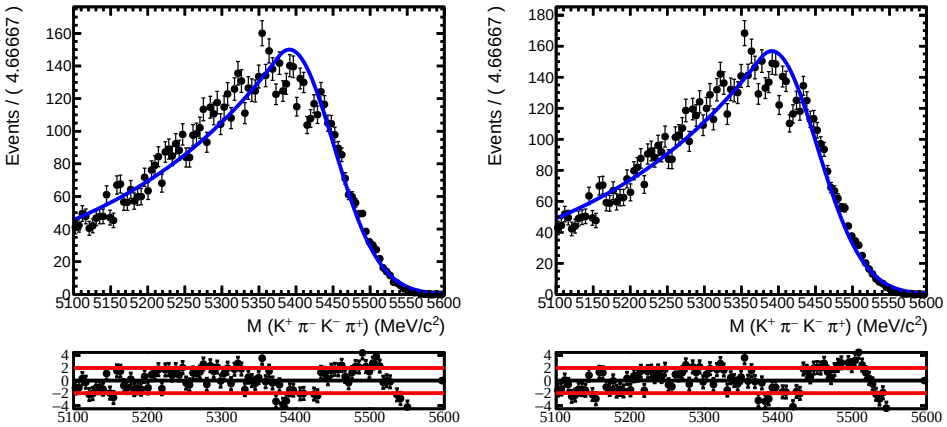

Figure 5.16: $\Lambda_b^0 \to K^{*0} p\pi$ RapidSim simulated events fitted with a Crystal-Ball (Table 5.21). Left: 2011. Right: 2012.

Table 5.21: Parameters obtained in the fit of the $\Lambda_b^0 \to K^{*0} p\pi$ RapidSim simulated events using a Crystal-Ball distribution (Fig. 5.16).

Parameters	2011	2012
μ	5391.1 ± 2.5	
σ_{CB}	60.2 ± 1.5	61.4 ± 1.5
a_{CB}	0.254 ± 0.012	
f_{CB}	100 ± 83	
N	7997 ± 89	8467 ± 92

Table 5.22: Results of the four-body invariant mass data fit (Fig. 5.17).

Parameters	2011	2012
μ_{B^0}	5284.15 ± 0.41	
σ_{B^0}	17.24 ± 0.64	17.41 ± 0.46
$N_{B^0 \to K^{*0}\bar{K}^{*0}}$	98 ± 12	248 ± 19
$N_{B_s^0 \to K^{*0}\bar{K}^{*0}}$	614 ± 26	1332 ± 38
$N_{B^0 \to \phi K^{*0}}$	138 ± 18	250 ± 30
$c_{PartReco}$	0.000 ± 0.021	
$N_{PartReco}$	41 ± 14	110 ± 25
$k_{CombBkg}$	$(-0.00 \pm 0.53) \times 10^{-3}$	$(-1.00 \pm 0.99) \times 10^{-3}$
$N_{CombBkg}$	6.1 ± 4.5	34 ± 11

Finally, the result of the four-body $K^+\pi^-K^-\pi^+$ invariant mass data fit is presented in Table 5.22 and Fig. 5.17. It is worth remarking that the combined 2011 and 2012 result yields more than three hundred $B^0 \to K^+\pi^-K^-\pi^+$ candidates, which is more than seven times the amount of events previously observed [183, 184]. To perform the amplitude analysis, the extended sWeight technique is applied to the final sample. The yields of Λ_b^0 decays are fixed to the values obtained in Table 5.18 and the $B^0 \to \rho^0 K^{*0}$ decay is extracted using negative weights, as explained in Chapter 5.7.1.

5.8 Amplitude analysis

The $B^0 \to K^{*0}\bar{K}^{*0}$ decay, where $K^{*0} \to K^+\pi^-$ and $\bar{K}^{*0} \to K^-\pi^+$, is a weak decay of a pseudoscalar particle into two vector mesons ($P \to VV$). From angular momentum conservation, three combinations are possible, in which the polarisations of the final-state vector meson fields are either longitudinal (A_0), or transverse to their directions of motion and parallel ($A_\parallel$) or perpendicular ($A_\perp$) to each other. To disentangle the fraction corresponding to the different contributions, an amplitude analysis is needed.

In the range of masses under study, $|M_{K\pi} - M_{K^{*0}}| < 150\,\text{MeV}/c^2$, the $K\pi$ pairs may not only come from the spin-1 resonance $K^*(892)^0$, but also from other spin states. This motivates that, besides the helicity angles, the $K^\pm\pi^\mp$ invariant masses are included in the analytical model.

Each of the spin states can have different resonant and non resonant contributions. For the S-wave, the spin-0 $K_0^*(1430)^0$ resonance plus a non-resonant component, $(K^\pm\pi^\mp)_0$,

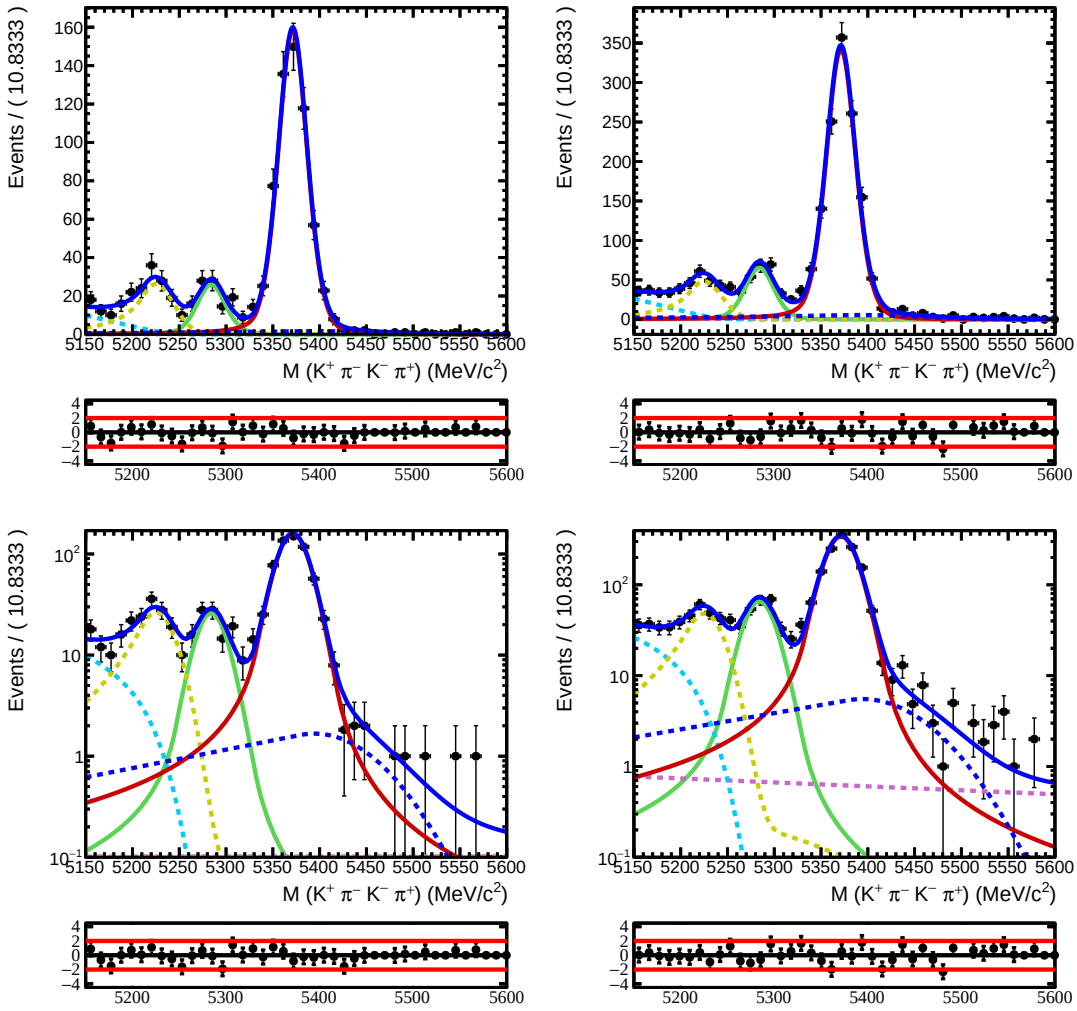

Figure 5.17: Simultaneous four-body invariant mass fit result of the 2011 (left) and 2012 (right) data samples (Table 5.22). The red line corresponds to the $B_s^0 \to K^+\pi^-K^-\pi^+$ component, the $B^0 \to K^+\pi^-K^-\pi^+$ decay is the green line, the dotted dark blue line is the $\Lambda_b^0 \to K^{*0}p\pi$ decay, the dotted yellow line is the $B^0 \to \phi K^{*0}$ decay, the dotted light blue line corresponds to the partially reconstructed background and the dotted pink line to the combinatorial background. The black points correspond to the data and the overall fit is represented by the thick blue line. In the bottom plots a logarithmic scale is used. The χ^2/ndf with 60 bins for the 2011 data is 0.879, and for the 2012 data it is 0.865.

are accounted for. For the P-wave, only the $K^*(892)^0$ resonance is considered, whereas other spin-1 resonances, like $K^*(1410)^0$ or $K^*(1680)^0$, with pole positions much above the fit region, are neglected. Resonances with spin numbers greater than 1, like the spin-2 $K_2^*(1430)^0$, are neither considered.

Both B^0 and $\bar{B}^0$ can reach the final state $K^+\pi^-K^-\pi^+$, therefore, the oscillation of the $B^0 - \bar{B}^0$ system must be considered. Due to the limited number of available events, an untagged and time-integrated analysis is performed.

5.8.1 Angle-mass distribution at time t=0

The dependence on the angles for the individual amplitudes, taking the combinations between the P-wave and the S-wave is given by [53, 74],

$$\begin{aligned}
\mathcal{A}_{VV} &= N \sum_{j=-1}^{1} A_j^{VV} Y_1^{-j}(\theta_1, -\phi) Y_1^j(\pi - \theta_2, 0), \\
\mathcal{A}_{VS} &= N A_0^{VS} Y_1^0(\theta_1, -\phi) Y_0^0(\pi - \theta_2, 0), \\
\mathcal{A}_{SV} &= N A_0^{SV} Y_0^0(\theta_1, -\phi) Y_1^0(\pi - \theta_2, 0), \\
\mathcal{A}_{SS} &= N A_0^{SS} Y_0^0(\theta_1, -\phi) Y_0^0(\pi - \theta_2, 0),
\end{aligned} \tag{5.11}$$

where N is a normalisation constant, and Y_l^m are the spherical harmonics. The magnitude $\theta_{1(2)}$ is defined as the angle between the direction of the $K^{+(-)}$ meson and the direction opposite to the B^0-meson momentum in the rest frame of K^{*0} ($\overline{K}^{*0}$) and ϕ is the angle between the decay planes of the two vector mesons in the B^0-meson rest frame, as can be seen in Fig. 5.18.

When including different resonances in the analysis, the invariant masses of the $K^{\pm}\pi^{\mp}$ pairs have to be introduced in the model. Moving from the helicity basis to the polarisation basis, $A_{\parallel} = \frac{A_+ + A_-}{\sqrt{2}}$ and $A_{\perp} = \frac{A_+ - A_-}{\sqrt{2}}$, and making explicit the Y_j^m expressions, the following equation is obtained [74],

$$\begin{aligned}
&\mathcal{A}_{VV} + \mathcal{A}_{VS} + \mathcal{A}_{SV} + \mathcal{A}_{SS} \\
&= -\frac{3N}{4\pi}\Bigg[\Big(A_0 \cos\theta_1 \cos\theta_2 + \frac{A_{\parallel}}{\sqrt{2}} \sin\theta_1 \sin\theta_2 \cos\phi \\
&\quad + i\frac{A_{\perp}}{\sqrt{2}} \sin\theta_1 \sin\theta_2 \sin\phi\Big)\, \mathcal{M}_1(m_1)\mathcal{M}_1(m_2) \\
&\quad - \frac{A_{VS}}{\sqrt{3}} \cos\theta_1 \mathcal{M}_1(m_1)\mathcal{M}_0(m_2) + \frac{A_{SV}}{\sqrt{3}} \cos\theta_2 \mathcal{M}_0(m_1)\mathcal{M}_1(m_2) \\
&\quad - \frac{A_{SS}}{3} \mathcal{M}_0(m_1)\mathcal{M}_0(m_2)\Bigg],
\end{aligned} \tag{5.12}$$

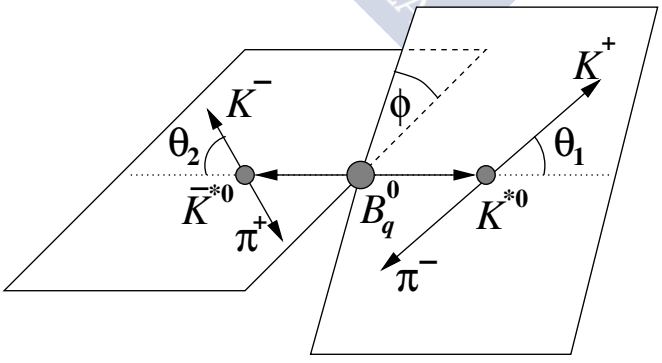

Figure 5.18: Definition of the angles involved in the amplitude analysis of the $B^0 \to K^+\pi^-K^-\pi^+$ decays.

where $\mathcal{M}_{1,0}(m)$ are the P- and S-wave propagators as functions of the corresponding two-body masses, $m_1 = m_{K^+\pi^-}$ and $m_2 = m_{K^-\pi^+}$, which are described in detail in Chapter 5.8.3.

As written in Eq. 5.12, the SV and VS amplitudes are not *CP* eigenstates. There is a more convenient way to represent them, applying the following transformation [53],

$$\begin{aligned} A_S^+ &= \frac{A_{VS} + A_{SV}}{\sqrt{2}}, \\ A_S^- &= \frac{A_{VS} - A_{SV}}{\sqrt{2}}, \end{aligned} \tag{5.13}$$

where the amplitudes A_S^+ and A_S^- are now *CP* eigenstates, with *CP* eigenvalues $\eta_+ = -1$ and $\eta_- = 1$. Using this notation, Eq. 5.12 can be reformulated as

$$\begin{aligned} &\mathcal{A}_{VV} + \mathcal{A}_{VS} + \mathcal{A}_{SV} + \mathcal{A}_{SS} \\ &= -\frac{3N}{4\pi}\Bigg[\Big(A_0 \cos\theta_1 \cos\theta_2 + \frac{A_\parallel}{\sqrt{2}} \sin\theta_1 \sin\theta_2 \cos\phi \\ &\quad + i\frac{A_\perp}{\sqrt{2}} \sin\theta_1 \sin\theta_2 \sin\phi\Big)\, \mathcal{M}_1(m_1)\mathcal{M}_1(m_2) \\ &\quad - \frac{A_S^+}{\sqrt{6}}\Big(\cos\theta_1 \mathcal{M}_1(m_1)\mathcal{M}_0(m_2) - \cos\theta_2 \mathcal{M}_0(m_1)\mathcal{M}_1(m_2)\Big) \\ &\quad - \frac{A_S^-}{\sqrt{6}}\Big(\cos\theta_1 \mathcal{M}_1(m_1)\mathcal{M}_0(m_2) + \cos\theta_2 \mathcal{M}_0(m_1)\mathcal{M}_1(m_2)\Big) \\ &\quad - \frac{A_{SS}}{3}\mathcal{M}_0(m_1)\mathcal{M}_0(m_2)\Bigg]. \end{aligned} \tag{5.14}$$

The amplitude $\mathcal{A}$ can be written in a more compact formula

$$\mathcal{A} = \sum_{i=1}^{6} A_i f_i(\cos\theta_1, \cos\theta_2, \phi, m_1, m_2), \tag{5.15}$$

where i indices the individual physical amplitudes. The values of the complex amplitudes A_i, and of the angle-mass terms, f_i are shown in Table 5.23. From this expression, the

Table 5.23: Amplitudes A_i, and angle-mass terms f_i.

i	A_i	f_i
1	A_0	$\cos\theta_1 \cos\theta_2 \mathcal{M}_1(m_1)\mathcal{M}_1(m_2)$
2	$A_\parallel$	$\frac{1}{\sqrt{2}} \sin\theta_1 \sin\theta_2 \cos\phi \mathcal{M}_1(m_1)\mathcal{M}_1(m_2)$
3	$A_\perp$	$\frac{i}{\sqrt{2}} \sin\theta_1 \sin\theta_2 \sin\phi \mathcal{M}_1(m_1)\mathcal{M}_1(m_2)$
4	A_S^+	$-\frac{1}{\sqrt{6}}(\cos\theta_1 \mathcal{M}_1(m_1)\mathcal{M}_0(m_2) - \cos\theta_2 \mathcal{M}_0(m_1)\mathcal{M}_1(m_2))$
5	A_S^-	$-\frac{1}{\sqrt{6}}(\cos\theta_1 \mathcal{M}_1(m_1)\mathcal{M}_0(m_2) + \cos\theta_2 \mathcal{M}_0(m_1)\mathcal{M}_1(m_2))$
6	A_{SS}	$-\frac{1}{3}\mathcal{M}_0(m_1)\mathcal{M}_0(m_2)$

decay rate at production (time $t = 0$) can be obtained, by squaring the amplitude:

$$\begin{aligned}\frac{\mathrm{d}^5\Gamma}{\mathrm{d}\cos\theta_1\mathrm{d}\cos\theta_2\mathrm{d}\phi\mathrm{d}m_1\mathrm{d}m_2} &\propto \Phi_4(m_1,m_2)|\mathcal{A}|^2 = \frac{9}{8\pi}\Phi_4(m_1,m_2)\left|\sum_{i=1}^{6}A_i f_i\right|^2 \\ &= \Phi_4(m_1,m_2)\sum_{i=1}^{6}\sum_{j\geq i}\mathcal{R}e[A_i A_j^* f_i f_j^*(2-\delta_{ij})] \\ &\equiv \sum_{i=1}^{6}\sum_{j\geq i}\mathcal{R}e[A_{ij}F_{ij}],\end{aligned} \tag{5.16}$$

with,

$$\delta_{ij} = \begin{cases} 1 & \text{if } i = j, \\ 0 & \text{if } i \neq j, \end{cases} \tag{5.17}$$

$$A_{ij} = A_i A_j^*, \tag{5.18}$$

$$F_{ij} = \Phi_4(m_1,m_2) f_i f_j^*(2-\delta_{ij}), \tag{5.19}$$

being Φ_4 the four-body phase space for $B^0 \to K^+\pi^-K^-\pi^+$ decays, given in Chapter 5.8.3.

For the *CP* conjugated decay, $\bar{B}^0 \to K^+\pi^-K^-\pi^+$, the amplitude is obtained from the B^0 amplitude by applying the transformation,

$$A_i \to \eta_i \bar{A}_i, \tag{5.20}$$

where η_i is the *CP* parity of the amplitude A_i, shown in Table 5.24.

5.8.2 Time dependent angle-mass distribution

The decay rate previously calculated is obtained for $t = 0$. Since the B^0 meson oscillates, the decay rate is going to evolve with time. In general, the time dependent amplitudes are given by

$$\begin{aligned}A_h(t) &= \left[g_+(t)A_h + \eta_h\frac{q}{p}g_-(t)\bar{A}_h\right], \\ \bar{A}_h(t) &= \left[\frac{p}{q}g_-(t)A_h + \eta_h g_+(t)\bar{A}_h\right],\end{aligned} \tag{5.21}$$

Table 5.24: *CP* eigenstates of the amplitudes contributing to the $B^0 \to K^+\pi^-K^-\pi^+$ decay.

A_i	η_i
A_0	1
$A_\parallel$	1
$A_\perp$	-1
A_S^+	-1
A_S^-	1
A_{SS}	1

with

$$\begin{aligned} g_+(t) &= \frac{1}{2}\left(e^{-(iM_L+\Gamma_L/2)t} + e^{-(iM_H+\Gamma_H/2)t}\right), \\ g_-(t) &= \frac{1}{2}\left(e^{-(iM_L+\Gamma_L/2)t} - e^{-(iM_H+\Gamma_H/2)t}\right), \end{aligned} \tag{5.22}$$

where Γ_L and Γ_H are the lifetimes of the light and the heavy mass eigenstates and M_L and M_H are their masses.

In the Standard Model, *CP* violation in mixing is expected to be small, $\left|\frac{q}{p}\right| \sim 1$. Using $\frac{q}{p} = e^{-i\phi_M}$, with ϕ_M being the mixing angle, the product A_{ij} in Eq. 5.16 is obtained depending on time as

$$\begin{aligned} A_{ij}(t) = A_i(t)A_j^*(t) = \frac{1}{2}e^{-\Gamma t}\Big[&(A_iA_j^* + \eta_i\eta_j\bar{A}_i\bar{A}_j^*)\cosh\left(\frac{\Delta\Gamma}{2}t\right) \\ &+(A_iA_j^* - \eta_i\eta_j\bar{A}_i\bar{A}_j^*)\cos\Delta mt \\ &-(\eta_i e^{-i\Phi_M}\bar{A}_iA_j^* + \eta_j e^{i\Phi_M}A_i\bar{A}_j^*)\sinh\left(\frac{\Delta\Gamma}{2}t\right) \\ &+i(\eta_i e^{-i\Phi_M}\bar{A}_iA_j^* - \eta_j e^{i\Phi_M}A_i\bar{A}_j^*)\sin\Delta mt\Big], \end{aligned} \tag{5.23}$$

where A_i and A_j are the complex amplitudes at $t = 0$, $\Gamma = \frac{\Gamma_L+\Gamma_H}{2}$, $\Delta\Gamma = \Gamma_L - \Gamma_H$ and $\Delta m = M_H - M_L$. The expression is written in a more compact way as [53],

$$\begin{aligned} A_{ij}(t) = \frac{1}{2}e^{-\Gamma t}\Big[&a_{ij}\cosh\left(\frac{\Delta\Gamma}{2}t\right) + c_{ij}\cos\Delta mt \\ &+b_{ij}\sinh\left(\frac{\Delta\Gamma}{2}t\right) + d_{ij}\sin\Delta mt\Big]. \end{aligned} \tag{5.24}$$

Going back to Eq. 5.16 and including the time evolution,

$$\begin{aligned} \frac{\mathrm{d}^6\Gamma}{\mathrm{d}t\,\mathrm{d}\cos\theta_1\,\mathrm{d}\cos\theta_2\,\mathrm{d}\phi\,\mathrm{d}m_1\,\mathrm{d}m_2} &\propto \sum_{i=1}^{6}\sum_{j\geq i}\mathcal{R}e[A_{ij}(t)F_{ij}] \\ &= \sum_{i=1}^{6}\sum_{j\geq i}\frac{1}{2}e^{-\Gamma t}\mathcal{R}e\Bigg[\Big[a_{ij}\cosh\left(\frac{\Delta\Gamma}{2}t\right) \\ &+ c_{ij}\cos\Delta mt + b_{ij}\sinh\left(\frac{\Delta\Gamma}{2}t\right) + d_{ij}\sin\Delta mt\Big]F_{ij}\Bigg]. \end{aligned} \tag{5.25}$$

For the *CP* conjugated decay, the expression reads very similar, changing $a_{ij} \to \bar{a}_{ij} = a_{ij}$, $b_{ij} \to \bar{b}_{ij} = b_{ij}$, $c_{ij} \to \bar{c}_{ij} = -c_{ij}$ and $d_{ij} \to \bar{d}_{ij} = -d_{ij}$. Therefore, in an untagged analysis only the terms going with a_{ij} and b_{ij} have to be considered because the others cancel out,

$$\frac{\mathrm{d}^6\Gamma + \mathrm{d}^6\overline{\Gamma}}{\mathrm{d}t\,\mathrm{d}\cos\theta_1\,\mathrm{d}\cos\theta_2\,\mathrm{d}\phi\,\mathrm{d}m_1\,\mathrm{d}m_2} \propto \sum_{i=1}^{6}\sum_{j\geq i}\mathcal{R}e\left[A_{ij}^{untagged}(t)F_{ij}\right] \tag{5.26}$$

where

$$A_{ij}^{untagged}(t) = A_{ij}(t) + \bar{A}_{ij}(t) = e^{-\Gamma t}\left[a_{ij}\cosh\left(\frac{\Delta\Gamma}{2}t\right) + b_{ij}\sinh\left(\frac{\Delta\Gamma}{2}t\right)\right]. \quad (5.27)$$

For the B^0 meson, we can impose another simplification. Since $\Delta\Gamma_d \sim 0$, the terms going with $\sinh\left(\frac{\Delta\Gamma}{2}t\right)$ are neglected, obtaining

$$A_{ij}^{untagged}(t) = e^{-\Gamma t}a_{ij}\cosh\left(\frac{\Delta\Gamma}{2}t\right), \quad (5.28)$$

and using

$$\int_0^\infty e^{-\Gamma t}\cosh\left(\frac{\Delta\Gamma}{2}t\right)dt = \frac{1}{2}\left(\frac{1}{\Gamma_H} + \frac{1}{\Gamma_L}\right), \quad (5.29)$$

the expression for the A_{ij} in an untagged and time-integrated analysis of a B^0 meson is

$$A_{ij}^{untagged} = a_{ij} = A_i A_j^* + \eta_i\eta_j\bar{A}_i\bar{A}_j^*. \quad (5.30)$$

Assuming that there is no *CP*-violation in the decay, namely $\bar{A}_i = A_i$,

$$A_{ij}^{untagged} = a_{ij} = A_i A_j^*\delta_{\eta_i\eta_j}. \quad (5.31)$$

Finally, the expression for the decay rate is

$$\frac{\mathrm{d}^5\Gamma^{untagged}}{\mathrm{d}\cos\theta_1\mathrm{d}\cos\theta_2\mathrm{d}\phi\mathrm{d}m_1\mathrm{d}m_2} \propto \sum_{i=1}^{6}\sum_{j\geq i}\mathcal{R}e[A_i A_j^* F_{ij}\delta_{\eta_i\eta_j}]. \quad (5.32)$$

From this equation, the terms with interference of a *CP*-even and a *CP*-odd eigenstate vanish. This means that the only terms of interference where $A_\perp$ appears are those with A_S^+, so the distribution is only sensitive to the difference $\delta_\perp - \delta_S^+$, and these phases cannot be calculated separately in an untagged and time-integrated analysis [74].

5.8.3 Invariant mass propagators

The mass propagators used to parametrise the spin-0 (S-wave) and spin-1 (P-wave) amplitudes of the $K^+\pi^-$ and $K^-\pi^+$ pairs are described below.

5.8.3.1 P-wave

For the case of the P-wave, only the K^{*0} resonance is considered in the analysis, and a relativistic spin-1 Breit-Wigner is used to parametrise it. The propagator of a relativistic generic spin-ℓ Breit-Wigner is defined by

$$\mathcal{R}_\ell(m) = \frac{m_R\Gamma_\ell(m)}{m_R^2 - m^2 - im_R\Gamma_\ell(m)}, \quad (5.33)$$

with m_R being the mass of the resonance and $\Gamma_\ell(m)$ the running width, defined as

$$\Gamma_\ell(m) = \Gamma_R\frac{\rho(m)}{\rho(m_R)}B_\ell^2(q, q_R), \quad (5.34)$$

Table 5.25: Values of the different parameters used in the mass propagators. m_R and Γ_R are the mass and the width of the spin-J resonance, R is the interaction radius, a the scattering length and b the effective range.

	$(K\pi)_0^{*0}$ J = 0	$K^*(892)^0$ J = 1
$m_R[\,\mathrm{MeV}/c^2]$	1425 ± 50	895.81 ± 0.19
$\Gamma_R[\,\mathrm{MeV}/c^2]$	270 ± 80	47.4 ± 0.6
$R[(\,\mathrm{GeV}/c)^{-1}]$	-	3.0 ± 0.5
$a[(\,\mathrm{GeV}/c)^{-1}]$	$1.95 \pm 0.09 \pm 0.06$	-
$b[(\,\mathrm{GeV}/c)^{-1}]$	$1.76 \pm 0.36 \pm 0.67$	-

where Γ_R is the nominal width of the resonance, $\rho(m)$ is the phase space factor $\rho(m) = \frac{2q}{m}$, $B_\ell(q, q_{K^{*0}})$ is the Blatt-Weisskopf centrifugal barrier factor for a generic spin-ℓ resonance and q is the momentum of a daughter in the resonance rest frame,

$$q(m, m_A, m_B) = \frac{\sqrt{(m^2 - (m_A + m_B)^2)(m^2 - (m_A - m_B)^2)}}{2M}, \tag{5.35}$$

where m_A and m_B are the masses of the daughters and q_R is the value of this momentum evaluated at the resonance mass, $m = m_R$. In the particular case of a spin-1 resonance, the expression of the Blatt-Weisskopf factor becomes

$$B_1(q, q_R) = \frac{q}{q_R}\sqrt{\frac{1 + (R\,q_R)^2}{1 + (R\,q)^2}}, \tag{5.36}$$

where R is the interaction radius, defined in Table 5.25. As explained before, for the P-wave only the K^{*0} resonance is considered, therefore m_R and Γ_R are the K^{*0} nominal mass and width, with values given in Table 5.25.

5.8.3.2 S-wave

For the S-wave amplitude, in the region of masses considered in the analysis, $|m_{K^\pm\pi^\mp} - M_{K^{*0}}| < 150\,\mathrm{MeV}/c^2$, the different components of the spectrum are not clearly established. There is certainly a resonance with spin-0 at $1430\,\mathrm{MeV}/c^2$, whose left tail enters into the analysis mass region, since it has a large width, $270\,\mathrm{MeV}/c^2$. In addition, a possible $K_0^*(800)$ or $\kappa(800)$ meson may exist. If it does not exist, a non-resonant contribution has to be considered. To parametrise the S-wave amplitude, the model used by the LASS collaboration [177] is employed. It consists of a sum of a Breit-Wigner resonance and a term parametrised as an effective range. The relative phase between both contributions is imposed by the S-matrix unitarity. The expression of the mass propagator for this parametrisation is given by

$$\mathcal{R}_0(m) = \frac{1}{\cot\delta_\beta - i} + e^{2i\delta_\beta}\frac{1}{\cot\delta_\alpha(m) - i}, \tag{5.37}$$

where

$$\cot\delta_\beta = \frac{1}{a\,q} + \frac{bq}{2}, \tag{5.38}$$

with q defined as in Eq. 5.35, a is the scattering length and b the effective range, and

$$\cot\delta_\alpha(m) = \frac{m_R^2 - m^2}{m_R\Gamma_0(m)}, \tag{5.39}$$

where m_R is the $K_0^*(1430)$ nominal mass, and $\Gamma_0(m)$, the running width for a spin-0 resonance, is

$$\Gamma_0(m) = \Gamma_R\frac{\rho(m)}{\rho(m_R)}, \tag{5.40}$$

with Γ_R being the nominal width of the $K_0^*(1430)$ resonance, whose value, along with the values of $m_{K_0^*(1430)}$, a and b are given in Table 5.25.

5.8.3.3 Phase space factor and normalisation

The relationship between the propagator and the Lorentz-invariant amplitude is given by

$$\mathcal{M}_J = N_J\frac{m}{q}\mathcal{R}_J, \tag{5.41}$$

where N_J is a complex normalisation factor. The magnitude of the normalisation ensures that the squared amplitudes are the fractions of each polarisation in the fitted mass range, and is calculated to fulfil

$$\int|\mathcal{M}_i(m_1)|^2|\mathcal{M}_j(m_2)|^2\Phi_4(m_1,m_2)\mathrm{d}m_1\mathrm{d}m_2 = 1, \tag{5.42}$$

where i and j are the different spins considered in the amplitude analysis, 0 and 1. The phase of the normalisation is chosen such that the phase of the propagator becomes zero at the nominal K^{*0} mass. This sets the definition of the S-wave amplitude phases (δ_S^-, δ_S^+ and δ_{SS}) as the phase difference between the S-wave and the P-wave amplitudes at the nominal K^{*0} mass.

To account for the four-body kinematics, the total squared amplitude has to be multiplied by the phase space factor. The 4 body phase space factor can be calculated recursively and, apart from a constant, the dependence is given by

$$\Phi_4(m_1,m_2) \propto q_B\ q_{K^{*0}}\ q_{\overline{K}^{*0}}, \tag{5.43}$$

where q_B is the momentum of the K^{*0} or the $\overline{K}^{*0}$ in the B^0 rest frame, and $q_{K^{*0}}$ ($q_{\overline{K}^{*0}}$) is the momentum of the K^+ (K^-) or the π^- (π^+) in the K^{*0} ($\overline{K}^{*0}$) rest frame.

5.8.4 Acceptance

The expression obtained for the decay rate, Eq. 5.32, could be used in an ideal fully efficient detector. The LHCb experiment, however, is a forward spectrometer and does not detect events outside a certain region. Besides the effects of detector geometry, there are some inefficiencies due to the selection and to the reconstruction in events which are within the acceptance. Because of this, a non-uniform efficiency has to be included to modify the model distribution before it can be compared to data. The method used to calculate the acceptance is that of the normalisation weights [195], which are obtained

exploiting a fully simulated MC. The normalisation weights include the dependency on the 5 variables being considered, the three polarisation angles and the two two-body invariant masses.

In a maximum likelihood fit, the equation that gives the optimal values of the parameters reads

$$\frac{\partial \ln \mathcal{L}}{\partial \lambda_n} = \frac{\partial}{\partial \lambda_n} \ln \prod_e \frac{\mathcal{P}(X_e|\vec{\lambda})}{\int \mathcal{P}(X|\vec{\lambda})\mathrm{d}^5X} = \frac{\partial}{\partial \lambda_n} \sum_e \ln \frac{\mathcal{P}(X_e|\vec{\lambda})}{\int \mathcal{P}(X|\vec{\lambda})\mathrm{d}^5X} = 0, \tag{5.44}$$

where $\mathcal{L}$ is the likelihood function, $X = \{\cos\theta_1, \cos\theta_2, \phi, m_1, m_2\}$, $\vec{\lambda}$ is the set of parameters to be measured, $\mathcal{P}(X|\vec{\lambda})$ is the PDF, given in Eq. 5.32, the index e represents the event in the dataset, and X_e is the value of X for event e.

Including an efficiency, $\epsilon(X)$, the likelihood maximisation becomes

$$\frac{\partial \ln \mathcal{L}}{\partial \lambda_n} = \frac{\partial}{\partial \lambda_n} \sum_e \ln \frac{\mathcal{P}(X_e|\vec{\lambda})\epsilon(X)}{\int \mathcal{P}(X|\vec{\lambda})\epsilon(X)\mathrm{d}^5X} = 0. \tag{5.45}$$

Using $\ln(AB) = \ln(A) + \ln(B)$ and considering that the efficiency does not depend on the parameters $\vec{\lambda}$, the previous expression can be written as

$$\frac{\partial \ln \mathcal{L}}{\partial \lambda_n} = \frac{\partial}{\partial \lambda_n} \sum_e \ln \frac{\mathcal{P}(X_e|\vec{\lambda})}{\int \mathcal{P}(X|\vec{\lambda})\epsilon(X)\mathrm{d}^5X} = 0, \tag{5.46}$$

where the efficiency only appears in the integral of the denominator. Writing the expression for the decay rate, the integral becomes

$$\int \mathcal{P}(X|\vec{\lambda})\epsilon(X)\mathrm{d}^5X = \int \sum_{i\leq j}\sum_{j=1}^{6} \mathcal{R}e[A_i A_j^* F_{ij}\delta_{\eta_i\eta_j}]\epsilon(X)\mathrm{d}^5X$$

$$= \sum_{i\leq j}\sum_{j=1}^{6} \mathcal{R}e[A_i A_j^* \int F_{ij}\delta_{\eta_i\eta_j}\epsilon(X)\mathrm{d}^5X] \equiv \sum_{i\leq j}\sum_{j=1}^{6} \mathcal{R}e[A_i A_j^* \omega_{ij}], \tag{5.47}$$

where the ω_{ij} are the complex normalisation weights. In the next paragraph, a method to obtain the normalisation weights from Monte Carlo is explained.

For a given event sample, distributed according the PDF $\mathcal{P}$, the effect of the efficiency on an arbitrary function $h(X)$ can be calculated as,

$$\frac{1}{N_{gen}} \sum_{accepted} h(X_e) = \frac{1}{N_{gen}} \sum_{generated} \epsilon(X_e)h(X_e) \sim \int \mathcal{P}(X)\epsilon(X)h(X)\mathrm{d}^5X. \tag{5.48}$$

If the function $h(X)$ is chosen as

$$h_{ij}(X) = F_{ij}\delta_{\eta_i\eta_j}\mathcal{P}^{-1}(X), \tag{5.49}$$

then,

$$\frac{1}{N_{gen}} \sum_{accepted} h_{ij}(X_e) = \frac{1}{N_{gen}} \sum_{generated} \epsilon(X_e)F_{ij}\delta_{\eta_i\eta_j}\mathcal{P}^{-1}(X_e) \sim \int F_{ij}\delta_{\eta_i\eta_j}\epsilon(X)\mathrm{d}^5X = \omega_{ij}, \tag{5.50}$$

and therefore ω_{ij} can be obtained using a fully simulated MC with the expression

$$\omega_{ij} = \frac{1}{N_{gen}} \sum_{accepted} F_{ij}\delta_{\eta_i\eta_j}\mathcal{P}^{-1}(X_e). \tag{5.51}$$

5.8.5 Fit model

In order to avoid non-physical values of the parameters during the minimisation, some of them are redefined as follows,

$$\begin{aligned} f_{\parallel} &= x(f_{\parallel}) \cdot (1 - f_L), \\ |A_S^+|^2 &= x(|A_S^+|^2) \cdot (1 - |A_S^-|^2), \\ |A_{SS}|^2 &= x(|A_{SS}|^2) \cdot (1 - |A_S^-|^2 - |A_S^+|^2), \end{aligned} \tag{5.52}$$

where now $x(f_{\parallel})$, $x(|A_S^+|^2)$ and $x(|A_{SS}|^2)$ are free to float within $(0, 1)$, ensuring that the sum of all the squared amplitudes is never greater than 1. The polarisation fractions of the VV amplitudes are defined as,

$$f_L = \frac{|A_0|^2}{|A_0|^2 + |A_{\parallel}|^2 + |A_{\perp}|^2}, \quad f_{\parallel,\perp} = \frac{|A_{\parallel,\perp}|^2}{|A_0|^2 + |A_{\parallel}|^2 + |A_{\perp}|^2}, \tag{5.53}$$

being f_L the fraction of $B^0 \to K^{*0}\overline{K}^{*0}$ events longitudinally polarised.

Additionally, the Monte Carlo and the data samples are separated in two trigger categories, TOS and noTOS, because the way in which the events are triggered has an effect in the acceptance. The TOS category corresponds to the events that pass the `L0HadronDecision_TOS` trigger line and the noTOS category corresponds to the events that pass the `L0Global_TIS` line and do not pass the `L0HadronDecision_TOS`. Therefore events that pass both trigger lines are included in the TOS category. Four independent categories are then included in the fit depending on the year and the trigger, 2011_TOS, 2011_noTOS, 2012_TOS and 2012_noTOS. A different set of normalisation weights is obtained for each category.

5.8.6 Fit result

Using the model previously explained, an unbinned extended maximum likelihood fit of the sWeighted data (obtained in the four-body invariant mass fit from Chapter 5.7.3) simultaneously for the four independent categories (2011_TOS, 2011_noTOS, 2012_TOS and 2012_noTOS) is performed. The result of the amplitude analysis is shown in Table 5.26. In Table 5.27, the correlation coefficients are shown.

5.8.7 Visualisation

The normalisation weights method, used to take into account the acceptance, has the disadvantage of not allowing to visualise the result of the fit. For the purpose of displaying the data and the fit result an alternative acceptance is calculated. This acceptance is factorised in each of the five variables of the PDF model describing the data. Legendre polynomials, P_i, up to order 5 are used for the parametrisation of the acceptance in $\cos\theta_1$ and $\cos\theta_2$ and up to order 2 for ϕ, m_1 and m_2 as,

$$\begin{aligned} &\varepsilon(\theta_1, \theta_2, \phi, m_1, m_2) = \\ &\sum_{i=0}^{5} c_i^{\theta_1} P_i(\cos\theta_1) \sum_{j=0}^{5} c_j^{\theta_2} P_j(\cos\theta_2) \sum_{k=0}^{2} c_k^{\phi} P_k(\phi') \sum_{l=0}^{2} c_l^{m_1} P_k(m_1') \sum_{n=0}^{2} c_n^{m_2} P_n(m_2'), \end{aligned} \tag{5.54}$$

Table 5.26: Amplitude analysis result of the $B^0 \to K^+\pi^-K^-\pi^+$ data fit. The parameters $f_\parallel$, $|A_S^+|^2$ and $|A_{SS}|^2$ are obtained indirectly, as explained in the text, and the uncertainties take the correlations into account.

Parameter	Value
f_L	0.707 ± 0.053
$x(f_\parallel)$	0.39 ± 0.10
$\lvert A_S^-\rvert^2$	0.389 ± 0.053
$x(\lvert A_S^+\rvert^2)$	0.012 ± 0.029
$x(\lvert A_{SS}\rvert^2)$	0.047 ± 0.027
$\delta_\parallel$	2.55 ± 0.23
$\delta_\perp - \delta_S^+$	5.42 ± 0.92
δ_S^-	5.11 ± 0.13
δ_{SS}	2.72 ± 0.33
$f_\parallel$	0.115 ± 0.033
$\lvert A_S^+\rvert^2$	0.008 ± 0.013
$\lvert A_{SS}\rvert^2$	0.029 ± 0.016
Overall S-wave	0.425 ± 0.051

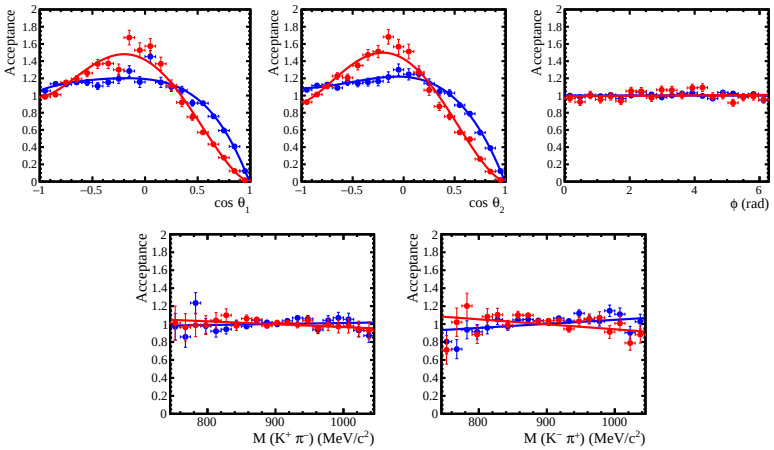

Figure 5.19: Acceptance used for the visualisation of the amplitude analysis fit. Legendre polynomials factorised in θ_1, θ_2, ϕ, m_1 and m_2 are used. The points correspond to the ratio of reconstructed over generated Monte Carlo events, used to extract the Legendre coefficients. In blue the TOS category and in red the noTOS category. Figures of 2012. The 2011 acceptance is shown in Fig. A.22.

where $m' = 2(m - m_{min})/(m_{max} - m_{min}) - 1$ and $\phi' = \phi/\pi$ are rescales of the invariant masses and of the azimutal angle.

To obtain the coefficients of the Legendre polynomials, the reconstructed MC events are divided by the generated ones, and the distribution for each variable is fitted with the expression shown in Eq. 5.54. In Fig. 5.19, the acceptance used for the visualisation is shown.

Table 5.27: Correlation coefficients among the different parameters measured in the $B^0 \to K^+\pi^-K^-\pi^+$ amplitude analysis.

Correlation	f_L	$x(f_\parallel)$	$\lvert A_S^-\rvert^2$	$x(\lvert A_S^+\rvert^2)$	$x(\lvert A_{SS}\rvert^2)$	$\delta_\parallel$	$\delta_\perp - \delta_S^+$	δ_S^-	δ_{SS}
f_L	1.000	0.164	−0.145	−0.028	0.016	−0.043	0.024	−0.159	0.022
$x(f_\parallel)$		1.000	0.029	0.086	−0.015	−0.077	0.044	−0.005	0.220
$\lvert A_S^-\rvert^2$			1.000	−0.182	−0.019	0.008	0.037	0.070	0.034
$x(\lvert A_S^+\rvert^2)$				1.000	−0.255	−0.103	−0.011	0.089	0.075
$x(\lvert A_{SS}\rvert^2)$					1.000	0.128	−0.090	−0.124	−0.237
$\delta_\parallel$						1.000	0.023	0.328	0.102
$\delta_\perp - \delta_S^+$							1.000	0.000	0.053
δ_S^-								1.000	0.202
δ_{SS}									1.000

In Fig. 5.20, the visualisation of the amplitude analysis result can be seen. The acceptance is parametrised with the Legendre polynomials and the parameters used are the result of the fit performed with the normalisation weights (Table 5.26). Only the figures of the 2012 samples are shown; the 2011 figures are in Appendix A.5.

5.8.8 Fit of the Monte Carlo simulated data

To test the self-consistency of the amplitude analysis method, an unbinned likelihood fit of the simulated data sample is performed after applying the corresponding normalisation weights. The datasets from both years are separated into trigger categories and fitted simultaneously, with a different set of normalisation weights used for each year and for each category. The simulated data are generated only with the P-wave contribution, and the parameters used for their generation are shown in the second column of Table 5.28. The amplitude model used for the fit is the same as previously explained. The normalisation weights are calculated with the same simulated dataset that is afterwards fitted and therefore the values obtained in the fit should be exactly the same as the ones used for the generation. The results are shown in the third column of Table 5.28. The agreement with the generated values is very good, as expected. It should be mentioned that, as commented when explaining the amplitude model, the $\delta_\perp$ phase only appears in the interference with another *CP*-odd state. If only the P-wave component is considered there is no other term with this *CP* parity and therefore the fit cannot determine $\delta_\perp$.

Another similar check is performed by splitting each subsample, defined by the year and the trigger category, in two halves, one with even event numbers and the other with odd event numbers. Then, normalisation weights determined from the first subsample are used to fit the second subsample, and the weights calculated from the second subsample are used to fit the first subsample. The results of this check are shown in the fourth and fifth column in Table 5.28, where it can be seen that the fitted values are in agreement with the generated ones.

5.8.9 Fit biases

A study of the fit biases is performed by generating and fitting a set of toy MC samples and comparing the values of the measured parameters with the generated ones. A set of

Table 5.28: Result of the reconstructed Monte Carlo fits and parameters used to generate it. In the third column, the normalisation weights are calculated with the same sample that is fitted afterwards. In the fourth and fifth column, the sample is divided in two subsamples, and the normalisation weights calculated with one subsample are used to fit the other subsample and vice versa.

Parameter	Generated	Fitted Full Sample	Fitted Subsample 1	Fitted Subsample 2
f_L	0.81	0.8100 ± 0.0019	0.8092 ± 0.0027	0.8109 ± 0.0027
$x(f_\parallel)$	0.5	0.5000 ± 0.0064	0.5019 ± 0.0093	0.4983 ± 0.0091
$\delta_\parallel$	π	3.14 ± 0.27	3.16 ± 0.22	3.14 ± 0.23
$\delta_\perp$	π	-	-	-
$f_\parallel$	0.095	0.0950 ± 0.0014	0.0958 ± 0.0021	0.0942 ± 0.0021

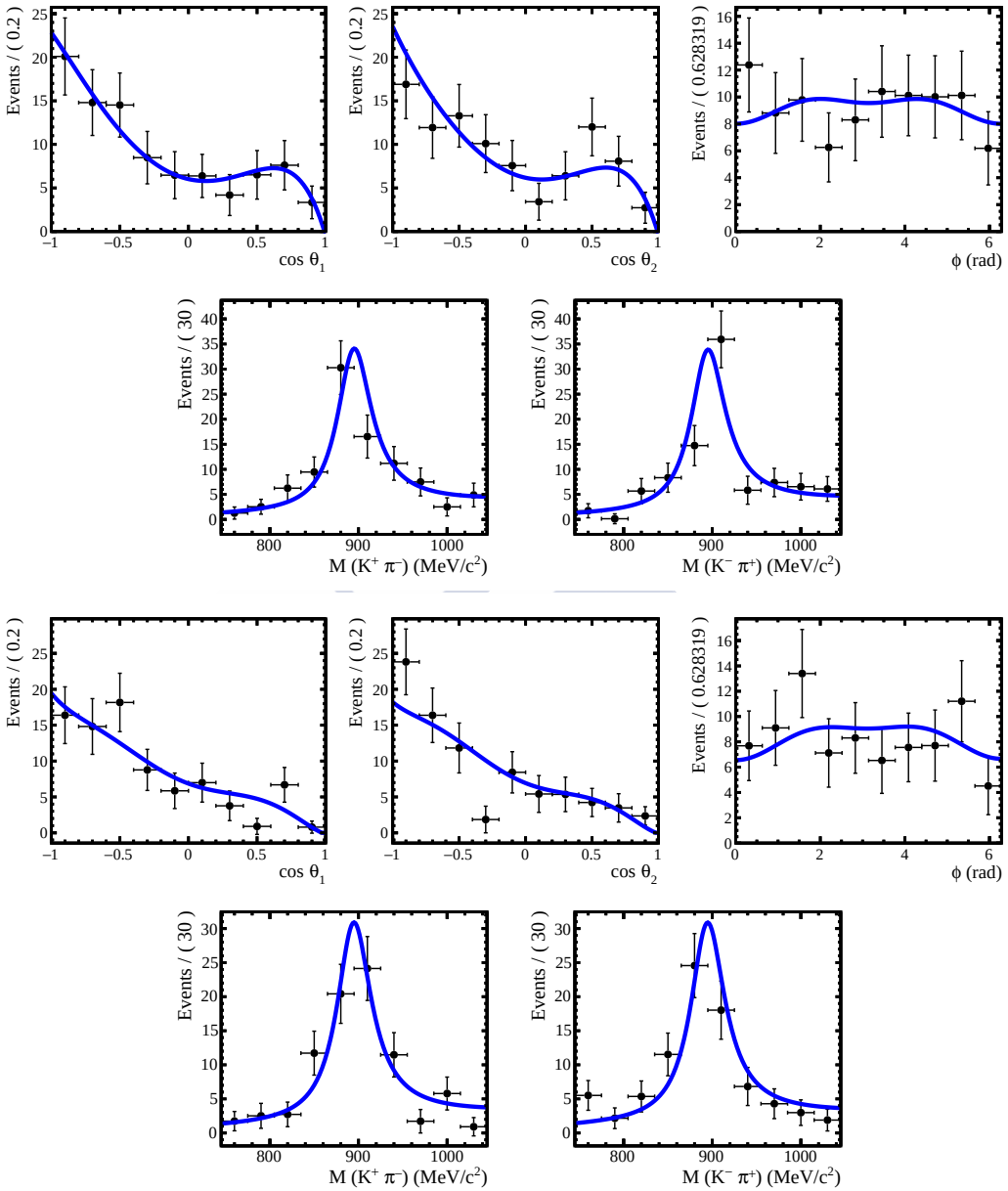

Figure 5.20: Visualisation of the $B^0 \to K^+\pi^-K^-\pi^+$ amplitude analysis result. The model with the acceptance parametrised as Legendre polynomials and the amplitude parameters obtained from the fit with the normalisation weights (Table 5.26) is superimposed to the sWeighted data. Only 2012 figures are shown. The 2011 visualisations can be seen in Fig. A.23. Top: TOS category. Bottom: noTOS category.

Table 5.29: Pull mean and width.

Parameter	Pull mean	Pull width
f_L	0.048 ± 0.032	1.002 ± 0.024
$x(f_\parallel)$	0.050 ± 0.032	1.010 ± 0.024
$\lvert A_S^- \rvert^2$	-0.0617 ± 0.032	1.004 ± 0.024
$x(\lvert A_S^+ \rvert^2)$	-0.0593 ± 0.037	1.127 ± 0.029
$x(\lvert A_{SS} \rvert^2)$	-0.0015 ± 0.034	1.050 ± 0.026
$\delta_\parallel$	0.049 ± 0.033	1.018 ± 0.025
$\delta_\perp - \delta_S^+$	0.044 ± 0.032	1.001 ± 0.024
δ_S^-	0.027 ± 0.033	1.025 ± 0.025
δ_{SS}	0.021 ± 0.032	1.007 ± 0.024

1000 samples is generated with 1000 events in each sample. The pull distributions are obtained as $\frac{r_{meas}-r_{gen}}{\sigma_r}$, where r_{meas} and r_{gen} are the measured and generated value of the parameter and σ_r is the estimated error in each of the individual experiments. The results of the Gaussian fits of the fitted parameters pull distributions are shown in Fig. 5.21. The mean and width of these Gaussian distributions are summarised in Table 5.29. A systematic uncertainty is assigned according to this study.

5.9 Systematic uncertainties of the amplitude analysis

Unfortunately the systematic uncertainties are not yet calculated. The sources that may introduce systematic uncertainties are listed below and the planned strategy to deal with them is briefly explained.

5.9.1 Fit biases

Use the study performed in Chapter 5.8.9 to assign a systematic uncertainty.

5.9.2 Acceptance model

Modify the normalisation weights used to peform the amplitude analysis, using for example the normalisation weights calculated with the $B_s^0 \to K^{*0}\overline{K}^{*}$ Monte Carlo, and define a systematic uncertainty according to the variation of the parameters with the two acceptance models.

5.9.3 S-wave mass model

Modify the lineshape used in Chapter 5.8.3.2 for the parametrisation of the S-wave.

5.9.4 Model parameters

Repeat the amplitude analysis modifying the values of the parameters entering into the mass propagators, shown in Table 5.25.

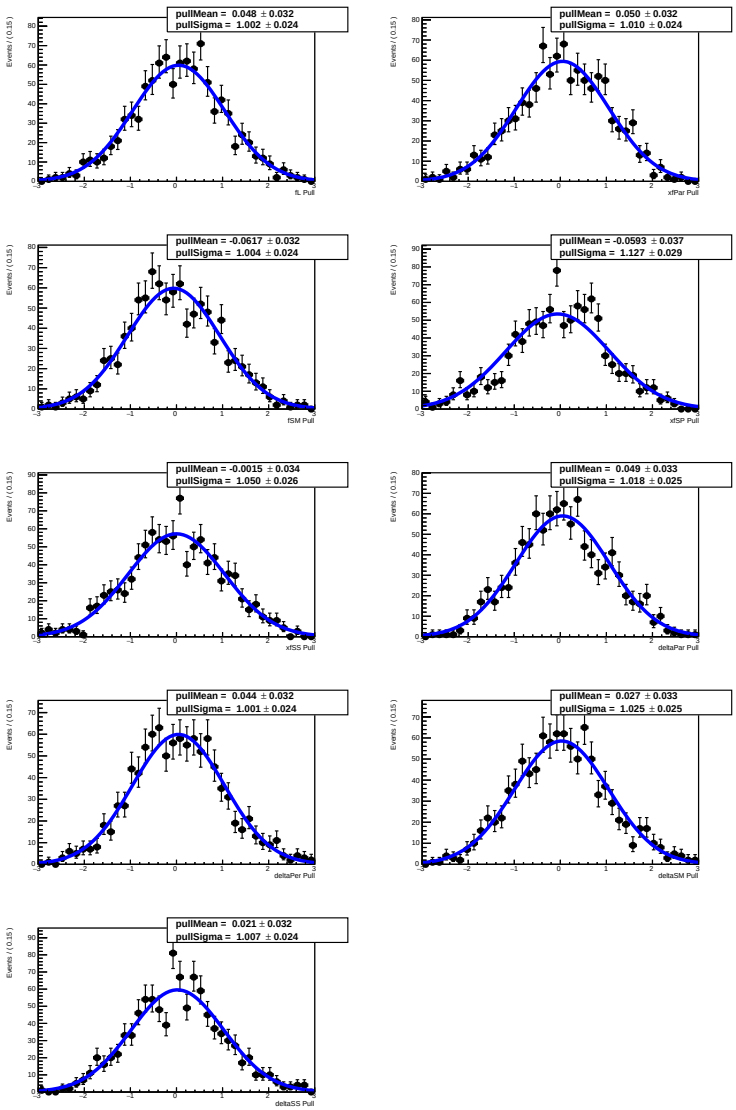

Figure 5.21: Pull distributions.

5.9.5 Monte Carlo statistics

To estimate a systematic uncertainty related to the statistics of the Monte Carlo, the data is fitted 1000 times after performing random variations of the normalisation weights according to their statistical uncertainties.

5.9.6 sWeighting procedure

Since the dataset used to obtain the amplitude analysis result is sWeighted, variations in the set of sWeights applied can lead to differences in this result. A systematic uncertainty is therefore assigned to the sWeights. The model used in the four-body invariant mass fit is modified and the differences in the amplitude fit result, obtained with the different

sWeights sets are compared. The lineshapes of the $B^0 \to K^{*0}\overline{K}^{*0}$, $B_s^0 \to K^{*0}\overline{K}^{*0}$ and $B^0 \to \phi K^{*0}$ are modified (2 Crystal-Ball, double or triple gaussian, ...), as well as the lineshape of the combinatorial background (polynomial of order 1, horizontal line, ...). Besides, the number of $B^0 \to \rho^0 K^{*0}$ decays injected as negative weights is modified, according to the uncertainties obtained in Table 5.17. Finally the yields of the Λ_b^0 decays, fixed in the four-body fit, are also changed within the statistical uncertainty of Table 5.18.

5.10 Comparative analysis of $B^0 \to K^{*0}\overline{K}^{*0}$ versus $B_s^0 \to K^{*0}\overline{K}^{*0}$

As mentioned in Chapter 5.1, the U-spin partners $B^0 \to K^{*0}\overline{K}^{*0}$ and $B_s^0 \to K^{*0}\overline{K}^{*0}$ decays have very different longitudinal polarisation fractions. In order to investigate the differences between these two decays, the fact that both final states are practically identical from the kinematic point of vue and therefore undergo the same trigger and selection biases, including angular acceptance, can be exploited. The $B_s^0 \to K^+\pi^-K^-\pi^+$ amplitude analysis performed in Ref. [189] is updated in this work analyzing the complete Run I sample. The results obtained in this work using only the 2011 data can be compared with the published measurements [74], testing the performance of our fitter. Besides, a direct comparison between the two decays is presented in Chapter 5.10.2.

5.10.1 Amplitude analysis of the $B_s^0 \to K^+\pi^-K^-\pi^+$ decay

The model used to fit this channel differs slightly from the one used for the $B^0 \to K^+\pi^-K^-\pi^+$ decay in Chapter 5.8. An untagged and time-integrated amplitude analysis is performed, so the obtention of the amplitude model follows the same path as the one shown for the B^0 up to Eq. 5.27. For the B^0 we assume that $\Delta\Gamma_d \sim 0$ and the expression is simplified. This assumption cannot be made for the B_s^0. The time-dependent expression that has to be used is then,

$$A_{ij}^{untagged} = A_{ij} + \bar{A}_{ij} = e^{-\Gamma t}\left[a_{ij}\cosh\left(\frac{\Delta\Gamma}{2}t\right) + b_{ij}\sinh\left(\frac{\Delta\Gamma}{2}t\right)\right]. \tag{5.55}$$

In this equation the decay-time acceptance is considered uniform, following Ref. [189]. In that analysis the effect of the decay-time acceptance is considered as a systematic effect and it is found to be small.

Integrating in time,

$$\int_0^\infty e^{-\Gamma t}\cosh\left(\frac{\Delta\Gamma}{2}t\right)dt = \frac{1}{2}\left(\frac{1}{\Gamma_H} + \frac{1}{\Gamma_L}\right), \int_0^\infty e^{-\Gamma t}\sinh\left(\frac{\Delta\Gamma}{2}t\right)dt = \frac{1}{2}\left(\frac{1}{\Gamma_H} - \frac{1}{\Gamma_L}\right), \tag{5.56}$$

and assuming SM,

$$A_{ij}^{untagged} = A_i A_j^* \delta_{\eta_i\eta_j}\left[\frac{1-\eta_i}{\Gamma_H} + \frac{1+\eta_i}{\Gamma_L}\right], \tag{5.57}$$

and the final expression for the decay rate is

$$\frac{d^5\Gamma}{d\cos\theta_1 d\cos\theta_2 d\phi dm_1 dm_2} \propto \sum_{i=1}^{6}\sum_{j\geq i}\mathcal{R}e\left[A_i A_j^*\left(\frac{1-\eta_i}{\Gamma_H} + \frac{1+\eta_i}{\Gamma_L}\right)F_{ij}\delta_{\eta_i\eta_j}\right], \tag{5.58}$$

with F_{ij} defined as explained in Eq. 5.19,

$$F_{ij} = \Phi_4(m_1, m_2) f_i f_j^* (2 - \delta_{ij}). \tag{5.59}$$

As well as in the case of the B^0 decay, in the B_s^0 decay there is no interference between a *CP*-even and a *CP*-odd state. Additionally, a factor $\frac{1}{\Gamma_L}$ appears in the terms with *CP*-even states and a factor $\frac{1}{\Gamma_H}$ in the *CP*-odd states.

Using this expression, an unbinned extended maximum likelihood fit of the dataset obtained in Chapter 5.7.3, with the sWeights calculated for the $B_s^0 \to K^+\pi^-K^-\pi^+$ decay is performed. In Table 5.30, the results obtained in this work and the ones obtained in Ref. [74] are shown. In Fig. 5.22, the visualisation of the result is presented, using an acceptance parametrised with Legendre polynomials, as explained in Chapter 5.8.7. In Table 5.31, the correlation coefficients measured in the fit are shown.

As can be seen, the 2011 results obtained in this work and the results in Ref. [74], where only 2011 data is studied, are in agreement. The different strategies followed in the two analyses can be responsible of the small discrepancies observed in the results: the selections are different; the background is extracted using different approaches, in Ref. [74], the background is parametrised in the amplitude fit, whereas in this analysis sWeights are obtained along with the insertion of negative weights; and the acceptances have different treatments, a parametrisation with Legendre polynomials is used in Ref. [74] and normalisation weights are calculated in this analysis.

In addition to this cross-check, the 2011+2012 result is also obtained, and it confirms the low longitudinal polarisation fraction of the $B_s^0 \to K^{*0}\overline{K}^{*0}$ decay, $f_L = 0.233 \pm 0.030$, and the large contribution of the scalar state.

Table 5.30: Result of the $B_s^0 \to K^+\pi^-K^-\pi^+$ untagged and time-integrated amplitude analysis in Ref. [74] and in this work. In Ref. [74] only 2011 data is analyzed.

Parameter	Ref. [74]	This analysis 2011	This analysis 2011 + 2012
f_L	0.201 ± 0.057	0.223 ± 0.058	0.233 ± 0.030
$x(f_\parallel)$	0.269 ± 0.055	0.230 ± 0.057	0.335 ± 0.032
$\lvert A_S^- \rvert^2$	0.485 ± 0.051	0.568 ± 0.036	0.540 ± 0.021
$x(\lvert A_S^+ \rvert^2)$	0.222 ± 0.058	0.084 ± 0.049	0.090 ± 0.025
$x(\lvert A_{SS} \rvert^2)$	0.164 ± 0.050	0.254 ± 0.047	0.251 ± 0.026
$\delta_\parallel$	2.17 ± 0.24	2.23 ± 0.23	2.34 ± 0.12
$\delta_\perp - \delta_S^+$	5.09 ± 0.21	4.81 ± 0.30	4.40 ± 0.17
δ_S^-	1.79 ± 0.19	1.87 ± 0.18	1.76 ± 0.10
δ_{SS}	1.06 ± 0.27	0.92 ± 0.23	1.02 ± 0.12
$f_\parallel$	0.215 ± 0.046	0.179 ± 0.046	0.257 ± 0.027
$\lvert A_S^+ \rvert^2$	0.114 ± 0.037	0.036 ± 0.023	0.041 ± 0.012
$\lvert A_{SS} \rvert^2$	0.066 ± 0.022	0.101 ± 0.020	0.105 ± 0.012
Overall S-wave	0.665 ± 0.067	0.705 ± 0.062	0.687 ± 0.037

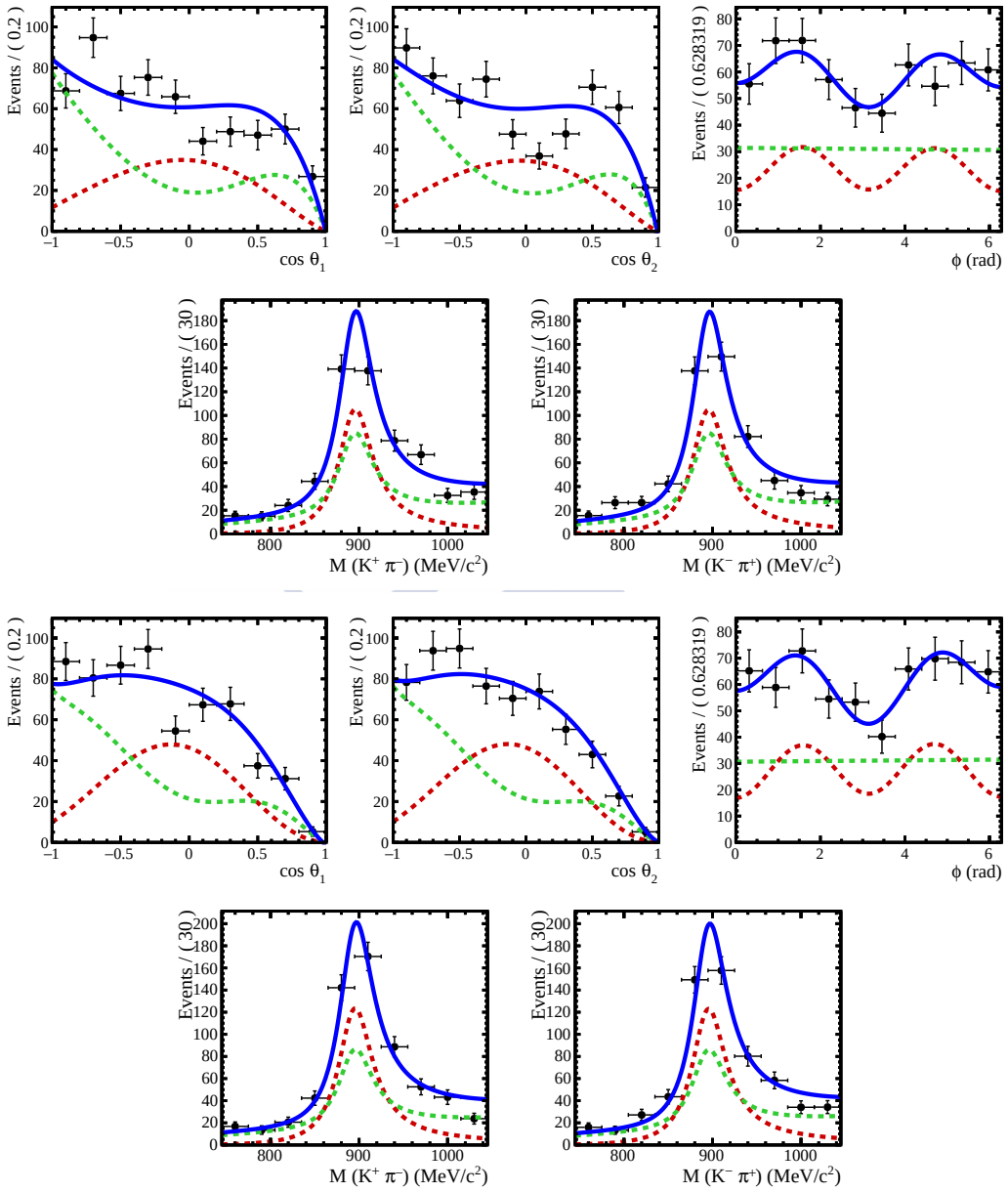

Figure 5.22: Visualisation of the result of the $B_s^0 \to K^+\pi^-K^-\pi^+$ amplitude analysis with the acceptance parametrised as Legendre polynomials. The solid dots represent the sWeighted data. The red dashed line is the P-wave component and the green dashed line is the S-wave component. Only figures of the 2012 data are shown. The 2011 visualisation is shown in Fig. A.24. Top: TOS category. Bottom: noTOS category.

Table 5.31: Correlation coefficients among the different parameters measured in the $B_s^0 \to K^+\pi^-K^-\pi^+$ amplitude analysis.

Correlation	f_L	$x(f_\parallel)$	$\lvert A_S^-\rvert^2$	$x(\lvert A_S^+\rvert^2)$	$x(\lvert A_{SS}\rvert^2)$	$\delta_\parallel$	$\delta_\perp - \delta_S^+$	δ_S^-	δ_{SS}
f_L	1.000	-0.006	-0.121	-0.075	-0.242	0.154	0.007	0.238	0.282
$x(f_\parallel)$		1.000	-0.096	0.057	-0.042	-0.005	0.014	0.022	0.009
$\lvert A_S^-\rvert^2$			1.000	-0.460	-0.062	0.256	-0.151	0.304	0.312
$x(\lvert A_S^+\rvert^2)$				1.000	-0.008	-0.153	0.153	-0.208	-0.214
$x(\lvert A_{SS}\rvert^2)$					1.000	-0.160	0.072	-0.264	-0.195
$\delta_\parallel$						1.000	-0.034	0.778	0.662
$\delta_\perp - \delta_S^+$							1.000	-0.023	-0.084
δ_S^-								1.000	0.810
δ_{SS}									1.000

USC UNIVERSIDADE DE SANTIAGO DE COMPOSTELA

5.10.2 Ratio of $B^0 \to K^{*0}\overline{K}^{*0}$ over $B_s^0 \to K^{*0}\overline{K}^{*0}$

To compare in a direct way the B^0 and B_s^0 decays, the ratio of B^0 events over B_s^0 events in bins of $\cos\theta$, ϕ and $m_{K\pi}$ is obtained. After adding together the $K^+\pi^-$ and $K^-\pi^+$ distributions, and the $\cos\theta_1$ and $\cos\theta_2$ distributions, which appear to be identical in the full simulation, 10 equal bins in the $\cos\theta$, ϕ and $m_{K\pi}$ distributions are taken and the yield ratios (normalised) at each bin determined. The ratio of the amplitude analyses models for the B^0 and for the B_s^0 obtained with the results previously measured are superimposed to the data, shown in Fig. 5.23.

For the $\cos\theta$ distribution, the probability of the B^0 data being different from the B_s^0 data is calculated fitting the ratio with an horizontal line fixed at 1, and is measured to be 4.8σ. On the other hand, the $\cos\theta$ distribution is more compatible with a parabola, which is expected if there is a different longitudinal K^* polarisation. In the ratio of the masses, the peak of the $K\pi$ mass distribution appears to be shifted between B^0 and B_s^0, which is indicated by a variation from a slight excess of the ratio to a depletion across the position of the K^{*0} pole. Such behaviour is expected as a result of the presence of different hadron phases in the interference terms, for B^0 and B_s^0, when account is taken of the strong asymmetry in the angular acceptance. In fact, our model with the best fit results is able to interpret correctly the observed behaviour in both distributions, neither of which is predicted to be constant. Similarly the azimuthal distribution of the ratio appears to be structured around π, in agreement with the model for the best fit.

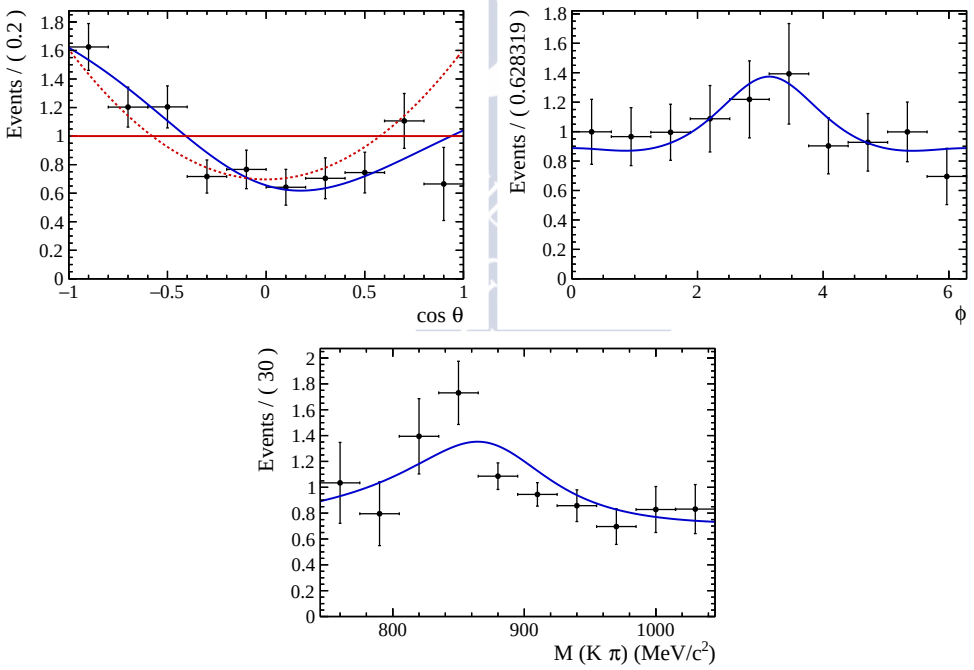

Figure 5.23: Ratio of $B^0 \to K^+\pi^-K^-\pi^+$ events over $B_s^0 \to K^+\pi^-K^-\pi^+$ events for the $\cos\theta$ (top left), the azimutal angle ϕ (top right) and the $K\pi$ invariant mass (bottom) with the ratio of the amplitude models superimposed (blue line). In the figure of the $\cos\theta$, an horizontal line (solid red line) and a parabola (dotted red line) are fitted to the data ratio.

5.11 Branching ratio

As mentioned in Chapter 5.1, the $B^0 \to K^{*0}\overline{K}^{*0}$ decay was already observed by the BaBar and Belle collaborations, and the measured branching ratios are not in good agreement. In order to clarify the discrepancy and provide the most accurate measurement, the branching ratio of the decay is obtained. Besides there are several theoretical predictions that can be tested. Since an absolute measurement is challenging, here the usual strategy of calculating the ratio of branching ratios with another decay whose BR is well known is followed. The obvious candidate to normalise the measurement is the $B_s^0 \to K^{*0}\overline{K}^{*0}$ decay. The final state is the same for both channels and the selection is common. As a result, most of the systematic effects should cancel. Moreover, there is a prediction scpecific to the ratio of longitudinal branching ratios that can be evaluated.

The formula for the ratio of branching ratios is given by

$$\frac{\mathcal{B}(B^0 \to K^{*0}\overline{K}^{*0})}{\mathcal{B}(B_s^0 \to K^{*0}\overline{K}^{*0})} = \frac{\varepsilon(B_s^0 \to K^{*0}\overline{K}^{*0})}{\varepsilon(B^0 \to K^{*0}\overline{K}^{*0})} \times \frac{f_s}{f_d} \times \frac{N_{B^0} \times f_{B^0 \to K^{*0}\overline{K}^{*0}}}{N_{B_s^0} \times f_{B_s^0 \to K^{*0}\overline{K}^{*0}}} \times \frac{\lambda_{f_L}(B_s^0 \to K^{*0}\overline{K}^{*0})}{\lambda_{f_L}(B^0 \to K^{*0}\overline{K}^{*0})}, \tag{5.60}$$

where $\varepsilon(B^0 \to K^{*0}\overline{K}^{*0})$ and $\varepsilon(B_s^0 \to K^{*0}\overline{K}^{*0})$ are the efficiencies of each decay, calculated in Chapter 5.6 and given in Table 5.10; the coefficients f_s and f_d are the b-quark hadronisation factors, that account for the different yields of B^0 and B_s^0 mesons and whose values are the same as used in Chapter 5.7.1; N_{B^0} and $N_{B_s^0}$ are the yields of $B^0 \to K^+\pi^-K^-\pi^+$ and $B_s^0 \to K^+\pi^-K^-\pi^+$ respectively, calculated in Chapter 5.7.3; and the purity factors $f_{B_{(s)}^0 \to K^{*0}\overline{K}^{*0}}$ and the overall efficiency corrections $\lambda_{f_L}(B_{(s)}^0 \to K^{*0}\overline{K}^{*0})$ are combined in

$$\kappa_{B_{(s)}^0 \to K^{*0}\overline{K}^{*0}} = \lambda_{f_L}(B_{(s)}^0 \to K^{*0}\overline{K}^{*0}) \times \frac{1}{f_{B_{(s)}^0 \to K^{*0}\overline{K}^{*0}}}, \tag{5.61}$$

which are calculated below for each decay.

5.11.1 Determination of $\kappa_{B^0 \to K^{*0}\overline{K}^{*0}}$ and $\kappa_{B_s^0 \to K^{*0}\overline{K}^{*0}}$

In the branching ratio calculation, Eq. 5.60, factors $\kappa_{B^0 \to K^{*0}\overline{K}^{*0}}$ and $\kappa_{B_s^0 \to K^{*0}\overline{K}^{*0}}$ are introduced. As commented, these parameters take into account two different effects, the purity and a correction to the overall efficiency. It is more convenient to calculate these two contributions together, as shown in the next paragraphs.

The purities are required to determine the amount of resonant decays $B^0 \to K^{*0}\overline{K}^{*0}$ and $B_s^0 \to K^{*0}\overline{K}^{*0}$ that are present in the yields obtained in Chapter 5.7.3, since these numbers correspond to the non-resonant decays $B^0 \to K^+\pi^-K^-\pi^+$ and $B_s^0 \to K^+\pi^-K^-\pi^+$. In order to measure the branching ratio of the decay $B^0 \to K^{*0}\overline{K}^{*0}$, where only the P-wave contributions are considered, the contributions from the S-wave and from the interference between the P- and the S-wave have to be removed.

The purity is calculated as the ratio of the distribution with the S-wave amplitudes set to zero and the total distribution, taking into account the acceptance,

$$f = \frac{\int \mathcal{P}(X; |A_S^+| = |A_S^-| = |A_{SS}| = 0)\epsilon(X)\mathrm{d}^5X}{\int \mathcal{P}(X)\epsilon(X)\mathrm{d}^5X} \tag{5.62}$$

where $X = \{\Omega, m_1, m_2\}$, $\mathcal{P}$ is the PDF (with $|A_S^+|$, $|A_S^-|$ and $|A_{SS}|$ set to zero in the numerator) and $\epsilon(X)$ is the acceptance. For the $B^0 \to K^{*0}\overline{K}^{*0}$ decay, using Eq. 5.47,

$$f_{B^0 \to K^{*0}\overline{K}^{*0}} = \frac{\sum_{i=1}^{3}\sum_{j\geq i}\mathcal{R}e[A_i A_j^* \omega_{ij}]}{\sum_{i=1}^{6}\sum_{j\geq i}\mathcal{R}e[A_i A_j^* \omega_{ij}]} \tag{5.63}$$

is obtained, where in the numerator the terms $|A_S^-|$, $|A_S^+|$ and $|A_{SS}|$ are set to zero and ω_{ij} are the normalisation weights. For the $B_s^0 \to K^{*0}\overline{K}^{*0}$ decay, the PDF is obtained from Eq. 5.58, and then the purity is

$$f_{B_s^0 \to K^{*0}\overline{K}^{*0}} = \frac{\sum_{i=1}^{3}\sum_{j\geq i}\mathcal{R}e[A_i A_j^* \left(\frac{1-\eta_i}{\Gamma_H} + \frac{1+\eta_i}{\Gamma_L}\right)\omega_{ij}]}{\sum_{i=1}^{6}\sum_{j\geq i}\mathcal{R}e[A_i A_j^* \left(\frac{1-\eta_i}{\Gamma_H} + \frac{1+\eta_i}{\Gamma_L}\right)\omega_{ij}]}. \tag{5.64}$$

The second term included in the κ factor is λ_{f_L}. The MC used for the obtention of the efficiencies is generated with a given polarisation. This polarisation can be different from the one measured in data and therefore the efficiencies calculated need to be corrected for this difference of polarisations.

The efficiency is proportional to the integral of the observed distribution divided by the integral of the physical distribution,

$$\epsilon \propto \frac{\int \mathcal{P}(X; |A_S^+| = |A_S^-| = |A_{SS}| = 0)\epsilon(X)\mathrm{d}^5X}{\int \mathcal{P}(X; |A_S^+| = |A_S^-| = |A_{SS}| = 0)\mathrm{d}^5X}. \tag{5.65}$$

For the calculation of the efficiencies in Chapter 5.6, simulated events are used, which are generated with a given choice of amplitudes that might differ from the one obtained in data. The correction factor is then,

$$\lambda_{f_L} = \frac{\int \mathcal{P}(X; |A_S^+| = |A_S^-| = |A_{SS}| = 0)\epsilon(X)\mathrm{d}^5X}{(1 - |A_S^-|^2 - |A_S^+|^2 - |A_{SS}|^2)\int \mathcal{P}^{MC}(X)\epsilon(X)\mathrm{d}^5X}, \tag{5.66}$$

where $\mathcal{P}^{MC}$ is the PDF used to generate the MC sample. For the $B^0 \to K^*K^{*0}$ decay,

$$\lambda_{f_L}(B^0 \to K^{*0}\overline{K}^{*0}) = \frac{\sum_{i=1}^{3}\sum_{j\geq i}\mathcal{R}e[A_i^{data} A_j^{*data} \omega_{ij}]}{(1 - |A_S^-|^2 - |A_S^+|^2 - |A_{SS}|^2)\sum_{i=1}^{3}\sum_{j\geq i}\mathcal{R}e[A_i^{MC} A_j^{*MC} \omega_{ij}]}, \tag{5.67}$$

and for the $B_s^0 \to K^*K^{*0}$ decay,

$$\lambda_{f_L}(B_s^0 \to K^{*0}\overline{K}^{*0}) = \frac{\sum_{i=1}^{3}\sum_{j\geq i}\mathcal{R}e[A_i^{data} A_j^{*data} \left(\frac{1-\eta_i}{\Gamma_H} + \frac{1+\eta_i}{\Gamma_L}\right)\omega_{ij}]}{(1 - |A_S^-|^2 - |A_S^+|^2 - |A_{SS}|^2)\sum_{i=1}^{3}\sum_{j\geq i}\mathcal{R}e[A_i^{MC} A_j^{*MC} \left(\frac{1-\eta_i}{\Gamma_H} + \frac{1+\eta_i}{\Gamma_L}\right)\omega_{ij}]}. \tag{5.68}$$

From the previous expressions, the κ factors are obtained,

$$\begin{aligned}\kappa_{B^0 \to K^{*0}\overline{K}^{*0}} &= \lambda_{f_L}(B^0 \to K^{*0}\overline{K}^{*0}) \times \frac{1}{f_{B^0 \to K^{*0}\overline{K}^{*0}}} \\ &= \frac{\sum_{i=1}^{6}\sum_{j\geq i}\mathcal{R}e[A_i A_j^* \omega_{ij}]}{(1 - |A_S^-|^2 - |A_S^+|^2 - |A_{SS}|^2)\sum_{i=1}^{3}\sum_{j\geq i}\mathcal{R}e[A_i^{MC} A_j^{*MC} \omega_{ij}]}\end{aligned} \tag{5.69}$$

and

$$\kappa_{B_s^0\to K^{*0}\overline{K}^{*0}} = \lambda_{f_L}(B_s^0\to K^{*0}\overline{K}^{*0}) \times \frac{1}{f_{B_s^0\to K^{*0}\overline{K}^{*0}}} = \frac{\sum_{i=1}^{6}\sum_{j\geq i}\mathcal{R}e[A_iA_j^*\left(\frac{1-\eta_i}{\Gamma_H}+\frac{1+\eta_i}{\Gamma_L}\right)\omega_{ij}]}{(1-|A_S^-|^2-|A_S^+|^2-|A_{SS}|^2)\sum_{i=1}^{3}\sum_{j\geq i}\mathcal{R}e[A_i^{MC}A_j^{*MC}\left(\frac{1-\eta_i}{\Gamma_H}+\frac{1+\eta_i}{\Gamma_L}\right)\omega_{ij}]}, \tag{5.70}$$

that can be obtained using the parameters measured in the amplitude analyses. The value of the ratio can be seen in Table 5.32.

5.11.2 Systematic uncertainties

Unfortunately the systematic uncertainties are not yet calculated. The various sources of systematic uncertainties that are considered are listed below with a brief explanation of the procedure to calculate them.

5.11.2.1 Four-body invariant mass fit

Modify the model used in the four-body invariant mass fit and use the variation in the yields to estimate the associated systematic uncertainty. Follow the alternatives described in Chapter 5.9.6.

5.11.2.2 Efficiencies

As explained in Chapter 5.6, all the efficiencies but the PID efficiency are calculated with MC. Since some level of disagreement can exist between the efficiencies calculated from MC and the ones in data, a systematic uncertainty is calculated. This uncertainty is expected to be small, because in the ratio of efficiencies $\varepsilon(B_s^0\to K^{*0}\overline{K}^{*0})/\varepsilon(B^0\to K^{*0}\overline{K}^{*0})$ most of the systematic effects should cancel.

For the tracking efficiency, the agreement between data and simulation is not guaranteed. The differences can be taken into account applying a track-by-track correction provided by the tracking group.

A further contribution to the systematic of the efficiencies comes from the imperfect description of the `L0HadronTOS` trigger in the simulation. The trigger efficiencies are recalculated using data-driven tables from calibration data.

Finally, even though the PID efficiencies are calculated with a data-driven technique, also a systematic uncertainty is assigned. A different binning scheme is used to obtain the efficiencies.

5.11.2.3 Amplitude analysis result

Since the result of the BR depends on the result of the amplitude analysis, a systematic uncertainty is assigned varying the results of the amplitude analysis within the uncertainties.

5.11.3 $\mathcal{B}(B^0 \to K^{*0}\overline{K}^{*0})/\mathcal{B}(B_s^0 \to K^{*0}\overline{K}^{*0})$ result

The result of the ratio of BR is obtained using Eq. 5.60, computed with the values summarised in Table 5.32 and after properly weighting each of the different data taking periods,

$$\frac{\mathcal{B}(B^0 \to K^{*0}\overline{K}^{*0})}{\mathcal{B}(B_s^0 \to K^{*0}\overline{K}^{*0})} = 0.0799 \pm 0.0073\,(\text{stat}) \pm 0.0037 \left(\frac{f_s}{f_d}\right). \tag{5.71}$$

Using the BR of the $B_s^0 \to K^{*0}\overline{K}^{*0}$ decay extracted from Ref. [74], $\mathcal{B}(B_s^0 \to K^{*0}\overline{K}^{*0}) = (10.8 \pm 2.1\,(\text{stat})) \times 10^{-6}$, the branching ratio of the $B^0 \to K^{*0}\overline{K}^{*0}$ decay is obtained to be

$$\mathcal{B}(B^0 \to K^{*0}\overline{K}^{*0}) = (8.6 \pm 1.9\,(\text{stat}) \pm 0.05\,(f_s/f_d)) \times 10^{-7}. \tag{5.72}$$

A theoretical prediction exists for the ratio of longitudinal branching ratios of $B^0 \to K^{*0}\overline{K}^{*0}$ and $B_s^0 \to K^{*0}\overline{K}^{*0}$, that can be obtained experimentally as [55],

$$R_{sd} = \frac{\mathcal{B}(B_s^0) f_L(B_s^0)}{\mathcal{B}(B^0) f_L(B^0)} \frac{1 - y^2}{1 + y\cos\phi_s}, \tag{5.73}$$

where $y = \Delta\Gamma_s/(2\Gamma_s)$. With the values of $\Delta\Gamma_s$, Γ_s and ϕ_s taken from Ref. [46], and with the measurements performed in this work, the experimental ratio is found to be

$$R_{sd} = 3.89 \pm 0.68\,(\text{stat}). \tag{5.74}$$

5.12 Summary

Both the $B^0 \to K^+\pi^-K^-\pi^+$ and the $B_s^0 \to K^+\pi^-K^-\pi^+$ decays are studied using $3\,\text{fb}^{-1}$ of data taken by LHCb in 2011 and 2012. Untagged and time-integrated amplitude analyses are performed, taking into account the three helicity angles and the two $K\pi$ invariant masses. The fractions of the different polarisations contributing in a window of $\pm 150\,\text{MeV}/c^2$ around the K^{*0} and $\overline{K}^{*0}$ masses are obtained. Six amplitudes are allowed in the fit, three belonging to the P-wave and three to the S-wave, along with their interferences. For the P-wave, only the $K^*(892)^0$ resonance is considered, whereas for the S-wave, the spin-0 $K_0^*(1430)^0$ resonance plus a non-resonant component $(K^\pm\pi^\mp)_0$ are included.

For the $B^0 \to K^+\pi^-K^-\pi^+$ mode this is the first study carried out at LHCb. All the steps of the fit model construction are described in Chapter 5.8, with the results and their statistical uncertainties summarised in Table 5.26. The visualisation of the fit is shown

Table 5.32: Values of the parameters used in the calculation of $\mathcal{B}(B^0 \to K^{*0}\overline{K}^{*0})/\mathcal{B}(B_s^0 \to K^{*0}\overline{K}^{*0})$.

Parameter	2011	2012
N_{B^0}	98 ± 12	248 ± 19
$N_{B_s^0}$	614 ± 26	1332 ± 38
$\varepsilon_{B_s^0 \to K^{*0}\overline{K}^{*0}}/\varepsilon_{B^0 \to K^{*0}\overline{K}^{*0}}$	1.1071 ± 0.0095	1.1167 ± 0.0074
$\kappa_{B_s^0 \to K^{*0}\overline{K}^{*0}}/\kappa_{B^0 \to K^{*0}\overline{K}^{*0}}$	1.57 ± 0.13	1.53 ± 0.12
f_s/f_d	0.262 ± 0.015	

in Fig. 5.20, and in Appendix A.5. The high polarisation of the vector-vector decay is confirmed by the measurement $f_L = 0.707 \pm 0.053\,(\text{stat})$, which is in agreement with the result obtained by BaBar, $f_L = 0.80^{+0.10}_{-0.12}\,(\text{stat}) \pm 0.06\,(\text{syst})$ [183], but with a reduction of the statistical uncertainty by a factor 2. The S-wave fraction is found to be rather large, (0.425 ± 0.051).

The study of the $B^0_s \to K^{*0}\overline{K}^{*0}$ decay updates a previous analysis [74]. The model for the amplitude analysis of this mode is developed in Chapter 5.10.1. Both the result of this thesis and of the previous analysis are shown in Table 5.30. There is good agreement between them, confirming the low longitudinal polarisation of the $B^0_s \to K^{*0}\overline{K}^{*0}$ decay, $f_L = 0.233 \pm 0.030$, and the large contribution of the S-wave, (0.687 ± 0.037).

A comparison between both decays is performed in Chapter 5.10.2. The significance of the B^0_s $\cos\theta$ distribution being different from the B^0 distribution is found to be 4.8σ.

In addition, the ratio of branching ratios $\mathcal{B}(B^0 \to K^{*0}\overline{K}^{*0})/\mathcal{B}(B^0_s \to K^{*0}\overline{K}^{*0})$ is measured in Chapter 5.11.3. The result, combining 2011 and 2012, can be seen in Eq. 5.71. Using the $B^0_s \to K^{*0}\overline{K}^{*0}$ BR from Ref. [74], the branching ratio of the $B^0 \to K^{*0}\overline{K}^{*0}$ is obtained, $\mathcal{B}(B^0 \to K^{*0}\overline{K}^{*0}) = (8.6 \pm 1.9\,(\text{stat})) \times 10^{-7}$. The result is in agreement with the previous measurement by BaBar, $[1.28^{+0.35}_{-0.30}\,(\text{stat}) \pm 0.11\,(\text{syst})] \times 10^{-6}$ and with the theoretical predictions [64].

Finally, a theoretical prediction for the relation of the longitudinal branching ratios of both channels is shown in Ref. [55], $R_{sd} = \mathcal{B}^{\text{long}}(B^0_s \to K^{*0}\overline{K}^{*0})/\mathcal{B}^{\text{long}}(B^0 \to K^{*0}\overline{K}^{*0}) = 16.4 \pm 5.2$. The experimental ratio is found to be, $R_{sd} = 3.89 \pm 0.68\,(\text{stat})$.

USC UNIVERSIDADE DE SANTIAGO DE COMPOSTELA

6 Conclusions

The study of *CP*-violation in Flavour Changing Neutral Currents is one of the most promising places to look for New Physics. These channels provide an excellent probe of new heavy particles entering the penguin quantum loops, which would induce experimental results different from the Standard Model expectation. In this work, data taken by the LHCb experiment are used to investigate this type of decays. Since the studied channels correspond to a B-meson decaying to two light vector mesons, different combinations of the final-state polarisations are allowed, and an amplitude analysis is needed to separate the different contributions. Two different analyses are described in the thesis.

Firstly, an study of the $B^0 \to K^{*0}\overline{K}^{*0}$ and $B_s^0 \to K^{*0}\overline{K}^{*0}$ decays is performed with $3\,\text{fb}^{-1}$ of data taken by LHCb at $\sqrt{s} = 7\,\text{TeV}$ ($1\,\text{fb}^{-1}$) and $\sqrt{s} = 8\,\text{TeV}$ ($2\,\text{fb}^{-1}$). This is the first analysis of the $B^0 \to K^{*0}\overline{K}^{*0}$ mode at LHCb.

In the first place, a flavour-untagged and time-integrated amplitude analysis of the rare decay $B^0 \to K^{*0}\overline{K}^{*0}$, first observed by BaBar [183], using a sizeable statistics of 346 events is performed. This analysis finds a strong longitudinal polarisation of the K^{*0}, $f_L = 0.707 \pm 0.053\,(\text{stat})$, thus confirming the earlier BaBar result of $f_L = 0.80^{+0.10}_{-0.12}\,(\text{stat}) \pm 0.06\,(\text{syst})$. However a strong scalar component (S-wave) of (0.425 ± 0.051) is also seen, which was not considered in the BaBar analysis.

Yet the strong longitudinal polarisation found for B^0 meson is at variance with the small f_L found for B_s^0 in the same final state, $f_L = 0.201 \pm 0.057\,(\text{stat}) \pm 0.040\,(\text{syst})$ [74]. This is surprising, therefore the $B_s^0 \to K^{*0}\overline{K}^{*0}$ angular analysis is reanalyzed with $3\,\text{fb}^{-1}$, and a detailed comparison between both decays, which are U-spin mirror of one another, is made. The result confirms the discrepancy and improves the precision in the value, $f_L = 0.233 \pm 0.030$ (stat), and corroborates the large contribution of the S-wave, (0.687 ± 0.037). Particular attention is given to the B^0/B_s^0 ratios of the angular $(\theta_{1,2}, \phi)$ and $K^{\pm}\pi^{\mp}$ mass distributions, since they are essentially insensitive to possible systematic biases caused by defficiencies in the detector simulation. The polar distribution shows incompatibility at the level of 4.8σ.

In the second place, the B^0/B_s^0 ratio of branching ratios in the $K^{*0}\overline{K}^{*0}$ final state is measured,

$$\frac{\mathcal{B}(B^0 \to K^{*0}\overline{K}^{*0})}{\mathcal{B}(B_s^0 \to K^{*0}\overline{K}^{*0})} = 0.0799 \pm 0.0073\,(\text{stat}) \pm 0.0036 \left(\frac{f_s}{f_d}\right).$$

Using the $B_s^0 \to K^{*0}\overline{K}^{*0}$ BR from Ref. [74], the branching ratio of the $B^0 \to K^{*0}\overline{K}^{*0}$ decay is obtained to be

$$\mathcal{B}(B^0 \to K^{*0}\overline{K}^{*0}) = (8.6 \pm 1.9\,(\text{stat})) \times 10^{-7},$$

that is in agreement with the previous measurement by BaBar, $[1.28^{+0.35}_{-0.30}\,(\text{stat})\pm 0.11\,(\text{syst})]\times 10^{-6}$ [183], and with the theoretical predictions, $(0.6^{+0.5}_{-0.3})\times 10^{-6}$ [64]. Some predictions concern specifically the longitudinal branching ratios [55, 56]. The experimental result is found to be, $\mathcal{B}^{\text{long}}(B^0_s\to K^{*0}\overline{K}^{*0})/\mathcal{B}^{\text{long}}(B^0\to K^{*0}\overline{K}^{*0}) = 3.89\pm 0.68\,(\text{stat})$, to be compared with the prediction, 16.4 ± 5.2.

Additionally, $1\,\text{fb}^{-1}$ of data taken in 2011 at $\sqrt{s}=7\,\text{TeV}$ are studied searching for the $B^0_s\to\phi\overline{K}^{*0}$ decay. A total of 29.9 ± 6.4 candidates of $B^0_s\to(K^+K^-)(K^-\pi^+)$ are found within the mass windows $746\,\text{MeV}/c^2 < M(K^\pm\pi^\mp) < 1046\,\text{MeV}/c^2$ and $1012.5\,\text{MeV}/c^2 < M(K^+K^-) < 1026.5\,\text{MeV}/c^2$. The analysis of the K^+K^- and the $K^-\pi^+$ mass distributions is consistent with $(84\pm 2)\%$ of the signal originating from resonant ϕ and $\overline{K}^{*0}$ mesons. The significance of the $B^0_s\to\phi\overline{K}^{*0}$ resonant contribution is calculated to be 6.5σ. This is the first observation of this channel.

The branching ratio $\mathcal{B}(B^0_s\to\phi\overline{K}^{*0})$ is determined with the result,

$$\mathcal{B}(B^0_s\to\phi\overline{K}^{*0}) = \left(1.09\pm 0.24\,(\text{stat})\pm 0.11\,(\text{syst})\pm 0.08\left(\frac{f_d}{f_s}\right)\right)\times 10^{-6},$$

using the $B^0\to\phi K^{*0}$ decay as a normalisation channel. This result is roughly three times the theoretical expectation in QCD factorisation of $(0.4^{+0.5}_{-0.3})\times 10^{-6}$ [64] and larger than the perturbative QCD value of $(0.65^{+0.33}_{-0.23})\times 10^{-6}$ [171], although the values are compatible within 1σ. Better precision on both the theoretical and experimental values would allow this channel to probe for physics beyond the SM.

An angular analysis of the $B^0_s\to\phi\overline{K}^{*0}$ decay results in the polarisation fractions and phase difference

$$\begin{aligned} f_L &= 0.46\pm 0.11\,(\text{stat})\pm 0.08\,(\text{syst}),\\ f_\parallel &= 0.27\pm 0.10\,(\text{stat})\pm 0.05\,(\text{syst}),\\ \delta_\parallel &= 2.38\pm 0.48\,(\text{stat})\pm 0.29\,(\text{syst}). \end{aligned}$$

The small value obtained for the longitudinal polarisation fraction follows the trend of the $b\to s$ penguin decays $B^0\to\phi K^{*0}$ and $B^0_s\to\phi\phi$. The result is compatible with the longitudinal polarisation fraction $f_L = 0.40\pm 0.14$ measured in $B^0\to\rho^0 K^{*0}$ decays [70], the penguin amplitude of which is related to $B^0_s\to\phi\overline{K}^{*0}$ by $d\leftrightarrow s$ exchange. Finally, the result is smaller than the prediction of perturbative QCD, $f_L = 0.712^{+0.042}_{-0.048}$, given in Ref. [171].

Summary

The Standard Model of Particle Physics (SM) is the theory which better explains the behaviour of the elementary particles composing the universe and the interactions among them. Despite its great success, there are still phenomena which cannot be described within the SM. Among the phenomena that the SM cannot explain, one of the most interesting is matter-antimatter asymmetry. In order to produce matter and antimatter at different rates, *CP*-symmetry violation is a necessary condition. The amount of *CP*-violation predicted by the SM is not enough to explain the large matter-antimmater imbalance. All the measurements of processes calculable in the SM have been in agreement with the predictions. Finding a *CP*-violating process not accounted for in the SM would therefore be of great importance to constrain the models that correctly describe the new physics (NP).

B-mesons are the ideal place to look for *CP*-violation. Loop-mediated penguin decays of *B*-mesons are sensitive probes for physics beyond the SM, in particular $b \to q$ flavour-changing neutral currents (FCNC) processes are very sensitive to deviations from the SM induced by NP particles circulating in the loop. Three FCNC decays are studied in this thesis: $B^0 \to K^{*0}\overline{K}^{*0}$, $B_s^0 \to K^{*0}\overline{K}^{*0}$ and $B_s^0 \to \phi\overline{K}^{*0}$. These decays are of the type $B_{(s)}^0 \to VV'$, where V and V' are light vector mesons, and an amplitude analysis is therefore needed to obtain the different polarisation fractions.

The LHCb experiment at the LHC collider was designed to study rare decays and *CP*-violation in *b*-hadron decays, with the hope of revealing physics beyond the SM. Data taken by the LHCb experiment in 2011 are analyzed to search for the $B_s^0 \to \phi\overline{K}^{*0}$ decay and data taken in 2011 and 2012 are analyzed to study the $B^0 \to K^{*0}\overline{K}^{*0}$ and $B_s^0 \to K^{*0}\overline{K}^{*0}$ decays.

S.1 The LHCb experiment

The LHCb (Large Hadron Collider beauty) experiment is one of the four main particle detectors placed in the 27 km long tunnel of the LHC (Large Hadron Collider). The main goal of the LHCb experiment is the study of Heavy Flavour physics, looking for indirect evidences of NP in *CP* violation and rare decays of beauty and charm hadrons.

To separate the decays of interest from the background, both displaced vertex and high transverse momentum signatures are exploited. Excellent vertex resolution is required to measure impact parameters and to achieve a good decay time resolution Good momentum and invariant mass resolution are important to minimise combinatorial background and resolve heavy-flavour decays with kinematically similar topologies. Charged

particle identification is essential to isolate suppressed decays and for b-quark flavour tagging. Finally, to benefit from the high event rate at the LHC, a high-bandwidth data acquisition system and a robust and selective trigger system are required.

S.1.1 The LHCb detector

The LHCb detector was designed as a single-arm spectrometer with a forward angular coverage from approximately 10 mrad to 300 (250) mrad in the bending (non-bending) plane, with respect to the beam axis. The main elements of the LHCb detector, shown in Fig. S.1, are:

- the magnet: warm dipole magnet to measure the momentum of the charged particles;
- the vertex locator (VELO): uses silicon microstrips detectors that give information about the track coordinates close to the interaction region;
- the tracking system: composed of the Tracker Turicensis (TT), a silicon microstrip detector situated upstream of the magnet, and of three Tracking Stations (T1, T2 and T3) downstream of the magnet, made of silicon microstrips in the regions close to the beam pipe (Inner Tracker or IT) and of straw-tubes in the outer region (Outer Tracker or OT);
- two RICH detectors (Ring Imaging CHerenkov): provide particle identification of charged tracks. The upstream detector, RICH1, uses aerogel and C_4F_{10} radiators to cover the low moment range, while the downstream detector, RICH2, covers the high momentum range using a CF_4 radiator;
- the calorimeter system: composed of a Scintillator Pad Detector (SPD), a Preshower (PS), an Electromagnetic Calorimeter (ECAL) and a Hadronic Calorimeter (HCAL);

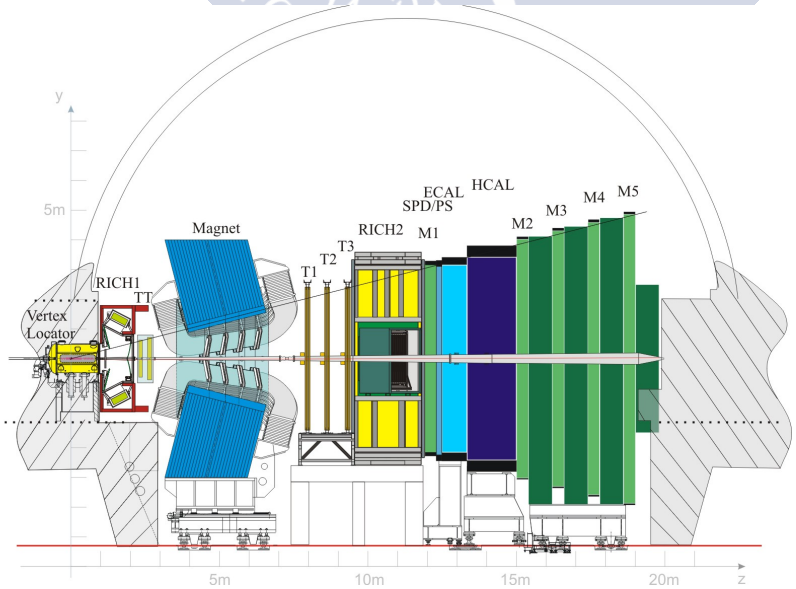

Figure S.1: General layout of the LHCb detector.

- the muon detection system: composed of Multi Wire Proportional Chamber (MWPC), except in the region with the highest rate, where Gas Electron Multipliers (GEM) are used.

Due to the available resources not all the collected information can be written to storage. The trigger reduces the several millions of events that are produced per second to just a few thousand. To reject uninteresting background events the trigger uses the distinctive features of the b- and c-hadron decays: tracks with significant non-zero impact parameter with respect to the primary vertex and high transverse momenta with respect to the beam axis.

S.2 First observation of the $B_s^0 \to \phi \overline{K}^{*0}$ decay

The mode $B_s^0 \to \phi \overline{K}^{*0}$ is the only $b \to d$ penguin decay into vector mesons that has not previously been observed. The most stringent previous experimental limit on the branching ratio is $\mathcal{B}(B_s^0 \to \phi \overline{K}^{*0}) < 1.0 \times 10^{-3}$ at the 90% confidence level, whereas calculations based on the QCD factorisation framework predict a value of $(0.4^{+0.5}_{-0.3}) \times 10^{-6}$ while in perturbative QCD a value of $(0.65^{+0.33}_{-0.23}) \times 10^{-6}$ is obtained.

The first observation of the $B_s^0 \to \phi \overline{K}^{*0}$ decay, with $\phi \to K^+K^-$ and $\overline{K}^{*0} \to K^-\pi^+$, is reported. A total of $1\,\text{fb}^{-1}$ of LHCb data collected in 2011 at $\sqrt{s} = 7\,\text{TeV}$ are analyzed to search for $B_s^0 \to \phi(K^+K^-)\overline{K}^{*0}(K^-\pi^+)$ decays. The branching ratio is measured using the mode $B^0 \to \phi K^{*0}$ as a reference. The study of the angular distributions in the $B_s^0 \to \phi \overline{K}^{*0}$ channel provides a measurement of its polarisation. A prediction of $f_0 = 0.712^{+0.042}_{-0.048}$ is made for the longitudinal polarisation fraction, using the perturbative QCD approach.

S.2.1 Selection

A first data reduction is performed applying a set of rectangular offline cuts. Additional selection requirements are implemented to remove charmed and charmless contamination from misidentified backgrounds.

Further background reduction is achieved by defining a multivariate discriminant from information regarding the event topology, the Geometrical Likelihood (GL). The GL is trained to optimise its discrimination power using a set of $B_s^0 \to \phi \overline{K}^{*0}$ simulated events for the signal and a sample of real data outside the signal region for the background.

S.2.2 Invariant mass spectrum

An extended maximum likelihood fit is used to fit the data passing the selection criteria. For the parametrisation of the invariant mass shape of the signal events a sample of $B^0 \to J/\psi K^{*0}$ events is used. Both, B^0 and B_s^0 are parametrised with identical shapes, differing only on the mass shift. The shape is described by the sum of a Crystal Ball (CB) and Gaussian functions that share a common mean. In addition, partially reconstructed B-meson decays where a pion is lost are described by a convolution of the ARGUS shape with a Gaussian distribution. The last contribution is an exponential function to account for combinatorial background. In Fig. S.2 the invariant mass distribution together with the fit contribution is shown.

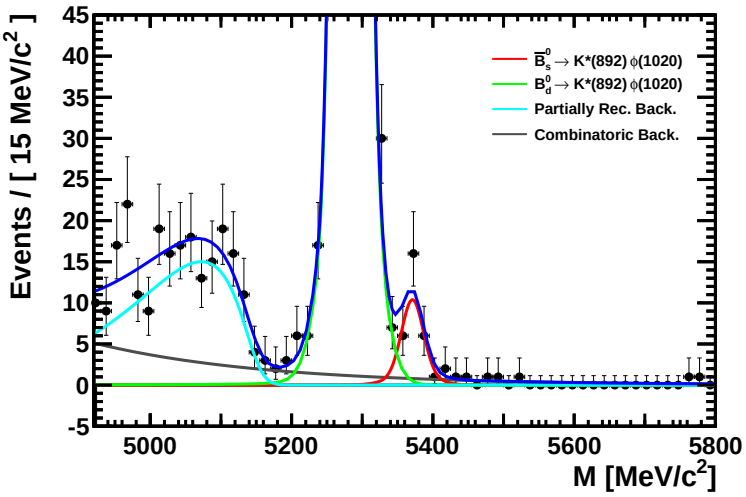

Figure S.2: Fit to the $KK\pi\pi$ mass distribution.

The yields of $B^0_s \to (K^+K^-)(K^-\pi^+)$ and $B^0 \to (K^+K^-)(\pi^+\pi^-)$ decays are 29.9 ± 6.4 and 1000 ± 32, respectively. A significance of 6.5σ is obtained including the systematic effects.

S.2.3 K^{*0} and ϕ purity in the signal

The amount of non-resonant (S-wave) contributions present in the K^+K^- and $K^-\pi^+$ final state systems must be subtracted to calculate the branching ratio. The S-wave component is evaluated for the $B^0 \to \phi K^{*0}$ channel and assumed to be of the same size in the $B^0_s \to \phi \bar{K}^{*0}$ decay. The K^+K^- and $K^+\pi^-$ mass distributions within a $\pm 30\,\text{MeV}/c^2$ window of the B^0 mass are described by the sum of a resonant spin-1 function plus a S-wave contribution.

The fraction of events from K^{*0} decays within a $\pm 150\,\text{MeV}/c^2$ window around the K^{*0} mass results in a purity of 0.89 ± 0.02. A purity of 0.950 ± 0.005 is found in a $\pm 7\,\text{MeV}/c^2$ window around the knwon ϕ mass. This means a total ϕK^{*0} purity of 0.84 ± 0.02.

S.2.4 Polarisation analysis

A flavour-averaged and time-integrated polarisation analysis is performed. The decay rate dependence on the polarisation angles can be written as

$$\frac{\mathrm{d}^3\Gamma}{\mathrm{d}\cos\theta_1\,\mathrm{d}\cos\theta_2\,\mathrm{d}\varphi} \propto |A_0|^2 \cos^2\theta_1 \cos^2\theta_2 + |A_\parallel|^2 \frac{1}{2} \sin^2\theta_1 \sin^2\theta_2 \cos^2\varphi + |A_\perp|^2 \frac{1}{2} \sin^2\theta_1 \sin^2\theta_2 \sin^2\varphi + |A_0||A_\parallel| \cos\delta_\parallel \frac{1}{2\sqrt{2}} \sin 2\theta_1 \sin 2\theta_2 \cos\varphi. \tag{S.1}$$

The acceptance is parametrised using simulated data as a function of θ_2. The acceptance is found not to depend on θ_1 and φ. A small correction is introduced for discrepancies

in the p_T spectrum and the trigger selection between simulation and data.

The data in a $\pm 30\,\mathrm{MeV}/c^2$ window around the B_s^0 mass are fitted to the angular distribution. The fit accounts for two additional contributions: the combinatorial background, parametrised from the distributions of events in the high-mass B sideband, and the tail of the $B^0 \to \phi K^{*0}$ decays, that are polarised with the values measured in previous analyses.

Systematic uncertainties due to the angular acceptance and to the model used to account for the combinatorial background are included, a systematic uncertainty is calculated modifying the set of events fitted and a last contribution is calculated including a possible S-wave fraction.

The final results are,

$$\begin{aligned} f_L &= 0.46 \pm 0.11\,(\mathrm{stat}) \pm 0.08\,(\mathrm{syst}), \\ f_\parallel &= 0.27 \pm 0.10\,(\mathrm{stat}) \pm 0.05\,(\mathrm{syst}), \\ \delta_\parallel &= 2.38 \pm 0.48\,(\mathrm{stat}) \pm 0.29\,(\mathrm{syst}), \end{aligned} \tag{S.2}$$

and are shown in Fig. S.3.

The small value obtained for the longitudinal polarisation fraction follows the trend of the $b \to s$ penguin decays. Finally, the result is smaller than the prediction of perturbative QCD, $f_L = 0.712^{+0.042}_{-0.048}$.

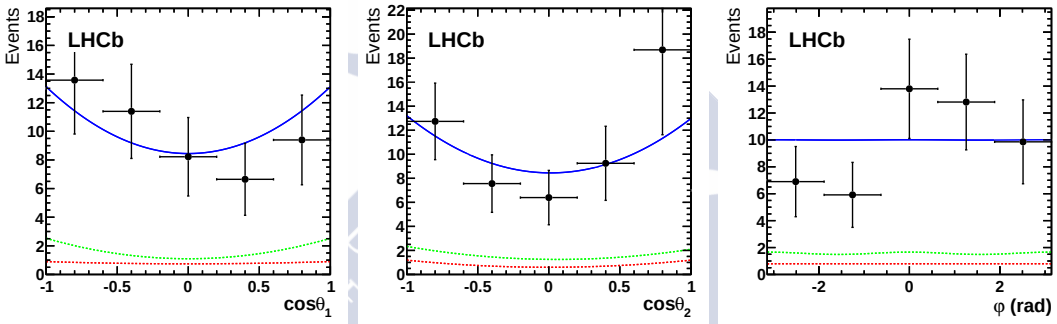

Figure S.3: Result of the fit to the angular distribution of the $B_s^0 \to \phi \overline{K}^{*0}$ candidates in $\cos\theta_1$, $\cos\theta_2$ and φ. The red dashed line and the green line correspond respectively to the combinatorial background and to the $B^0 \to \phi K^{*0}$ contributions in the B_s^0 region.

S.2.5 Determination of the $B_s^0 \to \phi \overline{K}^{*0}$ branching ratio

The branching ratio is calculated with the $B^0 \to \phi K^{*0}$ channel as normalisation. The value of the branching ratio is computed from

$$\mathcal{B}(B_s^0 \to \phi \overline{K}^{*0}) = \lambda_{f_L} \times \frac{f_d}{f_s} \times \mathcal{B}(B^0 \to \phi K^{*0}) \times \frac{N_s}{N_d}, \tag{S.3}$$

where N_s and N_d stand for the number of B_s^0 and B^0 candidates, $\frac{f_d}{f_s}$ is the ratio of hadronisation factors and λ_{f_L} is a correction factor to account for the different polarisation of the two channels.

Systematic uncertainties due to the four-body spectra fit model, to the longitudinal polarisation, to the purity, to the efficiency and to the particle identification are considered.

The final result obtained is

$$\mathcal{B}(B_s^0 \to \phi \overline{K}^{*0}) = \left(1.09 \pm 0.24\,(\text{stat}) \pm 0.11\,(\text{syst}) \pm 0.08\left(\frac{f_d}{f_s}\right)\right) \times 10^{-6}. \qquad \text{(S.4)}$$

The result is roughly three times the theoretical expectation in QCD factorisation of $(0.4^{+0.5}_{-0.3}) \times 10^{-6}$ and larger than the perturbative QCD value of $(0.65^{+0.33}_{-0.23}) \times 10^{-6}$, although the values are compatible within 1σ.

S.3 Study of the decays $B^0 \to K^{*0}\overline{K}^{*0}$ and $B_s^0 \to K^{*0}\overline{K}^{*0}$

The BaBar collaboration reported the discovery of the $B^0 \to K^{*0}\overline{K}^{*0}$ channel with 6σ significance and a measurement of its branching ratio $\mathcal{B}(B^0 \to K^{*0}\overline{K}^{*0}) = (1.28^{+0.35}_{-0.30} \pm 0.11) \times 10^{-6}$. This is in tension with the results of the Belle collaboration that published an upper limit of $\mathcal{B}(B^0 \to K^{*0}\overline{K}^{*0}) < 0.8 \times 10^{-6}$ at the 90% confidence level. The BaBar publication also reported a measurement of the longitudinal polarisation $f_0 = 0.80^{+0.12}_{-0.13}$, which is large compared to the value obtained for its U-spin partner, the $B_s^0 \to K^{*0}\overline{K}^{*0}$ decay, $f_L = 0.201 \pm 0.057 \pm 0.040$.

A total of $3\,\text{fb}^{-1}$ of LHCb data collected in 2011 ($1\,\text{fb}^{-1}$) and 2012 ($2\,\text{fb}^{-1}$) at $\sqrt{s} = 7\,\text{TeV}$ and $\sqrt{s} = 8\,\text{TeV}$ respectively is analyzed. An untagged and time-integrated amplitude analysis of the $B^0 \to K^+\pi^-K^-\pi^+$ decay in a mass window of $\pm 150\,\text{MeV}/c^2$ around the K^{*0} mass with the is presented. Special attention is paid to the measurement of the longitudinal polarisation fraction, trying to confirm the high value obtained by BaBar. An update, including the 2011 and 2012 datasets, of the $B_s^0 \to K^{*0}\overline{K}^{*0}$ untagged time-integrated amplitude analysis, published previously by LHCb with 2011 data, is performed. Additionally, a direct comparison between the $B^0 \to K^{*0}\overline{K}^{*0}$ and the $B_s^0 \to K^{*0}\overline{K}^{*0}$ decays to confirm the large difference in the measured polarisation fractions is presented. Finally, the ratio of branching ratios $\mathcal{B}(B^0 \to K^{*0}\overline{K}^{*0})/\mathcal{B}(B_s^0 \to K^{*0}\overline{K}^{*0})$ is measured.

S.3.1 Event selection

Some studies are carried out to try to identify the main sources of background that can pollute the signal. Potential peaking backgrounds with charm are negligible. After the stripping and trigger cuts, the fiducial region is defined and a cut to reject muons is applied.

To further increase the signal to background separation, a Multivariate Analysis (MVA) is performed. A Boosted Decision Tree with Gradient boost (BDTG) is the method chosen. The BDTG is trained using a set of simulated $B^0 \to K^{*0}\overline{K}^{*0}$ events for the signal and a data sample in the high B mass sideband for the background.

Three cross-feed backgrounds are identified: $B^0 \to \phi K^{*0}$, $B^0 \to \rho^0 K^{*0}$ and $\Lambda_b^0 \to p\pi K^{*0}$. To reduce their contribution, a set of cuts in the particle identification variables is included.

S.3.2 Four-body invariant mass fit

To perform the amplitude analyses, a $B^0_{(s)} \to K^+\pi^-K^-\pi^+$ background-free sample is achieved applying a set of sWeights obtained from the four-body invariant mass fit.

Six contributions are allowed in the four-body invariant mass fit. The $B^0 \to K^+\pi^-K^-\pi^+$ and $B^0_s \to K^+\pi^-K^-\pi^+$ decays are parametrised with identical shapes, Ipatia functions with the parameters obtained from simulation, differing only on the mass shift. The $B^0 \to \phi K^{*0}$ decay is modelled by the sum of a Crystal Ball and a Gaussian that share a common mean, whereas the $\Lambda^0_b \to p\pi K^{*0}$ decay is described with a single Crystal Ball. The parameters are obtained from simulation. In addition, the partially reconstructed background is described by a convolution of the ARGUS shape with a Gaussian distribution and to account for the combinatorial background, an exponential function is used.

The $B^0 \to \rho^0 K^{*0}$ events that survive the particle identification cuts are extracted with the application of negative weights. The $\Lambda^0_b \to p\pi K^{*0}$ contribution is fixed in the $K^+\pi^-K^-\pi^+$ invariant mass fit to the value obtained from a fit of the $p\pi K\pi$ mass.

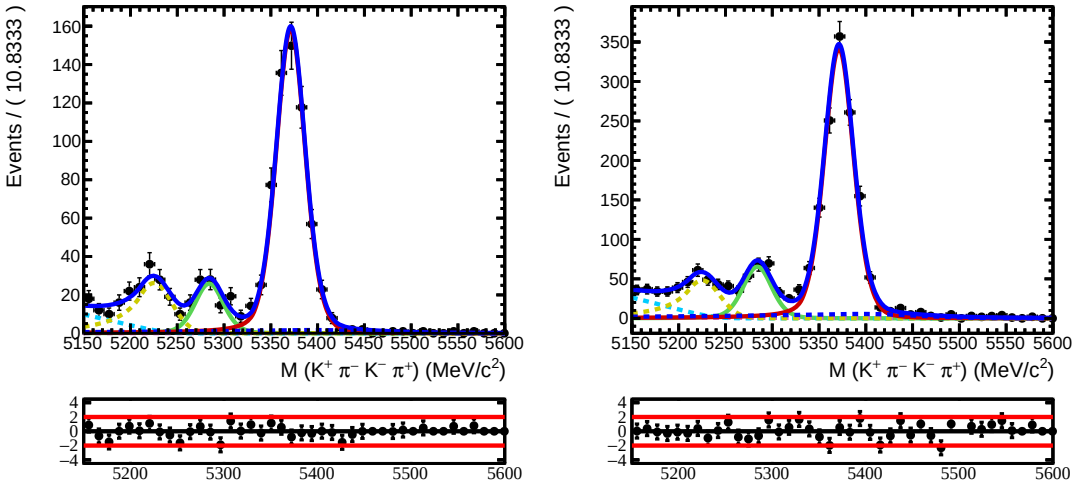

Figure S.4: Simultaneous four-body invariant mass fit result of the 2011 (left) and 2012 (right) data samples.

With the model described previously, an unbinned extended maximum likelihood fit is performed simultaneously for the 2011 and 2012 $K^+\pi^-K^-\pi^+$ invariant mass data samples. The fit is shown in Fig. S.4. The yields of $B^0 \to K^+\pi^-K^-\pi^+$ decays are 98 ± 12 in 2011 and 248 ± 19 in 2012, which means more than seven times the amount of events previously observed. The yields of $B^0_s \to K^+\pi^-K^-\pi^+$ are 614 ± 26 and 1332 ± 38 in 2011 and 2012, respectively.

S.4 Amplitude analysis of the $B^0 \to K^{*0}\overline{K}^{*0}$ decay

A flavour-averaged time-integrated amplitude analysis of the $B^0 \to K^+\pi^-K^-\pi^+$ decay is performed in a $K\pi$ window of $\pm 150\,\text{MeV}/c^2$ around the K^{*0} nominal mass. In this mass window, an scalar component (S) is found in addition to the vector resonance (V). The

decay is therefore described by six different amplitudes. Three of them are the amplitudes describing the $B \to V_1 V_2$ decay (P–wave), which, in the transversity basis, are: A_0, $A_\parallel$ and $A_\perp$. The other three (S–wave) correspond to the decays:[1] $B \to V_1 S_2$ (A_{VS}), $B \to S_1 V_2$ (A_{SV}) and $B \to S_1 S_2$ (A_{SS}).

It is convenient to define the linear combinations $A_s^+ = (A_{VS} + A_{SV})/\sqrt{2}$, $A_s^- = (A_{VS} - A_{SV})/\sqrt{2}$, so the decay rate can be entirely written in terms of amplitudes associated to *CP*-even (0, $\parallel$, S^- ,SS) and *CP*-odd ($\perp$, S^+) eigenstates.

Assuming no *CP*-violation, the decay rate, written as a function of the helicity angles (θ_1, θ_2 and ϕ) and the invariant masses of the $K^+\pi^-$ (m_1) and $K^-\pi^+$ (m_2) pairs, is given by

$$\frac{\mathrm{d}^5\Gamma}{\mathrm{d}\cos\theta_1 \mathrm{d}\cos\theta_2 \mathrm{d}\phi \mathrm{d}m_1 \mathrm{d}m_2} \propto \sum_{i=1}^{6} \sum_{j \geq i} \mathcal{R}e[A_i A_j^* F_{ij} \delta_{\eta_i \eta_j}], \tag{S.5}$$

where η_i is the *CP* parity of each amplitude A_i, $\delta_{\eta_i \eta_j} = 1$ if $i = j$ and 0 otherwise, and $F_{ij} = \Phi_4(m_1, m_2) f_i f_j^* (2 - \delta_{ij})$, with Φ_4 the four-body phase space factor and the angle-mass terms f_i defined in Table S.1.

Table S.1: Amplitudes A_i and angle-mass terms f_i.

i	A_i	f_i
1	A_0	$\cos\theta_1 \cos\theta_2 \mathcal{M}_1(m_1)\mathcal{M}_1(m_2)$
2	$A_\parallel$	$\frac{1}{\sqrt{2}} \sin\theta_1 \sin\theta_2 \cos\phi \mathcal{M}_1(m_1)\mathcal{M}_1(m_2)$
3	$A_\perp$	$\frac{i}{\sqrt{2}} \sin\theta_1 \sin\theta_2 \sin\phi \mathcal{M}_1(m_1)\mathcal{M}_1(m_2)$
4	A_S^+	$-\frac{1}{\sqrt{6}}(\cos\theta_1 \mathcal{M}_1(m_1)\mathcal{M}_0(m_2) - \cos\theta_2 \mathcal{M}_0(m_1)\mathcal{M}_1(m_2))$
5	A_S^-	$-\frac{1}{\sqrt{6}}(\cos\theta_1 \mathcal{M}_1(m_1)\mathcal{M}_0(m_2) + \cos\theta_2 \mathcal{M}_0(m_1)\mathcal{M}_1(m_2))$
6	A_{SS}	$-\frac{1}{3}\mathcal{M}_0(m_1)\mathcal{M}_0(m_2)$

A non-uniform efficiency has to be included to take into account the effects of detector geometry and the inefficiencies due to the selection and to the reconstruction. The angular acceptance has been tackled with the use of normalisation weights, obtained from a simulated sample of $B^0 \to K^{*0}\overline{K}^{*0}$. Since the normalisation weights do not allow to visualise the result of the fit, for this purpose a parametrised acceptance with Legendre polynomials is calculated.

The candidates are split in four categories, by year and according to their trigger path, since differences are found in the acceptance for each category, A simultaneous fit is performed. The result for one of the categories is shown in Fig. S.5. The longitudinal polarisation fraction, $f_L = 0.707 \pm 0.053$, is in agreement and confirms the large value measured by BaBar, $f_L = 0.80^{+0.12}_{-0.13}$, with a reduction of the statistical uncertainty by a factor 2. Unfortunately the systematic errors are still not calculated.

S.5 Amplitude analysis of the $B_s^0 \to K^{*0}\overline{K}^{*0}$ decay

An untagged time-integrated amplitude analysis of the $B_s^0 \to K^{*0}\overline{K}^{*0}$ decay was published by the LHCb experiment with the 2011 data. An update of this measurement is performed

[1] The underscript 1 (2) corresponds the $K^+\pi^-$ ($K^-\pi^+$) pair.

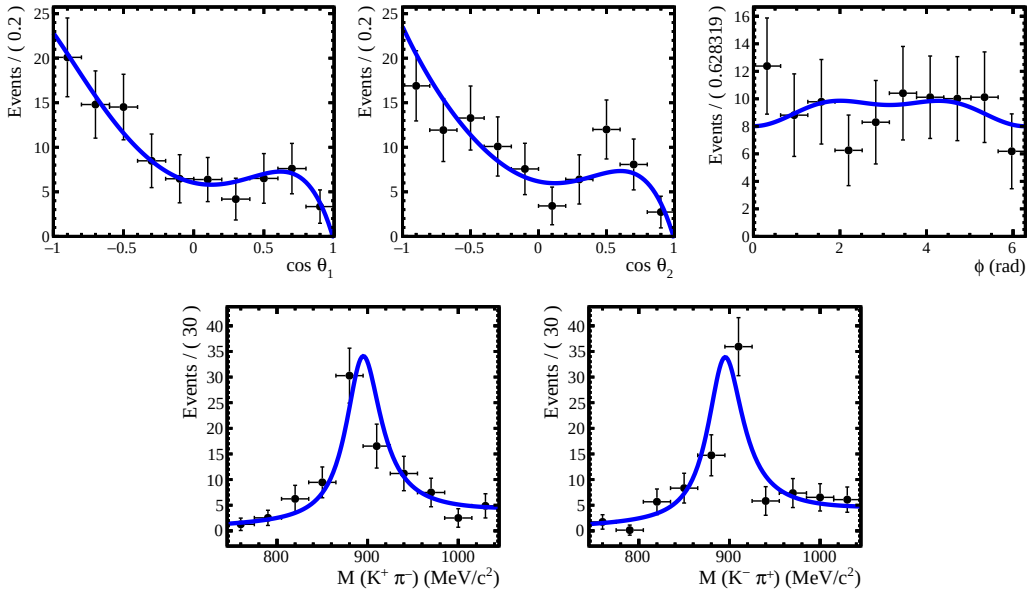

Figure S.5: Visualisation of the $B^0 \to K^+\pi^-K^-\pi^+$ amplitude analysis result.

including the 2012 data.

The decay rate for the B_s^0 decay is the same as for the B^0 decay, Eq. S.5, with a factor $\frac{1}{\Gamma_L}$ in the terms with *CP*-even states and a factor $\frac{1}{\Gamma_H}$ in the *CP*-odd states, where Γ_L and Γ_H are the lifetimes of the light and heavy B_s^0 mass eigenstates.

The results obtained using the 2011 data are in agreement with the published measurements. Additionally, the 2011 + 2012 results are also consistent with the previous measurements. In particular, the value of the longitudinal polarisation fraction in this work, 0.233 ± 0.030, is compatible with the published value, 0.201 ± 0.057, confirming the low polarisation of the $B_s^0 \to K^{*0}\overline{K}^{*0}$ decay. Moreover, a large S-wave contribution is found, (0.687 ± 0.037), comparable with the value already reported, (0.665 ± 0.067).

S.6 Comparative analysis of $B^0 \to K^{*0}\overline{K}^{*0}$ versus $B_s^0 \to K^{*0}\overline{K}^{*0}$

The polarisation of the $B^0 \to K^{*0}\overline{K}^{*0}$ and $B_s^0 \to K^{*0}\overline{K}^{*0}$ decays are found to be very different, even though the diagrams describing both processes are identical after a $d \leftrightarrow s$ exchange.

In order to investigate the differences between these two decays in a direct way, the fact that both final states are practically identical from the kinematic point of vue and therefore undergo the same trigger and selection biases is used. The ratio of B^0 events over B_s^0 events in bins of $\cos\theta$, ϕ and $m_{K\pi}$ is obtained.

For the $\cos\theta$ distribution, the probability of the B^0 data being different from the B_s^0 data is calculated fitting the ratio with an horizontal line fixed at 1, and is measured to be 4.8σ. In the ratio of the masses, the peak of the $K\pi$ mass distribution appears to be shifted between B^0 and B_s^0. Such behaviour is expected as a result of the presence of different hadron phases in the interference terms, for B^0 and B_s^0, when account is taken

of the strong asymmetry in the angular acceptance. Similarly the azimuthal distribution of the ratio appears to be structured around π, in agreement with the model for the best fit.

S.7 $\mathcal{B}\,(B^0 \to K^{*0}\overline{K}^{*0})/\mathcal{B}\,(B_s^0 \to K^{*0}\overline{K}^{*0})$

The ratio of branching ratios of the B^0 and B_s^0 decays into $K^{*0}\overline{K}^{*0}$ is obtained with

$$\frac{\mathcal{B}(B^0 \to K^{*0}\overline{K}^{*0})}{\mathcal{B}(B_s^0 \to K^{*0}\overline{K}^{*0})} = \frac{\varepsilon(B_s^0 \to K^{*0}\overline{K}^{*0})}{\varepsilon(B^0 \to K^{*0}\overline{K}^{*0})} \times \frac{f_s}{f_d} \times \frac{N_{B^0} \times f_{B^0 \to K^{*0}\overline{K}^{*0}}}{N_{B_s^0} \times f_{B_s^0 \to K^{*0}\overline{K}^{*0}}} \times \frac{\lambda_{f_L}(B_s^0 \to K^{*0}\overline{K}^{*0})}{\lambda_{f_L}(B^0 \to K^{*0}\overline{K}^{*0})}, \tag{S.6}$$

where $\varepsilon(B^0 \to K^{*0}\overline{K}^{*0})$ and $\varepsilon(B_s^0 \to K^{*0}\overline{K}^{*0})$ are the efficiencies of each decay, calculated using simulated data and data-driven techniques. The coefficients f_s and f_d are the b-quark hadronisation factors, that account for the different yields of B^0 and B_s^0 mesons. N_{B^0} and $N_{B_s^0}$ are the yields of $B^0 \to K^+\pi^-K^-\pi^+$ and $B_s^0 \to K^+\pi^-K^-\pi^+$ decays respectively. The purity factors $f_{B_{(s)}^0 \to K^{*0}\overline{K}^{*0}}$ determine the amount of resonant $B^0 \to K^{*0}\overline{K}^{*0}$ and $B_s^0 \to K^{*0}\overline{K}^{*0}$ decays. And $\lambda_{f_L}(B_{(s)}^0 \to K^{*0}\overline{K}^{*0})$ is a correction that accounts for the different efficiencies obtained in the simulation and in data, since the simulated events are not generated with the same polarisations as the data.

The result of the ratio of BR is obtained after properly weighting each of the different data taking periods,

$$\frac{\mathcal{B}(B^0 \to K^{*0}\overline{K}^{*0})}{\mathcal{B}(B_s^0 \to K^{*0}\overline{K}^{*0})} = 0.0799 \pm 0.0073\,(\text{stat}) \pm 0.0036 \left(\frac{f_s}{f_d}\right). \tag{S.7}$$

Using the $B_s^0 \to K^{*0}\overline{K}^{*0}$ BR, $\mathcal{B}(B_s^0 \to K^{*0}\overline{K}^{*0}) = (10.8 \pm 2.1\,(\text{stat})) \times 10^{-6}$, the branching ratio of the $B^0 \to K^{*0}\overline{K}^{*0}$ decay is obtained,

$$\mathcal{B}(B^0 \to K^{*0}\overline{K}^{*0}) = (8.6 \pm 1.9\,(\text{stat})) \times 10^{-7}. \tag{S.8}$$

The result is in agreement with the previous measurement by BaBar, $[1.28^{+0.35}_{-0.30}\,(\text{stat}) \pm 0.11\,(\text{syst})] \times 10^{-6}$ and with the theoretical predictions, $(0.6^{+0.5}_{-0.3}) \times 10^{-6}$. Finally, a theoretical prediction for the relation of the longitudinal branching ratios of both channels is shown in Ref. [55], $R_{sd} = \mathcal{B}^{\text{long}}(B_s^0 \to K^{*0}\overline{K}^{*0})/\mathcal{B}^{\text{long}}(B^0 \to K^{*0}\overline{K}^{*0}) = 16.4 \pm 5.2$. The experimental ratio is found to be, $R_{sd} = 3.89 \pm 0.68\,(\text{stat})$.

Resumo

O Modelo Estándar da Física de Partículas (SM polas súas siglas en inglés) é a teoría que mellor explica o comportamento das partículas elementais que compoñen o universo e a interacción entre elas. Pese ao seu éxito, hay algúns fenómenos físicos que non poden ser descritos dentro do SM. Entre os procesos que non poden ser descritos, un dos máis interesantes é a asimetría materia-antimateria. Para producir diferentes cantidades de materia e de antimateria, a violación da simetría *CP* é unha das condicións necesarias. A cantidade de violación *CP* predita polo SM non é suficiente para explicar o gran desequilibrio entre materia e antimateria. Ata agora, todos os procesos medidos que son calculables no SM están de acordo coas predicións. Encontrar un proceso no que se produza violación *CP* que non estea incluído no SM sería polo tanto de gran importancia para restrinixir os modelos que describen correctamente a nova física.

Os mesóns B son o lugar ideal para buscar violación *CP*. Desintegracións de tipo pingüín mediadas por diagramas con loops de mesóns B son procesos moi interesantes para buscar física máis aló do SM. Particularmente as correntes neutras con cambio de sabor (FCNC) do tipo $b \to q$ son procesos moi sensibles a desviacións das predicións do SM producidas por novas partículas pesadas que entran no loop. Tres desintegracións de tipo FCNC son estudadas nesta tese: $B^0 \to K^{*0}\overline{K}^{*0}$, $B_s^0 \to K^{*0}\overline{K}^{*0}$ e $B_s^0 \to \phi\overline{K}^{*0}$. Estas desintegracións son ademais do tipo $B_{(s)}^0 \to VV'$, onde V e V' son mesóns vectoriais lixeiros. Unha análise de amplitudes é polo tanto necesaria para obter as diferentes fraccións de polarización.

O experimento LHCb, situado no colisionador LHC, foi deseñado para estudar desintegracións raras e violación *CP* en desintegracións de hadróns cun quark b, co obxectivo de atopar física máis aló do SM. Os datos recollidos polo experimento LHCb en 2011 son analizados tratando de descubrir a desintegración $B_s^0 \to \phi\overline{K}^{*0}$, e os datos recollidos en 2011 e 2012 son analizados para estudar as desintegracións $B^0 \to K^{*0}\overline{K}^{*0}$ e $B_s^0 \to K^{*0}\overline{K}^{*0}$.

R.1 The LHCb experiment

O experimento LHCb é un dos catro detectores de partículas situados no túnel de 27 km de longo do colisionador LHC. O obxectivo principal do experimento LHCb é o estudo da física de sabor pesada, buscando probas indirectas de nova física en procesos con violación *CP* e en desintegracións raras de hadróns cos quarks encanto e beleza.

Para separar as desintegracións de interese da contaminación de fondo, búscanse vértices desprazados e partículas con momento grande. Unha moi boa resolución dos vértices é necesario para medir o parámetro de impacto e para conseguir unha boa resolución no

tempo de desintegración. Unha boa resolución na medida dos momentos e das masas invariantes é importante para minimizar o fondo combinatorio e diferenciar desintegracións con topoloxías moi similares dende o punto de vista cinemático. A identificación de partículas cargadas é esencial para illar desintegracións moi suprimidas e para o marcado de sabor dos quarks *b*. Finalmente, para beneficiarse do alto número de eventos que se producen no LHC, son nucesarios un sistema de adquisición de datos cun ancho de banda moi grande e un sistema de disparo (trigger) moi robusto e selectivo.

R.1.1 O detector LHCb

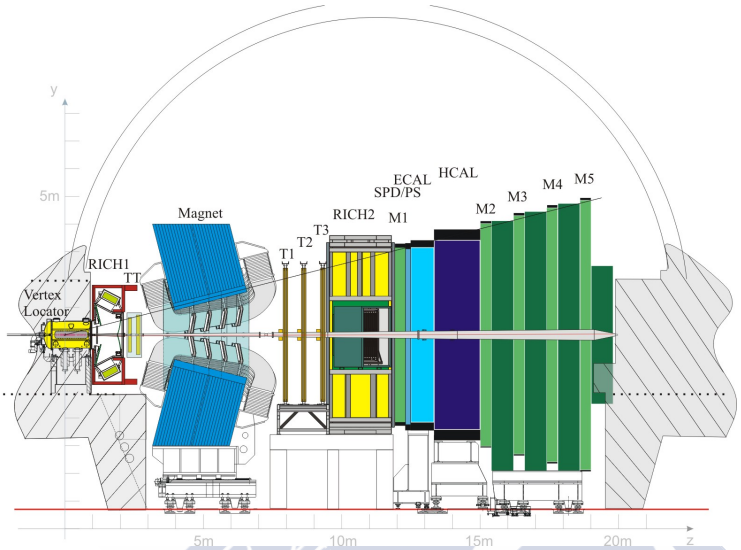

Figura R.1: Visión esquemática do detector LHCb.

O detector LHCb foi deseñado como un espectrómetro dun só brazo cunha cobertura angular na dirección cara adiante dende 10 mrad ata 300 (250) mrad no plano perpendicular ao campo magnético (paralelo ao campo magnético). Na Fig. Os principais elementos do detector, mostrado na Fig. R.1, son:

- o imán: un dipolo a temperatura ambiente para medir os momentos das partículas cargadas;
- o localizador de vértices (VELO): detector de microtiras de silicio que da información sobre as coordenadas das trazas preto da rexión de interacción;
- o sistema de trazado: composto polo Tracker Turicensis (TT), un detector de microtiras de silicio situado antes do imán, e tres estacións de trazado (T1, T2 e T3) despois do imán, formadas por microtiras de silicio na rexión máis cercana á tubería do feixe (Inner Tracker ou IT) e por tubos de deriva nas rexións máis externas (Outer Tracker ou OT);
- dous detectores de aneis Cherenkov (RICH): proporcionan a identificación das partículas cargadas. O detector situado antes do imán cubre o rango de baixo momento e o situado despois do imán cubre o rango de alto momento;

- o sistema de calorímetros: composto por unha capa escintiladora (SPD), un preshower (ps), un calorímetro electromagnético (ECAL) e un calorímetro hadrónico (HCAL);

- o sistema de detección de muóns: composto por unha cámara de multi-hilos (MWPC), excepto na rexión con máis taxa de eventos, onde se usan *Gas Electron Multipliers* (GEM).

Debido á falta de recursos, non toda a información recollida pode ser almacenada. O sistema de disparo reduce os millóns de eventos que se producen por segundo a tan só uns poucos miles. Para rexeitar fondo sen interese o sistema de disparo usa as características distintivas das desintegracións dos quarks b e c: trazas cun parámetro de impacto con respecto ao vértice primario significativamente distinto de cero e partículas cun momento transverso con respecto ao eixo do feixe moi alto.

R.2 Primeira observación da desintegración $B_s^0 \to \phi \overline{K}^{*0}$

A desintegración $B_s^0 \to \phi \overline{K}^{*0}$ é a única desintegración $b \to d$ de tipo pingüín en mesóns vectoriais que non foi aínda observada. O límite experimental máis estricto no coeficiente de ramificación (BR) é $\mathcal{B}(B_s^0 \to \phi \overline{K}^{*0}) < 1{,}0 \times 10^{-3}$ cun nivel de confianza do 90 %. Mentras que cálculos basados en QCD factorizada predín un valor de $(0{,}4^{+0{,}5}_{-0{,}3}) \times 10^{-6}$, en QCD perturbativa atópase un valor de $(0{,}65^{+0{,}33}_{-0{,}23}) \times 10^{-6}$.

A primeira observación da desintegración $B_s^0 \to \phi \overline{K}^{*0}$, con $\phi \to K^+K^-$ e $\overline{K}^{*0} \to K^-\pi^+$, é presentada. Un total de datos de $1\,\text{fb}^{-1}$ recollidos por LHCb en 2011 a unha enerxía de $\sqrt{s} = 7\,\text{TeV}$ é analizada buscando desintegracións $B_s^0 \to \phi(K^+K^-)\overline{K}^{*0}(K^-\pi^+)$. O coeficiente de ramificación mídese usando a desintegración $B^0 \to \phi K^{*0}$ como referencia. O estudio das distribución angulares na canle $B_s^0 \to \phi \overline{K}^{*0}$ da unha medida da polarización. A predición que se obtén para a polarización lonxitudinal usando QCD perturbativa é $f_0 = 0{,}712^{+0{,}042}_{-0{,}048}$.

R.2.1 Selección

Unha primeira redución dos datos conséguese aplicando un conxunto de cortes rectangulares. Criterios de selección adicionais son aplicados para eliminar contaminacións de desintegracións con e sen o quark c de fondo mal indetificado.

Unha redución máis estrita do fondo lógrase definindo un discrimante multivariado que usa a información da topoloxía do evento, a Geometrical Likelihood (GL). A GL adéstrase para optimizar o se poder de discriminación usando evento simulados de $B_s^0 \to \phi \overline{K}^{*0}$ para o sinal e unha mostra de datos reales fóra da rexión do sinal para o fondo.

R.2.2 Espectro da masa invariante de catro corpos

Un axuste de máxima verosimilitude é aplicado aos datos que pasan os criterios de selección mostrados previamente. Para a parametrización da forma na masa invariante dos eventos de sinal úsase unha mostra de datos reais de $B^0 \to J/\psi\, K^{*0}$. Tanto o B^0 como o B_s^0 son parametrizados coa mesma distribución, cunha diferencia no valor medio da masa.

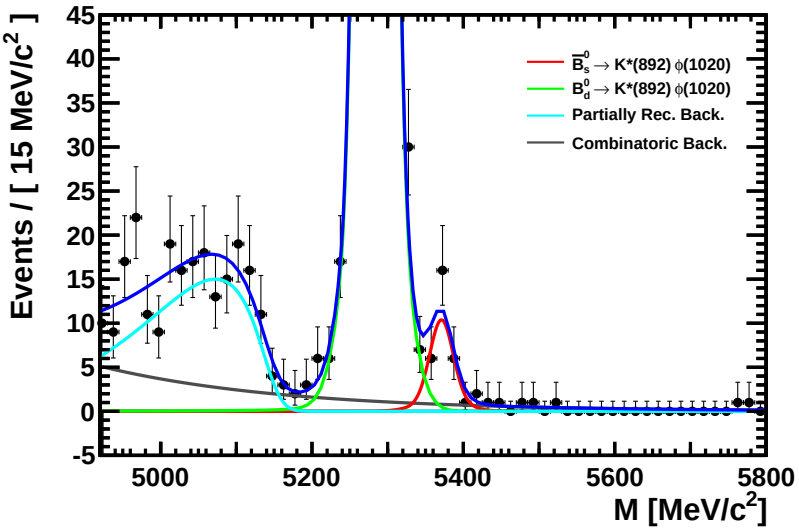

Figura R.2: Axuste da masa de catro corpos $KKK\pi$.

A forma é descrita pola suma dunha Crystal Ball (CB) e unha función Gaussiana, cun valor medio común. A maiores, desintegracións parcialmente reconstruídas de mesóns B, onde un pión non se detecta, son descritas pola convolución da función ARGUS cunha distribución Gaussiana. A última compoñente é unha función exponencial para ter en conta o fondo combinatorio. Na Fig. R.2 móstranse a distribución da masa invariante xunto coas contribucións do axuste.

Atópanse un total de $29{,}9 \pm 6{,}4$ eventos de $B^0_s \to (K^+K^-)(K^-\pi^+)$ e 1000 ± 32 eventos de $B^0 \to (K^+K^-)(\pi^+\pi^-)$. Obtense un valor unha significancia de $6{,}5\sigma$, tendo en conta os efectos sistemáticos.

R.2.3 Pureza de K^{*0} e ϕ no sinal

A cantidade de contribucións non resonantes (onda S) presentes nos sistemas K^+K^- e $K^-\pi^+$ debe ser subtraída para calcular o coeficiente de ramificación. A compoñente de onda S é evaluada para a canle $B^0 \to \phi K^{*0}$ e asúmese que é do mesmo tamaño que na desintegración $B^0_s \to \phi \overline{K}^{*0}$. A distribución das masas K^+K^- e $K^+\pi^-$ nunha ventá de $\pm 30\,\mathrm{MeV}/c^2$ arredor da masa do B^0 é descrita pola suma dunha compoñente resonante de espín 1 máis unha contribución de onda S.

A fracción de eventos de desintegracións de K^{*0} nunha ventá de masas de $\pm 150\,\mathrm{MeV}/c^2$ arredor da masa do K^{*0} resulta nunha pureza de $0{,}89 \pm 0{,}02$. Pola contra, a pureza encontrada nunha ventá de $\pm 7\,\mathrm{MeV}/c^2$ arredor da masa do ϕ é $0{,}950 \pm 0{,}005$. Isto significa que a pureza total de ϕK^{*0} é de $0{,}84 \pm 0{,}02$.

R.2.4 Análise de polarizacións

Unha análise de polarizacións sen marcado de sabor e integrada no tempo é levada a cabo. A fracción de desintegración diferencial nos tres ángulos de polarización pode escribirse

como,

$$\frac{\mathrm{d}^3\Gamma}{\mathrm{d}\cos\theta_1\,\mathrm{d}\cos\theta_2\,\mathrm{d}\varphi} \propto |A_0|^2\cos^2\theta_1\cos^2\theta_2 + |A_\parallel|^2\frac{1}{2}\sin^2\theta_1\sin^2\theta_2\cos^2\varphi + |A_\perp|^2\frac{1}{2}\sin^2\theta_1\sin^2\theta_2\sin^2\varphi + |A_0||A_\parallel|\cos\delta_\parallel\frac{1}{2\sqrt{2}}\sin 2\theta_1\sin 2\theta_2\cos\varphi. \tag{R.9}$$

A aceptancia é parametrizada coma unha función de θ_2 usando datos simulados. Atópase que a aceptancia non depende de θ_1 nin de φ. Unha pequena corrección é introducida debido a discrepancias entre a simulación e os datos no espectro de p_T e na selección de trigger.

Lévase a cabo un axuste coa distribución angular aos datos nunhá ventá de $\pm 30\,\mathrm{MeV}/c^2$ arredor da masa do B_s^0. O axuste inclúe dúas contribucións adicionais: un fondo combinatorio, parametrizado usando a distribución de eventos situados na parte de alta masa de catro corpos, e a cola de desintegracións $B^0 \to \phi K^{*0}$, que están polarizadas cos valores medidos en previas análises.

Calcúlanse incertezas sistemáticas debido á aceptancia angular e ao modelo usado para o fondo combinatorio, unha incerteza sistemática é calculada modificando o conxunto de eventos para os que se fai o axuste e, finalmente, unha contribución é calculada incluíndo unha fracción de onda S.

Os resultados finais son,

$$\begin{aligned} f_L &= 0{,}46 \pm 0{,}11\,(\mathrm{stat}) \pm 0{,}08\,(\mathrm{syst}), \\ f_\parallel &= 0{,}27 \pm 0{,}10\,(\mathrm{stat}) \pm 0{,}05\,(\mathrm{syst}), \\ \delta_\parallel &= 2{,}38 \pm 0{,}48\,(\mathrm{stat}) \pm 0{,}29\,(\mathrm{syst}), \end{aligned} \tag{R.10}$$

e móstranse na Fig. R.3.

O pequeno valor obtido para a fracción de polarización lonxitudinal segue a tendencia observada en outras desintegracións de tipo pingüín $b \to s$. Finalmente, o resultado é máis pequeno que a predición de QCD perturbativa, $f_L = 0{,}712^{+0{,}042}_{-0{,}048}$.

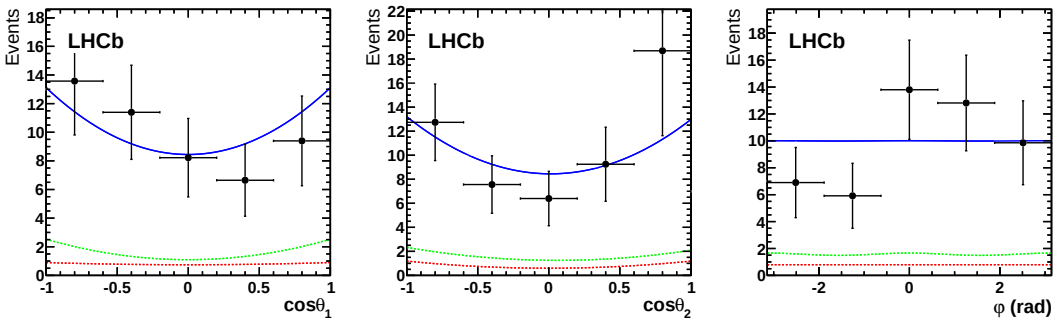

Figura R.3: Resultado do axuste da distribución angular aos eventos da desintegración $B_s^0 \to \phi\overline{K}^{*0}$ en $\cos\theta_1$, $\cos\theta_2$ e φ. A liña vermella punteada e a liña verde corresponden respectivamente ao fondo combinatorio e á contribución de $B^0 \to \phi K^{*0}$ na rexión do B_s^0.

R.2.5 Determinación do coeficiente de ramificación da desintegración $B_s^0 \to \phi\overline{K}^{*0}$

O coeficiente de ramificación calcúlase usando a canle $B^0 \to \phi K^{*0}$ como normalización. O seu valor compútase usando a expresión

$$\mathcal{B}(B_s^0 \to \phi\overline{K}^{*0}) = \lambda_{f_L} \times \frac{f_d}{f_s} \times \mathcal{B}(B^0 \to \phi K^{*0}) \times \frac{N_s}{N_d}, \tag{R.11}$$

onde N_s e N_d son o número de candidatos de B_s^0 e B^0, $\frac{f_d}{f_s}$ é a proporción dos factores de hadronización e λ_{f_L} é un factor de corrección que ten en conta as diferentes polarizacións das dúas canles.

Incertezas sistemáticas son calculadas debido ao modelo do axuste do espectro de catro corpos, á polarización lonxitudinal, á pureza, á eficiencia e á indentificación de partículas.

O resultado final é

$$\mathcal{B}(B_s^0 \to \phi\overline{K}^{*0}) = \left(1{,}09 \pm 0{,}24\,(\text{stat}) \pm 0{,}11\,(\text{syst}) \pm 0{,}08\left(\frac{f_d}{f_s}\right)\right) \times 10^{-6}. \tag{R.12}$$

O resultado é aproximadamente tres veces máis grande que o valor predito por QCD factorizada, $(0{,}4^{+0{,}5}_{-0{,}3}) \times 10^{-6}$, e maior que o predito por QCD perturbativa, $(0{,}65^{+0{,}33}_{-0{,}23}) \times 10^{-6}$, aínda que os valores son compatibles a 1σ.

R.3 Análise de amplitudes das desintegracións $B^0 \to K^{*0}\overline{K}^{*0}$ e $B_s^0 \to K^{*0}\overline{K}^{*0}$

A colaboración BaBar publicou o descobremento da canle $B^0 \to K^{*0}\overline{K}^{*0}$ cunha significancia estatística de 6σ e un coeficiente de ramificación de $\mathcal{B}(B^0 \to K^{*0}\overline{K}^{*0}) = (1{,}28^{+0{,}35}_{-0{,}30} \pm 0{,}11) \times 10^{-6}$. Este valor está en tensión cos resultados obtidos pola colaboración Belle, un límite superior de $\mathcal{B}(B^0 \to K^{*0}\overline{K}^{*0}) < 0{,}8 \times 10^{-6}$ cun nivel de confianza do 90 %. A publicación de BaBar tamén inclúe a medida da polarización lonxitudinal, $f_0 = 0{,}80^{+0{,}12}_{-0{,}13}$, que ten un valor grande comparada coa obtida na desintegración $B_s^0 \to K^{*0}\overline{K}^{*0}$, $f_L = 0{,}201 \pm 0{,}057 \pm 0{,}040$, que o modo rotado por U-espín.

Un total de $3\,\text{fb}^{-1}$ de datos recollidos por LHCb en 2011 ($1\,\text{fb}^{-1}$) e 2012 ($2\,\text{fb}^{-1}$) a unha enerxía de $\sqrt{s} = 7\,\text{TeV}$ e $\sqrt{s} = 8\,\text{TeV}$ respectivamente son analizados. Lévase a cabo unha análise de amplitudes sen marcado de sabor e integrada no tempo da canle $B^0 \to K^+\pi^-K^-\pi^+$ nunha ventá de masas de $\pm 150\,\text{MeV}/c^2$ arredor da masa do K^{*0}. Préstaselle especial atención á medida da fracción de polarización lonxitudinal, intentando confirmar o alto valor medido por BaBar. Realízase unha actualización da análise angular da desintegración $B_s^0 \to K^{*0}\overline{K}^{*0}$, publicada previamente por LHCb cos datos de 2011, aos que agora se lle engaden os datos de 2012. Adicionalmente, unha comparación directa entre as desintegracións $B^0 \to K^{*0}\overline{K}^{*0}$ e $B_s^0 \to K^{*0}\overline{K}^{*0}$ é realizada, tratando de confirmar a gran diferencia observada nas polarizacións. Finalmente, a proporción dos coeficientes de ramificación entre as dúas canles é medido, $\mathcal{B}(B^0 \to K^{*0}\overline{K}^{*0})/\mathcal{B}(B_s^0 \to K^{*0}\overline{K}^{*0})$.

R.3.1 Selección de eventos

Lévaronse a cabo algúns estudos tentando identificar as principais fontes de fondo que poden contaminar o sinal. Atópase que as contribucións de fondo con quarks c son insignificantes. Despois do stripping é dos cortes de trigger, a rexión fiducial é definida e un corte para rexeitar muóns é aplicado.

Para incrementar a separación entre o sinal e o fondo, unha análise multivariada (MVA) é aplicada. Unha BDTG (Boosted Decision Tree con Gradient boost) é o método elixido. A BDTG é adestrada usando unha mostra de eventos simulados de $B^0 \to K^{*0}\overline{K}^{*0}$ como sinal e unha mostra de datos situados na parte de alta masa de catro corpos como fondo.

Tres desintegracións mal identificados son identificadas: $B^0 \to \phi K^{*0}$, $B^0 \to \rho^0 K^{*0}$ e $\Lambda_b^0 \to p\pi K^{*0}$. Para reducir a súa contribución, un conxunto de cortes nas variables de identificación de partículas son incluídos.

R.3.2 Axuste da masa invariante dos catro corpos

Para realizar a análise de amplitudes, unha mostra de $B^0_{(s)} \to K^+\pi^-K^-\pi^+$ libre de fondo é conseguida aplicando un conxunto de sWeights obtidos no axuste da masa invariante dos catro corpos.

Seis contribucións entran no axuste. As desintegracións $B^0 \to K^+\pi^-K^-\pi^+$ e $B^0_s \to K^+\pi^-K^-\pi^+$ parametrízanse coa mesma forma, funcións Ipatia cos parámetros obtidos da simulación, e diferenciados soamente por un desplazamento na masa. A desintegración $B^0 \to \phi K^{*0}$ é modelada pola suma dunha función Crystal Ball e unha distribución Gaussiana que comparten a mesma media, mentras que a desintegración $\Lambda_b^0 \to p\pi K^{*0}$ é descrita cunha soa Crystal Ball. Os parámetros son obtidos coa simulación. Adicionalmente, o fondo parcialmente reconstruído é descrito por unha convolución dunha función ARGUS cunha distribución Gaussiana. Para ter en conta o fondo combinatorio, úsase unha función exponencial.

Os eventos de $B^0 \to \rho^0 K^{*0}$ que sobreviven aos cortes de identificación de partículas son extraídos coa aplicación de pesos negativos. A contribución de $\Lambda_b^0 \to p\pi K^{*0}$ é fixada no axuste da masa $K^+\pi^-K^-\pi^+$ ao valor obtido dun axuste á masa $p\pi K\pi$.

Co modelo descrito previamente realízase un axuste non bineado de máxima verosimilitude simultaneamente aos datos da masa invariante de catro corpos de 2011 e 2012. O axuste móstrase na Fig. R.4. Para a desintegración $B^0 \to K^+\pi^-K^-\pi^+$, obtéñense 98 ± 12 eventos en 2011 e 248 ± 19 en 2012, o que significa máis de sete veces o número de eventos observados previamente. Para a desintegración $B^0_s \to K^+\pi^-K^-\pi^+$ obtéñense 614 ± 26 e 1332 ± 38 eventos en 2011 e 2012, respectivamente.

R.4 Análise de amplitudes da desintegración $B^0 \to K^{*0}\overline{K}^{*0}$ decay

Unha análise de amplitudes da canle $B^0 \to K^+\pi^-K^-\pi^+$ sen marcado de sabor e integrada no tempo é realizada nunha ventá de $\pm 150\,\mathrm{MeV}/c^2$ na masa $K\pi$ arredor da masa do K^{*0}. Nesta ventá de masas, unha compoñente escalar (S) é atopada a maiores da resonancia vectorial (V). A desintegración é polo tanto descrita por seis amplitudes diferentes. Tres das cales describen a desintegración $B \to V_1V_2$ (onda P), que na base de transversidade

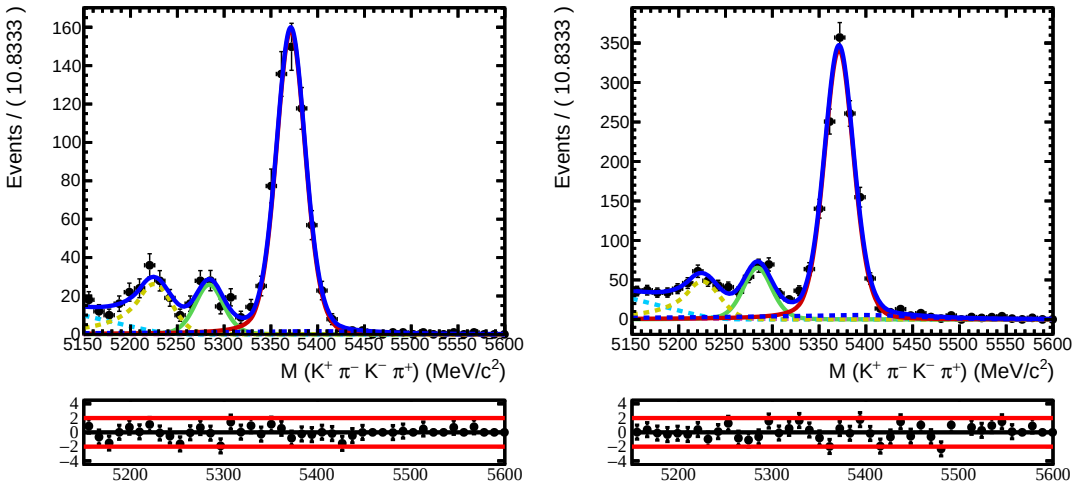

Figura R.4: Axuste simultáneo aos datos de 2011 (esquerda) e 2012 (dereita) na masa invariante de catro corpos.

son: A_0, $A_\parallel$ e $A_\perp$. As outras tres (onda S) corresponden ás desintegracións:[1] $B \to V_1 S_2$ (A_{VS}), $B \to S_1 V_2$ (A_{SV}) e $B \to S_1 S_2$ (A_{SS}).

É conveniente definir as combinacións lineais $A_s^+ = (A_{VS} + A_{SV})/\sqrt{2}$, $A_s^- = (A_{VS} - A_{SV})/\sqrt{2}$, para que a fracción de desintegración poda ser descrita por enteiro en termos de amplitudes asociadas a autoestados de *CP* pares (0, $\parallel$, S^- ,SS) e impares ($\perp$, S^+).

Se asumimos que non hay violación *CP*, a fracción de desintegración escrita en función dos ángulos de helicidade (θ_1, θ_2 e ϕ) e das masas invariantes das parellas $K^+\pi^-$ (m_1) e $K^-\pi^+$ (m_2) ven dada por,

$$\frac{\mathrm{d}^5\Gamma}{\mathrm{d}\cos\theta_1 \mathrm{d}\cos\theta_2 \mathrm{d}\phi \mathrm{d}m_1 \mathrm{d}m_2} \propto \sum_{i=1}^{6} \sum_{j \geq i} \mathcal{R}e[A_i A_j^* F_{ij} \delta_{\eta_i \eta_j}], \tag{R.13}$$

onde η_i é a paridade *CP* de cada amplitude A_i, $\delta_{\eta_i\eta_j} = 1$ se $i = j$ e 0 en calquera outro caso, e $F_{ij} = \Phi_4(m_1, m_2) f_i f_j^* (2 - \delta_{ij})$, con Φ_4 o factor de espacio de fase de catro corpos e os termos ángulos-masas f_i que veñen definidos na Táboa R.1.

Unha eficiencia non uniforme ten que ser incluída para ter en conta os efectos da xeometría do detector e os debidos ás ineficiencias producidas pola selección e a reconstrucción. Para incorporar a aceptancia angular, unha serie de pesos de normalización son calculados, usando unha mostra de eventos simulados de $B^0 \to K^{*0}\overline{K}^{*0}$. Posto que os pesos de normalización non permiten visualizar o resultado do axuste, unha aceptancia parametrizada con polinomios de Legendre é tamén calculada.

Os candidatos sepáranse en catro categorías, por ano e de acordo ao seu camiño de trigger, posto que se atoparon diferencias na aceptancia para cada categoría. Un axuste simultáneo é realizado. O resultado para unha das categorías pode ser visto na Fig. R.5. A fracción de polarización lonxitudinal $f_L = 0{,}707 \pm 0{,}053$, ten un valor compatible coa medida de BaBar, $f_L = 0{,}80^{+0{,}12}_{-0{,}13}$, cunha redución na incerteza estatística dun factor 2.

[1] O subíndice 1 (2) corresponde ás masas $K^+\pi^-$ ($K^-\pi^+$).

Táboa R.1: Amplitudes A_i e termos ángulos-masas f_i.

i	A_i	f_i
1	A_0	$\cos\theta_1 \cos\theta_2 \mathcal{M}_1(m_1)\mathcal{M}_1(m_2)$
2	$A_\parallel$	$\frac{1}{\sqrt{2}} \sin\theta_1 \sin\theta_2 \cos\phi \mathcal{M}_1(m_1)\mathcal{M}_1(m_2)$
3	$A_\perp$	$\frac{i}{\sqrt{2}} \sin\theta_1 \sin\theta_2 \sin\phi \mathcal{M}_1(m_1)\mathcal{M}_1(m_2)$
4	A_S^+	$-\frac{1}{\sqrt{6}}(\cos\theta_1 \mathcal{M}_1(m_1)\mathcal{M}_0(m_2) - \cos\theta_2 \mathcal{M}_0(m_1)\mathcal{M}_1(m_2))$
5	A_S^-	$-\frac{1}{\sqrt{6}}(\cos\theta_1 \mathcal{M}_1(m_1)\mathcal{M}_0(m_2) + \cos\theta_2 \mathcal{M}_0(m_1)\mathcal{M}_1(m_2))$
6	A_{SS}	$-\frac{1}{3}\mathcal{M}_0(m_1)\mathcal{M}_0(m_2)$

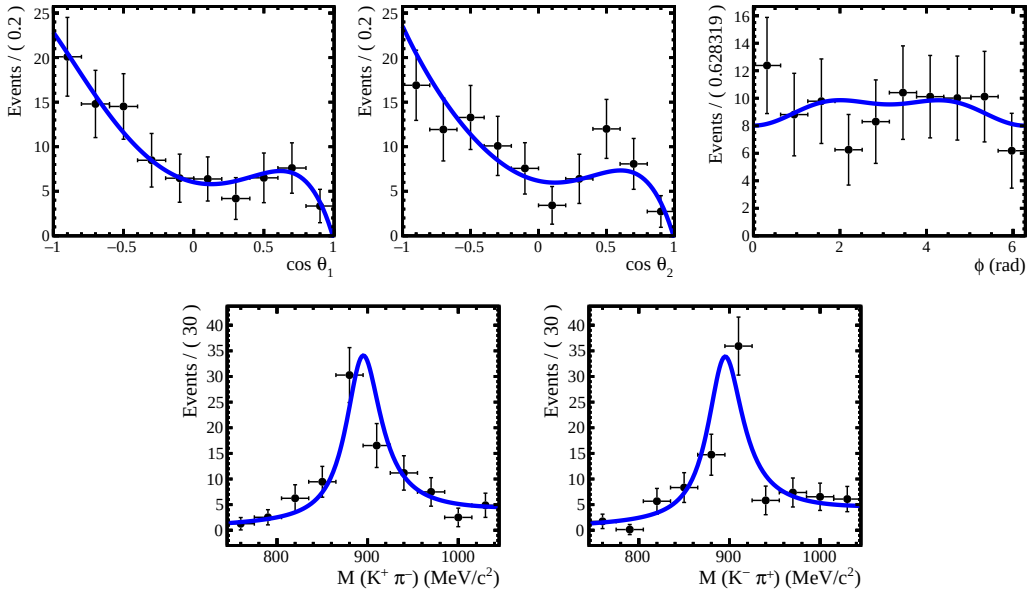

Figura R.5: Visualización do resultado da análise de amplitudes da desintegración $B^0 \to K^+\pi^-K^-\pi^+$.

Esta medida confirma a alta polarización lonxitudinal. Desafortunadamente as incertezas sistemáticas aínda non foron calculadas.

R.5 Análise de amplitudes da desintegración $B_s^0 \to K^{*0}\overline{K}^{*0}$ decay

Unha análise de amplitudes sen marcado de sabor e integrada no tempo da desintegración $B_s^0 \to K^{*0}\overline{K}^{*0}$ foi publicada por LHCb cos datos de 2011. Unha actualización desta medida é realizada incluíndo os datos de 2012.

A fracción de desintegración para a desintegración do B_s^0 ten a mesma forma que para a desintegración do B^0, Eq. R.13, cun factor $\frac{1}{\Gamma_L}$ nos termos con estados CP pares e un factor $\frac{1}{\Gamma_H}$ nos estados CP impares, onde Γ_L e Γ_H son os tempos de vida dos autoestados de masa lixeiro e pesado do B_s^0.

Os resultados obtidos usando os datos de 2011 concordan coas medidas publicadas.

A maiores, os resultados de 2011 + 2012 son tamén consistentes coas medidas previas. En particular, o valor obtido para a polarización lonxitudinal neste traballo, $0{,}233 \pm 0{,}030$, é compatible co valor publicado, $0{,}201 \pm 0{,}057$, o que confirma a baixa polarización da desintegración $B_s^0 \to K^{*0}\overline{K}^{*0}$. Ademais, a alta compoñente de onda S atopada, $(0{,}687 \pm 0{,}037)$, é comparable co valor xa publicado, $(0{,}665 \pm 0{,}067)$.

R.6 Análise comparativo das desintegracións $B^0 \to K^{*0}\overline{K}^{*0}$ e $B_s^0 \to K^{*0}\overline{K}^{*0}$

A polarización medida nas desintegracións $B^0 \to K^{*0}\overline{K}^{*0}$ e $B_s^0 \to K^{*0}\overline{K}^{*0}$ é moi diferente, aínda que os diagramas describindo ambos procesos sexan idénticos tras un intercambio de quarks $d \leftrightarrow s$.

Para investigar as diferencias entre estas dúas desintegracións dun modo directo, úsase o feito de que os estado finais son practicamente idénticos dende un punto de vista cinemático e polo tanto experimentan os mesmos sesgos introducidos polo trigger e pola selección. O cociente de eventos de B^0 entre eventos de B_s^0 en bins do $\cos\theta$, de ϕ e das masas $m_{K\pi}$ é obtido.

Para a distribución en $\cos\theta$, a probabilidade de que os datos de B^0 sexan diferentes aos datos de B_s^0 é calculada axustando unha recta horizontal fixada en 1 ao cociente de datos B^0/B_s^0. A significancia de que a distribución do $\cos\theta$ para B_s^0 sexa diferente que para B^0 calcúlase que é de $4{,}8\sigma$. Nas masas, o pico da distribución de masa $K\pi$ aparece desprazado entre B^0 e B_s^0. Este resultado é o esperado como resultado da presenza de diferentes fases nos termos de intereferencia, para B^0 e B_s^0, cando se ten en conta a forte asimetría na aceptancia angular. De forma similar a distribución acimutal aparece estruturada arredor de π, en acordo co modelo de mellor axuste.

R.7 $\mathcal{B}\,(B^0 \to K^{*0}\overline{K}^{*0})/\mathcal{B}\,(B_s^0 \to K^{*0}\overline{K}^{*0})$

O cociente dos coeficientes de ramificación entre as desintegracións de B^0 e de B_s^0 en $K^{*0}\overline{K}^{*0}$ obtense con,

$$\frac{\mathcal{B}(B^0 \to K^{*0}\overline{K}^{*0})}{\mathcal{B}(B_s^0 \to K^{*0}\overline{K}^{*0})} = \frac{\varepsilon(B_s^0 \to K^{*0}\overline{K}^{*0})}{\varepsilon(B^0 \to K^{*0}\overline{K}^{*0})} \times \frac{f_s}{f_d} \times \frac{N_{B^0} \times f_{B^0 \to K^{*0}\overline{K}^{*0}}}{N_{B_s^0} \times f_{B_s^0 \to K^{*0}\overline{K}^{*0}}} \times \frac{\lambda_{f_L}(B_s^0 \to K^{*0}\overline{K}^{*0})}{\lambda_{f_L}(B^0 \to K^{*0}\overline{K}^{*0})}, \tag{R.14}$$

onde $\varepsilon(B^0 \to K^{*0}\overline{K}^{*0})$ e $\varepsilon(B_s^0 \to K^{*0}\overline{K}^{*0})$ son as eficiencias de cada desintegración, calculadas usando a simulación e datos reais. Os coeficientes f_s e f_d son os factores de hadronización dos quarks b, que teñen en conta a diferencia do número de mesóns B^0 e B_s^0 producidos. N_{B^0} e $N_{B_s^0}$ son o número de eventos de $B^0 \to K^+\pi^-K^-\pi^+$ e de $B_s^0 \to K^+\pi^-K^-\pi^+$, respectivamente. The factores de pureza $f_{B_{(s)}^0 \to K^{*0}\overline{K}^{*0}}$ determinan a cantidade de desintegracións $B^0 \to K^{*0}\overline{K}^{*0}$ e $B_s^0 \to K^{*0}\overline{K}^{*0}$ resonantes. E $\lambda_{f_L}(B_{(s)}^0 \to K^{*0}\overline{K}^{*0})$ é unha corrección que ten en conta as diferentes eficiencies que se obteñen nos datos e na simulación debido a que os eventos simulados son xerados cunha polarización distinta aos datos reais.

O resultado da división dos coeficientes de ramificación é obtida despois de pesar os

distintos períodos de toma de datos,

$$\frac{\mathcal{B}(B^0 \to K^{*0}\overline{K}^{*0})}{\mathcal{B}(B_s^0 \to K^{*0}\overline{K}^{*0})} = 0{,}0799 \pm 0{,}0073\,(\text{stat}) \pm 0{,}0036 \left(\frac{f_s}{f_d}\right). \tag{R.15}$$

Usando o coeficiente de ramificación da desintegración $B_s^0 \to K^{*0}\overline{K}^{*0}$, $\mathcal{B}(B_s^0 \to K^{*0}\overline{K}^{*0}) = (10{,}8 \pm 2{,}1\,(\text{stat})) \times 10^{-6}$, o coeficiente de ramificación para a desintegración $B^0 \to K^{*0}\overline{K}^{*0}$ é,

$$\mathcal{B}(B^0 \to K^{*0}\overline{K}^{*0}) = (8{,}6 \pm 1{,}9\,(\text{stat})) \times 10^{-7}. \tag{R.16}$$

Este resultado é compatible coas medidas previas feitas por BaBar, $[1{,}28^{+0{,}35}_{-0{,}30}\,(\text{stat}) \pm 0{,}11\,(\text{syst})] \times 10^{-6}$ e coa predición teórica, $(0{,}6^{+0{,}5}_{-0{,}3}) \times 10^{-6}$. Por último, existe unha predición teórica para o cociente das partes lonxitudinais dos coeficientes de ramificación das dúas canles [55], $R_{sd} = \mathcal{B}^{\text{long}}(B_s^0 \to K^{*0}\overline{K}^{*0})/\mathcal{B}^{\text{long}}(B^0 \to K^{*0}\overline{K}^{*0}) = 16{,}4 \pm 5{,}2$. O cociente experimental medido é $R_{sd} = 3{,}89 \pm 0{,}68\,(\text{stat})$.

USC UNIVERSIDADE DE SANTIAGO DE COMPOSTELA

USC
UNIVERSIDADE
DE SANTIAGO
DE COMPOSTELA

APPENDIX

A

Study of the decays $B^0 \to K^{*0}\overline{K}^{*0}$ and $B_s^0 \to K^{*0}\overline{K}^{*0}$

A.1 RapidSim technical details

RapidSim is used to generate a sample of 10^7 events of the decay $\Lambda_b^0 \to K^{*0} p\pi$ at an energy $\sqrt{s} = 8\,\text{TeV}$. The K^{*0} decays into $K^{\pm}$ and $\pi^{\mp}$ and the proton is misidentified as a kaon. RapidSim is configured as follows:

Geometry LHCb.

Acceptance AllDownstream - All of the final-state particles are required to remain in the acceptance of the LHCb detector downstream of the dipole magnet.

Smear The LHCbGeneric smear option is used for all the final-state particles.

After generation the fiducial cuts shown in Table 5.4, $3 < p < 100\,\text{GeV}/c$ and $1.5 < \eta < 4.5$ are applied to the final-state particles. Also the stripping cuts in the p_T and in the invariant masses are applied (Table 5.2):

- $p_\text{T} > 500\,\text{MeV}/c$ for all the final-state particles,
- $p_\text{T} > 900\,\text{MeV}/c$ for the K^{*0} and for the $K^{misid}\pi$ pair,
- the masses of the K^{*0} and the $K^{misid}\pi$ pair are in a $\pm 150\,\text{MeV}/c^2$ window around the nominal K^{*0} mass,
- $5000 < M(K^{misid}\pi K\pi) < 5800\,\text{MeV}/c^2$,

where K^{misid} is the misidentified proton with the hypothesis of kaon.

A.2 MVA figures

In this appendix the MVA figures of Chapter 5.5.3 are presented. In Fig. A.1, Fig. A.2 and Fig. A.3, the distribution of the variables used to train the MVA are shown. In Fig. A.4, Fig. A.5 and Fig. A.6, the BDTG response is shown for signal and background, and for the testing and training samples. In Fig. A.7, Fig. A.8 and Fig. A.9, the linear correlations between the different variables for signal and background are shown. And in Fig. A.10, Fig. A.11 and Fig. A.12, the signal efficiency vs background rejection is shown.

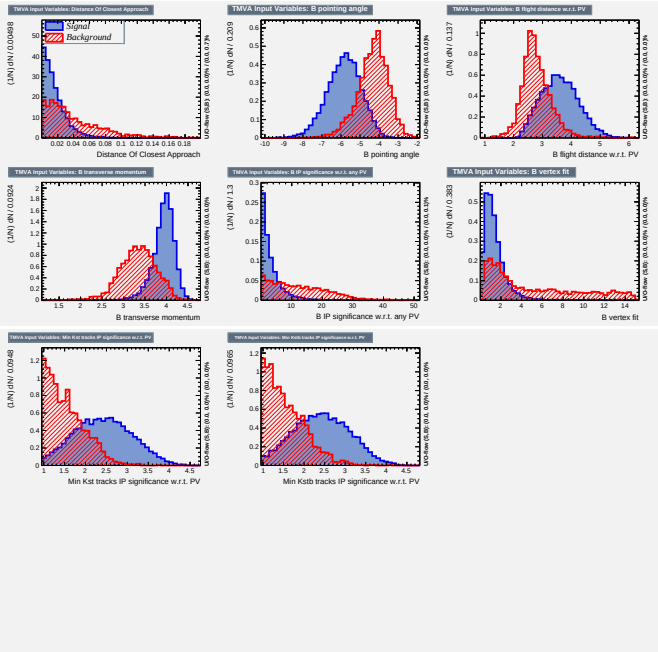

Figure A.1: Distribution of the variables used to train the MVA. Events from the signal sample in blue and from the background sample in red. 2011 BDTG1.

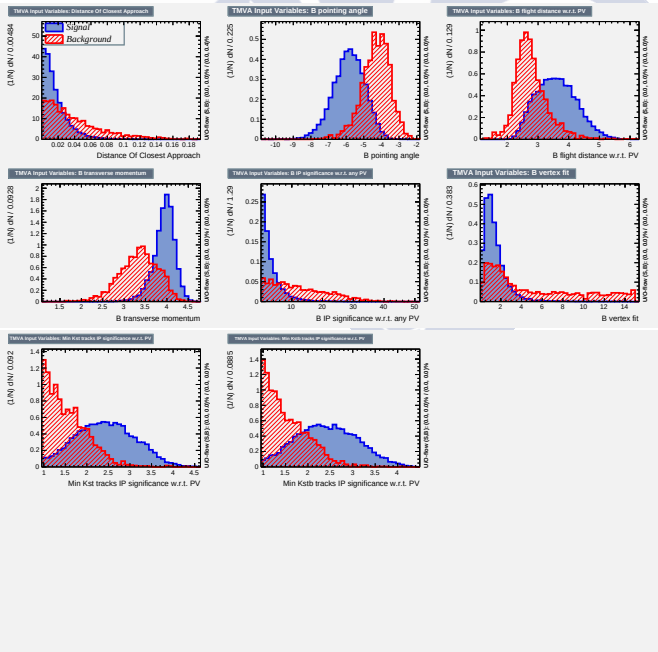

Figure A.2: Distribution of the variables used to train the MVA. Events from the signal sample in blue and from the background sample in red. 2011 BDTG2.

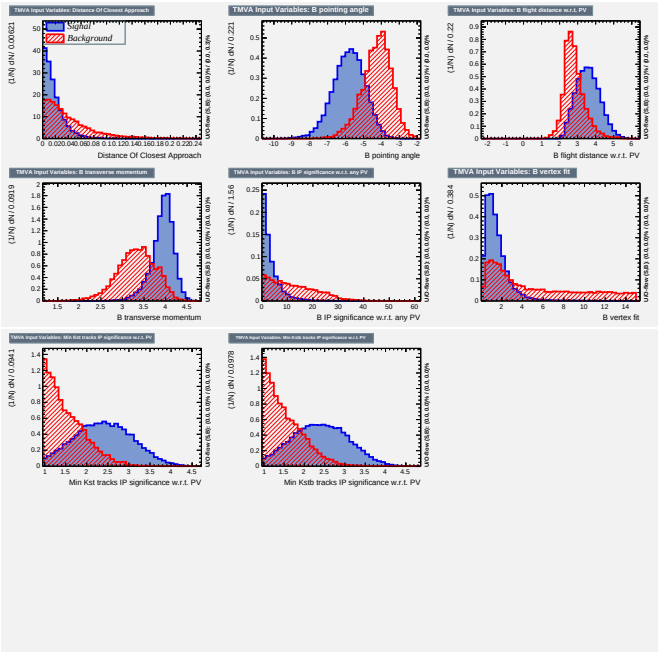

Figure A.3: Distribution of the variables used to train the MVA. Events from the signal sample in blue and from the background sample in red. 2012 BDTG2.

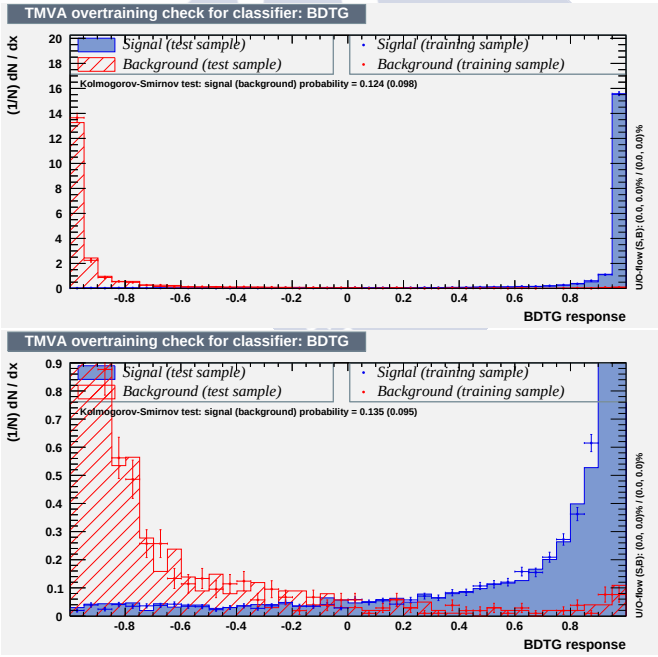

Figure A.4: Top: BDTG response for training and testing samples. Signal events in blue and background events in red. The points correspond to the training samples and the solid histograms to the testing samples. Bottom: Zoom of the same plot. 2011 BDTG1.

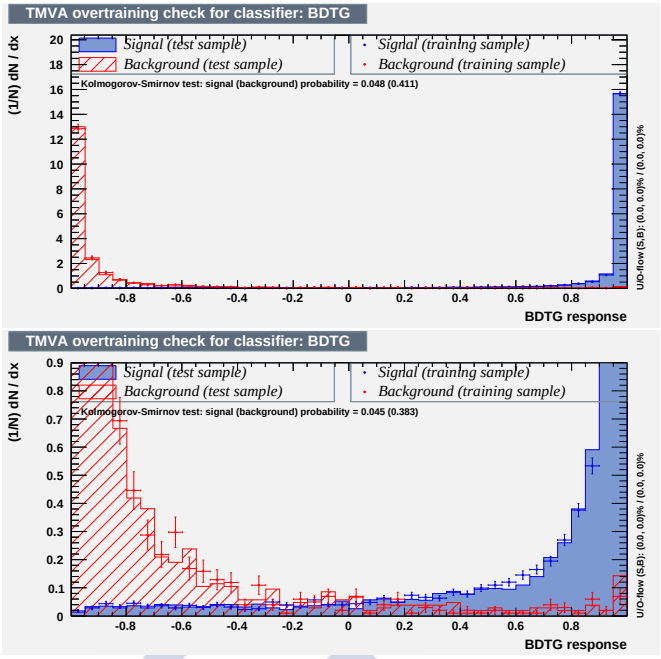

Figure A.5: Top: BDTG response for training and testing samples. Signal events and in blue and background events in red. The points correspond to the training samples and the solid histograms to the testing samples. Bottom: Zoom of the same plot. 2011 BDTG2.

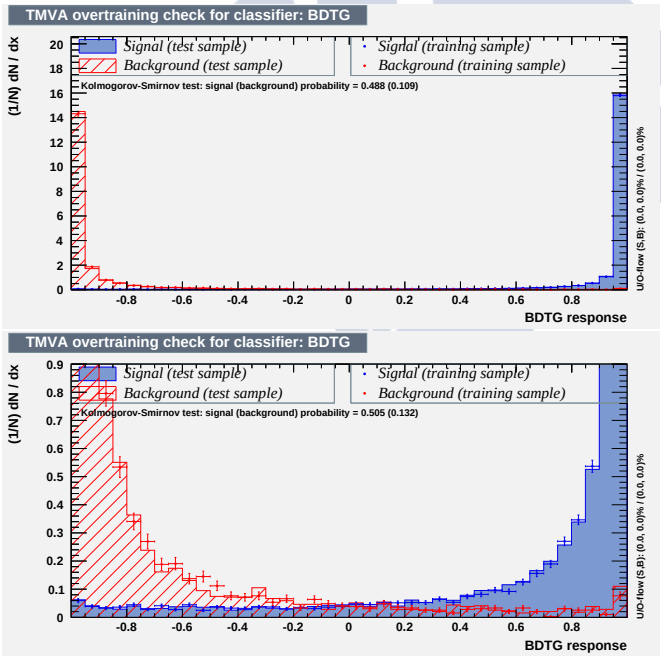

Figure A.6: Top: BDTG response for training and testing samples. Signal events in blue and background events in red. The points correspond to the training samples, and the solid histograms to the testing samples. Bottom: Zoom of the same plot. 2012 BDTG2.

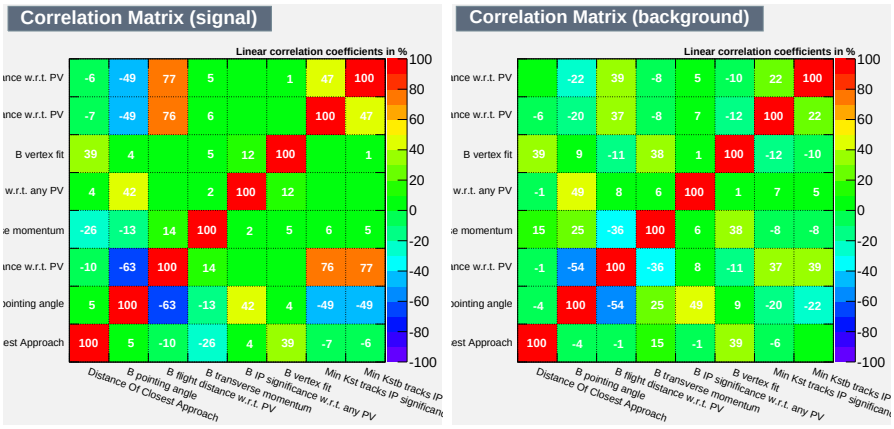

Figure A.7: Linear correlations between the variables used to train the MVA. Left: Signal. Right: Background. 2011 BDTG1.

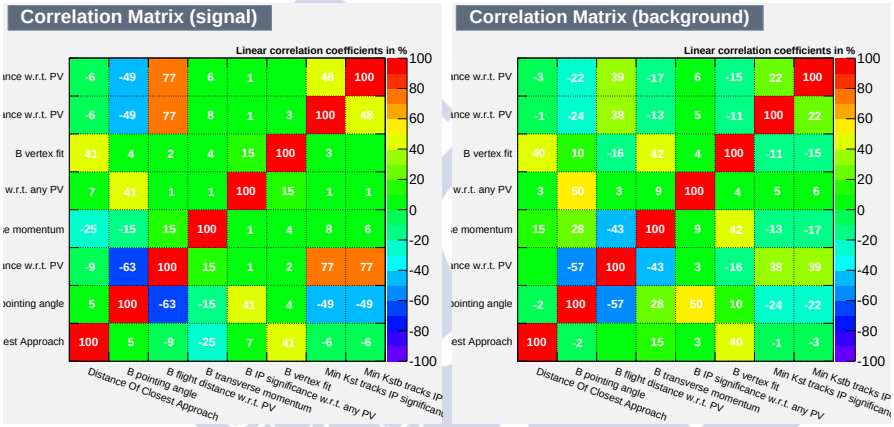

Figure A.8: Linear correlations between the variables used to train the MVA. Left: Signal. Right: Background. 2011 BDTG2.

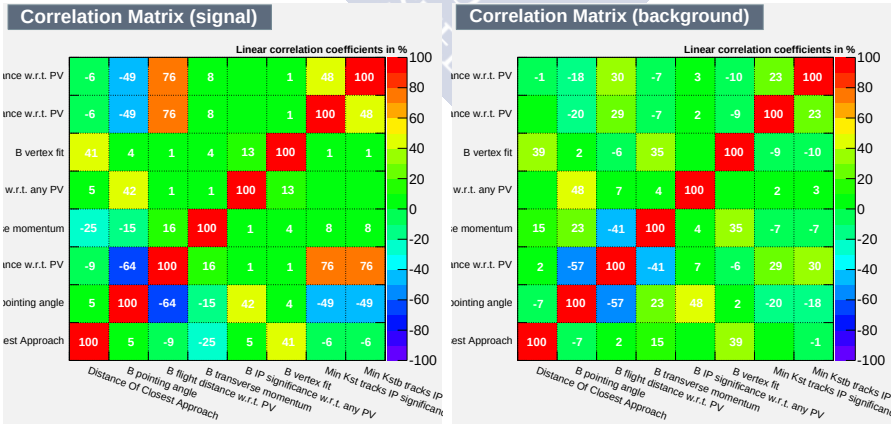

Figure A.9: Linear correlations between the variables used to train the MVA. Left: Signal. Right: Background. 2012 BDTG2.

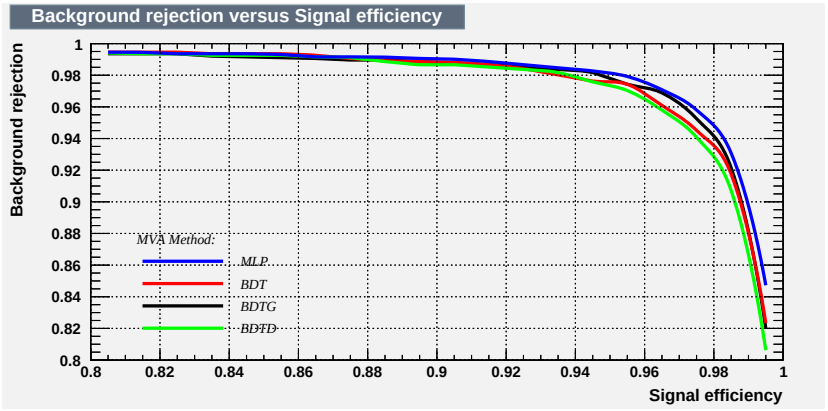

Figure A.10: Signal efficiency and background rejection for the MVA methods analyzed. Red: BDT. Black: BDTG. Green: BDTD. Blue: MLP. 2011 BDTG1.

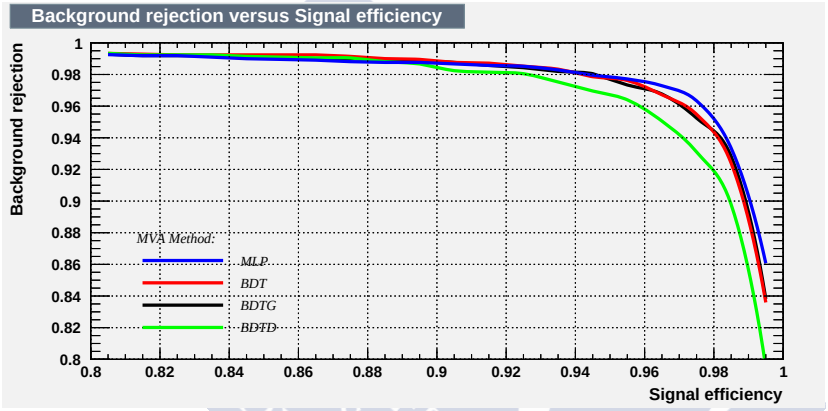

Figure A.11: Signal efficiency and background rejection for the MVA methods analyzed. Red: BDT. Black: BDTG. Green: BDTD. Blue: MLP. 2011 BDTG2.

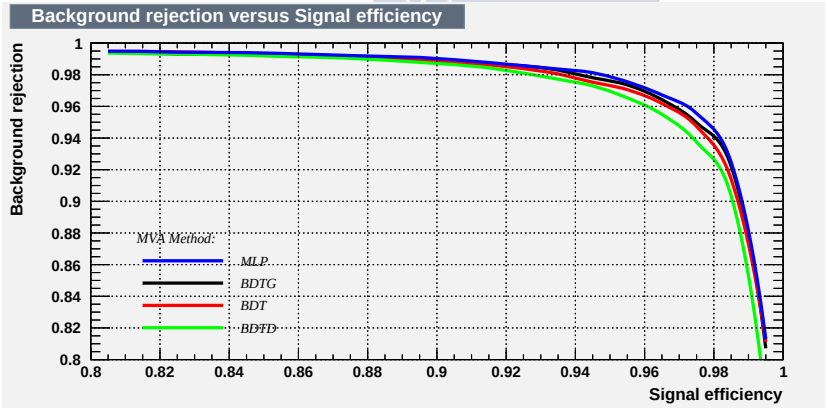

Figure A.12: Signal efficiency and background rejection for the MVA methods analyzed. Red: BDT. Black: BDTG. Green: BDTD. Blue: MLP. 2012 BDTG2.

A.3 Comparison data / simulation

In Fig. A.13, Fig. A.14, Fig. A.15, Fig. A.16, Fig. A.17, Fig. A.18, Fig. A.19 and Fig. A.20, the distributions of the variables used to train the MVA are shown in data and Monte Carlo. The data sample is obtained from the sWeighted $B_s^0 \to K^{*0}\overline{K}^{*0}$ events used in the FoM optimisation (Chapter 5.5.4, Fig. 5.8). In Fig. A.21, the output of the BDTG can also be seen.

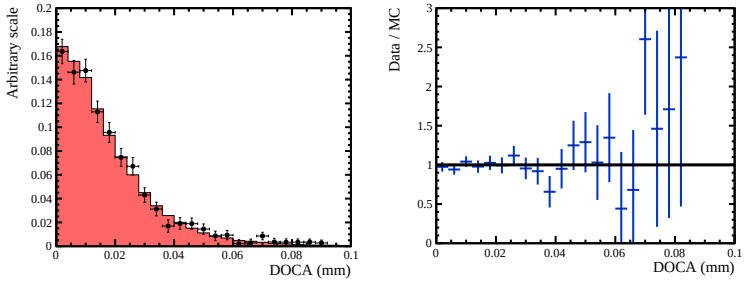

Figure A.13: Left: Comparison of the DOCA distribution in data (black points) and Monte Carlo (solid red histogram). Right: Ratio between data and Monte Carlo.

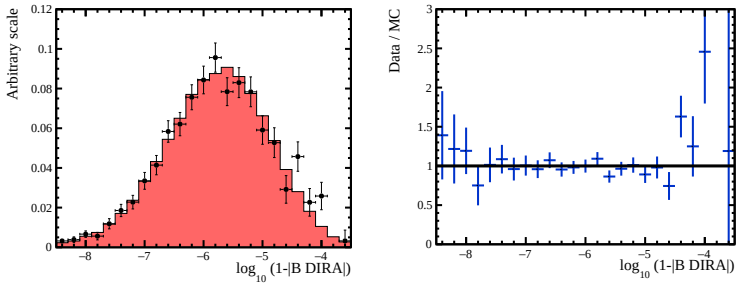

Figure A.14: Left: Comparison of the DIRA distribution in data (black points) and Monte Carlo (solid red histogram). Right: Ratio between data and Monte Carlo.

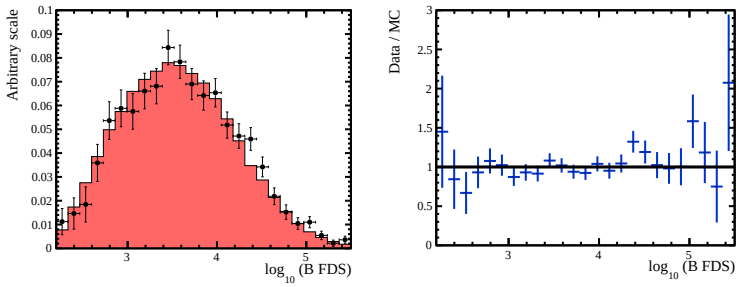

Figure A.15: Left: Comparison of the B^0 flight distance significance distribution in data (black points) and Monte Carlo (solid red histogram). Right: Ratio between data and Monte Carlo.

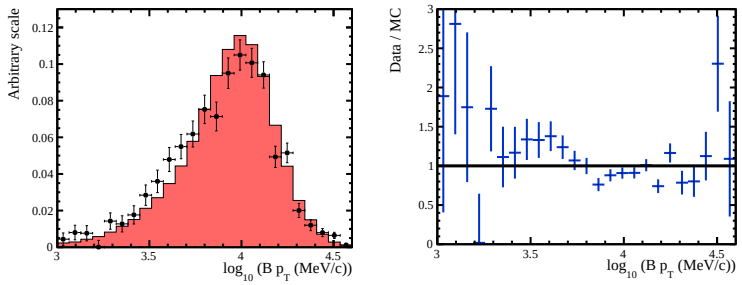

Figure A.16: Left: Comparison of the B^0 transverse momentum distribution in data (black points) and Monte Carlo (solid red histogram). Right: Ratio between data and Monte Carlo.

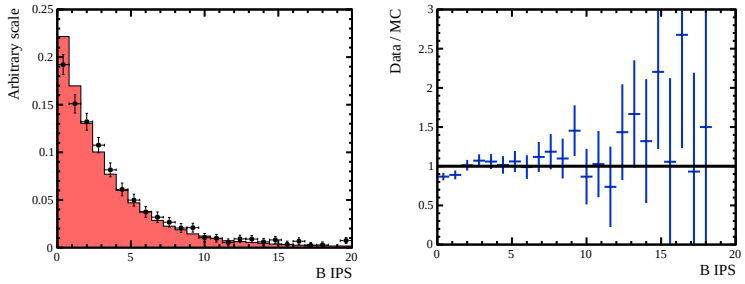

Figure A.17: Left: Comparison of the B^0 impact parameter significance distribution in data (black points) and Monte Carlo (solid red histogram). Right: Ratio between data and Monte Carlo.

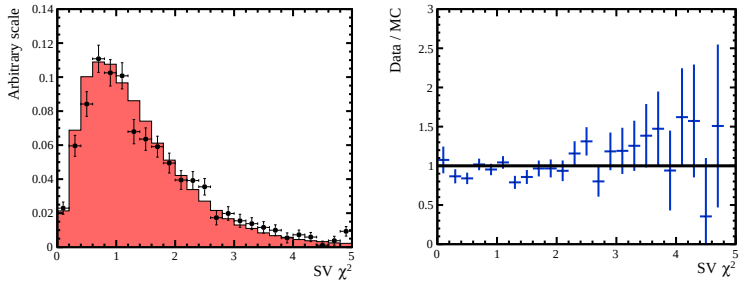

Figure A.18: Left: Comparison of the B^0 vertex fit distribution in data (black points) and Monte Carlo (solid red histogram). Right: Ratio between data and Monte Carlo.

A.4 Mass lineshape used to generate the Monte Carlo

As explained in Chapter 5.8.4, the acceptance is introduced in the amplitude analysis by using the normalisation weights. To calculate the value of each weight, Eq. 5.51, fully simulated MC data are used, and the exact PDF expression with which this MC is generated is also needed.

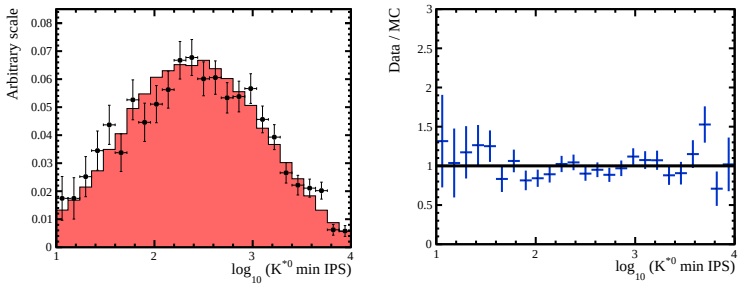

Figure A.19: Left: Comparison of the minimum IP significance of the K^{*0} tracks distribution in data (black points) and Monte Carlo (solid red histogram). Right: Ratio between data and Monte Carlo.

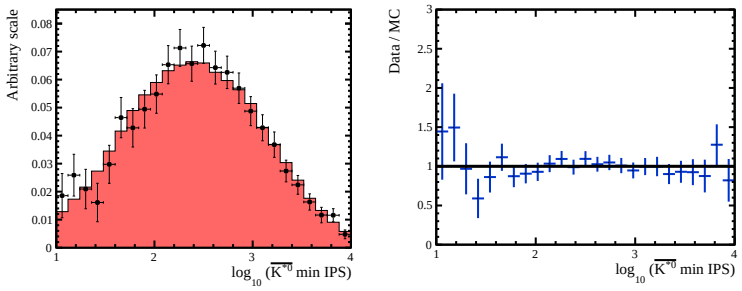

Figure A.20: Left: Comparison of the minimum IP significance of the $\overline{K}^{*0}$ tracks distribution in data (black points) and Monte Carlo (solid red histogram). Right: Ratio between data and Monte Carlo.

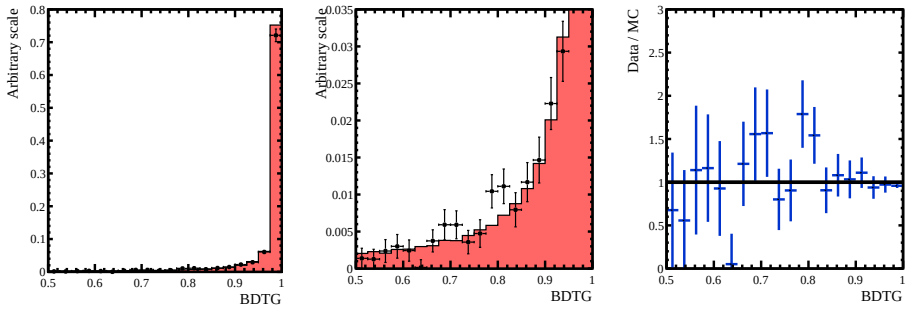

Figure A.21: Left: Comparison of the BDTG output distribution in data (black points) and Monte Carlo (solid red histogram). Middle: Same distribution zoomed in the y-axis. Right: Ratio between data and Monte Carlo.

Following Appendix D of Ref. [196], the expression for the PDF of the K^{*0} and $\overline{K}^{*0}$ masses used at generation can be expressed as

$$PDF = \left| \frac{\sqrt{m_1 \Gamma_{K^{*0}}(m_1)}}{m^2_{K^{*0}} - m^2_1 - i m_{K^{*0}} \Gamma_{K^{*0}}(m_1)} \right|^2 \left| \frac{\sqrt{m_2 \Gamma_{K^{*0}}(m_2)}}{m^2_{K^{*0}} - m^2_2 - i m_{K^{*0}} \Gamma_{K^{*0}}(m_2)} \right|^2 q_1 q_2, \quad \text{(A.1)}$$

where $m_{K^{*0}} = 896\,\text{MeV}/c^2$ is the K^{*0} and $\overline{K}^{*0}$ nominal masses, m_1 and m_2 are the $K^+\pi^-$ and $K^-\pi^+$ invariant masses, respectively, and,

$$
\begin{aligned}
q_1 &= \lambda(m_B, m_1, m_{K^{*0}}),\\
q_2 &= \lambda(m_B, m_{K^{*0}}, m_2),\\
\lambda(M, m_1, m_2) &\equiv \frac{\sqrt{(M^2-(m_1+m_2)^2)(M^2-(m_1-m_2)^2)}}{2M},\\
\Gamma_{K^{*0}}(m_1) &= \Gamma_{K^{*0}}\frac{m_{K^{*0}}}{m_1}\frac{B^2[q(m_1)]}{B^2[q(m_{K^{*0}})]}\left[\frac{q(m_1)}{q(m_{K^{*0}})}\right]^3,\\
\Gamma_{K^{*0}}(m_2) &= \Gamma_{K^{*0}}\frac{m_{K^{*0}}}{m_2}\frac{B^2[q(m_2)]}{B^2[q(m_{K^{*0}})]}\left[\frac{q(m_2)}{q(m_{K^{*0}})}\right]^3,\\
q(m_1) &= \lambda(m_1, m_K, m_\pi),\\
q(m_2) &= \lambda(m_2, m_K, m_\pi),\\
B[q] &= \frac{1}{\sqrt{1+(Rq)^2}},
\end{aligned}
$$

where $m_B = 5279.53$ is the B^0 mass, $\Gamma_{K^{*0}} = 50.3\,\text{MeV}/c^2$ is the K^{*0} ($\overline{K}^{*0}$) natural width, $m_K = 493.67\,\text{MeV}/c^2$ and $m_\pi = 139.57018$ are the kaon and pion masses and $R = 0.003/[\,\text{MeV}/c^2]$ is the range parameter.

A.5 Amplitude analysis figures for 2011

In Fig. A.22, the 2011 acceptance used for the visualisation is shown. In Fig. A.23, the 2011 $B^0 \to K^+\pi^-K^-\pi^+$ amplitude analysis figures are shown. In Fig. A.24, the visualisation of the 2011 figures of the $B_s^0 \to K^+\pi^-K^-\pi^+$ amplitude analysis is presented.

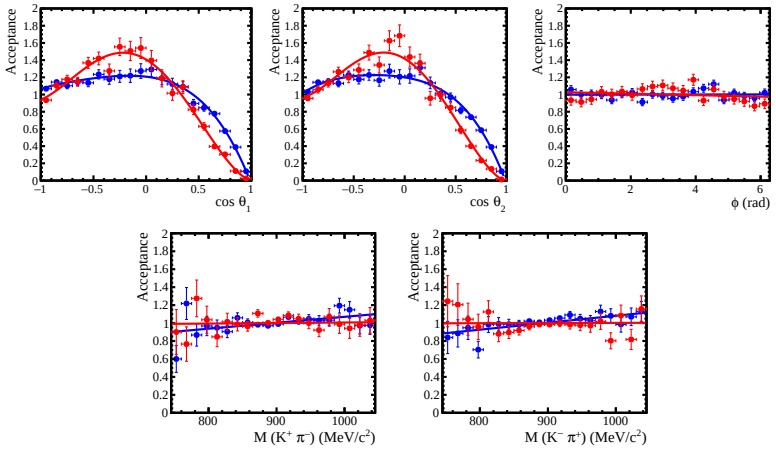

Figure A.22: Acceptance used for the visualisation of the amplitude analysis fit. Legendre polynomials factorised in θ_1, θ_2, ϕ, m_1 and m_2 are used. The points correspond to the Monte Carlo used to extract the Legendre coefficients. In blue the TOS category and in red the noTOS category. Figures of 2011.

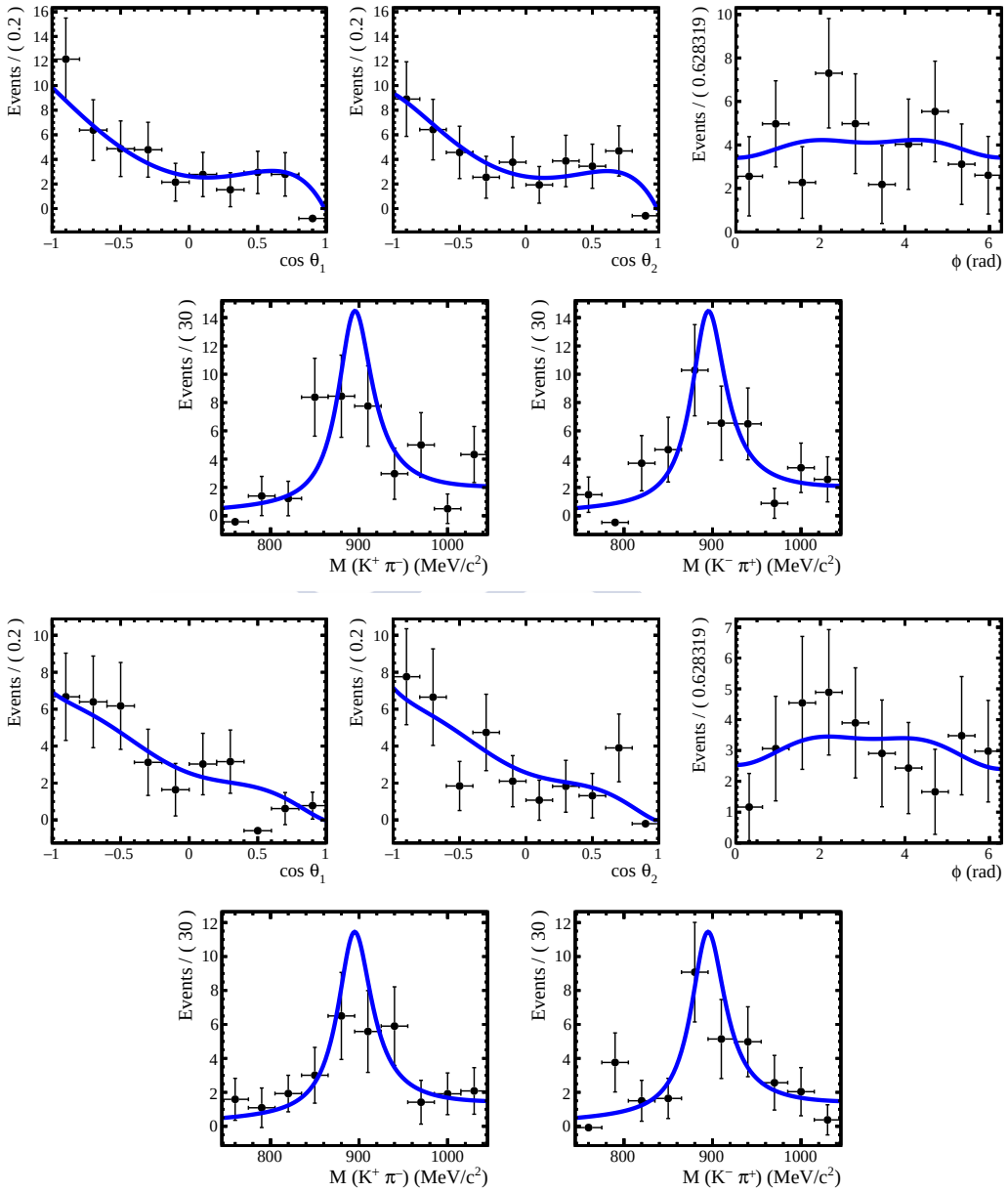

Figure A.23: Visualisation of the $B^0 \to K^+\pi^-K^-\pi^+$ amplitude analysis result with the acceptance parametrised as Legendre polynomials and the parameters obtained from the fit with the normalisation weights (Table 5.26). Figures of 2011 data. Top: TOS category. Bottom: noTOS category.

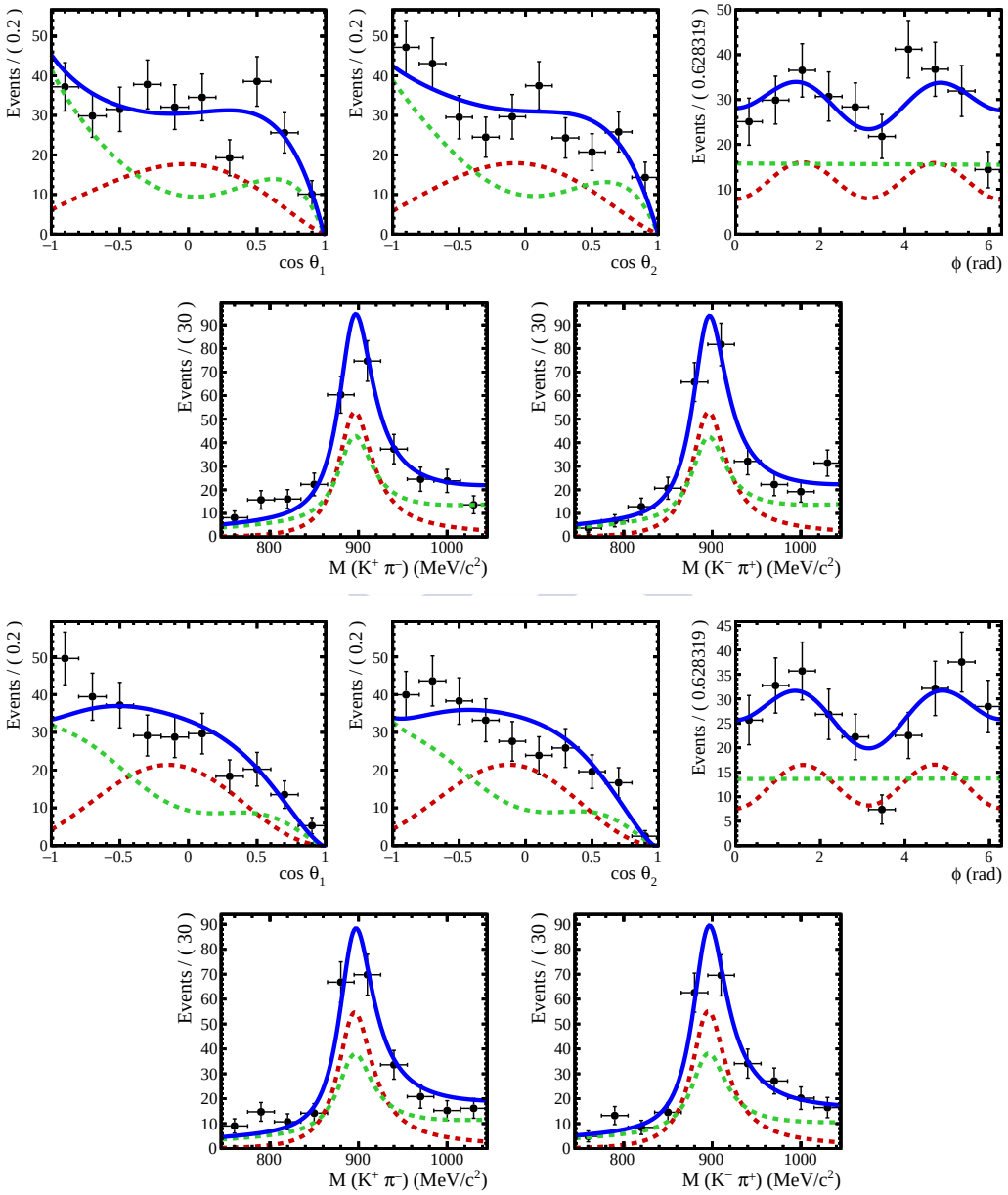

Figure A.24: Visualisation of the result of the $B_s^0 \to K^+\pi^-K^-\pi^+$ amplitude analysis with the acceptance parametrised as Legendre polynomials. The solid dots represent the sWeighted data. The red dashed line is the P-wave component and the green dashed line is the S-wave component. Figures of 2011 data. Top: TOS category. Bottom: noTOS category.

APPENDIX

B

First observation of the $B_s^0 \to \phi \overline{K}^{*0}$ decay

B.1 Data and simulation comparison

The results of the four-body mass spectrum allow making comparisons between data and Monte Carlo of some relevant variables. In particular, plots for the transverse momentum of the ϕ and the K^{*0} and its daughters have been produced. This is done for a $50\,\text{MeV}/c^2$ mass window around the B_s^0 and the B^0 masses. Whereas for the latter no background subtraction is performed in the data since the background contamination is tiny compared to the amount of $B^0 \to \phi K^{*0}$ sample, for the $B_s^0 \to \phi \overline{K}^{*0}$ the amount of signal, background and B^0 cross-feed within the mass window is computed and consequently subtracted to the signal. The p_T spectrum of the background is computed using the events in the high-mass sideband, $M_{KK\pi} > (M_{B_s^0} + 25\,\text{MeV}/c^2)$. The distributions for the ϕ and the K^{*0} are shown in Fig. B.1 for the B_s^0 decays and in Fig. B.2 for the B^0 decay. A Kolmogorov-Smirnov test was made to check the compatibility of the spectra, with the results shown in Table B.1.

B.2 Systematic effect due to the model on the cross-feed pollution

The effect of the B^0 cross-feed into the B_s^0 peak can change depending on the model used for the signal peaks. In particular, a computation changing the signals parametrisation from a Crystal-Ball plus a Gaussian into two concentric Gaussians is suggested. Fits with a double Gaussian are performed and compared with the Crystal-Ball plus Gaussian

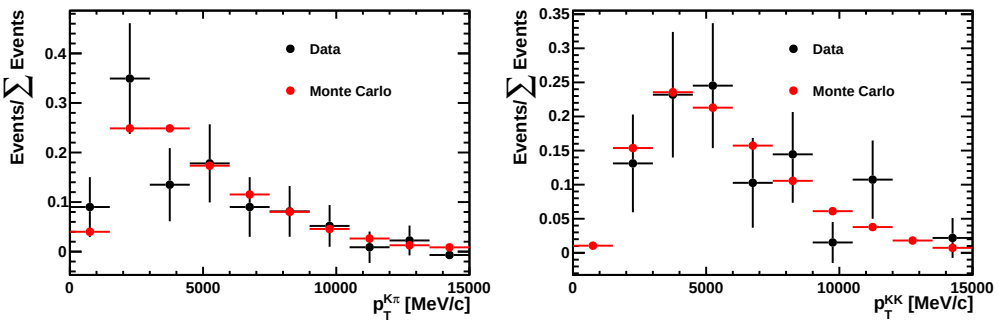

Figure B.1: Left: K^{*0} p_T spectrum from B_s^0 decays. Right: ϕ p_T spectrum from B_s^0 decays.

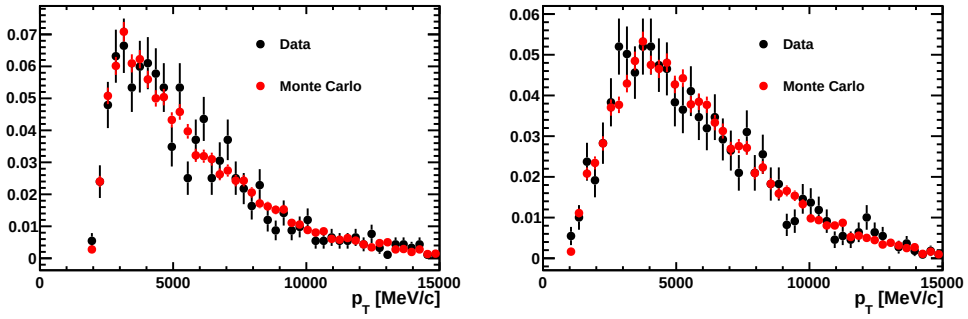

Figure B.2: Left: K^{*0} p_T spectrum from B^0 decays. Right: ϕ p_T spectrum from B^0 decays.

Table B.1: Results of the Kolmogorov-Smirnov test of the compatibility of the p_T spectra of the B-meson daughters.

K^{*0} from B^0 decays	ϕ from B^0 decays	$\overline{K}^{*0}$ from B_s^0 decays	ϕ from B_s^0 decays
0.997	0.540	0.589	0.999

model. It can be concluded that using a different model changes the signal result by: $31.1 - 29.9 = 1.2$. This is indeed a smaller effect than the one had previously been considered of 1.7 events.

B.3 Study of a possible pollution by $B^0_{d,s} \to \phi(\to K^+K^-)\rho^0(\to \pi^+\pi^-)$

One background which did not receive enough attention in the main text is due to possible kaon misidentification with pions. A possible contamination of the signal peak due to this effect is given by $B^0_{d,s} \to \phi(\to K^+K^-)\rho^0(\to \pi^+\pi^-)$ decays where one of the pions from the ρ^0 decay is misidentified as a kaon. Given the ρ^0 mass, 775.49 MeV/c^2, and its width, 149.1 MeV/c^2 [173], the shifted mass obtained when assigning the kaon mass to the misidentified pion is very likely to fall into the K^{*0} window.

Both modes $B^0_{d,s} \to \phi(\to K^+K^-)\rho^0(\to \pi^+\pi^-)$ are yet to be discovered and there are only upper limits for the corresponding branching ratios that are significantly more narrow for $\mathcal{B}(B^0 \to \phi\rho^0) < 3.3 \times 10^{-7}$ at 90% CL than for $\mathcal{B}(B_s^0 \to \phi\rho^0) < 6.17 \times 10^{-4}$ at 90% CL, both results from Ref. [173]. To estimate an upper limit for the $B^0 \to \phi\rho^0$ contamination a back of the envelope calculation can be used. As there are 1000.4 ± 32.3 $B^0 \to \phi K^{*0}$ events, this value can simply be multiplied for the ratio between this channel BR and the limit for $B^0 \to \phi\rho^0$. A factor of 3/2 must be added since the ρ^0 decays with almost 100% probability into two pions whereas the $\overline{K}^*$ does it only in two thirds of the cases into a $K\pi$ pair. Additionally the probability of mismatching a pion as a kaon must be computed. It has been done with Monte Carlo $B_s^0 \to \phi\overline{K}^{*0}$ events, obtaining a $(9.4 \pm 0.1)\%$ for such probability. The calculation gives, $N^{B^0 \to \phi\rho^0} \lesssim 4.7$.

The shape of $B^0 \to \phi\rho^0$ events has been obtained with a toy Monte Carlo that can be seen in Fig. B.3. The same is done for $B_s^0 \to \phi\rho^0$. These two histograms are included

in the four-body invariant mass fit with the caveat that $B^0 \to \phi\rho^0$ events are limited to be less than 4.7. Including these two distributions in the fit changes very little the results. Moreover, the fit including the signal hypothesis gives zero candidates for both $B^0 \to \phi\rho^0$ and $B_s^0 \to \phi\rho^0$ samples. It is only when the signal is removed, to compute the significance, that the fit increases the amount of these candidates to mimic the signal shape.

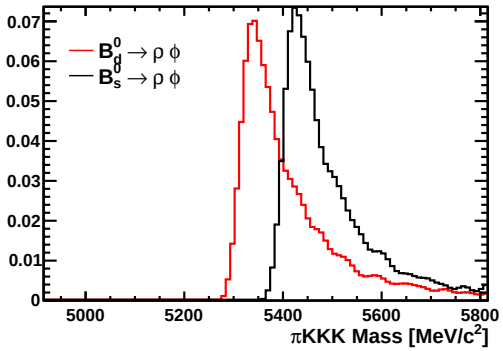

Figure B.3: πKKK mass for $B_{d,s}^0 \to \phi\rho^0$ events with pion-kaon misidentification in one of the pions of the ρ^0 decay. Produced with a toy Monte Carlo.

USC UNIVERSIDADE DE SANTIAGO DE COMPOSTELA

USC
UNIVERSIDADE
DE SANTIAGO
DE COMPOSTELA

Bibliography

[1] Particle Data Group, C. Patrignani *et al.*, *Review of particle physics*, Chin. Phys. **C40** (2016) 100001, and 2017 update. [Cited in pages 3, 13, 27, 98, and 112].

[2] A. Pomarol, *Beyond the Standard Model*, arXiv:1202.1391. [Cited in page 4].

[3] A. D. Sakharov, *Violation of CP invariance, C asymmetry, and baryon asymmetry of the universe*, Pisma Zh. Eksp. Teor. Fiz. **5** (1967) , [Translated in JETP Lett. 5, 24 (1967)]. [Cited in page 4].

[4] M. Kobayashi and T. Maskawa, *CP Violation in the Renormalizable Theory of Weak Interaction*, Prog. Theor. Phys. **49** (1973) 652. [Cited in pages 4 and 11].

[5] J. H. Christenson, J. W. Cronin, V. L. Fitch, and R. Turlay, *Evidence for the 2π Decay of the K_2^0 Meson*, Phys. Rev. Lett. **13** (1964) 138. [Cited in pages 4, 11, and 12].

[6] BaBar collaboration, B. Aubert *et al.*, *Observation of CP violation in the B^0 meson system*, Phys. Rev. Lett. **87** (2001) 091801, arXiv:hep-ex/0107013. [Cited in page 4].

[7] Belle collaboration, K. Abe *et al.*, *Observation of large CP violation in the neutral B meson system*, Phys. Rev. Lett. **87** (2001) 091802, arXiv:hep-ex/0107061. [Cited in page 4].

[8] BaBar collaboration, B. Aubert *et al.*, *The BaBar Detector: Upgrades, Operation and Performance*, Nucl. Instrum. Meth. **A729** (2013) 615, arXiv:1305.3560. [Cited in page 4].

[9] Belle collaboration, J. Brodzicka *et al.*, *Physics Achievements from the Belle Experiment*, PTEP **2012** (2012) 04D001, arXiv:1212.5342. [Cited in page 4].

[10] LHCb collaboration, R. Aaij *et al.*, *First observation of CP violation in the decays of B_s^0 mesons*, Phys. Rev. Lett. **110** (2013), no. 22 221601, arXiv:1304.6173. [Cited in page 4].

[11] M. Y. Han and Y. Nambu, *Three Triplet Model with Double SU(3) Symmetry*, Phys. Rev. **139** (1965) B1006. [Cited in page 5].

[12] S. L. Glashow, *Partial Symmetries of Weak Interactions*, Nucl. Phys. **22** (1961) 579. [Cited in page 5].

[13] S. Weinberg, *A Model of Leptons*, Phys. Rev. Lett. **19** (1967) 1264. [Cited in pages 5 and 8].

[14] A. Salam, *Weak and Electromagnetic Interactions*, Conf. Proc. **C680519** (1968) 367. [Cited in page 5].

[15] C.-N. Yang and R. L. Mills, *Conservation of Isotopic Spin and Isotopic Gauge Invariance*, Phys. Rev. **96** (1954) 191. [Cited in page 5].

[16] A. Pich, *The Standard model of Electroweak Interactions*, arXiv:0705.4264. [Cited in page 6].

[17] P. W. Higgs, *Broken Symmetries and the Masses of Gauge Bosons*, Phys. Rev. Lett. **13** (1964) 508. [Cited in page 8].

[18] F. Englert and R. Brout, *Broken Symmetry and the Mass of Gauge Vector Mesons*, Phys. Rev. Lett. **13** (1964) 321. [Cited in page 8].

[19] G. S. Guralnik, C. R. Hagen, and T. W. B. Kibble, *Global Conservation Laws and Massless Particles*, Phys. Rev. Lett. **13** (1964) 585. [Cited in page 8].

[20] N. Cabibbo, *Unitary Symmetry and Leptonic Decays*, Phys. Rev. Lett. **10** (1963) 531. [Cited in page 11].

[21] T. D. Lee and C.-N. Yang, *Question of Parity Conservation in Weak Interactions*, Phys. Rev. **104** (1956) 254. [Cited in page 11].

[22] C. S. Wu *et al.*, *Experimental Test of Parity Conservation in Beta Decay*, Phys. Rev. **105** (1957) 1413. [Cited in pages 11 and 12].

[23] R. L. Garwin, L. M. Lederman, and M. Weinrich, *Observations of the Failure of Conservation of Parity and Charge Conjugation in Meson Decays: The Magnetic Moment of the Free Muon*, Phys. Rev. **105** (1957) 1415. [Cited in pages 11 and 12].

[24] M. B. Gavela, P. Hernandez, J. Orloff, and O. Pene, *Standard model CP violation and baryon asymmetry*, Mod. Phys. Lett. **A9** (1994) 795, arXiv:hep-ph/9312215; M. B. Gavela *et al.*, *Standard model CP violation and baryon asymmetry. Part 2: Finite temperature*, Nucl. Phys. **B430** (1994) 382, arXiv:hep-ph/9406289. [Cited in page 11].

[25] G. C. Branco, L. Lavoura, and J. P. Silva, *CP Violation*, Int. Ser. Monogr. Phys. **103** (1999). [Cited in page 12].

[26] U. Nierste, *Three Lectures on Meson Mixing and CKM phenomenology*, 2009. arXiv:0904.1869. [Cited in page 12].

[27] P. Kooijman and N. Tuning, *Lectures on CP violation*, 2015. [Cited in page 12].

[28] BaBar collaboration, J. P. Lees *et al.*, *Observation of Time Reversal Violation in the B^0 Meson System*, Phys. Rev. Lett. **109** (2012) 211801, arXiv:1207.5832. [Cited in page 12].

[29] L. D. Landau, *On the conservation laws for weak interactions*, Nucl. Phys. **3** (1957) 127. [Cited in page 12].

[30] J. S. Schwinger, *The Theory of quantized fields. 1.*, Phys. Rev. **82** (1951) 914. [Cited in page 13].

[31] G. Luders, *On the Equivalence of Invariance under Time Reversal and under Particle-Antiparticle Conjugation for Relativistic Field Theories*, Kong. Dan. Vid. Sel. Mat. Fys. Med. **28N5** (1954), no. 5 1. [Cited in page 13].

[32] LHCb collaboration, R. Aaij *et al.*, *Search for violations of Lorentz invariance and CPT symmetry in $B^0_{(s)}$ mixing*, Phys. Rev. Lett. **116** (2016) 241601, arXiv:1603.04804. [Cited in page 13].

[33] CPLEAR collaboration, A. Angelopoulos *et al.*, *First direct observation of time reversal noninvariance in the neutral kaon system*, Phys. Lett. **B444** (1998) 43. [Cited in page 13].

[34] L.-L. Chau and W.-Y. Keung, *Comments on the Parametrization of the Kobayashi-Maskawa Matrix*, Phys. Rev. Lett. **53** (1984) 1802. [Cited in page 13].

[35] L. Wolfenstein, *Parametrization of the Kobayashi-Maskawa Matrix*, Phys. Rev. Lett. **51** (1983) 1945. [Cited in page 13].

[36] C. Jarlskog, *Commutator of the Quark Mass Matrices in the Standard Electroweak Model and a Measure of Maximal CP Violation*, Phys. Rev. Lett. **55** (1985) 1039; C. Jarlskog, *A Basis Independent Formulation of the Connection Between Quark Mass Matrices, CP Violation and Experiment*, Z. Phys. **C29** (1985) 491. [Cited in page 14].

[37] Belle collaboration, BaBar collaboration, A. J. Bevan *et al.*, *The Physics of the B Factories*, Eur. Phys. J. **C74** (2014) 3026, arXiv:1406.6311. [Cited in pages 15 and 27].

[38] J. Charles *et al.*, *Current status of the Standard Model CKM fit and constraints on $\Delta F = 2$ New Physics*, Phys. Rev. **D91** (2015), no. 7 073007, arXiv:1501.05013. [Cited in page 15].

[39] V. Weisskopf and E. P. Wigner, *Calculation of the natural brightness of spectral lines on the basis of Dirac's theory*, Z. Phys. **63** (1930) 54; V. Weisskopf and E. Wigner, *Over the natural line width in the radiation of the harmonius oscillator*, Z. Phys. **65** (1930) 18. [Cited in page 17].

[40] G. Buchalla, *Kaon and Charm Physics: Theory*, arXiv:hep-ph/0103166. [Cited in page 21].

[41] ARGUS collaboration, H. Albrecht *et al.*, *Observation of B^0- anti-B^0 mixing*, Phys. Lett. **B192** (1987) 245. [Cited in page 21].

[42] LHCb collaboration, R. Aaij *et al.*, *A precise measurement of the B^0 meson oscillation frequency*, Eur. Phys. J. C **76** (2016) 412, arXiv:1604.03475. [Cited in page 21].

[43] D0 collaboration, V. M. Abazov *et al.*, *First direct two-sided bound on the B^0_s oscillation frequency*, Phys. Rev. Lett. **97** (2006) 021802, arXiv:hep-ex/0603029; CDF collaboration, A. Abulencia *et al.*, *Observation of $B^0_s - \overline{B}^0_s$ Oscillations*, Phys. Rev. Lett. **97** (2006) 242003, arXiv:hep-ex/0609040. [Cited in page 21].

[44] LHCb collaboration, R. Aaij *et al.*, *Precision measurement of the $B_s^0 - \overline{B}_s^0$ oscillation frequency with the decay $B_s^0 \to D_s^- \pi^+$*, New J. Phys. **15** (2013) 053021, arXiv:1304.4741. [Cited in page 21].

[45] ATLAS collaboration, M. Aaboud *et al.*, *Measurement of the relative width difference of the $B^0 - \overline{B}^0$ system with the ATLAS detector*, JHEP **06** (2016) 081, arXiv:1605.07485. [Cited in page 21].

[46] LHCb collaboration, R. Aaij *et al.*, *Precision measurement of CP violation in $B_s^0 \to J/\psi K^+ K^-$ decays*, Phys. Rev. Lett. **114** (2015) 041801, arXiv:1411.3104. [Cited in pages 22 and 141].

[47] LHCb collaboration, R. Aaij *et al.*, *Measurement of the semileptonic CP asymmetry in $B^0 - \overline{B}^0$ mixing*, Phys. Rev. Lett. **114** (2015) 041601, arXiv:1409.8586. [Cited in page 23].

[48] Heavy Flavor Averaging Group, Y. Amhis *et al.*, *Averages of b-hadron, c-hadron, and τ-lepton properties as of summer 2016*, arXiv:1612.07233. [Cited in page 23].

[49] D0 collaboration, V. M. Abazov *et al.*, *Study of CP-violating charge asymmetries of single muons and like-sign dimuons in $p\bar{p}$ collisions*, Phys. Rev. **D89** (2014) 012002, arXiv:1310.0447. [Cited in page 23].

[50] LHCb collaboration, R. Aaij *et al.*, *Measurement of the CP asymmetry in $B_s^0 - \overline{B}_s^0$ mixing*, Phys. Rev. Lett. **117** (2016) 061803, arXiv:1605.09768. [Cited in page 23].

[51] M. Ciuchini, M. Pierini, and L. Silvestrini, *$B_s^0 \to K^{(*)0} \bar{K}^{(*)0}$ decays: The Golden channels for new physics searches*, Phys. Rev. Lett. **100** (2008) 031802, arXiv:hep-ph/0703137. [Cited in pages 24, 25, and 26].

[52] B. Bhattacharya, A. Datta, M. Imbeault, and D. London, *Measuring β_s with $B_s^0 \to K^{(*)0} \bar{K}^{(*)0}$ – a Reappraisal*, Phys. Lett. **B717** (2012) 403, arXiv:1203.3435. [Cited in pages 24, 25, 26, and 27].

[53] B. Bhattacharya, A. Datta, M. Duraisamy, and D. London, *Searching for new physics with $\overline{b} \to \overline{s}$ $B_s^0 \to V_1 V_2$ penguin decays*, Phys. Rev. **D88** (2013) 016007, arXiv:1306.1911. [Cited in pages 24, 25, 29, 118, 119, and 121].

[54] R. Fleischer and M. Gronau, *Studying new physics amplitudes in charmless B_s decays*, Phys. Lett. **B660** (2008) 212, arXiv:0709.4013. [Cited in pages 24 and 25].

[55] S. Descotes-Genon, J. Matias, and J. Virto, *An analysis of $B_{d,s}$ mixing angles in presence of new physics and an update of $B_s^0 \to K^{*0} \overline{K}^{*0}$*, Phys. Rev. **D85** (2012) 034010, arXiv:1111.4882. [Cited in pages 24, 25, 26, 91, 141, 142, 144, 154, and 165].

[56] S. Descotes-Genon, J. Matias, and J. Virto, *Penguin-mediated $B_{d,s} \to VV$ decays and the $B_s^0 - \overline{B}_s^0$ mixing angle*, Phys. Rev. **D76** (2007) 074005, arXiv:0705.0477. [Cited in pages 24, 25, 27, and 144].

[57] J. Virto, *Topics in Hadronic B Decays*, Ph.D. thesis, Universitat Autònoma de Barcelona, Spain, 2008, arXiv:0712.3367 [hep-ph]. [Cited in pages 24 and 27].

[58] G. Valencia, *Angular Correlations in the Decay $B \to VV$ and CP Violation*, Phys. Rev. **D39** (1989) 3339. [Cited in page 27].

[59] M. Gronau and J. L. Rosner, *Triple product asymmetries in K, $D_{(s)}$ and $B_{(s)}$ decays*, Phys. Rev. **D84** (2011) 096013, arXiv:1107.1232. [Cited in page 27].

[60] A. Datta and D. London, *Triple-product correlations in $B \to V_1 V_2$ decays and New Physics*, Int. J. Mod. Phys. **A19** (2004) 2505, arXiv:hep-ph/0303159. [Cited in page 27].

[61] G. Kramer and W. F. Palmer, *Branching ratios and CP asymmetries in the decay $B \to VV$*, Phys. Rev. **D45** (1992) 193. [Cited in page 28].

[62] S. Stone and L. Zhang, *S-waves and the Measurement of CP Violating Phases in B_s^0 Decays*, Phys. Rev. **D79** (2009) 074024, arXiv:0812.2832; Y. Xie, P. Clarke, G. Cowan, and F. Muheim, *Determination of $2\beta_s$ in $B_s^0 \to J/\psi K^+K^-$ Decays in the Presence of a K^+K^- S-Wave Contribution*, JHEP **09** (2009) 074, arXiv:0908.3627. [Cited in page 29].

[63] A. Ali, J. G. Korner, G. Kramer, and J. Willrodt, *Nonleptonic Weak Decays of Bottom Mesons*, Z. Phys. **C1** (1979) 269; M. Suzuki, *Helicity conservation in inclusive nonleptonic decay $B \to VX$: Test of long-distance final-state interaction*, Phys. Rev. **D66** (2002) 054018, arXiv:hep-ph/0206291; C.-H. Chen, Y.-Y. Keum, and H.-n. Li, *Perturbative QCD analysis of $B \to \phi K^{*0}$ decays*, Phys. Rev. **D66** (2002) 054013, arXiv:hep-ph/0204166. [Cited in page 29].

[64] M. Beneke, J. Rohrer, and D. Yang, *Branching fractions, polarisation and asymmetries of $B \to VV$ decays*, Nucl. Phys. **B774** (2007) 64, arXiv:hep-ph/0612290. [Cited in pages 29, 61, 90, 91, 142, and 144].

[65] H.-Y. Cheng and K.-C. Yang, *Branching Ratios and Polarization in $B \to VV$, VA, AA Decays*, Phys. Rev. **D78** (2008) 094001, arXiv:0805.0329. [Cited in page 29].

[66] H.-Y. Cheng, C.-K. Chua, and A. Soni, *Final state interactions in hadronic B decays*, Phys. Rev. **D71** (2005) 014030, arXiv:hep-ph/0409317. [Cited in page 29].

[67] Belle collaboration, A. Somov *et al.*, *Improved measurement of CP-violating parameters in $B^0 \to \rho^+\rho^-$ decays*, Phys. Rev. **D76** (2007) 011104, arXiv:hep-ex/0702009; BaBar collaboration, B. Aubert *et al.*, *A Study of $B^0 \to \rho^+\rho^-$ Decays and Constraints on the CKM Angle α*, Phys. Rev. **D76** (2007) 052007, arXiv:0705.2157. [Cited in page 30].

[68] Belle collaboration, J. Zhang *et al.*, *Observation of $B^+ \to \rho^+\rho^0$*, Phys. Rev. Lett. **91** (2003) 221801, arXiv:hep-ex/0306007; BaBar collaboration, B. Aubert *et al.*, *Improved Measurement of $B^+ \to \rho^+\rho^0$ and Determination of the Quark-Mixing Phase Angle α*, Phys. Rev. Lett. **102** (2009) 141802, arXiv:0901.3522. [Cited in page 30].

[69] BaBar collaboration, B. Aubert *et al.*, *Observation of B Meson Decays to ωK^* and Improved Measurements for $\omega\rho$ and ωf_0*, Phys. Rev. **D79** (2009) 052005, arXiv:0901.3703. [Cited in page 30].

[70] BaBar collaboration, J. P. Lees *et al.*, *B^0 meson decays to $\rho^0 K^{*0}$, $f_0 K^{*0}$, and $\rho^- K^{*+}$, including higher K^* resonances*, Phys. Rev. **D85** (2012) 072005, arXiv:1112.3896. [Cited in pages 30, 112, and 144].

[71] Belle collaboration, K.-F. Chen *et al.*, *Measurement of polarization and triple-product correlations in $B \to \phi K^*$ decays*, Phys. Rev. Lett. **94** (2005) 221804, arXiv:hep-ex/0503013. [Cited in page 30].

[72] BaBar collaboration, B. Aubert *et al.*, *Time-dependent and time-integrated angular analysis of $B \to \varphi K_S^0 \pi^0$ and $\varphi K^\pm \pi^\mp$*, Phys. Rev. **D78** (2008) 092008, arXiv:0808.3586. [Cited in pages 30, 74, 76, 83, and 87].

[73] LHCb collaboration, R. Aaij *et al.*, *Measurement of polarization amplitudes and CP asymmetries in $B^0 \to \phi K^*(892)^0$*, JHEP **05** (2014) 069, arXiv:1403.2888. [Cited in pages 30 and 91].

[74] LHCb collaboration, R. Aaij *et al.*, *Measurement of CP asymmetries and polarisation fractions in $B_s^0 \to K^{*0}\overline{K}^{*0}$ decays*, JHEP **07** (2015) 166, arXiv:1503.05362. [Cited in pages 30, 91, 118, 122, 133, 134, 141, 142, and 143].

[75] LHCb collaboration, R. Aaij *et al.*, *Measurement of CP violation in $B_s^0 \to \phi\phi$ decays*, Phys. Rev. **D90** (2014) 052011, arXiv:1407.2222. [Cited in pages 30 and 91].

[76] LHCb collaboration, *The LHCb detector at the LHC*, JINST **3** (2008) S08005. [Cited in page 31].

[77] L. Evans and P. Bryant, *LHC machine*, JINST **3** (2008) S08001. [Cited in page 31].

[78] LHCb collaboration, *LHC-B: a dedicated LHC collider beauty experiment for precision measurements of CP-violation*, CERN-LHCC-95-005. [Cited in page 31].

[79] LHCb collaboration, *LHCb: a Large Hadron Collider beauty experiment for precision measurements of CP-violation and rare decays*, CERN-LHCC-98-004. [Cited in page 31].

[80] LHCb collaboration, *LHCb reoptimized detector design and performance*, CERN-LHCC-2003-030. [Cited in pages 31, 38, 40, and 45].

[81] LHCb collaboration, *Roadmap for selected key measurements of LHCb*, arXiv:0912.4179. [Cited in page 31].

[82] LHCb collaboration, CMS collaboration, *Observation of the rare $B_s^0 \to \mu^+\mu^-$ decay from the combined analysis of CMS and LHCb data*, Nature **522** (2015) 68, arXiv:1411.4413. [Cited in page 31].

[83] LHCb collaboration, *Angular analysis of the $B^0 \to K^{*0}\mu^+\mu^-$ decay using 3 fb^{-1} of integrated luminosity*, JHEP **02** (2016) 104, arXiv:1512.04442. [Cited in page 31].

[84] LHCb collaboration, *First observation of CP Violation in the decays of B_s^0 mesons*, Phys. Rev. Lett. **110** (2013) 221601, arXiv:1304.6173. [Cited in page 31].

[85] LHCb collaboration, *Determination of the $X(3872)$ meson quantum numbers*, Phys. Rev. Lett. **110** (2013) 222001, arXiv:1302.6269. [Cited in page 31].

[86] LHCb collaboration, *Observation of the resonant character of the $Z(4430)^-$ state*, Phys. Rev. Lett. **112** (2014) 222002, arXiv:1404.1903. [Cited in page 31].

[87] LHCb collaboration, *Observation of $J/\psi\,\phi$ structures consistent with exotic states from amplitude analysis of $B^+ \to J/\psi\,\phi K^+$ decays*, arXiv:1606.07895. [Cited in page 31].

[88] LHCb collaboration, *Observation of $J/\psi\,p$ Resonances Consistent with pentaquark states in $\Lambda_b^0 \to J/\psi\,K^-p$ decays*, Phys. Rev. Lett. **115** (2015) 072001, arXiv:1507.03414. [Cited in page 31].

[89] LHCb collaboration, *Measurement of the ratio of branching fractions $\mathcal{B}(\bar{B}^0 \to D^{*+}\tau^-\bar{\nu}_\tau)/\mathcal{B}(\bar{B}^0 \to D^{*+}\mu^-\bar{\nu}_\mu)$*, Phys. Rev. Lett. **115** (2015) 111803, arXiv:1506.08614, [Addendum: Phys. Rev. Lett.115,no.15,159901(2015)]. [Cited in page 31].

[90] LHCb collaboration, *Measurement of the forward-backward asymmetry in $Z/\gamma^* \to \mu^+\mu^-$ decays and determination of the effective weak mixing angle*, JHEP **11** (2015) 190, arXiv:1509.07645. [Cited in page 31].

[91] LHCb collaboration, *Measurements of long-range near-side angular correlations in $\sqrt{s_{NN}} = 5$ TeV proton-lead collisions in the forward region*, Phys. Lett. **B762** (2016) 473, arXiv:1512.00439. [Cited in page 31].

[92] ATLAS collaboration, *ATLAS: technical proposal for a general-purpose pp experiment at the Large Hadron Collider at CERN*, CERN-LHCC-94-43. [Cited in page 33].

[93] ATLAS collaboration, *The ATLAS experiment at the CERN Large Hadron Collider*, JINST **3** (2008) S08003. [Cited in page 33].

[94] CMS collaboration, *CMS, the Compact Muon Solenoid: technical proposal*, CERN-LHCC-94-38. [Cited in page 33].

[95] CMS collaboration, *The CMS experiment at the CERN LHC*, JINST **3** (2008) S08004. [Cited in page 33].

[96] ATLAS collaboration, *Observation of a new particle in the search for the Standard Model Higgs boson with the ATLAS detector at the LHC*, Phys. Lett. **B716** (2012) 1, arXiv:1207.7214. [Cited in page 34].

[97] CMS collaboration, *Observation of a new boson at a mass of 125 GeV with the CMS experiment at the LHC*, Phys. Lett. **B716** (2012) 30, arXiv:1207.7235. [Cited in page 34].

[98] ALICE collaboration, *ALICE: technical proposal for a large ion collider experiment at the CERN LHC*, CERN-LHCC-95-71. [Cited in page 34].

[99] ALICE collaboration, *The ALICE experiment at the CERN LHC*, JINST **3** (2008) S08002. [Cited in page 34].

[100] TOTEM collaboration, *The TOTEM experiment at the CERN Large Hadron Collider*, JINST **3** (2008) S08007. [Cited in page 34].

[101] MoEDAL collaboration, *Technical design report of the MoEDAL experiment*, CERN-LHCC-2009-006. [Cited in page 34].

[102] LHCf collaboration, *The LHCf detector at the CERN Large Hadron Collider*, JINST **3** (2008) S08006. [Cited in page 34].

[103] X. Cid Vidal, *Search for the rare decays $B^0_{(s)} \to \mu^+\mu^-$ and $K^0_S \to \mu^+\mu^-$ with 1 fb^{-1} at LHCb*, Ph.D. thesis, Universidade de Santiago de Compostela, Spain, 2012, CERN-THESIS-2012-154. [Cited in page 36].

[104] P. Álvarez Cartelle, *Study of the penguin-dominated decay $B^0_s \to K^{*0}\overline{K}^{*0}$ at LHCb*, Ph.D. thesis, Universidade de Santiago de Compostela, Spain, 2014, CERN-THESIS-2014-293. [Cited in page 36].

[105] V. J. Rives Molina, *Study of b-hadron decays into two hadrons and a photon at LHCb and first observation of b-baryon radiative decays*, Ph.D. thesis, Universitat de Barcelona, Spain, 2016, CERN-THESIS-2016-158. [Cited in page 36].

[106] C. Vázquez Sierra, *An approach to new physics at LHCb: study of penguin pollution to $\phi_s(B^0_s \to J/\psi\,\phi)$ using $B^0_s \to J/\psi\,\overline{K}^{*0}$ decays, and search for a light A^0_1 Higgs boson in the NMSSM.*, Ph.D. thesis, Universidade de Santiago de Compostela, Spain, 2016, CERN-THESIS-2016-281. [Cited in page 36].

[107] L. Henry, *Charmless hadronic three-body decays of neutral B mesons with a K^0_S in the final state in the LHCb experiment: branching fractions and an amplitude analysis*, Ph.D. thesis, Université Pierre et Marie Curie, Paris, France, 2016, CERN-THESIS-2016-203. [Cited in page 36].

[108] P. Ruiz Valls, *Photon polarization in $B^0_s \to \phi\gamma$ decays at the LHCb experiment*, Ph.D. thesis, Universitat de València, Spain, 2016, CERN-THESIS-2016-217. [Cited in page 36].

[109] M. Borsato, *Study of the $B^0 \to K^{*0}e^+e^-$ decay with the LHCb detector and development of a novel concept of PID detector: the Focusing DIRC*, Ph.D. thesis, Université Sorbonne Paris Cité, France, 2015, CERN-THESIS-2015-219. [Cited in page 36].

[110] LHCb collaboration, *LHCb magnet technical design report*, CERN-LHCC-2000-007. [Cited in page 36].

[111] J. André *et al.*, *Status of the LHCb magnet system*, IEEE Trans. Appl. Supercond. **12** (2002), no. 1 336. [Cited in page 36].

[112] J. André *et al.*, *Status of the LHCb dipole magnet*, IEEE Trans. Appl. Supercond. **14** (2004), no. 2 509. [Cited in page 36].

[113] M. Vesterinen, *Considerations on the LHCb dipole magnet polarity reversal*, LHCb-PUB-2014-006. [Cited in pages 37 and 60].

[114] LHCb collaboration, *LHCb vertex locator technical design report*, CERN-LHCC-2001-011. [Cited in page 37].

[115] J. Gassner, M. Needham, and O. Steinkamp, *Layout and expected performance of the LHCb TT station*, LHCb-2003-140. [Cited in page 38].

[116] LHCb collaboration, *LHCb inner tracker technical design report*, CERN-LHCC-2002-029. [Cited in page 38].

[117] LHCb collaboration, *LHCb outer tracker technical design report*, CERN-LHCC-2001-024. [Cited in page 39].

[118] LHCb RICH collaboration, *LHCb RICH1 engineering design review report*, LHCb-2004-121. [Cited in page 40].

[119] LHCb collaboration, *LHCb RICH technical design report*, CERN-LHCC-2000-037. [Cited in page 40].

[120] LHCb RICH collaboration, *LHCb RICH2 engineering design review report*, LHCb-2002-009. [Cited in page 40].

[121] LHCb collaboration, *LHCb calorimeters technical design report*, CERN-LHCC-2000-036. [Cited in page 41].

[122] LHCb collaboration, *LHCb muon system technical design report*, CERN-LHCC-2001-010. [Cited in page 42].

[123] LHCb collaboration, *LHCb addendum to the muon system technical design report*, CERN-LHCC-2003-002. [Cited in page 42].

[124] LHCb collaboration, *LHCb second addendum to the muon system technical design report*, CERN-LHCC-2005-012. [Cited in page 42].

[125] LHCb collaboration, *LHCb detector performance*, Int. J. Mod. Phys. **A30** (2015), no. 07 1530022, arXiv:1412.6352. [Cited in page 43].

[126] P. Mato, *GAUDI-architecture design document*, LHCb-98-064; G. Barrand *et al.*, *GAUDI - A software architecture and framework for building HEP data processing applications*, Comput. Phys. Commun. **140** (2001) 45. [Cited in page 43].

[127] LHCb collaboration, *LHCb computing technical design report*, CERN-LHCC-2005-019. [Cited in page 45].

[128] C. Eck *et al.*, *LHC computing Grid: technical design report*, CERN-LHCC-2005-024; I. Bird *et al.*, *Update of the Computing Models of the WLCG and the LHC Experiments*, CERN-LHCC-2014-014. [Cited in page 45].

[129] A. Tsaregorodtsev *et al.*, *DIRAC: A community grid solution*, J. Phys. Conf. Ser. **119** (2008) 062048; A. Tsaregorodtsev *et al.*, *DIRAC Distributed Computing Services*, J. Phys. Conf. Ser. **513** (2014) 032096. [Cited in page 45].

[130] K. Harrison *et al.*, *GANGA: A User Grid interface for Atlas and LHCb*, CHEP 2003 Proceedings, **C0303241** TUCT002, arXiv:cs/0306085; J. T. Mościcki *et al.*, *Ganga : A tool for computational-task management and easy access to Grid resources*, Comput. Phys. Commun. **180** (2009) 2303, arXiv:0902.2685. [Cited in page 45].

[131] LHCb collaboration, *LHCb trigger system technical design report*, CERN-LHCC-2003-031. [Cited in page 45].

[132] A. Martín Sánchez, P. Robbe, and M.-H. Schune, *Performances of the LHCb L0 calorimeter trigger*, LHCb-PUB-2011-026. [Cited in page 46].

[133] A. Martín Sánchez, *CP violation studies on the $\overline{B} \to D\overline{K}^{*0}$ decays and hadronic trigger performance with the LHCb detector at CERN*, Ph.D. thesis, Université Paris-Sud XI, Orsay, France, 2013, CERN-THESIS-2013-311. [Cited in page 46].

[134] R. Aaij and J. Albrecht, *Muon triggers in the high level trigger of LHCb*, LHCb-PUB-2011-017. [Cited in page 46].

[135] R. Aaij *et al.*, *The LHCb trigger and its performance in* 2011, JINST **8** (2013) P04022, arXiv:1211.3055. [Cited in page 47].

[136] LHCb HLT project, *Performance of the LHCb high level trigger in* 2012, J. Phys. Conf. Ser. **513** (2014) 012001, arXiv:1310.8544. [Cited in page 47].

[137] S. Tolk, J. Albrecht, F. Dettori, and A. Pellegrino, *Data driven trigger efficiency determination at LHCb*, LHCb-PUB-2014-039. [Cited in page 48].

[138] V. V. Gligorov, *A single track HLT1 trigger*, LHCb-PUB-2011-003. [Cited in page 48].

[139] V. V. Gligorov and M. Williams, *Efficient, reliable and fast high-level triggering using a bonsai boosted decision tree*, JINST **8** (2013) P02013, arXiv:1210.6861. [Cited in page 49].

[140] LHCb collaboration, *LHCb online system, data acquisition and experiment control: technical design report*, CERN-LHCC-2001-040. [Cited in page 49].

[141] N. Tatsuya, E. Aslanides, A. Smith, and W. Witzeling, *Addendum to the LHCb online system technical design report*, CERN-LHCC-2005-039. [Cited in page 49].

[142] F. Alessio *et al.*, *The LHCb Data Acquisition during LHC Run 1*, J. Phys. Conf. Ser. **513** (2014) 012033. [Cited in page 49].

[143] G. Haefeli *et al.*, *The LHCb DAQ interface board TELL1*, Nucl. Instrum. Meth. **A560** (2006) 494. [Cited in page 49].

[144] E. Bos, *Reconstruction of Charged Particles in the LHCb Experiment*, Ph.D. thesis, Vrije Universiteit, Amsterdam, The Netherlands, 2010, CERN-THESIS-2010-049. [Cited in page 51].

[145] D. Hutchcroft, *VELO pattern recognition*, LHCb-2007-013. [Cited in page 51].

[146] O. Callot, *FastVelo, a fast and efficient pattern recognition package for the VELO*, LHCb-PUB-2011-001. [Cited in page 51].

[147] O. Callot and S. Hansmann-Menzemer, *The forward tracking: algorithm and performance studies*, LHCb-2007-015. [Cited in page 52].

[148] M. Needham and J. Van Tilburg, *Performance of the track matching*, LHCb-2007-020. [Cited in page 52].

[149] M. Needham, *Performance of the track matching*, LHCb-2007-129. [Cited in page 52].

[150] O. Callot and M. Schiller, *PatSeeding: a standalone track reconstruction algorithm*, LHCb-2008-042. [Cited in page 52].

[151] R. Fruhwirth, *Application of Kalman filtering to track and vertex fitting*, Nucl. Instrum. Meth. **A262** (1987) 444. [Cited in page 52].

[152] J. A. N. van Tilburg, *Track Simulation and Reconstruction in LHCb*, Ph.D. thesis, Vrije Universiteit, Amsterdam, The Netherlands, 2005, CERN-THESIS-2005-040. [Cited in pages 52 and 57].

[153] A. Jaeger *et al.*, *Measurement of the track finding efficiency*, LHCb-PUB-2011-025. [Cited in page 52].

[154] LHCb collaboration, *Measurement of the track reconstruction efficiency at LHCb*, JINST **10** (2015), no. 02 P02007, arXiv:1408.1251. [Cited in page 52].

[155] M. Krasowski *et al.*, *Primary vertex reconstruction*, LHCb-2007-011. [Cited in page 53].

[156] LHCb collaboration, *Precision measurement of the B_s^0-$\overline{B}_s^0$ oscillation frequency with the decay $B_s^0 \to D_s^- \pi^+$*, New J. Phys. **15** (2013) 053021, arXiv:1304.4741. [Cited in page 53].

[157] LHCb RICH collaboration, *Performance of the LHCb RICH detector at the LHC*, Eur. Phys. J. **C73** (2013) 2431, arXiv:1211.6759. [Cited in page 53].

[158] O. Deschamps *et al.*, *Photon and neutral pion reconstruction*, LHCb-2003-091. [Cited in page 54].

[159] H. Terrier and I. Belyaev, *Particle identification with LHCb calorimeters*, LHCb-2003-092. [Cited in page 54].

[160] F. Archilli *et al.*, *Performance of the muon identification at LHCb*, JINST **8** (2013) P10020, arXiv:1306.0249. [Cited in page 55].

[161] M. Clemencic *et al.*, *The LHCb simulation application, Gauss: Design, evolution and experience*, J. Phys. Conf. Ser. **331** (2011) 032023. [Cited in page 57].

[162] T. Sjöstrand, S. Mrenna, and P. Skands, *PYTHIA 6.4 physics and manual*, JHEP **05** (2006) 026, arXiv:hep-ph/0603175; T. Sjöstrand, S. Mrenna, and P. Skands, *A brief introduction to PYTHIA 8.1*, Comput. Phys. Commun. **178** (2008) 852, arXiv:0710.3820. [Cited in page 57].

[163] I. Belyaev *et al.*, *Handling of the generation of primary events in Gauss, the LHCb simulation framework*, J. Phys. Conf. Ser. **331** (2011) 032047. [Cited in page 57].

[164] D. J. Lange, *The EvtGen particle decay simulation package*, Nucl. Instrum. Meth. **A462** (2001) 152. [Cited in page 57].

[165] P. Golonka and Z. Was, *PHOTOS Monte Carlo: A precision tool for QED corrections in Z and W decays*, Eur. Phys. J. **C45** (2006) 97, arXiv:hep-ph/0506026. [Cited in page 57].

[166] Geant4 collaboration, S. Agostinelli *et al.*, *Geant4: A simulation toolkit*, Nucl. Instrum. Meth. **A506** (2003) 250; Geant4 collaboration, J. Allison *et al.*, *Geant4 developments and applications*, IEEE Trans. Nucl. Sci. **53** (2006) 270. [Cited in page 57].

[167] R. Alemany-Fernandez, F. Follin, and R. Jacobsson, *The LHCb Online Luminosity Control and Monitoring*, CERN-ACC-2013-0028. [Cited in page 59].

[168] M. Frank *et al.*, *Deferred High Level Trigger in LHCb: A Boost to CPU Resource Utilization*, J. Phys. Conf. Ser. **513** (2014) 012006. [Cited in page 59].

[169] M. Gronau, O. F. Hernández, D. London, and J. L. Rosner, *Electroweak penguins and two-body B decays*, Phys. Rev. **D52** (1995) 6374, arXiv:hep-ph/9504327. [Cited in page 61].

[170] Particle Data Group, J. Beringer *et al.*, *Review of particle physics*, Phys. Rev. **D86** (2012) 010001. [Cited in page 61].

[171] A. Ali *et al.*, *Charmless non-leptonic B_s^0 decays to PP, PV and VV final states in the perturbative QCD approach*, Phys. Rev. **D76** (2007) 074018, arXiv:hep-ph/0703162. [Cited in pages 61, 62, 90, and 144].

[172] B. Adeva *et al.*, *First observation of the decay $B_s^0 \to K^{*0}\overline{K}^{*0}$*, LHCb-ANA-2011-035. [Cited in pages 62 and 67].

[173] Particle Data Group, K. Nakamura *et al.*, *Review of particle physics*, J. Phys. **G37** (2010) 075021. [Cited in pages 63, 64, 78, and 180].

[174] T. Skwarnicki, *A study of the radiative CASCADE transitions between the Upsilon-Prime and Upsilon resonances*, Ph.D. thesis, INP, Cracow, Poland, 1986, DESY-F31-86-02. [Cited in pages 65 and 97].

[175] ARGUS collaboration, H. Albrecht *et al.*, *Exclusive Hadronic Decays of B Mesons*, Z. Phys. **C48** (1990) 543. [Cited in pages 67 and 99].

[176] A. Hoecker *et al.*, *TMVA - Toolkit for Multivariate Data Analysis*, PoS **ACAT** (2007) 040, arXiv:physics/0703039. [Cited in pages 67 and 100].

[177] LASS collaboration, D. Aston *et al.*, *A study of $K^-\pi^+$ scattering in the reaction $K^-p \to K^-\pi^+n$ at 11 GeV/c*, Nucl. Phys. **B296** (1988) 493. [Cited in pages 76 and 123].

[178] R. Aaij *et al.*, *Tagged time-dependent angular analysis of $B^0_s \to J/\psi\phi$ decays with $\sim 337\, pb^{-1}$*, LHCb-ANA-2011-036. [Cited in page 76].

[179] LHCb collaboration, R. Aaij *et al.*, *Determination of f_s/f_d for 7 TeV pp collisions and a measurement of the branching fraction of the decay $B^0 \to D^-K^+$*, Phys. Rev. Lett. **107** (2011) 211801, arXiv:1106.4435. [Cited in page 79].

[180] B. Adeva *et al.*, *Analysis of $B^0 \to \phi K^{*0}$*, LHCb-ANA-2012-033. [Cited in page 80].

[181] G. J. Feldman and R. D. Cousins, *A Unified Approach to the Classical Statistical Analysis of Small Signals*, Phys. Rev. **D57** (1998) 3873, arXiv:physics/9711021. [Cited in page 89].

[182] W. A. Rolke, A. M. López, and J. Conrad, *Limits and Confidence Intervals in the Presence of Nuisance Parameters*, Nucl. Instrum. Meth. **A551** (2005) 493, arXiv:physics/0403059. [Cited in page 89].

[183] BaBar collaboration, B. Aubert *et al.*, *Observation of $B^0 \to K^{*0}\overline{K}^{*0}$ and search for $B^0 \to K^{*0}K^{*0}$*, Phys. Rev. Lett. **100** (2008) 081801, arXiv:0708.2248. [Cited in pages 91, 116, 142, 143, and 144].

[184] Belle collaboration, C.-C. Chiang *et al.*, *Search for $B^0 \to K^{*0}\overline{K}^{*0}$, $B^0 \to K^{*0}K^{*0}$ and $B^0 \to K^+\pi^-K^\mp\pi^\pm$ Decays*, Phys. Rev. **D81** (2010) 071101, arXiv:1001.4595. [Cited in pages 91 and 116].

[185] M. Pivk and F. R. Le Diberder, *${}_s\mathcal{P}lot$: A statistical tool to unfold data distributions*, Nucl. Instrum. Meth. **A555** (2005) 356, arXiv:physics/0402083. [Cited in pages 96, 108, and 112].

[186] E. Ben Haim and L. Henry, *Correcting ${}_s\mathcal{P}lots$ in the presence of fixed yields*, LHCb-INT-2016-014. [Cited in pages 96 and 112].

[187] D. Martínez Santos and F. Dupertuis, *Mass distributions marginalized over per-event errors*, Nucl. Instrum. Meth. **A764** (2014) 150, arXiv:1312.5000. [Cited in page 97].

[188] G. A. Cowan, D. C. Craik, and M. D. Needham, *RapidSim: an application for the fast simulation of heavy-quark hadron decays*, Comput. Phys. Commun. **214** (2017) 239, arXiv:1612.07489. [Cited in page 98].

[189] B. Adeva *et al.*, *Analysis of $B^0_s \to K^{*0}\overline{K}^{*0}$*, LHCb-ANA-2012-109. [Cited in pages 103 and 133].

[190] A. A. Gallas Torreira *et al.*, *Study of the $B^0 \to \rho^0(770)K^*(892)^0$ mode and amplitude analysis of $B^0 \to (\pi^\pm\pi^\pm)(Kp\pi^-)$ decays*, LHCb-ANA-2016-076. [Cited in page 104].

[191] J. Garcia Pardinas *et al.*, *Measurement of the CP-violating phase $\phi_s^{d\bar{d}}$ in quasi-two-body $B_s^0 \to (K^+\pi^-)(K^-\pi^+)$ decays*, LHCb-ANA-2016-014. [Cited in page 104].

[192] L. Anderlini *et al.*, *The PIDCalib package*, LHCb-PUB-2016-021. [Cited in page 108].

[193] LHCb collaboration, R. Aaij *et al.*, *Measurement of $\sigma(pp \to b\bar{b}X)$ at $\sqrt{s} = 7$ TeV in the forward region*, Phys. Lett. **B694** (2010) 209, arXiv:1009.2731. [Cited in page 112].

[194] LHCb collaboration, R. Aaij *et al.*, *Production of J/ψ and Υ mesons in pp collisions at $\sqrt{s} = 8$ TeV*, JHEP **06** (2013) 064, arXiv:1304.6977. [Cited in page 112].

[195] R. Aaij *et al.*, *Tagged time-dependent analysis of $B_s^0 \to J/\psi K^+K^-$ and $B_s^0 \to J/\psi\pi^+\pi^-$ decays with 1.0 fb^{-1}*, LHCb-ANA-2012-067. [Cited in page 124].

[196] M. Grabalosa Gandara *et al.*, *First observation of the $B^0 \to \rho^0\rho^0$ decay and amplitude analysis of $B^0 \to (\pi^+\pi^-)(\pi^+\pi^-)$ decays*, LHCb-ANA-2013-054. [Cited in page 175].

USC UNIVERSIDADE DE SANTIAGO DE COMPOSTELA